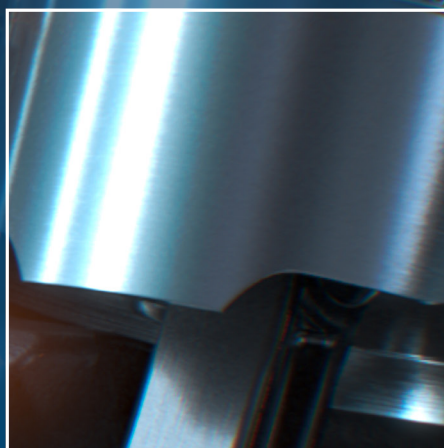
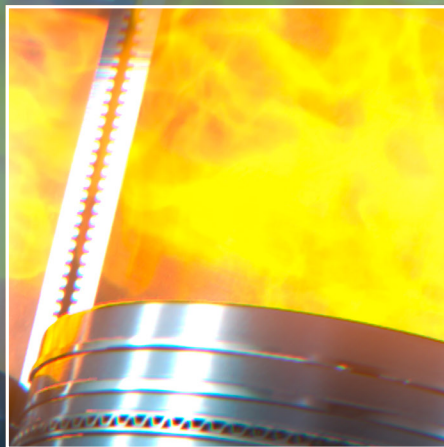


Dynamic Pressure and Temperature Measurement and Calibration



**Special Journal for the Economy and Science Official
Information Bulletin of the Physikalisch-Technische Bundesanstalt
Braunschweig and Berlin**

Volume 132, No. 4, December 2022

**Dynamic Pressure and
Temperature Measurement
and Calibration**

Inhalt

▪ Foreword	5
<i>R. Wynands</i>	
▪ Where research meets industry	7
<i>C. Adolfse</i>	
▪ The DynPT project – an overview	9
<i>R. Wynands, R. Högstöm</i>	
▪ Development of a dynamic pressure standard for calibrations of dynamic pressure sensors at TUBITAK UME	13
<i>Y. Durgut, R. Yilmaz, A. Hamarat</i>	
▪ Of squids and spheres: PTB's drop-weight apparatus	17
<i>R. Wynands, S. Quabis, S. Derksen, O. Slanina</i>	
▪ Guideline on the development of dynamic pressure standards covering the pressure range from 0.1 MPa to 400 MPa with response times in the range of μ s to ms.	25
<i>R. Högstöm, S. Saxholm, M. Aspiala, J. Hämäläinen, J. Salminen, C. Sarraf, R. Wynands, S. Quabis, Y. Durgut, G. Jönsson, E. Amer, M. Liverts, S. Sundarapandian, C. Adolfse</i>	
▪ Validation of dynamic temperature calibration methods for the range up to 3000 °C, with a response time below 1 ms	59
<i>S. Sundarapandian, M. Liverts, G. Jönsson, P. Broberg, A. Fateev, G. Sutton, D. Lowe, R. Högstöm, S. Saxholm</i>	
▪ Validation of IR-based and UV-based sensors for dynamic temperature measurements	73
<i>A. Fateev, A. Öster</i>	
▪ Validation of a fiber optic based dynamic thermometer	83
<i>G. Sutton, D. Lowe, A. Sposito, A. Öster, V. Grahn, P. Nyberg, J. Hyvönen, J. Leino</i>	
▪ Validation of a prototype commercial dynamic pressure sensor	107
<i>E. Amer, G. Jönsson</i>	
▪ Validation of a novel dynamic pressure sensor	115
<i>M. Aspiala, J. Hämäläinen, T. Sillanpää, S. Nyssönen, S. Saxholm, R. Högstöm, J. Salminen</i>	

Foreword

Robert Wynands¹

¹ Priv.-Doz. Dr. Robert Wynands (PTB), Department "Velocity", E-mail: robert.wynands@ptb.de

The world is dynamic, not static. And so is the field of measurement. Dynamic quantities need to be measured with sensors that are characterized for and calibrated with dynamic loads. In this volume of PTB Mitteilungen the focus is on dynamic measurements of pressure (ambient to 400 MPa) and temperature (ambient to 3000 °C) with temporal resolution of milliseconds or faster. This is an important range for applications, for instance the optimization of internal combustion engines (that continue to be with us for some time to come, running on different types of fuel), control of industrial processes, and safety testing.

Currently, however, sensors for pressure and temperature can be calibrated only with static loads, not on the time scales of milliseconds required by many applications. At those faster time scales, sensors are known to exhibit dynamic responses different from the static ones. Therefore, calibration facilities for truly dynamic calibration of pressure and temperature sensors are needed.

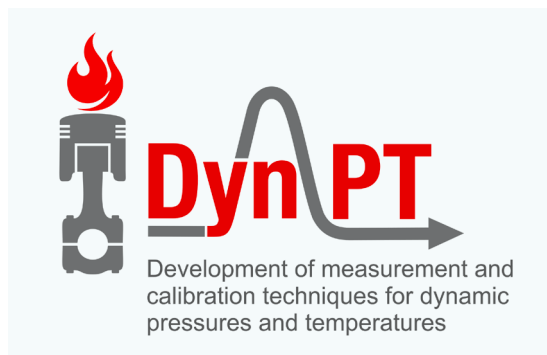


Figure 1:
The DynPT logo

In particular, the question of traceability of such dynamic pressures and temperatures must be addressed.

Furthermore, the sensors used in dynamic applications often must withstand harsh conditions. Better sensors with better lifetime would be beneficial for those applications.

To improve the state of the art of dynamic measurement and calibration of pressure and



Figure 2:
The DynPT team just before the start of the project, taken in "static mode". See the figure in the next article for the picture taken in "dynamic mode"

temperature, a group of European metrologists teamed up under the name of “DynPT” (Fig. 1), with partial funding by the European Union within the EMPIR programme (Fig. 2). They could build upon foundations laid in another European project (“Dynamic”) co-funded under the EMRP program from 2011-2014. The DynPT project started in 2018 with a consortium coordinated by VTT MIKES, the Finnish national metrology institute, and composed of scientists and engineers from national metrology institutes, universities, and industry. Several of the project’s results have been collected in the present volume of PTB Mitteilungen. Most of them constitute deliverables of the project that in this way find a wider distribution.

Like in all areas of society, the project had to deal with the special challenges posed by the COVID-19 pandemic. For instance, key parts of the project were the testing of sensor prototypes of one partner at test ranges operated by another partner. When travel restrictions and laboratory closures came into effect, these activities were severely impacted. Nevertheless, basically all objectives of the project were met: New sensors, new measurement techniques, new calibration options for dynamic measurements of pressure and temperature are available now. Which is not to say that there might not be room for improvement in the coming years!

Where research meets industry

Carel Adolfse¹

¹ Carel Adolfse
(Minerva
meettechniek B.V.,
The Netherlands),
E-mail: carel.adolfse@minerva-calibration.com

On January 18, 2017 I was invited for a meeting at VSL, our national metrology institute (NMI) in the Netherlands, to propose a technical challenge we were working on which might have the potential to be signed up for an EMPIR project. I have been partially involved in another EMPIR project 14IND06 in the field of small differential and low absolute pressures so I had basic knowledge on what EMPIR and Horizon 2020 were about and I was enthusiastic to promote our technical challenge with the potential that I could share my challenge with a group of scientists and researchers.

Although I have been working a long time in metrology, before 14IND06 I did not have any idea that Europe has a vision to make the European research and innovation system more competitive on a global scale and that there is a significant budget available.

During that day in 2017 at VSL a wide variety of technical challenges were presented by different

companies, but none of the challenges presented made it to EMPIR.

VSL suggested that it might be interesting for us to join a project which was close to our proposal. Our proposal was related to fast and precise control of pressures up to 400 MPa where in our static pressure world “fast” means a timescale of 30 seconds. A proposal from the Finnish NMI (VTT MIKES) amongst others was also about generating quickly changing pressures in that range, but in this case “fast” meant generating pressure pulses in milliseconds. I was intrigued both by the subject and the opportunity to join a European group of scientists and researchers which in the case of this project also perfectly reflects one of the goals to link the scientific community to industry.

It took me like 5 minutes to decide to join the project and here we are in 2021. A lot has happened since the start in 2018 in the project but also in the rest of the world. Luckily, we were able



Figure 1:
Group photo after
the project has
started. Note the in-
crease in dynamics
from the previous
photo (see Fig. 2 in
the previous article
in this volume)

to meet each other in person during a couple of meetings and workshops before COVID-19 hit. It is amazing, though, that despite COVID-19 travel restrictions we were able to have efficient and meaningful online meetings and workshops since the beginning of 2020 and were able to complete basically all deliverables.

Having said that, I strongly hope that in the future meetings in person will be the standard again as although we all think we live our lives dedicated to the rules of physics, we remain social beings where real contact with others is so important!

Many thanks to all the colleagues in this project for all the work they performed and all the knowledge shared:

Anders, Christophe, Alexander, Gavin, Gerard, Gustav, Michael, Markus, Menne, Robert, Sembian, Sari, Susanne, Yasin, Richard and all others who have made this project a success.

This project (17IND07) has received funding from the EMPIR programme co-financed by the Participating States and from the European Union's Horizon 2020 research and innovation programme.

References

- [1] Project website:
<https://dynamic-pretemp.com/>
- [2] Euramet project page:
<https://www.euramet.org/research-innovation/search-research-projects/details/project/development-of-measurement-and-calibration-techniques-for-dynamic-pressures-and-temperatures/>
- [3] LinkedIn group:
<https://www.linkedin.com/groups/12123594>

The DynPT project – an overview

Robert Wynands¹, Richard Högström²

¹ Priv.-Doz. Dr. Robert Wynands (PTB), Department "Velocity", E-mail: robert.wynands@ptb.de

² Dr. Richard Högström (VTT), National Metrology Institute VTT MIKES, E-mail: richard.hogstrom@vtt.fi

Introduction

The DynPT project, under its full name of "Development of measurement and calibration techniques for dynamic pressures and temperatures", had the overall objective of improving the accuracy and reliability of pressure and temperature measurements in dynamically changing conditions. It received funding within the 2017 "industry" call of the EMPIR framework, and thus was co-financed by the Participating States and from the European Union's Horizon 2020 research and innovation programme. The consortium comprised a total of 11 partner institutions, with 7 National Metrology Institutes, two universities, and two industrial partners (Fig. 1), so that good coverage of the interest of a wide range of stakeholders could be achieved:

1. VTT Technical Research Centre of Finland Ltd, Centre for Metrology MIKES, Espoo, Finland
2. ENSAM, École Nationale Supérieure d'Arts et Métiers, France
3. NPL, NPL Management Limited, United Kingdom
4. PTB, Physikalisch-Technische Bundesanstalt, Germany
5. RISE, RISE Research Institutes of Sweden AB, Sweden
6. TUBITAK, Türkiye Bilimsel ve Teknolojik Arastirma Kurumu, Turkey
7. VSL, VSL B.V., Netherlands

8. DTU, Danmarks Tekniske Universitet, Denmark
9. KTH, Kungliga Tekniska Högskolan, Sweden
10. Minerva, Minerva meettechniek B.V., The Netherlands
11. Wärtsilä, Wärtsilä Finland Oy, Finland.

Dynamic measurements are a key requirement for process control in several demanding applications, such as automotive, marine and turbine engines for modern fuels, manufacturing processes, and ammunition and product safety. Establishing SI traceability for these measurements will significantly improve the quality of measurements and thus support the innovation potential and competitiveness of European industry. The project aimed at this purpose through the development of dynamic measurement standards and methods

Figure 1: The DynPT consortium represents a wide European cross-section



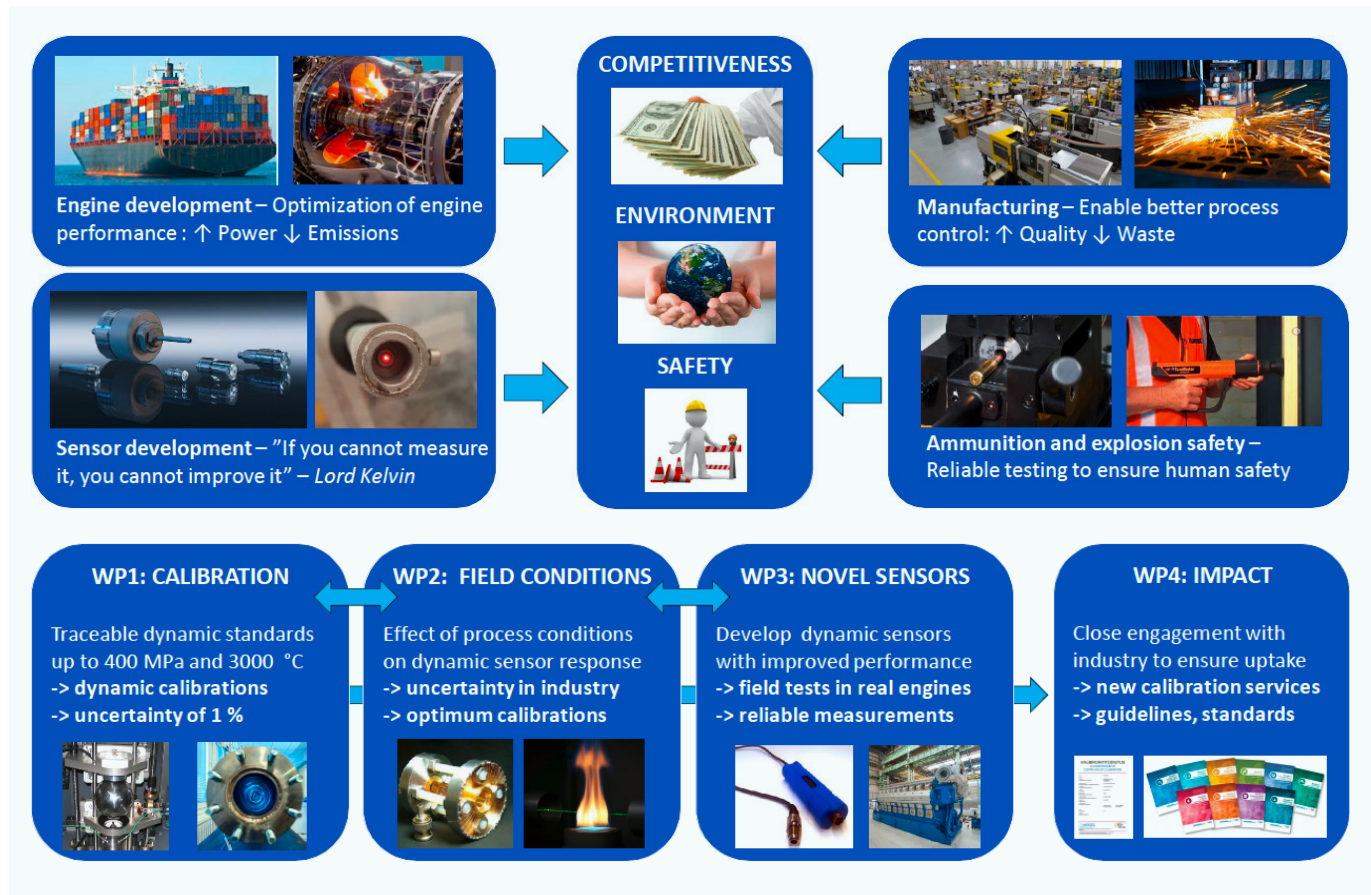


Figure 2: Workpackage structure and objectives

and through characterized sensor technologies including means of estimating measurement uncertainties in real process conditions.

2. DESCRIPTION OF THE WORK

The project had five specific objectives:

1. To provide traceability for dynamic pressure and temperature through development of measurement standards and validated calibration procedures.
2. To quantify the effects of influencing quantities on the response of dynamic pressure and temperature sensors, in order to determine the appropriate calibration procedures and measurement uncertainties for industrial measurements.
3. To develop new measurement methods and sensors for measuring dynamic pressure and temperature in demanding industrial applications, and to demonstrate the improved accuracy and reliability obtained with those.
4. To validate all methods and sensors developed in this project through demonstrations in selected industrial applications.

5. To ensure by close engagement with industry that the developed calibration and measurement techniques and technology are adopted by them.

The workpackage structure is illustrated in Figure 2.

Immediate project goals

The challenge is that in many industrial applications pressure and temperature measurements are performed under dynamically changing conditions. The research performed in this project improved the accuracy and reliability of pressure and temperature measurements in these challenging conditions. The three-year project (plus a half-year extension to mitigate the COVID-19-related impediments for joint work) has fulfilled its objectives.

New calibration services: Traceable dynamic pressure calibration services have been introduced by VTT (Finland) and ENSAM (France). These services are already available to customers. The services are based on the dynamic pressure primary measurement standards. A drop weight device is ready for service with a liquid pressure medium in the dynamic pressure range of approximately 3 MPa to 40 MPa, with expanded

measurement uncertainty of approximately 1.5 % ($k = 2$). A collective standard (fast opening device and shock tube combined) is ready for service with a gaseous pressure medium in the dynamic pressure range approximately 0.01 MPa to 0.5 MPa and a frequency range of 1 Hz to 10 kHz. Both methods are providing metrological traceability to the SI units for dynamic pressure.

Emphasis has been placed on bridging the gap between the lower-pressure range (covered by shock tubes) and the higher-pressure range (covered by drop-weight devices), see Figure 3. While the project brought some progress in this respect, the gap is not yet satisfactorily closed, and work in this direction is still on-going.

New secondary calibrator: A dynamic pressure secondary calibrator for pressures up to 30 MPa was also developed in the project. It is designed to be suitable for industrial field use, and traceability is provided through a reference sensor, which is calibrated using a dynamic pressure primary measurement standard.

Heating option: In many cases of industrial applications where dynamic pressures are measured, dynamic temperature changes take place at the same time. As a result of this project, validated calibration procedures now enable calibrations at conditions that better correspond to actual use of dynamic pressure sensors. For this purpose, the project has developed and applied a heating option for the dynamic pressure sensor to be calibrated. This means in practice that the pressure calibration can be performed at elevated temperatures.

Novel dynamic temperature sensor: A novel fiber-optics ultra-high-speed combustion pyrometer has been successfully designed, developed, and tested during the project. The new instrument is traceably calibrated to the international temperature scale ITS-90 over the range 1073 K to 2873 K, with residuals < 1 %. Its speed was proved in test with the fireball generated by explosive charges.

Novel dynamic pressure sensor: An improved and novel dynamic pressure sensor was designed during the project (Figure 4). Its measuring range is up to approximately 35 MPa and operating temperature range is up to 400 °C. Due to its robust (patented) structure the sensor lifetime should be very much extended compared to many existing products.

Long-term goals

The project has helped along the path towards four long-term goals:

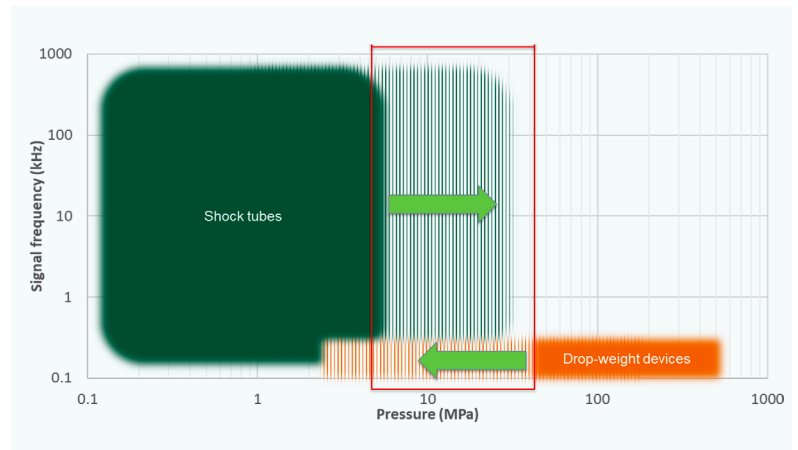


Figure 3: Bridging the gap between lower and higher dynamic pressures available for traceable dynamic calibration. The cross-hatched range is what was aimed for in the DynPT project.

1. That metrologically traceable dynamic pressure and temperature calibrations are actively used, and as a default, among the end users at all user levels (National Metrology Institutes, accredited calibration laboratories, industrial end users, sensor and calibrator manufacturers).
2. That the novel and reliable dynamic pressure and temperature sensors developed during the project are widely available and used.
3. That dynamic pressure calibrators, which are suitable for everyday industrial use, are available on the market.
4. That calibration and measurement guides are available, findable, and widely used.

This last goal, in particular, is actually reached with this volume of PTB Mitteilungen. Some of the project's deliverables were in the form of guides and other publications. Rather than letting them sit in some reporting folder, this volume brings these guides to the light and makes them available to the end user.

Reference

- [1] <https://dynamic-prestemp.com>



Figure 4: A robust pressure sensor based on a patented design

Development of a dynamic pressure standard for calibrations of dynamic pressure sensors at TUBITAK UME

Y. Durgut¹, R. Yilmaz², A. Hamarat³

In many important areas such as combustion analysis, automotive industry, turbomachines, aerodynamics, fluid power and control, measurements of time-varying (dynamic) pressures are required, with amplitudes from a few Pascal (Pa) to a few Giga Pascal (GPa) and frequencies ranging from below 1 Hz to approximately 1 MHz. Pressure values that vary depending on time are defined as dynamic pressure. Dynamic pressure transducers with very fast response times are used to reliably measure dynamic pressure. This type of transducer must be calibrated against a reference dynamic pressure to be applied.

This study aims to introduce a newly developed primary level dynamic pressure standard to be used in the traceable dynamic calibration of dynamic pressure sensors according to the International System of Units (SI). The primary level system was developed at TÜBİTAK UME National Metrology Institute. It works based on a dropping mass principle. The reference pressure created by this system is obtained by dividing the impact effect created by the mass dropped on the piston-cylinder by the piston-cylinder area. The measurement range of the developed system is from 50 MPa to 500 MPa with a 2 % ($k = 2$) uncertainty level. The observed signal during the measurement is a half-sine-shaped signal and (3–5) milliseconds wide.

1. Introduction

Pressure is the result of the motion and transfer of the momentum of molecules in a transmitting fluid (gas or liquid) to a surface where pressure is said to act on a microscopic level. The magnitude of applied pressure changes with the number and the momentum of molecules impacting the surface on which pressure is measured. On a macroscopic level pressure p is generally defined as the total

force F , perpendicular to a surface of area A , as given in Equation (1):

$$p = \frac{F}{A} \quad (1)$$

where p is the pressure, F is the force and A is the area.

The pressure is defined as static when it remains constant for a significant amount of time. Generally, it is expected to be unchanged during the complete measurement. However, there are some phenomena where pressure varies significantly in a short time. In such cases, pressure is said to be dynamic pressure. In that case, the measurand is not a single time-invariant value of pressure, but rather a time-dependent pressure function as given in equation (2).

$$p = p(t). \quad (2)$$

It is very frequent to see applications of dynamic pressure measurement around us. Accurate dynamic pressure measurements are necessary for product development, diagnosis and troubleshooting, control of production processes and product maintenance in several application areas. Briefly, some of the application areas are combustion engines, further automotive applications like the development of airbag systems, turbomachinery, aerodynamics, acoustics, production processes, fluid power and control, robotics, medicine and ergonomics, blast waves, and ballistics [1].

Dynamic pressure converters, whose response times are quite fast, are used to reliably measure dynamic pressure values. Since internationally recognized measurement methods and reference measurement devices are still under development in the field of dynamic pressure, verification and calibration of dynamic pressure converters are performed using static pressure devices [2, 3]. This

¹ Dr. Yasin Durgut, TUBITAK National Metrology Institute (TUBITAK UME), Turkey, E-mail: yasin.durgut@tubitak.gov.tr

² Recep Yilmaz, TUBITAK National Metrology Institute (TUBITAK UME), Turkey, E-mail: yilmaz.recep@tubitak.gov.tr

³ Abdullah Hamarat, TUBITAK National Metrology Institute (TUBITAK UME), Turkey, E-mail: abdullah.hamarat@tubitak.gov.tr

can lead to significant measurement errors because the dynamic and static properties of pressure transducers may differ significantly. Since the need for dynamic pressure measurements has increased significantly in recent years, it is necessary to calibrate dynamic pressure transducers against a dynamic reference pressure. For this purpose, measurement methods and devices have emerged that adopt different approaches [2, 3]. In a method known as the shock tube method, a rapid increase in pressure is achieved thanks to a ruptured diaphragm. This method can measure pressures up to 20 MPa with a measurement uncertainty of 1 %. But in this method, there are limits such as the low measurement range, the shape of the signal formed, and the impractical use. The need to change the measurement diaphragm after each measurement and the inability to reach high dynamic pressure values are the main problems in the shock tube [2].

Another method is the stepped pressure generator, which can produce reference pressures at the primary level of different amplitudes thanks to a quick-opening valve. With this method, a pressure of up to 830 MPa has been reached. But

the pressure that can be obtained can be gradual, as in the shock tube [2].

Another method is to obtain a primary level of reference pressure using a drop-weight system. In this method, the instantaneous pulse pressure is created by dropping the mass on the piston-cylinder unit. This pressure pulse is used as a reference dynamic pressure source. Previously, this method was used as a secondary standard, by connecting a reference sensor to the same piston-cylinder unit as the sensor to be calibrated. But since the reference pressure needs to be determined at the primary level, drop-weight systems have been developed and started to be used as primary level dynamic reference pressure calibration systems.

In the PTB measurement system, the reference pressure is based on the principle of measuring the changing refractive index of the fluid used in the piston-cylinder with the help of a laser vibrometer. In the VTT MIKES system, it is aimed to measure the acceleration of the moving mass. Studies conducted at the National Institute of Metrology of TUBITAK UME also work according to the drop-weight principle, similar to the VTT MIKES system. But unlike the VTT MIKES system, spherical type laser reflectors were used to avoid losing laser signal synchronization during the acceleration measurement, and the distance the laser light has to travel is shortened. In addition, measuring a single acceleration value during the piston-cylinder impact of the falling mass is not sufficient, since the mass will be subjected to axial rotation movements due to the vibrations that occur during the fall of the mass. For this reason, the time-dependent displacement value of three different points of the falling mass is measured with the help of a laser interferometer. From this, an average acceleration value for the falling mass can be calculated.

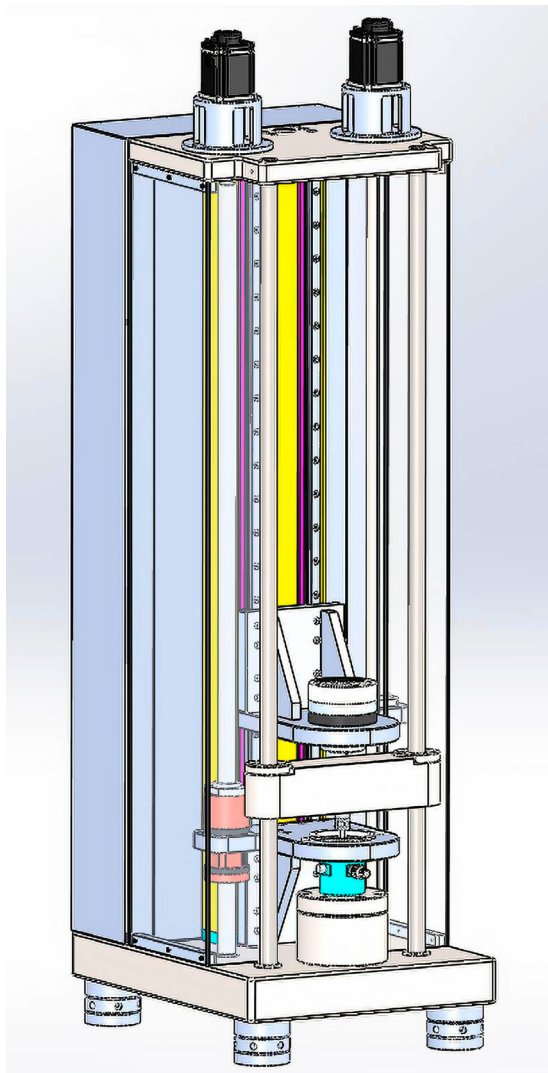
2. Material and method

The primary level dynamic pressure standards with dropping mass consist of a piston-cylinder unit connected to an oil-filled volume and test sensors connected to the same volume. The piston-cylinder unit transmits the short pressure pulse generated by the impact of the mass falling on it from a certain height to the test sensor via the transmission fluid. The reference pressure value generated by this system is calculated by various methods depending on the working principle.

2.1 Design of the system

The system is composed of a base, two servo motors with a programmable logic controller (PLC), an

Figure 1:
Schematic picture
of the system
developed at
TUBITAK UME



electromagnet, a dropping mass guided by two guiding rods, a laser interferometer, a measurement head unit including a piston-cylinder unit, a test sensor hole, and the pressure transmission liquid. An electromagnet is used to move the guided mass upward and downward. A laser interferometer is measuring the displacement of the dropping mass versus time. The shock acceleration of the mass is determined by the second derivative of the displacement. One of the motors is used to move the electromagnet while the second motor moves the rebound system to catch the dropping mass. The collection of data about the displacement of the falling mass against time is carried out with a data collection system that works with a high acquisition speed. In this way, it is possible to measure the maximum value of the acceleration of the mass hitting the piston cylinder. To avoid memory problems on the system computer, the data is not collected continuously, and the start of data collection is triggered by the separation of the falling mass from the electromagnet [4].

A schematic picture of the system developed at TUBITAK UME is given in Fig. 1.

The primary level dynamic pressure standard developed at TUBITAK is shown in Fig. 2.

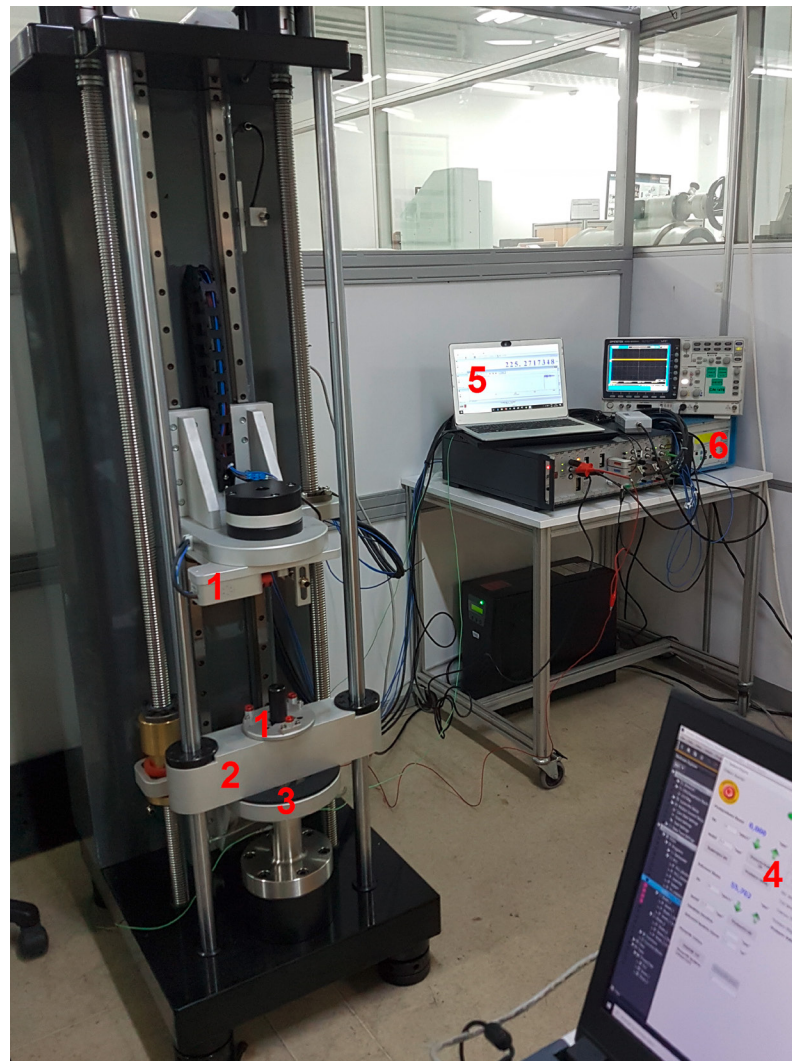
A detailed schematic design of the measurement head unit of the system is given in Fig. 3.

2.2 Working principle

The total force value is multiplied by the total moving mass by adding the local gravitational acceleration in that area to this average impact acceleration. This falling mass creates a pressure pulse when hitting the piston-cylinder set in a volume filled with liquid, to which the sensors to be tested are connected. The pressure pulse value formed is also divided by the total force in the piston-cylinder area. The area of the piston-cylinder unit is obtained by combining the separately measured form data of the piston and cylinder parts with an integration method.

Different types of liquid have been used to transmit the impact pressure to the piston-cylinder and the sensor to be tested. The fact that the physical properties of these liquids are different also causes the signal periods and frequencies obtained in the system to be different.

The resulting reference pressure is calculated by dividing the impact force, calculated by the measured acceleration value, by the piston-cylinder area. Pressure measurements made with this device can be increased from around 50 MPa to 500 MPa by increasing the mass's drop height. The width of the half-sine signal obtained according to the type of fluid used under the piston-cylinder is around (3–5) milliseconds.



Development work is ongoing in the system and measurements can be made with an uncertainty of 2 % for the current situation ($k = 2$).

The force in formula (1) is the multiplication of the weight of the total mass and the acceleration of this total mass value. The acceleration of the total mass is subjected to free fall in the system. In this mass group, there is the free-falling mass, the piston mass moving with this mass, and the mass of the oil in the closed volume. The total mass is called m_{total} . The acceleration of the total mass is calculated by adding the gravity acceleration to the shock acceleration. From here, the reference pressure can be expressed in more detail with the formula (3).

$$\frac{m_{\text{total}} \cdot (a_{m, \text{maximum}} + g)}{A} \quad (3)$$

where m_{total} is the total moving mass, $a_{m, \text{maximum}}$ is the maximum shock acceleration of the dropping mass, and g is the local gravity acceleration.

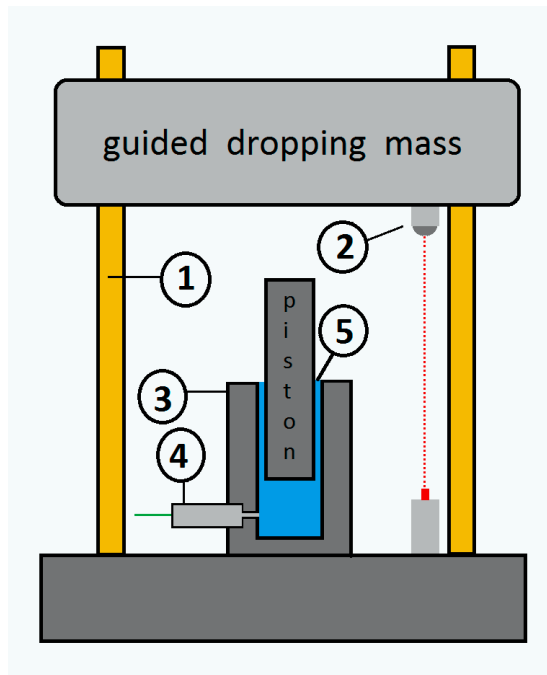
The effective area of the piston-cylinder unit is determined by dimensional measurements. To calculate the effective area of the piston-cylinder with dimensional methods, data were obtained

Figure 2: Dynamic pressure standard developed at TUBITAK.

1. Laser head and laser retroreflector,
2. Dropping mass,
3. Measuring head,
4. Controlling software for the dynamic pressure system,
5. Control system for the laser interferometer,
6. Amplifier for dynamic test sensors

Figure 3:
Schematic diagram
of the measurement
head.

1) Guiding rods for
the dropping mass,
2) Laser Interfero-
meter,
3) Piston-cylinder
unit,
4) Dynamic test
sensor,
5) Fluid used as the
pressure transmissi-
on medium.



at 8 points in the form of X, Y and Z coordinates at 45-degree intervals in each circular cross-section with a coordinate measuring machine (CMM). Piston and cylinder height is 20 mm and the working range is determined as 15.5 mm. A total of $24 \times 155 = 3720$ data points belonging to the piston and cylinder were obtained by taking $8 \times 3 = 24$ X, Y, and Z data every 0.1 mm along the height of 15.5 mm. The average radius values for each section were found by compiling the data obtained from the CMM device in an Excel program. Radius values are used in the calculation of other parameters in Dadson's theory [5], which are used to determine the effective area with dimensional data at zero pressure. Simpson's 3/8 rule, one of the numerical integral calculation methods, was used to solve the integrals in the equation, and the solution was implemented in a numerical integration solver program.

3. Conclusions

This study aims to develop a dynamic pressure standard that is expected to operate at the primary level to calibrate dynamic pressure sensors. System design, basic elements and working principles are explained. The working pressure range is from 40 MPa to 500 MPa with an expanded uncertainty from 1.5 % to 5 %. The developed system works with liquid media. The impact signal shape produced by the standard is a half-sine with (3–5) ms width.

In future studies, it is aimed that the repeatability and the stability of the standard be increased. It is expected to get more precise measurement results.

Acknowledgments

This study was carried out within the scope of the “Development of Measurement and Calibration Techniques for Dynamic Pressure and Temperature Techniques project (short name: 17IND07 DynPT)” supported by the European Union within the scope of EMPIR European Joint Research projects. EMPIR research projects are funded by the European Union's Horizon 2020 research and innovation program and EMPIR participating states.

References

- [1] J. Hjelmgren, Dynamic Measurement of Pressure – A Literature Survey, SP Measurement Technology REPORT vol. 34, SP Swedish National Testing and Research Institute, 2002
- [2] J. Salminen, R. Högström, S. Saxholm, A. Lakka, K. Riski, M. Heinonen, Development of a primary standard for dynamic pressure based on drop weight method covering a range of 10 MPa–400 MPa, *Metrologia*, Volume 55, Number 2, p 52, 2018. <https://doi.org/10.1088/1681-7575/aaa847>
- [3] J. Salminen, S. Saxholm, J. Hämäläinen, R. Högström, Advances in the traceable calibration of cylinder pressure transducers, *Metrologia*, Volume 57, Number 4, 045006, 2020. <https://doi.org/10.1088/1681-7575/ab8fb9>
- [4] Y. Durgut, E. Bağcı, E. Akşahin, A. T. İnce, An investigation on characterization of dynamic pressure transducers using material impact test machine, *Journal of the Brazilian Society of Mechanical Sciences and Engineering*, pp 1–11, 2017. DOI: <https://doi.org/10.1007/s40430-017-0763-3>
- [5] R. S. Dadson, S. L. Lewis, G. N. Peggs, The pressure balance — Theory and practice, National Physical Laboratory, London: HMSO, pp xii + 290

Of squids and spheres: PTB's drop-weight apparatus

R. Wynands¹, S. Quabis², S. Derksen³, O. Slanina⁴

Introduction

For pressures above a few ten MPa, dynamic pressure standards based on a dropping weight are the method of choice. This method is based on generating a pressure pulse by dropping a weight onto a piston-cylinder assembly connected to a liquid-filled measurement chamber. The customer device to be calibrated (device under test, DUT) is connected to this fluid and its response to the pressure pulse is recorded and compared to the amplitude of the pressure pulse applied.

In a drop-weight apparatus, half-sine shaped pressure pulses with a duration of a few milliseconds can be generated with peak amplitudes reaching several hundred megapascal. A wide pressure range can be covered, but the frequency range is limited to several hundred hertz. Fortunately, however, for many high-pressure applications where accurate and reliable measurements of dynamic pressure are needed, signal frequencies are in the range of drop-weight devices. Therefore, despite their inherent limitations, drop-weight devices are considered well suited for providing traceability for dynamic pressure in the high-pressure range.

This is especially true for our main interest, the traceable measurement of the dynamic pressure developing inside an ammunition cartridge while it is fired. International regulations [1] limit the pressure to a caliber-specific maximum, to prevent damage to the weapon or powder-operated tool, which in turn protects the user from harm by exploding devices. The good match between the pulse in a drop-weight device and the pressure pulse inside a firing cartridge is illustrated in Fig. 1 for the case of a common hunting caliber, .30-06 Spring.

Two different principles of operation can be used in a drop-weight machine intended for primary calibrations. One is to monitor the

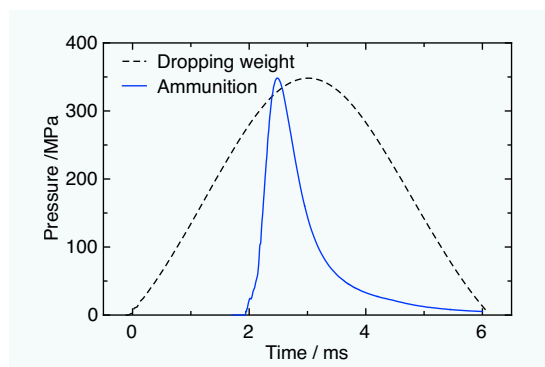
deceleration of the weight after it has hit the piston and to integrate the motion to obtain the force acting on the dropping mass. When the area of the piston is known, this gives the pressure inside the fluid. This operating principle is explained, for instance, in the contribution by Durgut et al. in this volume.

The other method is described here, the so-called refractive index method.

Experimental setup

The general idea of the refractive index method is to make use of a physical mechanism that is so fast that there is no relevant difference between static excitation and excitation at kHz frequencies [2]. In this way, the static response of a medium can be transferred to the kHz dynamic range.

The experimental setup (Figure 2) illustrates the principle. A steel ball (7 kg) drops onto a piston-cylinder assembly filled with a hydraulic, optically transparent liquid (in the following, for simplicity we assume sebacate, but other liquids are possible). The motion of the piston compresses the liquid so that its density increases, and with it its index of refraction. A laser beam passes the cell via sapphire windows. The optical path length, i. e., the integral of the product of index of refraction and distance travelled in the medium,



¹ Priv.-Doz. Dr. Robert Wynands (PTB), Department "Velocity", E-mail: robert.wynands@ptb.de

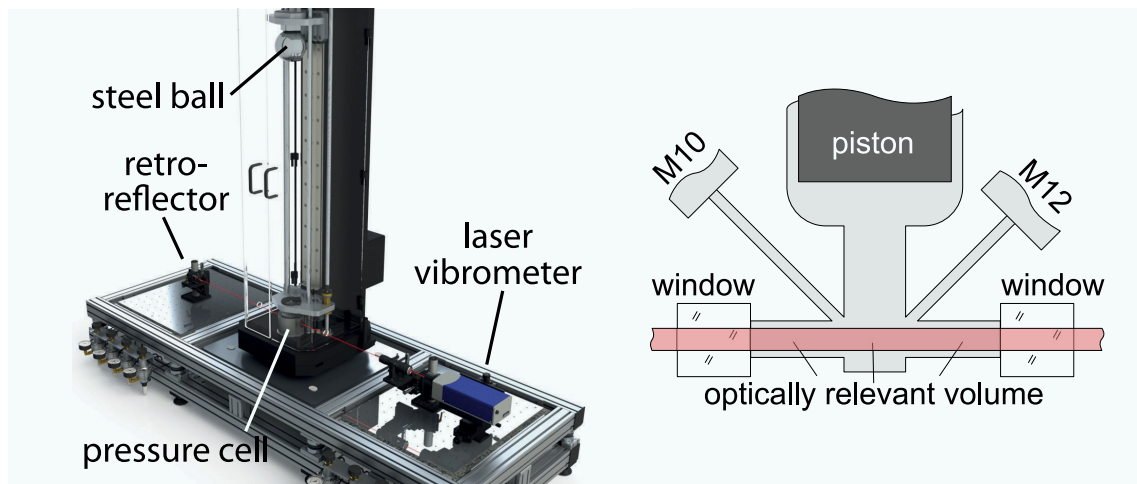
² Dr. Susanne Quabis (PTB), Working Group "Dynamic Pressure Measurement", E-mail: susanne.quabis@ptb.de

³ Stanislaw Derksen (PTB), Working Group "Dynamic Pressure Measurement", E-mail: stanislaw.derksen@ptb.de

⁴ Oliver Slanina (PTB), Working Group "Dynamic Pressure Measurement", E-mail: oliver.slani-na@ptb.de

Figure 1: Comparison of the dynamic pressure pulse shapes inside a hunting cartridge of caliber .30-06 Spring. (solid blue line) and in the PTB drop-weight apparatus (dashed line) when a 7 kg steel ball is dropped from a height of 1 m.

Figure 2: Setup of the drop-weight device with laser-interferometric detection of the index of refraction in a pressurized medium. The sketch illustrates the optically relevant volume and the two threaded slots (marked M10 and M12) for attaching a DUT.



can be measured interferometrically, for instance with a commercial laser vibrometer. When the geometrical length of the cell is known, the index of refraction can be determined. In parallel, the customer's sensor (device under test, DUT) is connected to the same volume and its signal output recorded. When the connection between dynamic pressure p_{dyn} inside the liquid and its refractive index n is known, the sensitivity of the DUT can be established as a function of time over the evolution of the pulse. An important advantage is that the exact shape of the pulse is irrelevant, so neither the piston's shape nor details of its motion need to be known.

A commercial vibrometer is used to detect the change of optical path length during the compression of the fluid. Its sampling rate and its slew rate (ability to track fast changes of path length) are fully sufficient [3]. In fact, the uncertainty due to the measurement of changes of the optical path length – the actual quantity measured! – is negligible.

Motion of the piston

An interesting detail is that the piston is not pushed into the fluid but actually it is hammered

in (Fig. 3). In quick and quickening succession of elastic collisions the piston bounces off the heavy dropping ball and shoots off into the liquid where it is rapidly stopped, only to be caught again by the dropping ball, etc.

The “squid effect”

During early experiments one observed a total drop-out of the vibrometer signal shortly after the pulse had ended [3]. This could be traced back to large bubbles being introduced into the fluid due to cavitation. When the piston travels upwards after having reached the point of maximum compression, it acquires kinetic energy and overshoots its resting position. This tears the fluid apart, causing the formation of bubbles (Fig. 4). It can take several minutes before the medium has re-stabilized and is ready for the next drop of the weight.

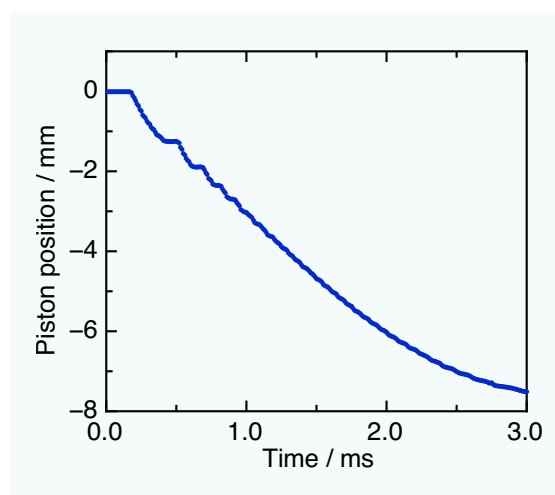
To avoid the cavitation process, two polyimide strings were added to the setup. The piston is free to travel into the cell but on the way up it is stopped at its resting position (Fig. 5). The volume below the piston therefore never exceeds the starting volume, and cavitation is avoided.

This finding might be important for other drop-weight devices. Even when no optical detection within the fluid is used the bubbles introduced might lead to reproducibility issues when drops are following too quickly after each other. Furthermore, some of the bubbles might get trapped at internal cell walls, where they might change the local behaviour of the medium. In a device operating as a secondary standard by comparing the DUT with a reference sensor, this might lead to differences in the actual pressure load that each sensor sees, thus causing calibration errors.

Window motion

Since the laser vibrometer measures the optical

Figure 3: At the beginning of the impact of the weight onto the piston the latter's movement is a series of quick accelerations until after a while weight and piston travel into the fluid together



path length, i. e., the integral of the product of index of refraction and geometrical path length, one needs to consider the effect of changes of the cell length, for instance due to the outward motion of the windows when the cell expands under the internal pressure. The size of this effect can be measured with the help of a second laser vibrometer. For this auxiliary experiment, one vibrometer each is placed on a side of the cell and focused on the respective window [3]. The sum of the distance signals from vibrometer to window gives the change of cell length with high precision (Fig. 6). It changes at a rate of

$$b_{\text{cell}} = 0.200 \text{ } \mu\text{m/MPa}.$$

A finer detail is the length of the optical path inside the sapphire windows. Due to the construction of the cell, they get compressed during the pulse. The amount of compression can be measured in the auxiliary experiment, too, by looking at the period of the interference fringes on the amplitude signal of the vibrometer, caused by multiple reflections inside a window (Fig. 7). With the known (and pressure-independent) index of refraction of sapphire one arrives at a compression rate

$$n(T) = n_0 - 0.00037129 \times \left(\frac{T}{^\circ\text{C}} - 20\right) - 7.5653 \times 10^{-6} \times \left(\frac{T}{^\circ\text{C}} - 20\right)^2. \quad (3)$$

$$b_{\text{sapph}} = -0.0114 \text{ } \mu\text{m/MPa}.$$

When the geometric length of the cell and the thickness of the windows are corrected with the rates b_{cell} and b_{sapph} , the pressure-dependent index of refraction of the fluid can be extracted from the total optical path change.

Establishing traceability

There are two different routes to provide traceability by establishing the link between dynamic pressure p_{dyn} inside the liquid and its refractive index n . Both routes need a quantitative way to relate the measured index of refraction to the density ρ of the medium. For dilute transparent gases, the Clausius-Mossotti relation provides this link:

$$\rho = \frac{n^2 - 1}{n^2 + 2} \times \frac{1}{K_{\text{CM}}}, \quad (1)$$

where K_{CM} is a constant containing the molecular polarizability.

The constant K_{CM} is a combination of natural constants:

$$K_{\text{CM}} = \frac{N_A \beta}{3 \epsilon_0 M_{\text{mol}}}. \quad (2)$$

Here N_A is the Avogadro constant, β the molecular polarizability, ϵ_0 the permittivity of vacuum, and M_{mol} the molar mass of the fluid. The constant K_{CM} can be obtained by inserting into the Clausius-Mossotti equation the calibrated values of n_0 and ρ_0 at ambient pressure $p_0 = 0.101325 \text{ MPa}$. In the range between $18 \text{ }^\circ\text{C}$ and $22 \text{ }^\circ\text{C}$, the temperature

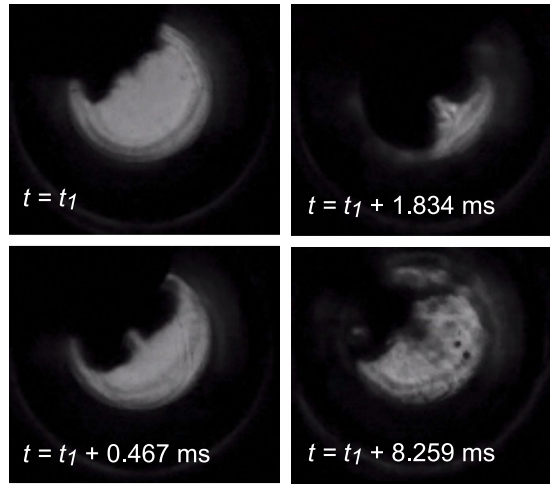


Figure 4: Four frames of a high-speed camera movie showing the propagation of cavitation bubbles into the optical volume. The visual impression when watching the movie is that of ink being injected from above, like from a squid trapped inside the cell. In the last frame, the bubbles have begun to close but some small, rather stable bubbles can remain for several minutes

dependence of n_0 is given by a second-order polynomial in temperature T . For each of the wavelengths listed in a PTB calibration sheet for n_0 , the coefficients are tabulated. Interpolation of the coefficients to the vibrometer wavelength results in

This gives $n_0 = 1.449110$ at $T = 20 \text{ }^\circ\text{C}$ and ambient pressure with a relative uncertainty of 5×10^{-6} . With $\rho_0 = 914.074 \text{ kg/m}^3$ (calibrated at PTB) at the same temperature and ambient pressure one obtains $K_{\text{CM}} = 0.000293566 \text{ m}^3/\text{kg}$ with a relative uncertainty of $6.6 \times 10^{-9} \text{ m}^3/\text{kg}$. Under the assumption that the molecular polarizability of sebacate does not change within the temperature range around room temperature, one could expect that K_{CM} determined from $\rho(T)$ and $n(T)$ should be constant. Although at first glance this does not

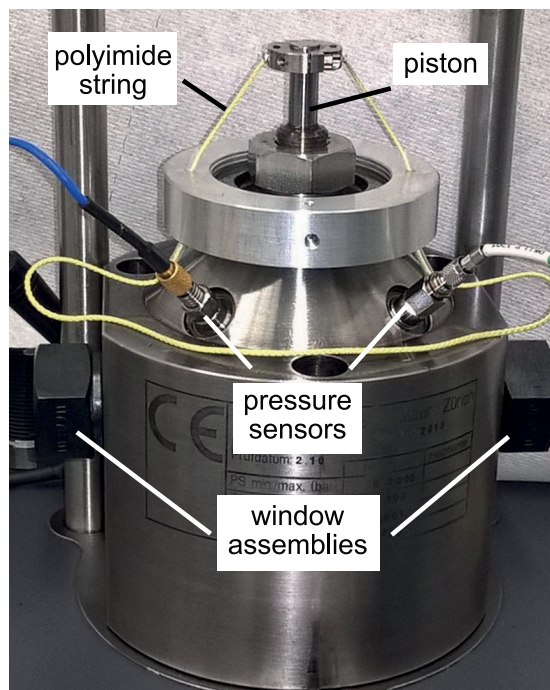


Figure 5: Detail of the pressure cell, showing the polyimide strings needed to prevent the formation of cavitation bubbles

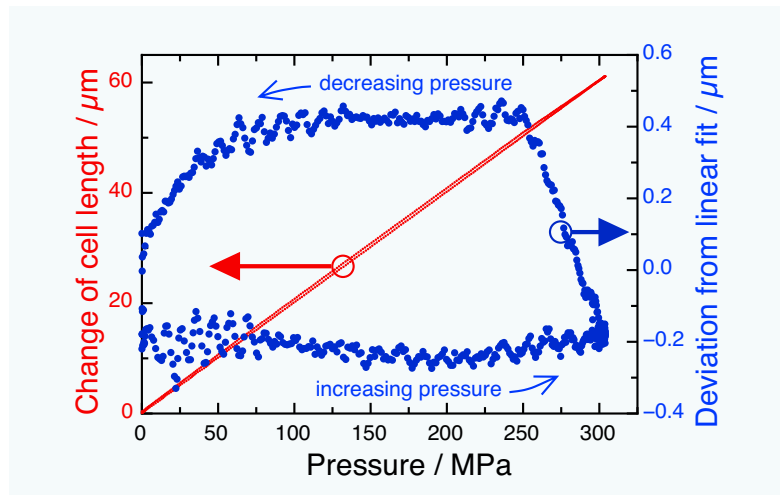


Figure 6: Change of the geometrical dimension of the cell

seem to be the case (Fig. 8) one must bear in mind the measurement uncertainties of these two input quantities. Compared to the uncertainty, the temperature dependence of the calculated K_{CM} is not significant near the operating temperature of 22 °C (where the calculated $K_{CM} = 0.0002935451 \text{ m}^3/\text{kg}$).

With the molar mass $M_{mol} = 426.68 \text{ g/mol}$ specified by the supplier (we assume an uncertainty of 10 μg/mol here) the value of K_{CM} given above implies a molecular polarizability of sebacate of $(5.52496 \pm 0.00018) \times 10^{-39} \text{ Fm}^2$ or $(3.32721 \pm 0.00011) \times 10^{-15} \text{ Fm}^2/\text{mol}$. Because K_{CM} (when determined from Eq. 1) is proportional to $1/\rho_0$, the combination $\rho_0 K_{CM}$, and therefore all indices of refraction determined using Eq. 1, are independent of ρ_0 .

It has long been known that the Clausius-Mossotti equation does not necessarily hold exactly in liquids, because the local environment of a molecule might not be isotropic [4]. An additional anisotropy might be added due to the shear forces encountered when the liquid is moved

along the cell volume during compression and relaxation; mechanically induced birefringence has been observed in a sebacic acid ester closely related to sebacate [5]. In our case, the optically active volume has a diameter smaller than the bore hole in the cell so that molecules near the walls do not contribute to the optical signal. Mechanically induced birefringence therefore does not play a role here. In addition, the dependence between density and index turns out to be closely linear. Therefore, the validity of the Clausius-Mossotti equation is assumed for the time being.

We will now discuss both traceability routes in turn. Common to both of them is that they establish traceability of dynamic pressure in a primary way. In particular, no measurements of dynamic pressure are needed that rely on measurements with statically calibrated sensors. This also holds for the material parameters that enter the evaluation.

Traceability route 1: Isothermal-adiabatic method

Following the original idea [2], the setup is operated in two steps. First, the piston is replaced by a fixed pressure duct, and pressure is increased very slowly (hours), monitored by a statically calibrated pressure sensor (relative calibration uncertainties of less than 10^{-4} are possible, i. e., negligibly small for our purposes here). This process is isothermal and provides a relation between optical path change Δs_{iso} and static pressure p_{iso} . From Δs_{iso} one obtains n_{iso} when the cell length is known, including the small correction due to the motion of the windows.

Using the Clausius-Mossotti relation, the measured n_{iso} can be converted into the density ρ_{iso} as a function of static pressure p_{iso} .

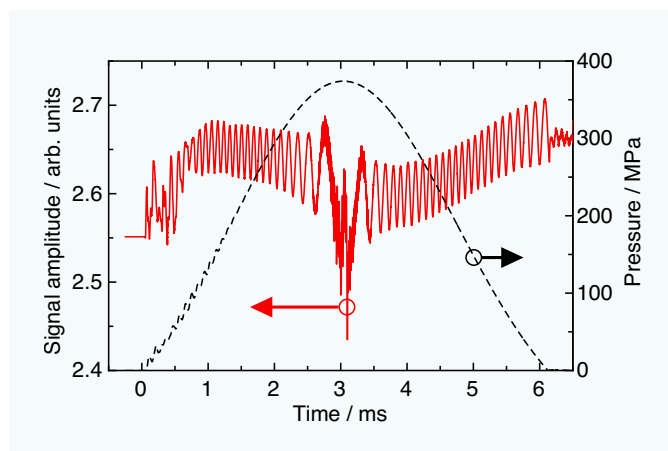


Figure 7: Interference fringes on the amplitude signal of the vibrometer. The changing period reflects the changing compression speed of the window during the pressure pulse and can be used to determine the compression rate b_{sapph} .

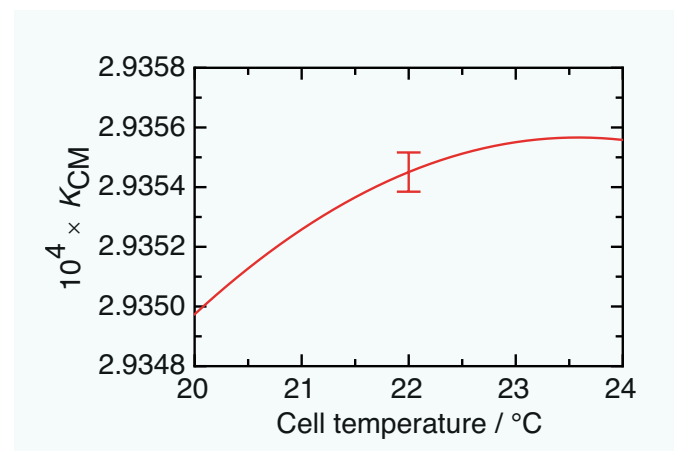


Figure 8: Apparent temperature dependence of K_{CM} , as calculated from the temperature dependence of ρ and n . The error bar ($k = 1$) is based on the uncertainties of ρ and n .

The isothermal experiment can also be used to determine the isothermal bulk modulus K_T or its inverse, the isothermal compressibility κ_T :

$$\frac{1}{K_T} = \kappa_T = \frac{1}{\varrho} \left(\frac{d\varrho}{dp} \right)_T. \quad (4)$$

For this purpose, the 12650 data points of isothermal pressure as a function of density are reduced by averaging 50 points each into one synthetic data point. Then, for each pair of adjacent synthetic data points i and $i - 1$, Eq. (4) is discretized by forming the quotient

$$K_T = \varrho_i \times \frac{p_i - p_{i-1}}{\varrho_i - \varrho_{i-1}}. \quad (5)$$

It was checked that the cloud of points $K_T(p_i)$ for the branch of increasing pressure overlaps with the data points for the decreasing branch (dots in Fig. 9). A parabola is fitted to these points, with the coefficients in Table 1. A linear fit instead of a quadratic one basically gives the same result except for a small overestimation of the experimental data at the highest pressures. From the quadratic fit one obtains $K_T = (1603.23 \pm 5.4)$ MPa at ambient pressure.

constant term	(1602.02 ± 5.4) MPa
linear term	11.9359 ± 0.072
quadratic term	$(-0.003177 \pm 0.00019)/\text{MPa}$

Table 1: Coefficients for the quadratic fit of the pressure-dependent bulk modulus K_T of sebacate

In a second step, the experiment is run dynamically, with the weight dropping onto the piston while monitoring the optical path Δs_{adi} with the laser interferometer. This process is adiabatic, as can be seen by the fact that the weight bounces up to almost the same height from which it was dropped; only a few percent are missing, probably due to friction of the piston and due to the kinetic energy transferred to piston and fluid on the way up. From Δs_{adi} one obtains n_{adi} and ρ_{adi} in the same way as in the first step.

A complication arises because the connection between density and pressure depends on the character of the thermodynamic process:

$$\frac{dp}{p} = \left(\kappa_T - \alpha \frac{\partial T}{\partial p} \right) \times dp. \quad (6)$$

The first term on the right-hand side is the isothermal compressibility (applicable in the first experimental step here), whereas the second term gives the additional contribution due to adiabatic heating in the dynamic case. Here α is the volume thermal expansion coefficient. The effect can be seen in Fig. 10, where the isothermal and the adiabatic compression in the PTB drop-

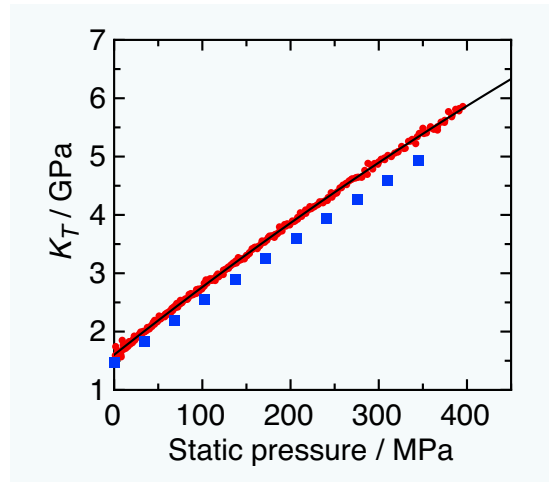


Figure 9: Isothermal bulk modulus of sebacate, as determined from the isothermal compression step of the experiment. Small red dots: experimental data; solid line: parabolic fit. The blue squares indicate data from [6]

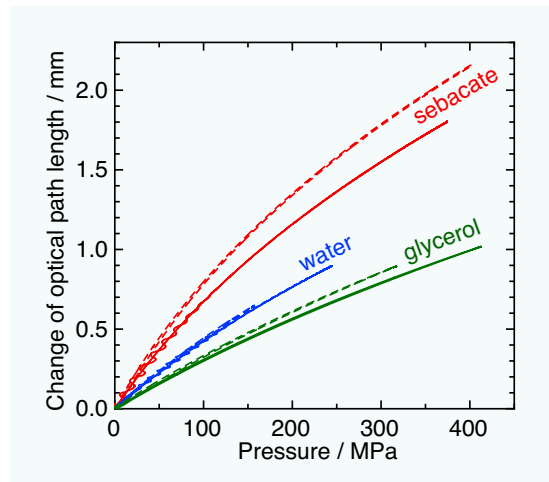


Figure 10: Comparison of isothermal and adiabatic compression for sebacate, water, and glycerol. Solid lines: adiabatic compression; dashed lines: isothermal compression

weight apparatus are compared for three different hydraulic fluids: sebacate, water, and glycerol.

Relation (6) can be used to translate between the isothermal step 1 and the adiabatic step 2 by calculating a correction factor r . Details have been provided in [3].

All material parameters are pressure dependent in general. The pressure dependence of $\partial T/\partial p$ has been measured by Ardia [7], that of κ_T in the isothermal part of the experiment (Fig. 9). No literature data for $\alpha(p)$ could be found, so older data [8] was rearranged to represent sebacate density as a function of temperature for different fixed pressures. The derivative with respect to temperature gives α as a function of pressure (Fig. 11). This data can be fitted by a polynomial of fourth order (Table 2).

The result of following traceability route 1 is illustrated in Fig. 12, where two sets of two curves of dynamic pressure p_{dyn} as a function of time are compared. The solid lines show the dynamic pressure extracted via the optical route, as explained above. The dashed black lines give the signal p_{val} of a piezoelectric transducer used as a reference for validation purposes. This sensor has been calibrated statically, but it has a fast response (resonance frequency well above 10 kHz), so that

Figure 11: Thermal volume expansion coefficient of sebacate for $T = 22\text{ °C}$ as a function of pressure, derived from data in [8]. The solid line is a fit of a fourth-order polynomial to the data points.

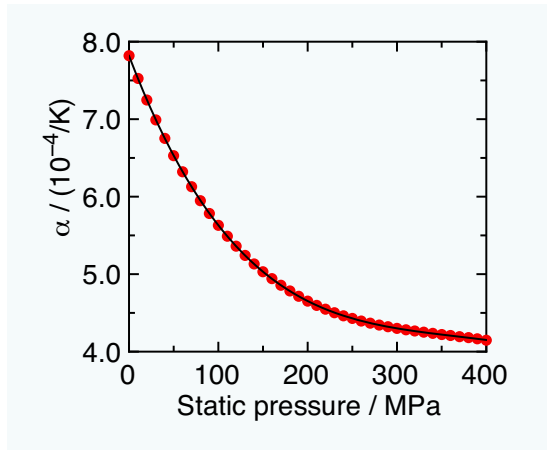
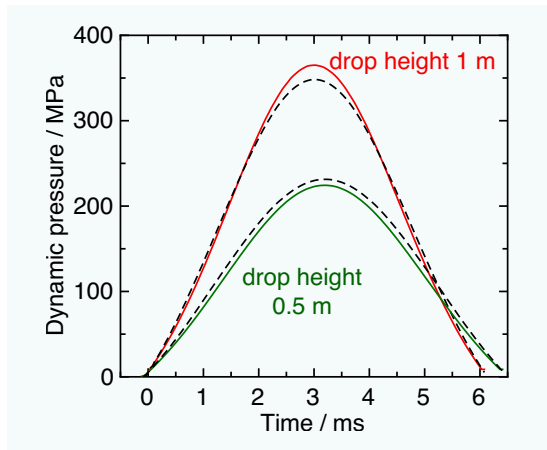


Figure 12: Dynamic pressure as a function of time determined along traceability route 1 (solid lines) and the output p_{val} from a validation sensor (dashed lines), for two different drop heights of the weight



its output is suitable for the purpose of validation of the drop-weight method.

The dynamic pressure p_{dyn} deviates from p_{val} in that it is too low for lower pressures and too high for higher pressures (Fig. 13). The fact that in Fig. 13b the green and the red curve are almost overlapping is an indication that the difference is primarily pressure-dependent and not dependent on the slope of the pressure-vs-time curve. For the 1 m case, the difference in peak amplitudes is about 5 %.

Central to the applicability of this route 1 is that the material parameters κ_T , α , and $\partial T/\partial p$ must be known, including their pressure dependence and experimental uncertainty. A further caveat is that the “sebacate” used by one research team to determine one property might not be of exactly the same chemical composition as the “sebacate” used

Table 2: Coefficients for the quartic fit of the pressure-dependent coefficient of thermal volume expansion α of sebacate at $T = 22\text{ °C}$

constant term	$(7.81709 \pm 0.00080) \times 10^{-4}/\text{K}$
linear term	$(-3.0260 \pm 0.0028) \times 10^{-6}/\text{K}/\text{MPa}$
quadratic term	$(9.706 \pm 0.029) \times 10^{-9}/\text{K}/\text{MPa}^2$
third-order term	$(-1.378 \pm 0.011) \times 10^{-11}/\text{K}/\text{MPa}^3$
fourth-order term	$(6.755 \pm 0.14) \times 10^{-15}/\text{K}/\text{MPa}^4$

by another team to determine another property. One can therefore speculate that the observed difference is partly due to insufficiently known material parameters and in particular, insufficient consistency when used together in Eq. (6). This indicates a potential challenge for use of the device as a calibration facility because the properties of the hydraulic liquid might have to be monitored closely, including their reproducibility when supply runs out and new fluid must be procured.

The measurement uncertainty along route 1 obviously depends on the uncertainties of the material parameters, which, however, are not always available directly from the source. When reasonable proxies are sought, one finds a relative uncertainty of a peak pressure of 350 MPa of order 2 % (coverage factor $k = 1$), i. e., smaller than the deviations observed between p_{dyn} and p_{val} . Interestingly, the length of the optically relevant volume drops out in first order. Furthermore, the density of the fluid at ambient conditions cancels out exactly, and only its pressure dependence remains. These last two facts are strong points of traceability route 1.

Traceability route 2: Speed of sound method

Along traceability route 2, the isothermal part of the experiment is not needed, only the dynamic part. From Δs_{dyn} , n_{dyn} is obtained using the (pressure-dependent) geometry data of the cell, then ρ_{dyn} is determined via the Clausius-Mossotti relation. The relation between pressure and density,

$$d\rho = \frac{1}{v_s^2} dp \quad (7)$$

can be integrated when the speed of sound, v_s , is known. Here one can use the sebacate data given by Bair [6] as a function of pressure and temperature. By modelling the pressure dependence of this data phenomenologically with a square-root function,

$$v_s = \text{const} + m \sqrt{p - x_0}, \quad (8)$$

Eq. (7) can be integrated analytically and the result solved numerically for the final pressure p_{dyn} (Fig. 14).

Along traceability route 2, p_{dyn} comes out about 10 % too low. Except for the assumption about the validity of the Clausius-Mossotti relation, there are two important parameters entering along traceability route 2: The length of the optical volume (known to within 0.1 mm, corresponding to a contribution of about 15 % to the total uncertainty) and the speed of sound (62 %). For the speed-of-sound data used here [6]

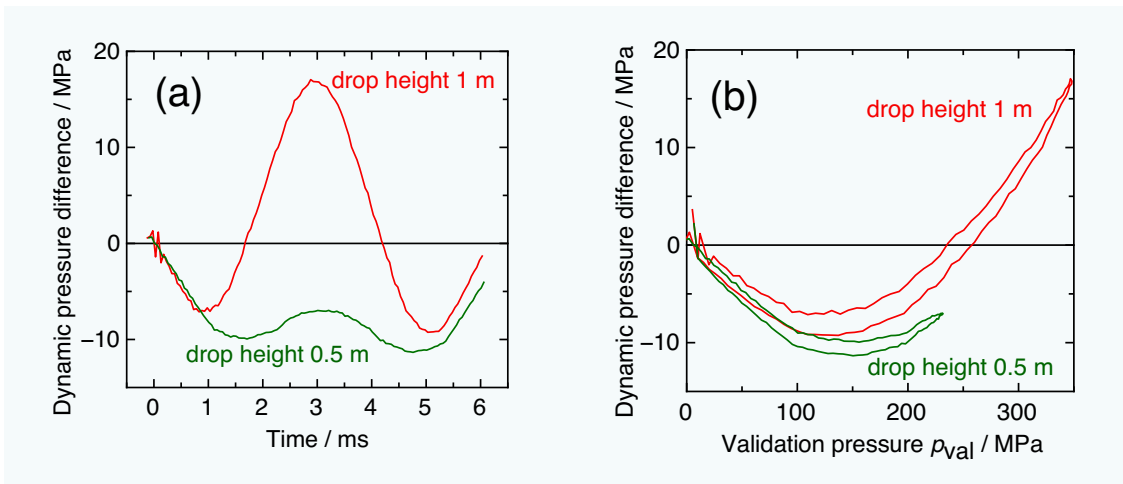


Figure 13: Difference between p_{dyn} determined along traceability route 1 and the pressure p_{val} provided by the high-speed validation sensor recorded at the same time (a: vs. time, b: vs. p_{val})

no measurement uncertainty is given and could not be found in the underlying primary literature, either. Speed of sound measurements in other fluids were made with uncertainties of order 0.3 % or less. The measurements in [6], however, were performed in the ultrasound range (1.5 MHz), whereas the half-sine pulse here corresponds to about 85 Hz. It is well-known that the damping of a sound wave strongly depends on frequency, so also the speed of sound must depend on frequency.

To explore the situation of the difference between p_{dyn} and p_{val} , the evaluation of the dynamic drop data was performed again with the experimental values of the speed of sound increased by an adjustable factor. For a factor of 1.038 one finds that the maximum pressure for a drop height of 1 m is reproduced to within better than 0.1 % (Fig. 15), while at the same time matching the pulse shape very well (Fig. 16). For a drop height of 0.5 m, this same adjustment factor of 1.038 leads to a difference in peak amplitude of 1.7 %. Overall, this could indicate that the speed of sound measured at ultrasound frequencies might not be fully valid at low acoustic frequencies and that it is off not only by a constant factor but by a slightly pressure-dependent one.

The uncertainty of dynamic pressure determination using traceability route 2 is dominated, obviously, by the uncertainty of the pressure-dependent speed of sound in the hydraulic medium. When a speed uncertainty of 0.3 % is assumed, corresponding to the order of magnitude of speed of sound measurements in other fluids, one arrives at a relative uncertainty for a peak pressure of 350 MPa of order 1 % (coverage factor $k = 1$). The short path between density and dynamic pressure is a strong point of this traceability route 2.

Synchronicity

The measurement of the pressure takes place in two separate zones: at the sensing surface of

the DUT and averaged over the optical volume (see Fig. 2). Therefore, it is important to look for delays between the two signals, for instance, due to propagation effects within the fluid. When calibration is performed only regarding the maximum pressure, calibration is easily accomplished by recording both vibrometer and DUT signal with the same acquisition system and then separately looking for the maximum of each signal. This is sufficient because the evaluation procedure is strictly monotonic, i. e., does not cause a change of signal shape that is asymmetric with respect to the maximum.

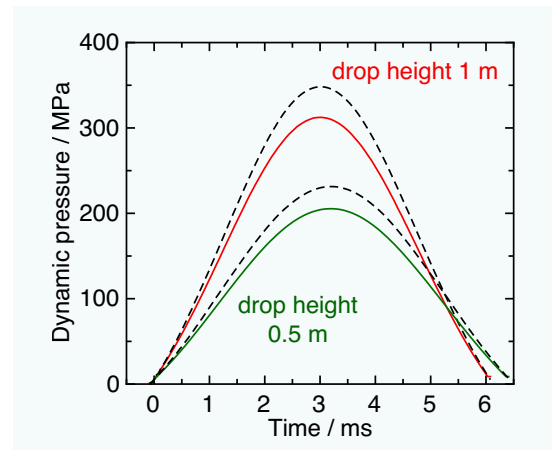


Figure 14: Dynamic pressure as a function of time, determined along traceability route 2 (solid lines), and the output p_{val} from a validation sensor (dashed lines), for two different drop heights of the weight

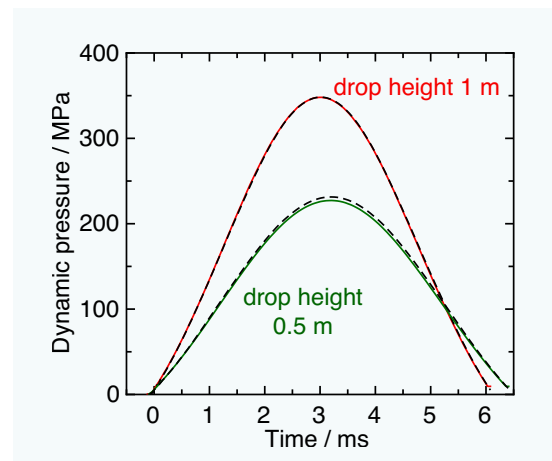
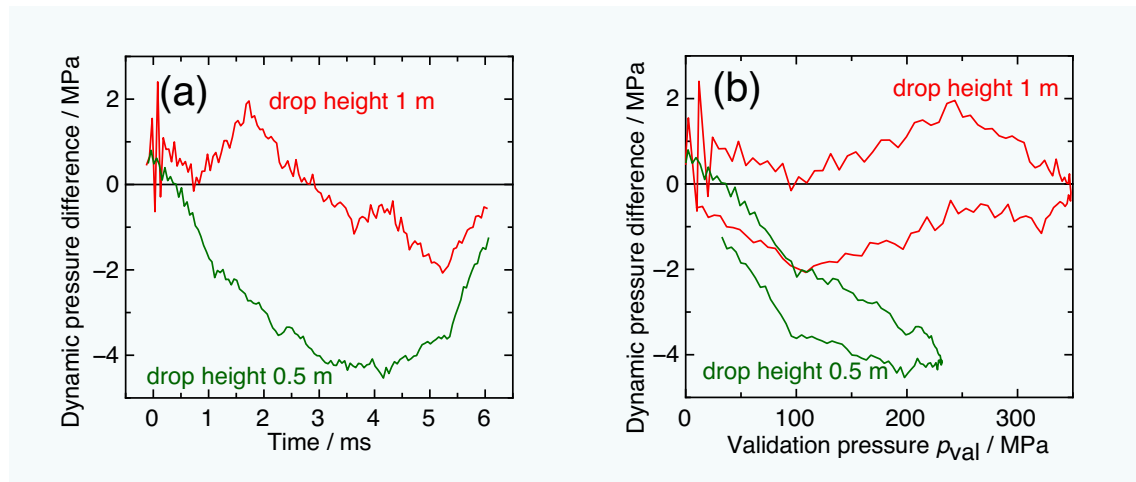


Figure 15: Dynamic pressure as a function of time determined along traceability route 2 (solid lines) and the signal from a validation sensor (dashed black lines), for two different drop heights of the weight. Here, during data evaluation the speed of sound was numerically increased by 3.8 %.

Figure 16:
Difference between ρ_{dyn} determined with a speed of sound numerically increased by 3.8 % and the pressure ρ_{val} provided by the high-speed validation sensor, recorded at the same time (a: vs. time, b: vs. ρ_{val})



For calibration along the full shape of the pulse, one needs to consider the slope of the pressure curves and apply a correction depending on the delay (as observed via the shift of the maxima), or alternatively shift one of the data streams by the corresponding delay before comparing it to the other data stream. Otherwise, calibration errors of about 1 MPa are theoretically possible.

Practical operation of the device

Operation of the drop-weight device is rather complex. In particular, filling of the cell with the hydraulic fluid requires great care to avoid forming or trapping bubbles. It is best performed by placing the cell in a glove box or a similar device, in a mild vacuum. Since a partial refill is required after each change of DUT and a complete refill after one or two dozen drops of the weight (due to the unavoidable loss of fluid along the piston), calibration of a customer DUT is a time-consuming process. For institutions that charge calibration cost according to time needed, it might turn out that operation of the device is not cost-effective, i. e., too expensive for customers.

Use of the device for secondary calibrations

In principle, the drop-weight apparatus could be used as a secondary calibration device. This can be accomplished in two ways: Either by using one of the sensor slots for a reference sensor and the other for the DUT, or by using both sensors for DUTs and performing the evaluation like along traceability route 2, but with a fitted correction factor for the speed of sound.

In both cases, care must be taken to avoid air bubbles that might cause a difference in the response of the two sensor channels. Also, the question of synchronicity must be studied carefully, something that is dependent on the exact structure of the pressure cell.

Acknowledgement

Our deceased colleague Jörg Herbst contributed to the experimental work presented here. We have also profited from the work by many PTB colleagues, in particular in the working groups 1.71, 3.32, 3.33, 4.21, and 5.31, who provided data and calibrations of equipment, cell dimensions and the fluid. This work has been part of the DynPT project, which has received funding from the EMPIR programme co-financed by the Participating States and from the European Union's Horizon 2020 research and innovation programme.

References

- [1] Commission internationale permanente pour l'épreuve des armes à feu portatives (C.I.P.), <https://www.cip-bopb.org>
- [2] T. Bruns, E. Franke, M. Kobusch, *Metrologia* **50**, 580 (2013)
- [3] O. Slanina, S. Quabis, S. Derksen, J. Herbst, R. Wynands, *Appl. Phys. B* **126**, 175 (2020)
- [4] W. E. Danforth, Jr., *Phys. Rev.* **38**, 1224 (1931)
- [5] D. Vorländer, U. Kirchner, *Z. physikal. Chemie* **152A**, 47 (1931)
- [6] S. S. Bair, "High-pressure rheology for quantitative elasto-hydrodynamics", Elsevier Science (Amsterdam etc., 2007)
- [7] A. Ardia, "Process Considerations on the Application of High Pressure Treatment at Elevated Temperature Levels for Food Preservation", PhD Thesis, TU Berlin (2004)
- [8] ASME Research Committee on Lubrication, "Viscosity and density of over 40 lubricating fluids of known composition at pressures to 150,000 psi and temperatures to 425 F", The American Society of Mechanical Engineers (New York, 1957)

Guideline on the development of dynamic pressure standards covering the pressure range from 0.1 MPa to 400 MPa with response times in the range of μs to ms

R. Högström¹, S. Saxholm², M. Aspiala³, J. Hämäläinen⁴, J. Salminen⁵, C. Sarraf⁶, R. Wynands⁷, S. Quabis⁸, Y. Durgut⁹, G. Jönsson¹⁰, E. Amer¹¹, M. Liverts¹², S. Sundarapandian¹³, C. Adolfse¹⁴

Preface

This article is an abridged version of deliverable D1 in the EMPIR project 17IND07 – DynPT: “Guideline on the development of dynamic pressure standards covering the pressure range from 0.1 MPa to 400 MPa (with response times in the range of μs to ms) with a target uncertainty of 1 %, including guidelines on the presentation of measurement data independent of the measurement technique (shock tube or drop-weight)”. This project has received funding from the EMPIR programme co-financed by the Participating States and from the European Union’s Horizon 2020 research and innovation programme.

The report has been prepared by Teknologian tutkimuskeskus VTT Oy (VTT) together with project partners from Ecole Nationale Supérieure d’Arts et Métiers (ENSAM), Physikalisch-Technische Bundesanstalt (PTB), VSL B.V. (VSL), Türkiye Bilimsel ve Teknolojik Arastirma Kurumu (TUBITAK), National RISE Research Institutes of Sweden AB (RISE), Kungliga Tekniska Högskolan (KTH) and Minerva meettechniek B.V. (Minerva).

1. Introduction

This report gives guidelines for development of dynamic pressure measurement standards including different techniques needed to cover a wide pressure range from 0.1 MPa to 400 MPa and response times from microseconds to milliseconds. This guideline covers the key aspects that need to be considered when designing, constructing, and validating a dynamic

pressure standard. Ideas for further development of dynamic pressure standards are given to achieve the target uncertainty of 1 %. Finally, a proposal for presenting the measurement data independently of the measurement technique will be given. The guidelines are based on the experience and expertise of the project partners and latest research findings and developments within the DynPT project.

2. Overview of different techniques

The two main approaches for realizing primary standards for dynamic pressure are based on shock tubes and drop-weight techniques. The corresponding pressure and frequency ranges covered with these techniques are shown in Figure 1. Shaded areas in Figure 1 show new developments undertaken in this project with the aim to extend the measurement ranges of both methods to close the gap between shock tubes and drop-weight devices. This is important for investigating the equivalence of dynamic pressure realizations using different methods and to enable traceability in the pressure range from 5 MPa to 40 MPa, which is of special interest to combustion engine applications where accurate and reliable, i. e., traceable, measurements are needed.

As seen in Figure 1, shock tubes typically operate in the low pressure and high frequency range, whereas drop-weight devices are applicable for higher pressures and limited to low frequencies. The operating principle of shock tubes is based on sudden expansion of a gas at high pressure into a gas at low pressure inside a closed long tube, which gives rise to a shock wave propagating along the

¹ Dr. Richard Högström (VTT), *National Metrology Institute VTT MIKES*, E-mail: richard.hogstrom@vtt.fi

² Sari Saxholm (VTT), *National Metrology Institute VTT MIKES*, E-mail: sari.saxholm@vtt.fi

³ Dr. Markus Aspiala (VTT), *National Metrology Institute VTT MIKES*, E-mail: markus.aspiala@vtt.fi

⁴ Jussi Hämäläinen (VTT), *National Metrology Institute VTT MIKES*, E-mail: jussi.hamalainen@vtt.fi

⁵ Juho Salminen (VTT), *National Metrology Institute VTT MIKES*, E-mail: juho.salminen@vaisala.com

⁶ Prof. Dr. Christophe Sarraf (ENSAM), *Laboratoire de Métrologie Dynamique*, E-mail: christophe.sarraf@ensam.eu

⁷ Priv.-Doz. Dr. Robert Wynands (PTB), *Department “Velocity”*, E-mail: robert.wynands@ptb.de

⁸ Dr. Susanne Quabis (PTB), *Working Group “Dynamic Pressure Measurement”*, E-mail: susanne.quabis@ptb.de

⁹ Dr. Yasin Durgut (TUBITAK UME), E-mail: yasin.durgut@tubitak.gov.tr

¹⁰ Dr. Gustav Jönsson (RISE), E-mail: gustav.jonsson@ri.se

¹¹ Dr. Eynas Amer (RISE), E-mail: eynas.amer@ri.se

¹² Dr. Michael Liverts (KTH), E-mail: liverts@mech.kth.se

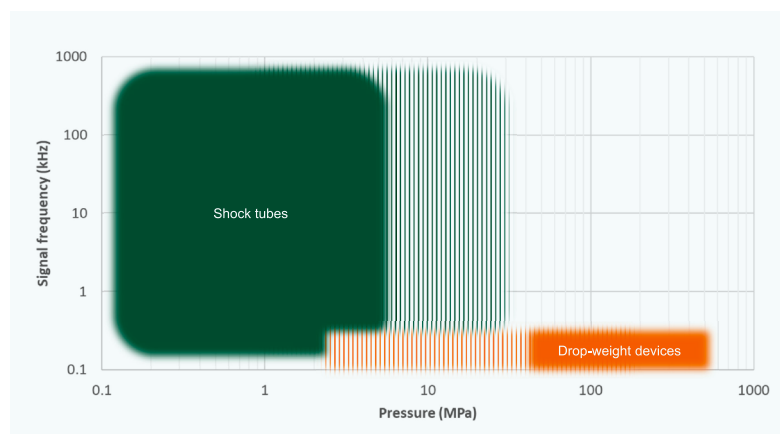
¹³ Dr. Sembian Sundarapandian (KTH), E-mail: sembian@kth.se

¹⁴ Carel Adolfse (Minerva meettechniek B.V., The Netherlands), E-mail: carel.adolfse@minerva-calibration.com

tube. The shock wave produces a rapid, step-like, increase in pressure and temperature, which makes it ideal for calibrating dynamic sensors at highly transient conditions. The time dependent behavior of the pressure step can be calculated based on shock tube theory [1] and accurate measurements of shock wave velocity, static pressures, and temperatures. Owing to the step-like pressure profile, all frequencies in the range limited by the rise time and duration of the step are generated. Rise times are typically on the order of a few hundred nanoseconds and step durations on the order of milliseconds. This translates into a frequency range from less than a kilohertz up to a megahertz. Therefore, the relevant frequency range of high-frequency dynamic pressure sensors is readily covered with the shock tube. However, the maximum pressure amplitude of shock tubes is limited to a few megapascal due to high mechanical requirements. The pressure difference of the expanding gas required for creating higher pressure step amplitudes becomes increasingly larger according to shock wave theory [2], making it an impractical solution for high pressure applications.

For higher pressures, dynamic pressure standards based on the drop weight method are more suitable. The method is based on generating a pressure pulse by dropping a weight onto a piston-cylinder assembly connected to a liquid-filled measurement chamber. In this way, half-sine shaped pressure pulses with a few millisecond duration can be generated with peak amplitudes from a few megapascal up to hundreds of megapascal. With the drop weight method, a very wide pressure range can be covered, but the frequency range is limited to a few tenths of a kilohertz and lower. A combination of high pressure and high frequency would require a considerable amount of energy and there are currently no solutions for generating such pressure signals in a controlled and SI traceable manner. Fortunately, however, in many high-pressure applications where accurate and reliable measurements of dynamic pressure are need, e. g.,

Figure 1: Overview of the pressure and frequency ranges of different techniques for realizing dynamic pressure measurement standards



combustion engines and ammunition testing, signal frequencies are in the range of drop-weight devices. Therefore, despite their inherent limitations, drop-weight devices are considered well-suited for providing traceability for dynamic pressure in the high-pressure range.

In the upcoming sections, general guidelines for designing and constructing dynamic pressure standards based on shock tubes and drop-weight devices will be given. Means to establish traceability and evaluating uncertainties will be presented, including ideas for further development and ways of presenting measurement data.

3. Drop-weight devices

3.1 Operating principle

The main components of a drop-weight device are shown in Figure 2. In the drop-weight device, a pressure pulse is generated by dropping a weight onto a piston, which is connected to a liquid-filled chamber of the measurement head. The impact force causes the liquid to compress inside the measurement chamber, giving rise to a pressure pulse. Sensors under calibration are connected to the measurement chamber through sensor channels on the side of the measurement head, hence the same pressure is sensed by all sensors. Different types of liquids can be used to transmit the impact force to the sensor under calibration. The fact that the physical properties of these liquids are different also causes the signal periods and frequencies obtained in the system to be different.

There are two main approaches for determining the pressure inside the chamber independently from the sensors, namely, by measuring the force acting on the fluid, referred to as the interferometric method [3, 4, 5], or by measuring the pressure-dependent properties of the compressed fluid, the so-called refractive index method [6, 7]. In this report, guidelines for developing primary dynamic pressure standards based on these two approaches are given.

3.2 Dimensioning of mechanical design

Drop-weight devices are frequently modelled as mass-spring systems [8, 9]. This approximation is useful when designing the dimensions of the device, e. g., mass of the drop-weight, drop height, volume of measurement chamber, pressure medium, etc. According to the model, the peak pressure P_{\max} can be derived as

$$P_{\max} = \sqrt{\frac{2mgK}{V_0}} \cdot \sqrt{h}, \quad (1)$$

where m is the mass of the drop-weight, g is the

local gravitational acceleration, K is the bulk modulus of the liquid inside the measurement chamber, V_0 is the volume of the measurement chamber, and h is the drop height of the weight. Moreover, the pulse width τ can be derived as

$$\tau = \frac{\pi}{A_0} \sqrt{\frac{V_0}{K}}, \tag{2}$$

where A_0 is the piston surface area. As an example, a drop-weight with a mass of 11 kg, when dropped from a height of 1 m onto a piston with a surface area of 79 mm², will induce a pressure pulse with maximum amplitude of about 400 MPa and a pulse duration of 5 ms, when the chamber volume is 12 cm³ and glycerol with a bulk modulus of 7.5 GPa [10] is used as the pressure medium. Although the spring-mass model [8] describes the behavior of the drop-weight system quite well, it is not a good basis for establishing traceability, partly because there is very limited published data on the pressure-dependent bulk modulus of liquids at high pressures. In addition, the data sets hardly include any information on the uncertainty or traceability of bulk modulus measurements. Instead, other approaches based on measurement of acceleration of the dropped weight during impact and measurements of the change of refractive index of the pressurized media have been developed within the DynPT project to provide traceability to SI units. The guidelines given in the next sections will describe design principles for developing dynamic pressure measurement standards based on the two approaches.

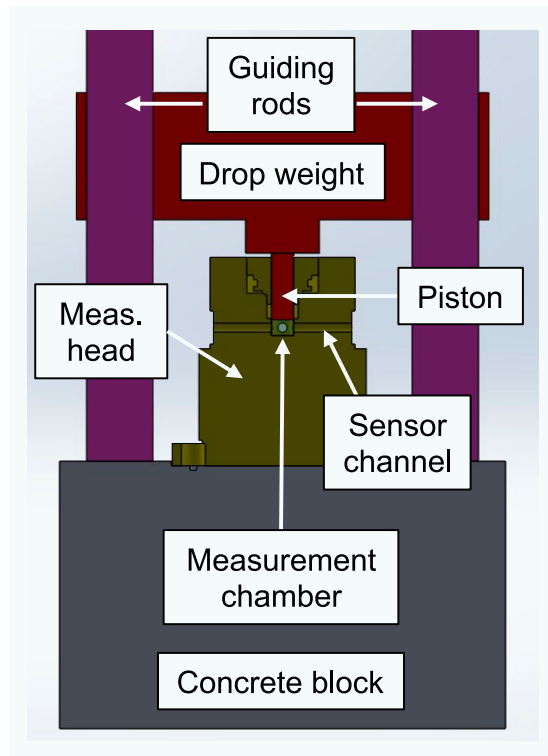


Figure 2: Mechanical drawing of a drop-weight device showing the main components

3.3 SI traceability

The pressure inside the measurement chamber can be derived independently of the properties of the pressurized fluid using the well-known relation

$$P(t) = \frac{F(t)}{A} = \frac{ma(t)}{A}, \tag{3}$$

where F is the impact force acting on the piston and A is the effective area of the piston cylinder unit, m is the mass of the impact mass (dropped

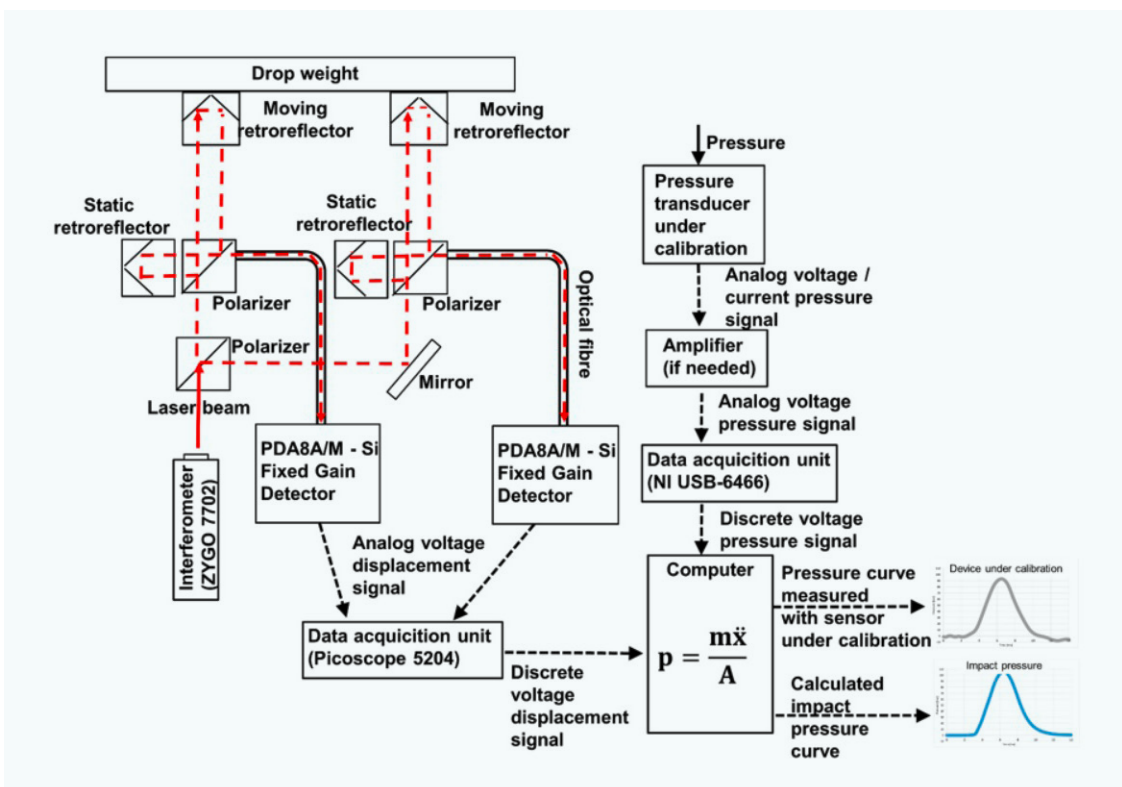


Figure 3: Schematic and signal flow of the VTT MIKES primary dynamic pressure standard [4]

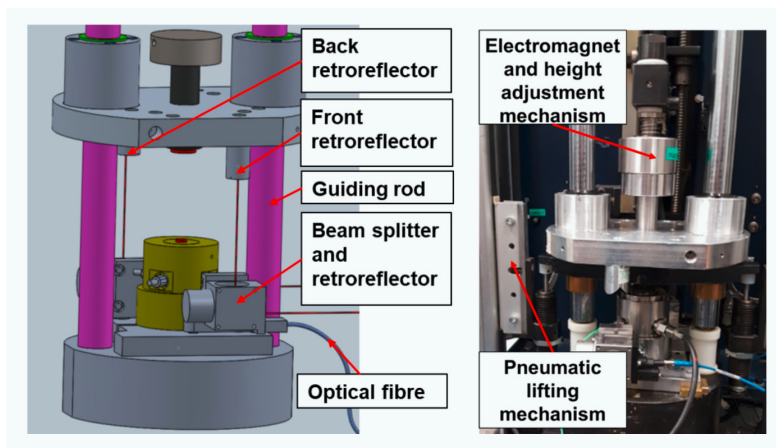


Figure 4: Picture of the VTT MIKES dynamic pressure standard and a schematic showing the main components of the interferometric measurement [4]

weight, piston, and pressure media) and a is the acceleration of the impact mass.

The mass and effective area can be accurately and SI-traceably determined by weighing and geometrical measurements. The acceleration measurement is more demanding and needs to be made in real-time as the drop-weight hits the piston. Acceleration sensors would be an obvious solution, but these are not considered primary, because the sensors need to be calibrated separately, e. g., by means of laser interferometry [11]. To realize a primary measurement of acceleration, laser interferometry is applied directly for measuring acceleration (positive or negative) of the impact mass. Moreover, this approach shortens the traceability route (no need for accelerometers) and thus in principle improves the uncertainty level that can be achieved.

In the next sections, guidelines and examples on realizing the interferometric measurement will be given, as well as aspects that need to be considered when validating the measurement standard.

3.3.1 Interferometric measurement of acceleration

Accurate and traceable measurement of the acceleration is the most important measurement for realizing a dynamic pressure primary standard based on the interferometric method. The inherent accuracy of an interferometric measurement is many orders better than is required for this application. Many different commercial solutions are available that fulfil the accuracy requirements. However, due to the dynamic nature of the measurement, the sampling rate and dynamics of the interferometric setup need to be considered.

In the VTT MIKES dynamic pressure primary standard [4], a dual-beam heterodyne Michelson interferometer setup is applied for accurately measuring the acceleration of the drop-weight during impact (Figure 3 and Figure 4). A 10 MHz HeNe laser is used as a traceable wavelength source. The sampling frequency of the interferometric setup is 250 MHz. The interferometric measurement inherently measures displacement, and therefore acceleration can be derived as the second derivative of the displacement.

The impact of the drop-weight onto the piston will inevitably induce vibrations and tiny deformations in the system, which will induce errors in the interferometric measurement. To minimize these effects, the construction of the device needs to be robust, and the device needs to be firmly fixed to the ground. In the VTT MIKES device, the calibrator frame stands on a granite block, which lies on the concrete floor. Also, all optical components are firmly fixed with screws and the retroreflectors attached to the drop-weight are made from metal to minimize vibration and deformations. In addition, the gap between the guiding rods and the drop-weight needs to be optimized to minimize friction and tilting of the

Table 1: Uncertainty budget for the VTT MIKES dynamic pressure standard

Uncertainty component	Source of uncertainty	Standard uncertainty (%)
$u(m_{tot})$	Impact mass (incl. drop-weight, piston and media)	< 0.1
$u(A)$	Effective area of piston-cylinder unit	< 0.1
$u(a_d)$	Deformation of drop-weight	0.8
$u(a_n)$	Vibration induced noise	0.2
$u(a_t)$	Tilt of the drop-weight	0.1
$u(a_f)$	Friction between piston and cylinder	0.4
$u(\delta P)$	Spread of calibration results	0.4
Combined standard uncertainty ($k = 1$)		1.0
Expanded uncertainty ($k = 2$)		2.0

drop-weight during impact. In the worst case, excessive tilt might cause misalignment of the interferometric signal and complete loss of the signal. Tilting might also cause increased friction between the drop-mass and the guiding rods, causing a stick-slip motion of the weight. Any spurious forces due to friction or misalignment of the interferometric measurement caused by deformations and tilting will cause errors when measuring the vertical force that is induced on the piston, i. e., the acceleration of the impact mass.

3.3.2 Uncertainty estimation of dynamic pressure

The main variables to be determined traceably in a drop-weight apparatus based on measurement of the impact force are the acceleration and mass of the impact mass, and the effective area of the piston-cylinder assembly. The most dominant source of uncertainty is related to measuring of the acceleration of the impact mass. Although the interferometric measurement is inherently very accurate, the dynamic impact makes the measurement very challenging, e. g., due to vibration, deformation, and tilt of the drop-weight

Uncertainty source	Means of estimating uncertainties	Potential improvements
$u(m_{\text{tot}})$, Impact mass	Mass of drop-weight, piston and pressurized media can be traceably and accurately determined by weighing using calibrated weighing scales and mass standards	NO. Contribution to uncertainty is currently negligible.
$u(A)$, Effective area of piston-cylinder unit	The effective area of the piston-cylinder unit can be determined by means of geometrical measurements, as for static pressure balances	NO. Contribution to uncertainty is currently negligible.
$u(a_d)$, Deformation of drop-weight	Numerical simulations of deformation give an estimate of the magnitude of error	YES. By optimizing impact mass geometry, material and acceleration measurement point, further improvements can be made.
$u(a_n)$, Vibration induced noise	Investigation of the pressure value at different low-pass cut-off frequencies gives an indication of the robustness of the method of filtering high-frequency noise	YES. Careful design of mechanical structure to avoid structural vibrations in the measured signal frequency range.
$u(a_t)$, Tilt of the drop-weight	The uncertainty of tilt can be estimated from deviations in acceleration measured at different locations on the drop-mass	YES. Tolerances of guiding rods can be further improved to minimize tilting. Also locating the acceleration measurement point(s) closer to the middle of the drop-weight will reduce the influence of tilt.
$u(a_f)$, Friction between piston and cylinder	The uncertainty of friction depends, among other things, on the eccentricity of impact and it can be estimated using the relationship given in [12].	YES. By careful alignment of the impact force, this uncertainty can be reduced further.
$u(\delta P)$, Spread of calibration results	Vibration, tilting and deformation of the drop-weight will also cause random variations of the results, which are shown as a spread in calibration results.	YES. Improvements to the above-mentioned points will eventually also reduce the spread of results (to the extent by which it is caused by the reference and not the DUT).

Table 2:
Means of determining uncertainties and potential improvements.

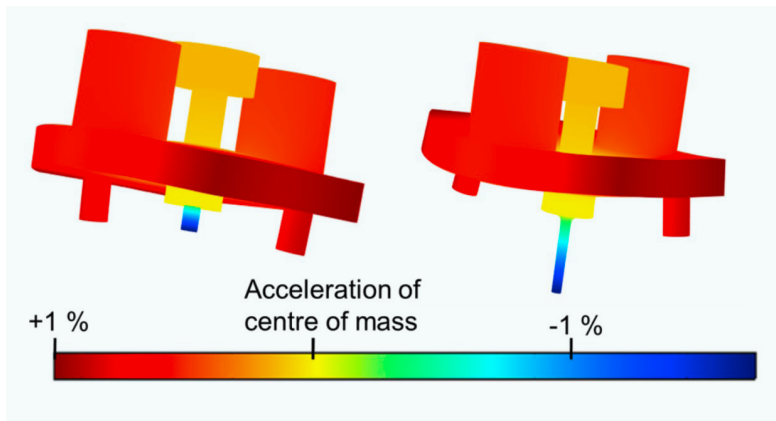


Figure 5: FEM simulation of the influence of the deformation on the measured acceleration at maximum impact force (left figure) and after impact (right figure). Compared to the acceleration of the center of mass, mirrors experience about 1 % higher acceleration [4]

due to impact. The main uncertainty sources of the VTT MIKES primary dynamic pressure standard are given in Table 1. The uncertainty of dynamic pressure can be calculated according to Eq. (4).

$$u^2(P) = u^2(m_{\text{tot}}) + u^2(A) + u^2(a_d) + u^2(a_n) + u^2(a_i) + u^2(a_j) + u^2(\delta P) \quad (4)$$

The deformation of the drop-weight is currently the largest uncertainty component in the current design. When the drop-weight hits the piston, the impact force deforms the weight (Figure 5). This will cause an error in the acceleration measurement performed at the edge of the drop-weight (see Figure 4). A summary of means of determining the uncertainties and potential ways of improving it is given in Table 2. More details on development, validation, and evaluation of uncertainties of a dynamic pressure standard are given in [4].

3.4 Example of the design and validation of a drop-weight device

Another primary level dynamic pressure calibration system has been developed at TÜBİTAK UME National Metrology Institute. It works based on a dropping mass principle. The reference pressure created by this system is obtained by dividing the created impact force value by the area of the piston-cylinder. The piston-cylinder unit transmits the short-term pressure pulse generated by the impact of the mass falling from a certain height to the test sensors via a transmission fluid.

Primary level dynamic pressure standards with dropping mass consist of a measuring head, interferometric system and base. The measuring head includes a piston-cylinder unit, sensors under test and a small volume where the piston-cylinder and sensors to be tested are connected. The base of the developed standard is a concrete construction and includes a dropping mass guided with two rods, an electromagnet to catch and carry the mass, step motors to move the electromagnet and an interferometric system located on the

base, as well, and it is used to calculate the shock acceleration of the dropping mass by measuring the displacement of the mass versus time.

3.4.1 Design of the system

The system is composed of a base, two servo engines with PLC controlling by software, an electromagnet, dropping mass guided by two rods, laser interferometer, measurement head unit including piston-cylinder unit, holes for test sensors, pressure transmission liquid. The electromagnet is used to move the guided mass upward and downward. A laser interferometer is measuring the displacement of the dropping mass versus time. The acceleration of the mass is determined as the second derivative of the displacement. One of the motors is used to move the electromagnet, whereas the second motor moves the rebound mechanism

to catch the dropping mass after the first hit of the piston. The collection of data about the displacement of the falling mass against time is carried out with a data collection system that works with a high acquisition speed. In this way, it is possible to measure the maximum value of the acceleration of the mass hitting the piston cylinder. To avoid memory problems on the system computer, the data is not collected continuously, and the start of data collection is triggered by the separation of the falling mass from the electromagnet.

A schematic picture of the developed system at TÜBİTAK UME is given in Figure 6a and measuring head and dropping mass are shown in Figure 6b.

3.4.2 Working principle

The falling mass creates a pressure pulse when hitting the piston-cylinder set in a volume filled with liquid, to which the sensors to be tested are connected. The reference pressure is calculated by dividing this impact by the piston-cylinder area. The area of the piston-cylinder unit is obtained by combining the separately measured dimensional form data of the piston and cylinder parts with a spatial integration method. The developed dynamic pressure standard is given in Figure 7.

The reference dynamic pressure in the developed system is calculated using equation (5). The force is determined by multiplying the weight of the total mass and the acceleration of this total mass value. In this total mass group, there is the free-falling mass (subject to free fall before impact), the piston mass moving with this mass during measurement, and the mass of the oil in the closed volume. The total mass is indicated as m_{total} . The

acceleration of the total mass is calculated by adding the local acceleration of gravity to the impact acceleration.

$$P_{\max} = \frac{m_{\text{total}} \cdot (a_{m, \text{maximum}} + g)}{A}, \quad (5)$$

where, $a_{m, \text{maximum}}$ is the maximum impact acceleration of the dropping mass, g is the local gravitational acceleration value.

The pressure measurements range of the developed system is from 20 MPa to 500 MPa. The width of the half-sine signal obtained according to the type of fluid used under the piston-cylinder is around (3–5) milliseconds. Measurements can be made with an uncertainty of 2 % ($k = 2$) for pressures up to 150 MPa and the uncertainty value increases with increasing pressure. Different types of liquids are used to transmit the impact pressure to the piston-cylinder and the sensor to be tested. The fact that the physical properties of these liquids are different also causes the signal periods and frequencies obtained in the system to be different.

3.5 Refractive index method

The general idea of the refractive index method is to make use of a physical mechanism that is so fast that there is no relevant difference between static excitation and excitation at kHz frequencies [6]. In this way, the static response of a medium can be transferred to the kHz dynamic range.

The experimental setup (Figure 8) illustrates the principle. A weight drops onto a piston-cylinder assembly filled with a hydraulic, optically transparent liquid (in the following, for simplicity we assume sebacate, but other liquids are possible). The motion of the piston compresses the liquid so that its density increases, and with it its index of refraction. A laser beam passes through the cell. The optical path length, i. e., the product of index of refraction and distance travelled in the medium, can be measured interferometrically, for instance with a commercial laser vibrometer. When the geometrical length of the cell is known, the index of refraction can be determined. In parallel, the customer's sensor (device under test, DUT) is connected to the same volume and its signal output recorded. When the connection between dynamic pressure p_{dyn} inside the liquid and its refractive index n is known, the sensitivity of the DUT can be established as a function of time over the evolution of the pulse. An important advantage is that the exact shape of the pulse is irrelevant.

There are two different routes to provide this connection between pressure and refractive index. Both routes need a quantitative way to relate the measured index of refraction to the density ρ of the medium. For dilute transparent gases, the Clausius-Mossotti relation provides this link:

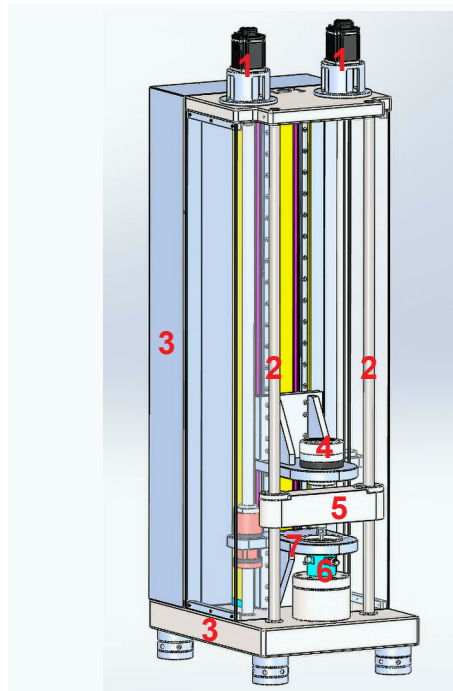


Figure 6a:
Schematic picture of the system at TUBITAK UME.

1. Servo engines,
2. Guiding rods for the dropping mass,
3. Base of the system,
4. Electromagnet,
5. Guided dropping mass,
6. Measuring head
7. Rebound mechanism

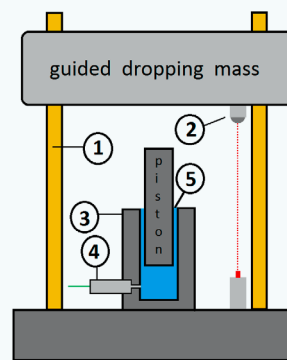


Figure 6b:
Measuring head and dropping mass of the developed system.

1. Guiding rods for the dropping mass,
2. Laser interferometer,
3. Piston-cylinder unit,
4. Sensor under test,
5. Fluid used as the pressure transmission medium

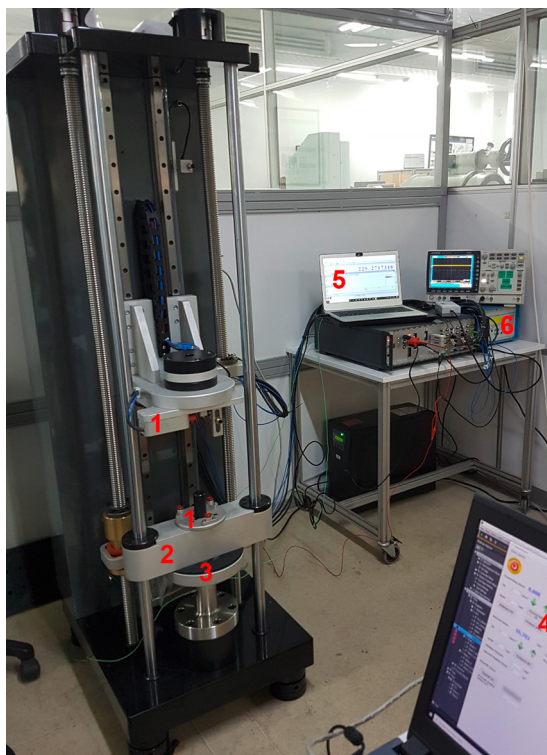
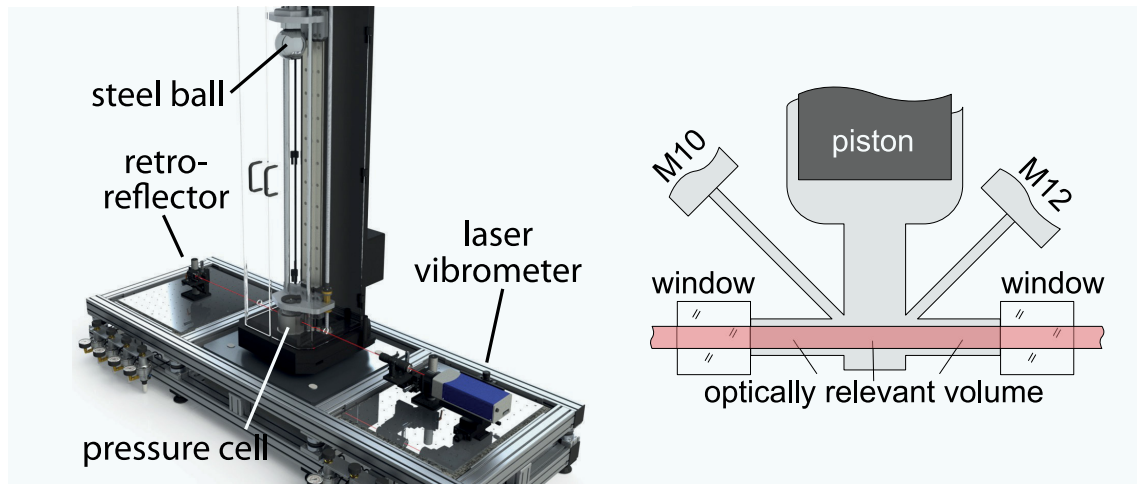


Figure 7:
Developed dynamic pressure calibration system.

1. Laser head and laser retroreflector,
2. Dropping mass,
3. Measuring head,
4. Controlling software for the dynamic pressure system,
5. Control system for the laser interferometer,
6. Amplifier for dynamic test sensors

Figure 8: Setup of the drop-weight device with laser-interferometric detection of the index of refraction in a pressurized medium. The sketch on the right illustrates the optically relevant volume and the two threaded slots (marked M10 and M12) for attaching the DUT.



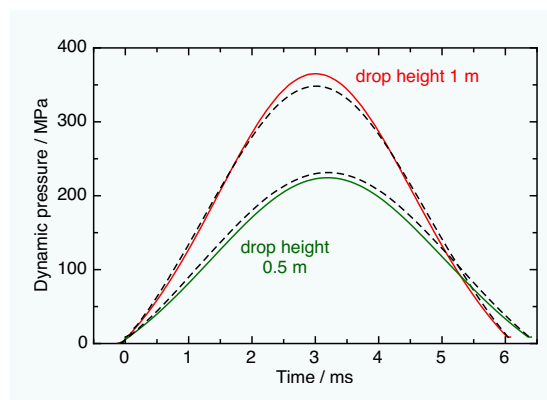
$$\rho = \frac{n^2 - 1}{n^2 + 2} \times \frac{1}{K_{CM}},$$

where K_{CM} is a constant containing the molecular polarizability. Although some doubt is warranted about the validity of this relation also for liquids under pressure [13] the dependence between density and index turns out to be closely linear. Therefore, the validity of the Clausius-Mossotti equation is assumed for the time being.

3.5.2.1 Traceability route 1: Isothermal-adiabatic method

Following the original idea [6], the setup is operated in two steps. First, the piston is replaced by a fixed pressure duct, and pressure is increased very slowly (hours), monitored by a statically calibrated pressure sensor (relative calibration uncertainties of less than 10^{-4} are possible, i. e., negligibly small for our purposes here). This process is isothermal and provides a relation between optical path change Δs_{iso} and static pressure p_{iso} . From Δs_{iso} one obtains n_{iso} when the cell length is known. A minor complication is the expansion of the cell when the fluid inside is pressurized. However, all relevant quantities can be measured with sufficient precision [7] so that a correction can be applied; cell expansion and window movement under pressure therefore are not an issue.

Figure 9: Dynamic pressure as a function of time determined along traceability route 1 (solid lines) and the output p_{val} from a validation sensor (dashed lines), for two different drop heights of the weight



- (6) Using the Clausius-Mossotti relation, the measured n_{iso} can be converted into the density ρ_{iso} as a function of static pressure p_{iso} .

In a second step, the experiment is run dynamically, with the weight dropping onto the piston while monitoring the optical path Δs_{adi} with the laser interferometer. This process is adiabatic in nature, as can be seen by the fact that the weight bounces up to almost the same height from which it was dropped; only a few percent are missing, mostly due to friction of the piston and due to the kinetic energy transferred to piston and fluid on the way up. From Δs_{adi} one obtains n_{adi} and ρ_{adi} in the same way as in the first step.

A complication arises because the connection between density and pressure depends on the character of the thermodynamic process:

$$\frac{dp}{p} = \left(\kappa_T - \alpha \frac{dT}{dp} \right) \times dp. \quad (7)$$

The first term on the right-hand side is the isothermal compressibility (applicable in the first experimental step here), whereas the second term give the additional contribution due to adiabatic heating in the dynamic case. Here α is the volume thermal expansion coefficient. This relation can be used to translate between the isothermal step 1 and the adiabatic step 2 by calculating a correction factor r . Details have been provided in a publication generated within this project [7]. The result of following this traceability route 1 is shown in Figure 9.

In this Figure 9 two sets of two curves of dynamic pressure p_{dyn} as a function of time are compared. The solid lines show the dynamic pressure extracted via the optical route, as explained above. The dashed black lines give the signal p_{val} of a piezoelectric transducer used as a reference for validation purposes. This sensor has been calibrated statically, but it has a fast response (resonance frequency well above 10 kHz), so that its output should be suitable for the purpose of validation of the drop-weight method.

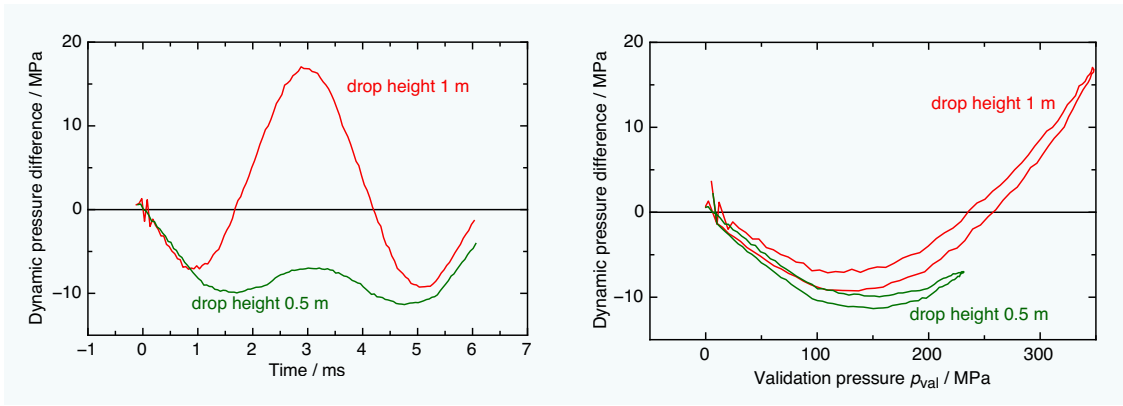


Figure 10: Difference between p_{dyn} determined along traceability route 1 and the pressure p_{val} provided by the high-speed validation sensor, recorded at the same time (left: vs. time, right: vs. p_{val})

The dynamic pressure p_{dyn} deviates from p_{val} in that it is too low for lower pressures and too high for higher pressures (Figure 10). The fact that in the plot on the right side of Figure 10 the green and the red curve are almost overlapping is an indication that the difference is primarily pressure-dependent and not dependent on the slope of the pressure-vs-time curve. For the 1 m case, the difference in peak amplitudes is about 5 %.

Central to the applicability of this route 1 is that the material parameters κ_T , α , and $\partial T/\partial p$ must be known, including their pressure dependence. A thorough literature search has provided a useable set of parameters – however, of unknown experimental uncertainty. A further caveat is that the “sebacate” used by one research team to determine one property might not be of exactly the same chemical composition as the “sebacate” used by another team to determine another property. One can therefore speculate that the observed difference is partly due to insufficiently known material parameters and in particular, insufficient consistency when used together in Eq. (7). This indicates a potential challenge for a later use of the device as a calibration facility because the properties of the hydraulic liquid will have to be monitored closely, including their reproducibility when supply runs out and new fluid must be procured.

The measurement uncertainty along route 1 obviously depends on the uncertainties of the material parameters, which, however, are not available directly from the sources. When reasonable proxies are sought, one finds a relative uncertainty of a peak pressure of 350 MPa of order 2 % (coverage factor $k = 1$), i. e., smaller than the deviations observed between p_{dyn} and p_{val} . Interestingly, the length of the optically relevant volume drops out in first order. Furthermore, the density of the fluid at ambient conditions cancels out exactly, and only its pressure dependence remains. These last two facts are strong points of traceability route 1.

3.5.2.2 Traceability route 2: Speed of sound method

Along traceability route 2, the isothermal part of the experiment is not needed, only the dynamic part. From Δs_{dyn} , n_{dyn} is obtained using the (pressure-dependent) geometry data of the cell, then p_{dyn} is determined via the Clausius-Mossotti relation. The relation between pressure and density,

$$d\rho = \frac{1}{v_s^2} dp \tag{8}$$

can be integrated when the speed of sound, v_s , is known. Here one can use the sebacate data given by [14] as a function of pressure and temperature. By modelling the pressure dependence of this data phenomenologically with a square-root function,

$$v_s = \text{const} + m \sqrt{p - x_0}, \tag{9}$$

Eq. (8) can be integrated analytically and the result solved numerically for the final pressure p_{dyn} (Figure 11).

Along traceability route 2, p_{dyn} comes out about 10 % too low. Except for the assumption about the validity of the Clausius-Mossotti relation, there are two important parameters entering along traceability route 2: The length of the optical volume (known to within 0.1 mm, corresponding to a contribution of about 15 % to the total uncertainty) and the speed of sound (62 %). For the speed-of-sound data used here [14] no

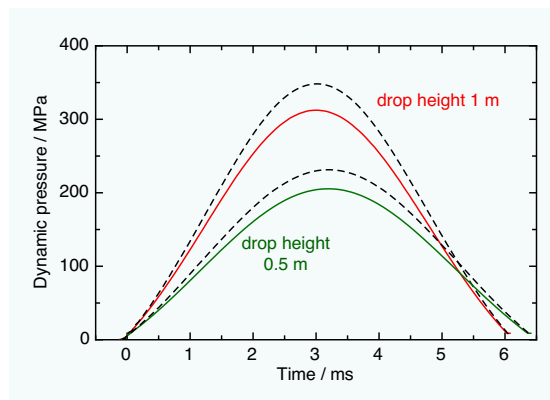
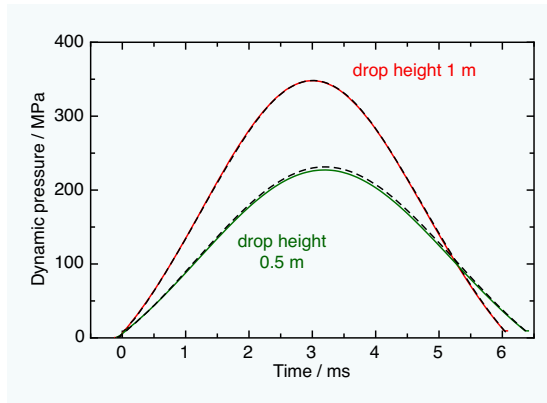


Figure 11: Dynamic pressure as a function of time, determined along traceability route 2 (solid lines), and the output p_{val} from a validation sensor (dashed lines), for two different drop heights of the weight

Figure 12: Dynamic pressure as a function of time determined along traceability route 2 (solid lines) and the signal from a validation sensor (dashed black lines), for two different drop heights of the weight. Here, during data evaluation the speed of sound was numerically increased by 3.8 %



measurement uncertainty is given and could not be found in the underlying primary literature, either. Speed of sound measurements in other fluids were made with uncertainties of order 0.3 % or less. The measurements in [14], however, were made in the ultrasound range (1.5 MHz), whereas the half-sine pulse here corresponds to about 80 Hz. It is well-known that the damping of a sound wave strongly depends on frequency, so also the speed of sound must depend on frequency.

To explore the situation of the systematic deviations, the evaluation of the dynamic drop data was performed again with the experimental values of the speed of sound increased by an adjustable factor. For a factor of 1.038 one finds that the maximum pressure for a drop height of 1 m is reproduced to within better than 0.1 % (Figure 12), while at the same time matching the pulse shape very well (Figure 13). For a drop height of 0.5 m, this same adjustment factor of 1.038 leads to a difference in peak amplitude of 1.7 %. Overall, this could indicate that the speed of sound measured at ultrasound frequencies might not be fully valid at low acoustic frequencies and that it is off not only by a constant factor, but by a slightly pressure-dependent one.

The uncertainty of dynamic pressure determination using traceability route 2 is dominated, obviously, by the uncertainty of the pressure-dependent speed of sound in the hydraulic medium. When a speed uncertainty of 0.3 % is assumed, corresponding to the order of magnitude of speed of sound measurements in

other fluids, one arrives at a relative uncertainty for a peak pressure of 350 MPa of order 1 % (coverage factor $k = 1$).

3.5.2.3 Practical considerations

Vibrometer uncertainty

A commercial vibrometer was used to detect the change of optical path length during the compression of the fluid. Its sampling rate and its slew rate (ability to track fast changes of path length) are fully sufficient [7]. In fact, the uncertainty due to the optical path length – the actual quantity measured! – is negligible.

Synchronicity

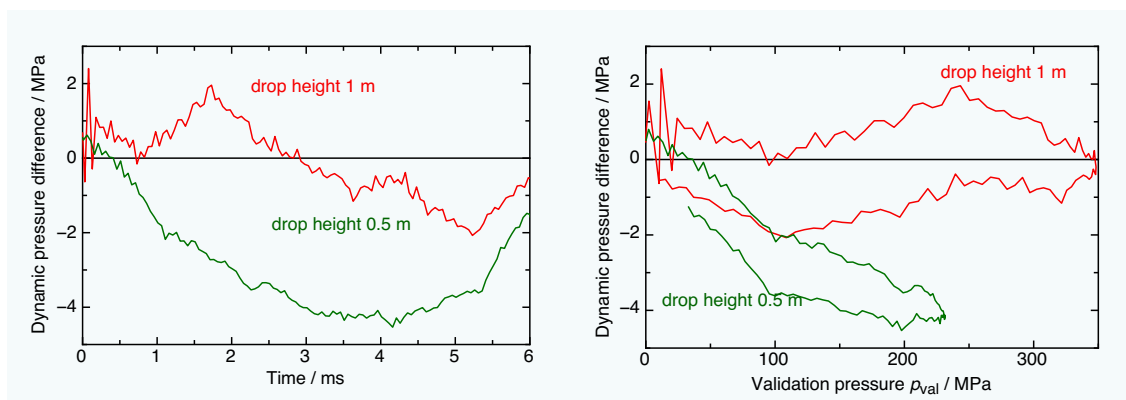
The measurement of the pressure takes place in two separate zones: at the sensing surface of the DUT and averaged over the optical volume (see Figure 8). Therefore, it is important to look for delays between the two signals. When calibration is performed only regarding the maximum pressure, calibration is easily accomplished by recording both vibrometer and DUT signals with the same acquisition system and then separately looking for the maximum of each signal. This is sufficient because the evaluation procedure is strictly monotonic, i. e., does not cause a change of signal shape that is asymmetric with respect to the maximum.

For calibration along the full shape of the pulse, one needs to consider the slope of the pressure curves and apply a correction depending on the delay (as observed via the shift of the maxima). Otherwise, calibration errors of about 1 MPa are theoretically possible.

Operation of the device

Operation of the drop-weight device is rather complex. Filling of the cell with the hydraulic fluid requires great care to avoid forming or trapping bubbles. It is best performed by placing the cell in a glove box or a similar device, in a mild vacuum.

Figure 13: Difference between p_{dyn} determined with a speed of sound numerically increased by 3.8 % and the pressure p_{val} provided by the high-speed validation sensor, recorded at the same time (left: vs. time, right: vs. p_{val})



Since a partial refill is required after each change of DUT and a complete refill after one or two dozen drops of the weight (due to the unavoidable loss of fluid along the piston), calibration of a customer DUT is a time-consuming process. For institutions that charge calibration cost according to time needed, it might turn out that operation of the device is not cost-effective, i. e., too expensive for customers.

Cavitation

During early experiments one observed a total drop-out of the vibrometer signal shortly after the pulse had ended [7]. This could be traced back to large bubbles being introduced into the fluid due to cavitation. When the piston travels upwards after having reached the point of maximum compression, it acquires kinetic energy and overshoots its resting position. This tears the fluid apart, causing the formation of bubbles. It takes up to several minutes before the medium is ready for the next drop of the weight. To avoid this process, the piston is held back by two polyimide strings: It can still travel into the cell freely but is stopped at its resting position on the way up (Figure 14).

This finding might also be important for other drop-weight devices. Even when no optical detection within the fluid is used the bubbles introduced might lead to reproducibility issues when the weight drops are following too quickly after each other. Furthermore, some of the bubbles might get trapped at internal cell walls, where they might change the overall behavior of the medium. In a device operating as a secondary standard by comparing the DUT with a reference sensor, this might lead to differences in the actual pressure load that each sensor sees, thus causing calibration errors.

Use of the device for secondary calibrations

In principle, the drop-weight apparatus could be used as a secondary calibration device. This can be accomplished in two ways: Either by using one of the sensor slots for a reference sensor and the other for the DUT, or by using both sensors for DUTs and performing the evaluation like along traceability route 2, but with a fitted correction factor for the speed of sound.

In both cases, care must be taken to avoid air bubbles that might cause a difference in the response of the two sensor channels. Also, the question of synchronicity must be studied carefully, something that is dependent on the exact structure of the pressure cell.

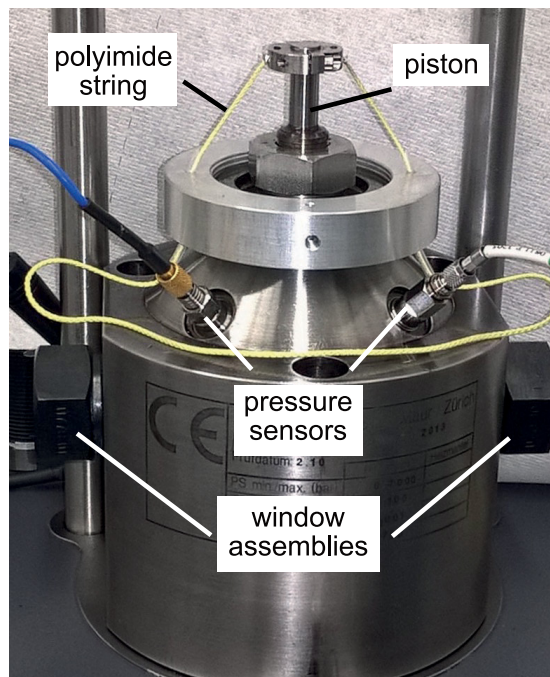


Figure 14: Detail of the pressure cell, showing the polyimide strings needed to prevent the formation of cavitation bubbles

4. Shock tubes and fast-opening devices

Aperiodic generators are used to generate dynamic pressure excitations over large frequency ranges.

Two types of step generators are used for dynamic pressure calibration in gaseous media: Shock Tubes (ST) and Fast-Opening Devices (FOD).

Fast-Opening Devices. The transducers are excited in a frequency range which extends from steady state to a few hundred Hertz by the pressure steps generated by the FOD. The best FOD known have a rise time in the order of 0.25 ms.

Shock Tubes: This equipment is able to generate strong temperature and pressure steps. For pressure calibration it is used differently: Shock tubes generate aperiodic inputs for primary calibration, with useful final uncertainty, in the range from 25 Hz to 30 kHz. Rise times can be much less than a microsecond. However, imperfections in the step limit the calibration range in terms of frequency. Operating conditions are set to produce a step as close as possible to a theoretical, perfect one. The persistence time (duration of the upper level of the step) can reach 50 ms and the low frequencies excited depend on this time. The shock tube is referred to as chronometric, when fitted with shock detectors for Mach number measurement.

4.1 Conventional shock tube

By “conventional” shock tube we mean shock tubes where the driven section has a constant cross-section profile along the shock propagation direction, e. g., a straight constant-radius pipe. Shocks propagating inside this geometry obey relations given below.

Conservation of mass:

$$\rho_1 u_1 = \rho_2 u_2 \tag{10}$$

Conservation of momentum:

$$\rho_1 u_1^2 + p_1 = \rho_2 u_2^2 + p_2 \tag{11}$$

Conservation of energy:

$$\frac{1}{2} u_1^2 + h_1 = \frac{1}{2} u_2^2 + h_2. \tag{12}$$

Here u , ρ , p and h denote the particle velocity, mass density, pressure, and specific enthalpy of the regions on either side of the shock. Particle velocity is relative to the shock front. The shock relations above describe the relations in what is occurring. They do not give any information about the driver pressures or how to realize the shock wave. The equations above may be solved numerically, but they may also be rewritten using the assumptions of a non-reactive, ideal, and calorically perfect gas according to below:

$$h = c_p T = c_v T + p v \tag{13}$$

$$\frac{1}{\rho} \equiv v = \frac{RT}{p} \tag{14}$$

$$\frac{c_p}{c_v} \equiv \gamma \tag{15}$$

$$a = \sqrt{\gamma RT} \tag{16}$$

$$M_s \equiv \frac{W}{a} \tag{17}$$

Here T , v , R , c_p , and c_v denote the absolute temperature, specific volume, specific gas constant and the specific heat capacities at constant pressure and volume, respectively. γ is referred to as the specific heat ratio, a is the speed of sound, W is the shock propagation speed in the laboratory frame and M_s is the Mach number of the shock propagation in the gas.

Using the assumptions above and rearranging, the following relations are valid for non-reactive gases at low temperatures and pressures:

$$p_2 = p_1 \left(1 + \left(\frac{2 \cdot \gamma_1}{\gamma_1 + 1} \right) \cdot (M_s^2 - 1) \right) \tag{18}$$

$$p_5 = p_2 \frac{\left(\frac{\gamma_1 + 1}{\gamma_1 - 1} + 2 \right) \cdot \frac{p_2}{p_1} - 1}{\frac{\gamma_1 + 1}{\gamma_1 - 1} + \frac{p_2}{p_1}} \tag{19}$$

In the equations above, p_1 represents the static pressure in the driven section before the shock arrives, p_2 represents the pressure immediately behind the shock front, p_5 represents the pressure behind the shock after it has reflected at the end plate of the shock tube. The end plate is where the sensor under test is placed during calibration.

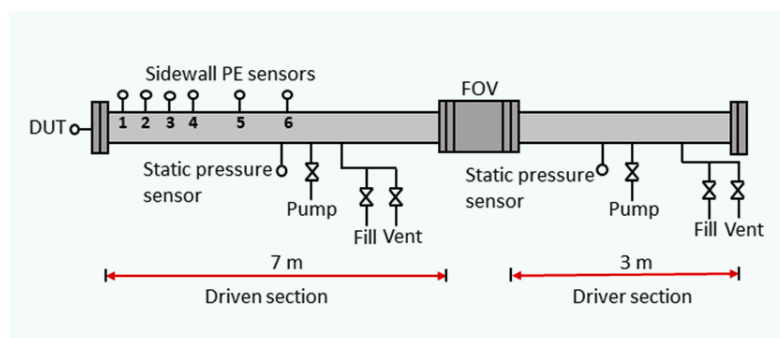
These expressions are of particular interest as they allow the resulting step pressure amplitude, across the shock front, to be calculated from literature gas properties, static initial conditions, and shock propagation speed. All pressures in the governing equations are in absolute pressure. The pressure step amplitude is thus the difference between p_5 and p_1 . Figure 15 illustrates the shock tube at RISE which has been constructed to determine step pressure using these relations.

Shock propagation speed at the device under test (DUT) is determined by fitting a quadratic function to the time of arrival of the shock front at the positions of the sidewall sensors. The speed of the shock front is taken as $dx(x_{DUT})/dt$. The positions of the sidewall sensors have been determined by traceable methods. The time of arrival at the respective sensor is taken as at the center of the leading edge of the pressure step. The sensor signals are collected by individual parallel channels on an 8-channel oscilloscope. Driver pressure is monitored only for nominal control of the final pressure step. It is not used to evaluate the actual step pressure.

Sources of uncertainty in p_5 are the input parameters to equations (18) and (19). They are evaluated independently and assigned an uncertainty distribution. To evaluate their effect on the uncertainty in p_5 a Monte Carlo approach is used. By calculating p_5 many times, each time randomly and independently varying the exact value of the input parameters according to their uncertainty distributions, a total uncertainty distribution for p_5 is obtained. The input parameters are assumed uncorrelated. The final uncertainty in step pressure is the root of the square sums of uncertainty in p_5 and p_1 .

In order to extract information that describes the sensor behavior in general terms, and not only in response to a pressure step, we seek the sensor response function in frequency space. The response function is given by the ratio between the sensor response signal and the stimuli (pressure step) in frequency space. Figure 16 shows how a Gaussian window is applied to both the sensor response signal and the ideal pressure step, with amplitude determined according to the method described above. The window is used to condition the signals so that a Fast Fourier Transform (FFT)

Figure 15: Schematic drawing of the shock tube at RISE: Positions of pressure sensors and gas manifold are shown. The tube is circular with an inner diameter of 100 mm. Type k thermocouples are spot welded at two positions onto the driven section



may be used. From the figure it can also be seen that the leading edges of sensor response and step pressure are aligned in time. This is done as we lack accurate temporal information about the actual time of shockwave impact on the sensor. Furthermore, the window is narrow, on the order of 1 ms. This effectively limits the lower end of the frequencies that can be analyzed. It also limits the pressure to the closest vicinity of the shock front, which is also the region where we expect the model we use to describe the step pressure to be most reliable.

Figure 17 shows the resulting amplitude part of the FFTs of the windowed signal and pressure. Since we have no accurate temporal information about the actual impact of the pressure step on the sensor, we are unable to assign uncertainties to the phase part of the of the sensor response. Thus, we do not consider the phase here.

The relative uncertainty in step pressure amplitude is valid also in frequency space. If several repetitive measurements are made at a pressure level using same sampling frequency and the response function is obtained using the same window, the total uncertainty due to uncertainty in reference pressure and due to variance width may be calculated at each discrete frequency.

Figure 18 shows the resulting amplitude part of the response function for a sensor as evaluated at three pressure step levels and averaged over three repetitions at each level. Uncertainty is presented in Figure 19. For lower frequencies the uncertainty is dominated by the uncertainty in reference pressure. At higher frequencies the uncertainty is dominated by variance in measurement between the repetitions. To which extent the variance is originating from the sensor or secondary effects during the experiment remains an open question. The uncertainty in reference pressure (step pressure) may be lowered by lowering the uncertainties in the input parameters. The validity of the model may be confirmed by comparison with alternative methods.

4.2 Primary dynamic pressure measurement standards in gas

4.2.1 Collective standard: determination of dynamic measurement uncertainty of a reference pressure sensor using a “collective standard” – CSM Method

4.2.1.1 Introduction

Within the DynPT project, ENSAM has improved its existing dynamic pressure measurement standards based on step generators, developed a

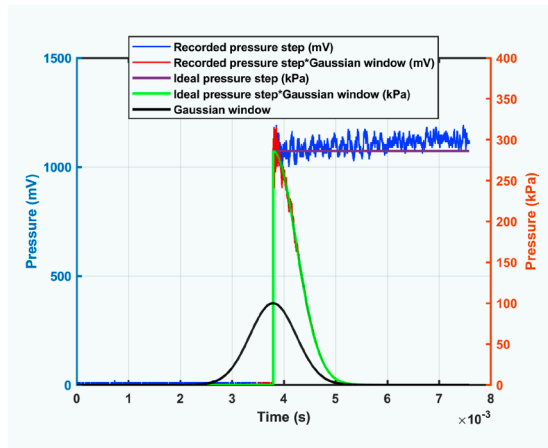


Figure 16: Typical sensor response signal and ideal pressure step in the time domain. The sensor signal is plotted on the left axis and the ideal pressure step plotted on the right. Also included here is a Gaussian window and the resulting windowed signal and pressure step

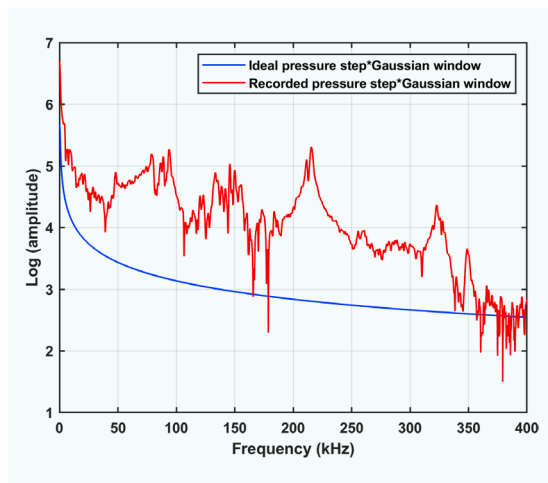


Figure 17: Amplitude part of the FFT of an ideal pressure step and sensor signal, respectively. Natural logarithm on vertical axis

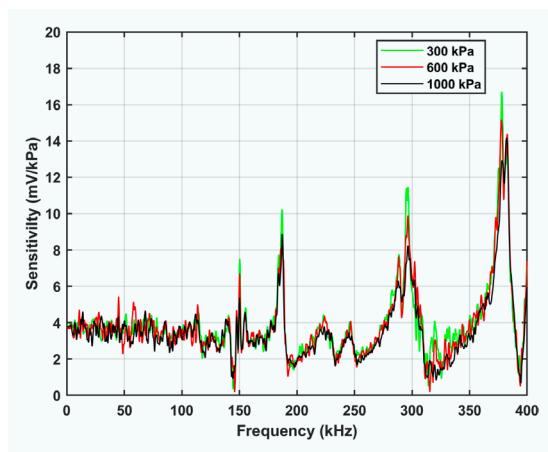


Figure 18: Final response function of a sensor at three pressure levels and averaged over three repetitions at each level. Results from different repetitions are evaluated identically, albeit with individual reference pressures, and the resulting response functions are averaged pointwise at each discrete frequency

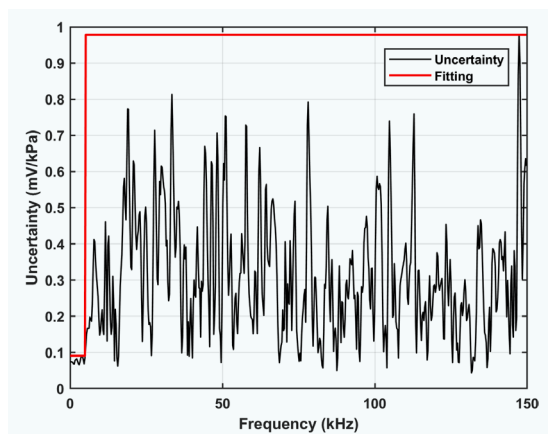


Figure 19: Evaluation of uncertainty. At low frequencies the uncertainty in reference pressure is dominant but at higher pressures the repeatability, or magnitude of the variance, is dominant. The fitted uncertainty is the highest uncertainty within a frequency range

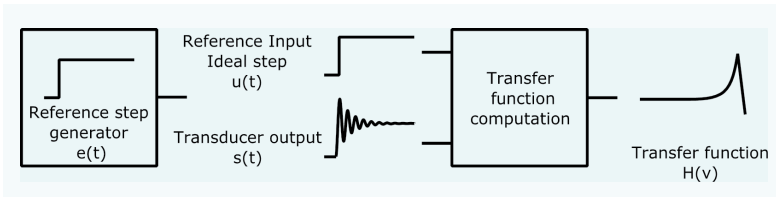


Figure 20: Schematic representation of the main steps of the dynamic calibration procedure of a primary reference sensor

new fast-opening device and shock tubes, with the aim to provide traceable calibrations of reference transducers in gas in extended pressure and frequency ranges and with reduced uncertainties. Two ranges of maximum pressures have been targeted, 0.5 MPa and 5 MPa. At the current state, the frequency range from 1 Hz to 30 kHz is fully covered at 0.5 MPa. A new 5 MPa shock tube has been designed and is currently under construction (status as of October 2021). The shock tube will aim to extend the frequency range of the collective standard method from 100 Hz to 1.5 kHz to close the gap in frequency range between fast-opening devices and high frequency shock tubes in the pressure range up to 5 MPa. Today, fast-opening devices are used in the low frequency range and shock tubes based on the Mach number method are applied at frequencies up to 30 kHz. Principles, methods, equipment, and results are briefly presented below.

4.2.1.2 Principle

The dynamic calibration of a reference pressure transducer involves determining the sensor response and corresponding measurement uncertainty over a frequency range within a pressure range. Calibration is performed from a primary reference producing a step of pressure in a gas and is called the LNE-ENSAM collective standard. The pressure is traced from LNE static references and the dynamic reference is an ideal step.

4.2.1.3 Method

The collective standard method allows the evaluation of the dynamic sensitivity and uncertainty of a reference sensor. For this, the gain of the transfer function of the sensor is calculated based on a perfect response; other sources of uncertainty identified are also considered.

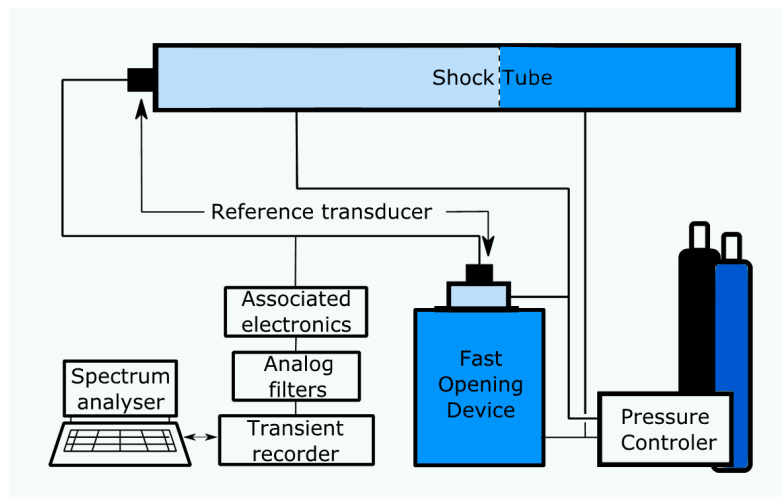
The transfer function is determined by applying to the input of the measurement chain a pressure step $e(t)$ produced by a reference generator. The output signal of the sensor to be calibrated is $s(t)$. A signal from a perfect step $u(t)$ is considered for the calculation. The transfer function $H(v)$ is defined as the ratio of the Fourier transform of the output $S(v)$ to the Fourier transform of the input $U(v)$. The schematic representation is given in Figure 20. The transfer function is a complex number represented as a gain (amplitude ratio) curve versus frequency and a phase curve in degrees. In the collective standard method, the gain curve is used to define uncertainty, since a constant unity gain is expected over the entire frequency range for a primary reference sensor. (Another method: the working sensor calibration by comparison, will provide the transfer function of a sensor with associated uncertainty on non-uniform dynamic sensitivity).

4.2.1.4 Equipment

A primary generator produces the input pressure step. Four different generators are needed to cover the frequency range from 1 Hz to 30 kHz, considering the frequency excitation limits of each of them. The low frequency excitation generator is a fast-opening device; it is followed by three shock tubes for higher frequencies. Figure 21 shows the equipment required for dynamic calibration. The Fast-Opening Device (FOD, DOR) consists of a large chamber inflated to pressure P_1 and a small chamber to pressure P_2 ; they are separated by an opening device. When the device opens, an amplitude step $P_2 - P_1$ is generated. The shock tube (TC) is made up of two chambers; the High Pressure (HP) and Low Pressure (LP) chamber; they are each closed by a bottom and separated by a membrane. Upon bursting of the membrane, an incident shock wave propagates in the LP chamber and then reflects off the bottom of the tube. It is the reflected shock wave and the resulting pressure rise that is used for calibration. To these means is added a reference manometer for quasi-static calibration of the sensor. Quasi-static pressure and voltage calibrations (QSP, QST) are part of the collective standard method.

The four frequency ranges covered by four subsets overlap; LF: 1 Hz to 50 Hz, MF: 40 Hz to 500 Hz, HF: 400 Hz to 5 kHz and HHF 4 kHz to 30 kHz. These ranges were chosen according to the capabilities of the generators, to exclude

Figure 21: Equipment involved in the dynamic calibration of a reference sensor by the collective standard method



the range where in a shock tube the spectral content of the step is contaminated by pressure fluctuations due to the curvature of the membrane and on FOD when it is limited by the rise time of the step. The measurand is generated by a reference generator developed and implemented to produce a pressure step as close to the ideal step as possible. The shock tubes are operated at Mach 1.1 to produce a step with full frequency content, but with as low as possible viscous, thermal, and acceleration effects. The signal from the sensor to be calibrated and associated electronics is filtered, converted to digital and then stored in memory using a transient recorder. The transient response is transferred to a microcomputer and the transfer function is calculated using the EDYCAP software which computes Discrete Fourier Transforms, DFT, by segment approximation. Uncertainty assessment procedures are implemented.

4.2.1.5 Step Generators

The pre-existing low pressure 0.5 MPa step generators were used in the project and optimized to reach the project target. They are shown in

Table 3: DOR16, DOR20, TCR, TCHF. A new high frequency shock tube TCMach was designed to extend the range to 30 kHz. This shock tube is also used in the 5 MPa range and with the chronometric method called Mach number method. A voltage step generator is also needed to calibrate dynamically the acquisition chain with its filters. The one used is based on an ampoule of mercury (not represented here).

Details of the developed step generators and shock tubes are given below:

- DOR16 is a rotating valve step generator. It is used for quasi-static calibration by manually generating long-lasting square functions.
- DOR20 is a valve fast opening device. It has been improved during the project by reducing the volume of the low-pressure chamber to optimize for a faster rise time of the step.
- TCR is the historical LNE-ENSAM shock tube that produces steps lasting 50 ms. Its range of frequency is limited by pressure fluctuations induced by membrane curvature peaking

Generators of the 0.5 MPa range

- a) Fast opening device DOR16: quasi-static
- b) Fast opening device DOR20: 1 Hz to 100 Hz
- c) Shock tube TCR: 0.02 kHz to 1 kHz
- d) Shock tube TCHF: 0.25 kHz to 10 kHz
- e) Shock tube TCMach: 1 kHz to 30 kHz

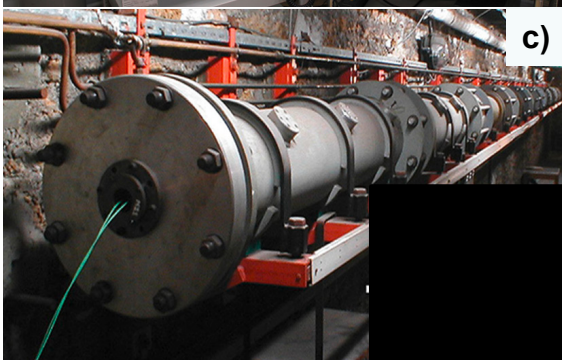
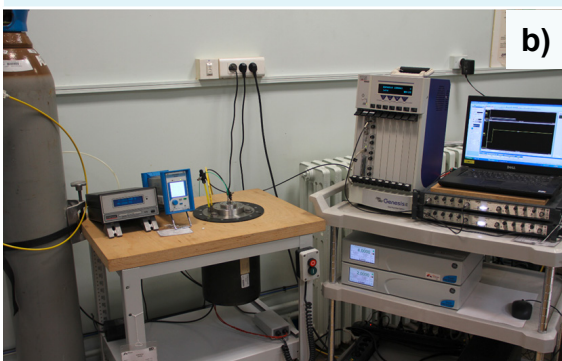
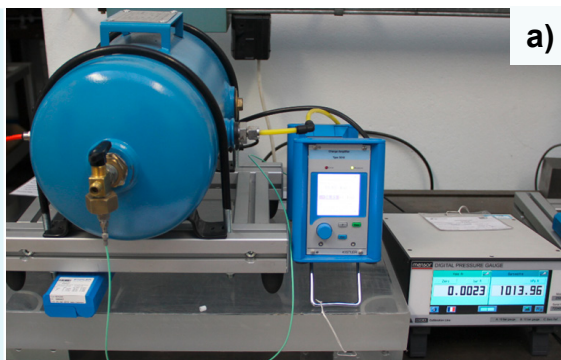


Table 3: Generators of pressure used for the 0.5 MPa range calibration

like a mode at 2 kHz with a sufficiently poor contribution at 500 Hz.

- TCHF is a high frequency shock tube producing steps lasting 5 ms. It has been optimized in the project by reducing inner form deviations, by testing attenuators of membrane induced pressure fluctuations, and has been transformed to permit calibration by comparison. Its 35 mm diameter pushes the membrane mode above 12 kHz.
- TCMach is a shock tube also used in the collective standard method. Its 10.6 mm inner diameter pushes the membrane mode above 45 kHz.

gain and that of the measured transfer function. The model for establishing the final uncertainty follows equation (21) and the cause-and-effect diagram in Figure 22.

$$\Delta P_{ref} = \frac{\Delta U_{ref}}{S_{ref} * G_{ref}} \tag{20}$$

$$u^2_{\Delta P_{ref}} = \left(\frac{1}{S_{ref} * G_{ref}}\right)^2 u^2_{\Delta U_{ref}} + \left(\frac{\Delta P_{ref}}{S_{ref}}\right)^2 u^2_{S_{ref}} + \left(\frac{\Delta P_{ref}}{G_{ref}}\right)^2 u^2_{G_{ref}} \tag{21}$$

The sources of uncertainty retained for their potential significance are detailed in Table 4.

4.2.1.6 Model

The dynamic pressure measurement follows equation (20), where ΔP_{ref} is the measurand and ΔU_{ref} is the output voltage signal of the sensor. The dynamic sensitivity of the sensor results from the product $S_{ref} * G_{ref}$. For the primary calibration G_{ref} is set equal to 1 and the dynamic uncertainty results from the difference established between this ideal

4.2.1.7 Example: Calibration of a reference transducer at 0.5 MPa at 1 Hz to 30 kHz

As an example, we present the calibration of a reference transducer (Table 5).

Results of Calibration

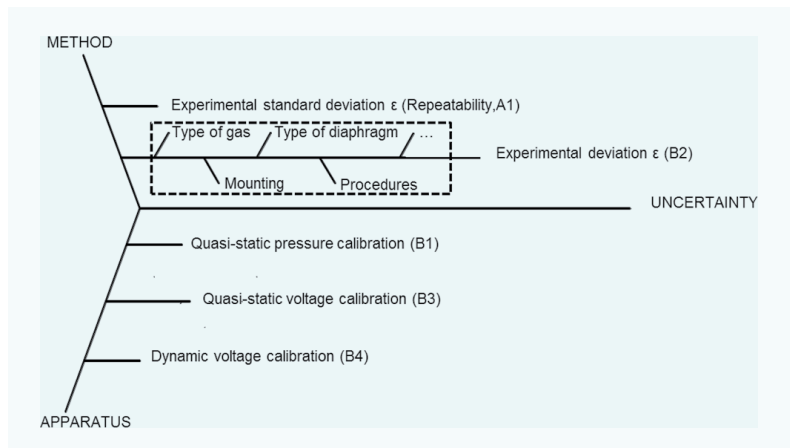
Sensitivity of the sensor under test obtained for $S_{ref} = 1.0159$ V/bar with $u = 6.3 \times 10^{-4}$ V/bar, $k = 2$, i. e., $u = 0.06$ % full range or 311 Pa. Figure 23 illustrates the result of the uncertainty calculation.

Table 4: Parameters for calculating the uncertainty components involved in the substitution method

Source	Type	Comment	Distribution
Repeatability	A1	Standard deviation to evaluate the dispersion of the average of samples considered 4 by 4 in frequency domain of the transfer function. Re-dimensionalized in pressure by the sensitivity obtained during the quasi-static calibration phase of the reference sensor.	$\sqrt{4}$
Dynamic gain $u_{G_{ref}}$	B2	Average of differences between the gain measured and ideal gain ($G_{ideal} = 1$). Evaluated for each frequency.	$\sqrt{3}$
Quasi-static sensitivity of the transducer $u_{S_{ref}}$	B1	Quasi-static calibration of the transducer, detailed in [15]	2
Quasi-static sensitivity of acquisition chain	B3	Quasi-static calibration of the acquisition system, involved in B4 and detailed in [15]	2
Dynamic gain of acquisition chain $u_{\Delta U_{ref}}$	B4	Dynamic calibration of the acquisition system. Done with voltage reference steps generator by following an equivalent method as for dynamic pressure, detailed in [15]	2
Processing	B6	Evaluation of processing of FRF uncertainty. From differences between computational results of time models and their theoretical FRFs (involved in B4); [15] shows quasi normal distributions	2

Discussion

When considering the components of the overall uncertainty in the high frequency range (1 kHz to 30 kHz) shown in Figure 24, it can be noticed that the dynamic component of the acquisition system B4 is greater than expected; it is significant compared to the uncertainty due to pressure gain discrepancy B2. The use of the Butterworth analog filter of 8th order at 99.9 kHz is therefore to be questioned. A simulation shows that the final uncertainty at 30 kHz can be reduced by a factor of about 2 if the discrepancy due to the acquisition chain remains below 2 %.



4.2.2 Determination of dynamic measurement uncertainty of a reference pressure sensor using a primary chronometric method called “Mach Number” – MNM Method

4.2.2.1 Introduction

ENSAM has developed and built a new shock tube to provide traceable calibrations of dynamic sensitivity of reference transducers in gas at high frequency, i. e., 1 kHz to 30 kHz. A pressure range up to 5 MPa is targeted, but the shock tube can be used at 0.5 MPa under certain conditions. Principles, methods, equipment, and results are briefly presented below.

4.2.2.2 Principle

The dynamic calibration of a reference pressure transducer is performed with a primary reference chronometric shock tube producing a step of pressure in gas and called LNE-ENSAM ST-10M-FK1-30-CO-CH or TCMach (the former abbreviation stands for: Shock Tube, 10 MPa, 1 to 30 kHz, COlective standard, CHronometric). The sensitivity is determined in the dynamic regime. The method refers to the Rankine-Hugoniot theory to trace the amplitude of a step existing only in the dynamic regime in the tube. Applying this theory requires traceable measurements of static pressure, temperature, distance, and time of arrival of the shock. Traceability of these measurements are established through LNE or

Figure 22: Sources of uncertainties in the primary calibration of a reference sensor

Device	Manufacturer	Type	Serial	Settings
Pressure transducer	KISTLER	601A	1381286	-15.22 pC/bar
Charge amplifier	KISTLER	5018A	4395531	1 bar/V, long
Voltage step generator	GE1	Quasi static	GE01	1 to 5 V
Pressure step generator	DOR16	Quasi static	LMD5	Air up to 5 bar
Pressure step generator	DOR20	Low frequency	LMD1	Air, step (2-4) bar
Pressure step generator	TCR	Middle frequency	LMD2	Air, step (2-3) bar
Pressure step generator	TCHF	High frequency	LMD3	Air, step (2-3.7) bar
Pressure step generator	TCMach	Higher frequency	LMD10	Air, step (2-5.5) bar
Analog filter	KEMO	VBF813	1048854	Butt., 3, 40, 99.9 kHz
Transient recorder	NICOLET	HBM GENESIS	05.01.8255	5 kHz, 50 kHz, 1 MHz
Processing	ENSAM	EDYCAP	V03.76	-

Table 5: Experimental setup

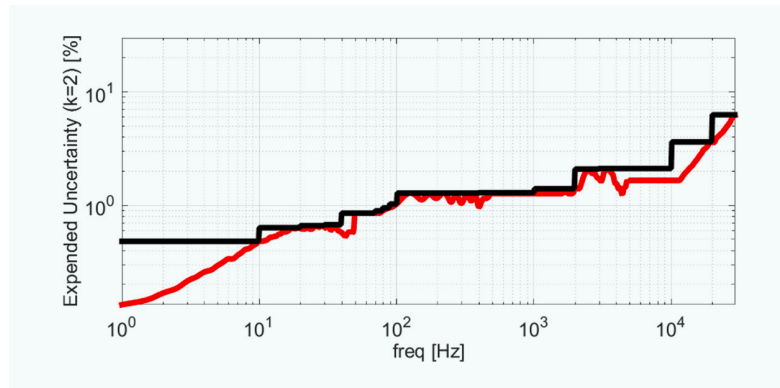


Figure 23: Graphical representation of the extended uncertainty $k = 2$ on pressure measurement. Raw data in red for information.

DAkkS accredited laboratories. The dynamic reference is a unitary step used as a basis for calculating a DFT on the frequency dependent input signal which allows the evaluation of the uncertainty of the dynamic frequency dependent measurement.

4.2.2.3 Model

The dynamic sensitivity measurement S_{dyn_c} results from the product $S_c * G_{dyn_c}$ following equation (22), where S_c is equivalent to a quasi-static sensitivity in the frequency domain excited by the shock tube and G_{dyn_c} is the dynamic gain, theoretically frequency dependent, but for primary calibration the choice is made to assume that G_{dyn_c} equals to 1 over the frequency range, since the tube does not produce perfect steps even if a primary reference tube is used.

S_c is given by equation (23), where ΔU_c is the output voltage signal of the sensor and ΔP_{ref} the amplitude of the step generated in the tube. The amplitudes ΔU_c are first measured over a time corresponding to the inverse of the low frequency of the calibration range, here 1 ms for 1 kHz. ΔP_{ref} is traceable following Rankine-Hugoniot theory and model equations (25) and (26) and equations (27) and (28) for the Mach number. Equation (25) was transcribed by Schewpe [16] for a tube filled with the same diatomic gas.

The sensitivity S_c and its uncertainty are determined from the slope of a linear regression $\Delta U = f(\Delta P)$ over seven different tests. Four tests are carried out

under almost identical pressure and temperature conditions where dynamic response is evaluated. Three more tests are carried out at higher and lower ΔP of about 75 %, 125 % and 150 % of the principal test. The uncertainty on dynamic sensitivity is then evaluated from equation (24). The dynamic uncertainty $u_{G_{dyn_c}}$ results principally from the difference established between this ideal gain and that of the measured transfer function, its repeatability, and the computation of the DFT. The uncertainty due to dynamic voltage measurement is evaluated from equation (23), where this time U is considered frequency dependent. As it was noted previously in Section 4.2, dynamic calibration of the acquisition chain in voltage is done with a step generator following the collective standard method. Remember that the historic method consists of generating a supposedly perfect voltage step and to consider the deviation from the perfect response to evaluate the dynamic uncertainty. An alternative, but less satisfactory method, that does not refer to the direct response of the chain, but to specifications of its components, could also be used.

$$S_{dyn_c} = S_c * G_{dyn_c} \tag{22}$$

$$S_c = \frac{\Delta U_c}{\Delta P_{ref}} \tag{23}$$

$$u_{S_{dyn_c}}^2 = (G_{dyn_c})^2 u_{S_c}^2 + (S_c)^2 u_{G_{dyn_c}}^2, \tag{24}$$

$$\text{where } u_{G_{dyn_c}}^2 = \left(\frac{1}{\Delta P_{ref} * S_c}\right)^2 u_{\Delta U_{dyn_c}}^2 + u_{G_{dyn_c}(\text{deviation } \epsilon)}$$

On each test, the Mach number is determined three times using four shock detectors. The amplitude of the steps ΔP_{ref} of each test is given by the theoretical shock tube equation (25) and Mach number equation (27) and associated uncertainty assessment equations (26) and (28). More details are given in [17].

$$\Delta P = \frac{7}{3} P_1 (M_s^2 - 1) \frac{2 + 4M_s^2}{5 + M_s^2} \tag{25}$$

$$u_{\Delta p} = M_s \sqrt{u_{p_1}^2 \left(\frac{\Delta p}{p_1}\right)^2 + u_{M_s}^2 \left(56 p_1 M_s \frac{M_s^4 + 10 M_s^2 - 2}{3(M_s^2 + 5)^2}\right)^2} \tag{26}$$

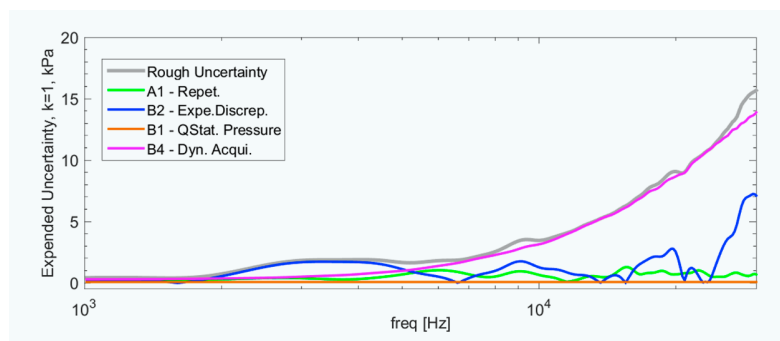
$$M_s = \left(\frac{V_s}{\sqrt{\gamma r T_1}}\right) \tag{27}$$

$$u_{M_s} = M_s \sqrt{\frac{u_{\Delta l}^2}{\Delta l^2} + \frac{u_{\Delta t_1}^2}{\Delta t_1^4} + \frac{u_v^2}{4 \gamma^2} + \frac{u_r^2}{4 r^2} + \frac{u_{T_1}^2}{4 T_1^2}} \tag{28}$$

The cause-and-effect diagram summarizing the final uncertainty model is drawn in Figure 26. A table of the influence parameters on ΔP_{ref} and a graph of the final contributions on S_{dyn_c} will be drawn in the example to follow.

Details on the dominant uncertainty sources of ΔP are given in Table 6.

Figure 24: Uncertainty components of the preliminary estimation of the overall uncertainty in the high frequency range



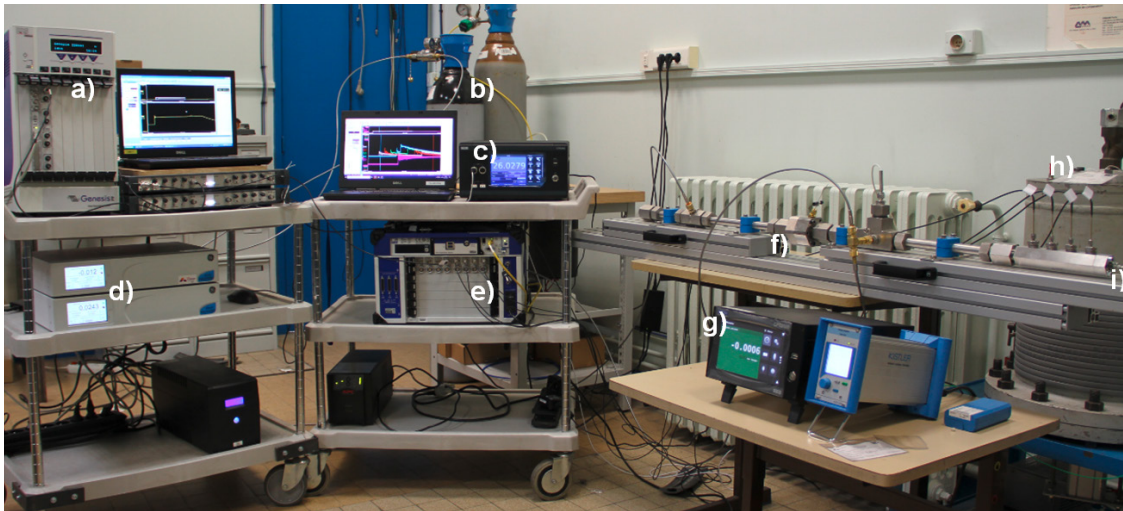
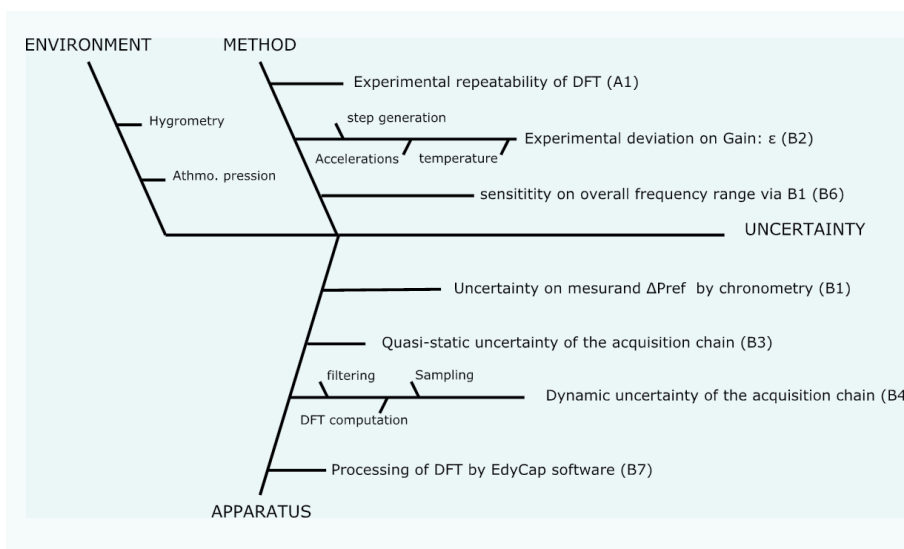


Figure 25: Equipment of chronometric shock tube 5 MPa, [1-30] kHz TCMach. a) Transient recorder A. b) Gas supply. c) Temperature recorder. d) Pressure controllers. e) Transient recorder B. f) Shock tube. g) Pressure recorder. h) Shock detectors. i) Transducer under test

Figure 26: Uncertainty sources in a dynamic primary calibration of a reference sensor using the chronometric method, i.e., “Mach Number” method



4.2.2.4 Calibration of a reference transducer by chronometric “Mach Number” method at 5 MPa and at 1 Hz–30 kHz

As an example, we present the calibration of a reference transducer, at Mach number $M \approx 1.05$ instead of 1.1 (Table 7).

Results of Calibration

Sensitivity of the sensor at 1 kHz obtained for the conditioner settings is $S_c = 0.0933 \text{ V/bar}$ with $u = 6.1 \times 10^{-3} \text{ V/bar}$ ($k = 2$), i.e., $u = 6.6 \%$. Figure 27 gives the results of the uncertainty calculation over the frequency range.

Discussion

Table 8 is given as an example of the uncertainty components of ΔP . The point with the greatest relative uncertainty out of 7 is chosen. ΔI is measured in three dimensions (DAKKS traceable measurement). Δt is defined manually on

chronometric records with repeatability and reproducibility estimated at 15 times steps when sampling at 250 MHz. These results will evolve with the continuous improvement of the method which is only at its beginning.

The linear regression line is treated according to the York algorithm and plotted in Figure 28. Developments are to be carried out to optimize the choice of the points and the results according to the capabilities of the tube and the cost of the

Figure 27: Graphical representation of the extended uncertainty $k = 2$ of the dynamic sensitivity. Raw data in red for information.

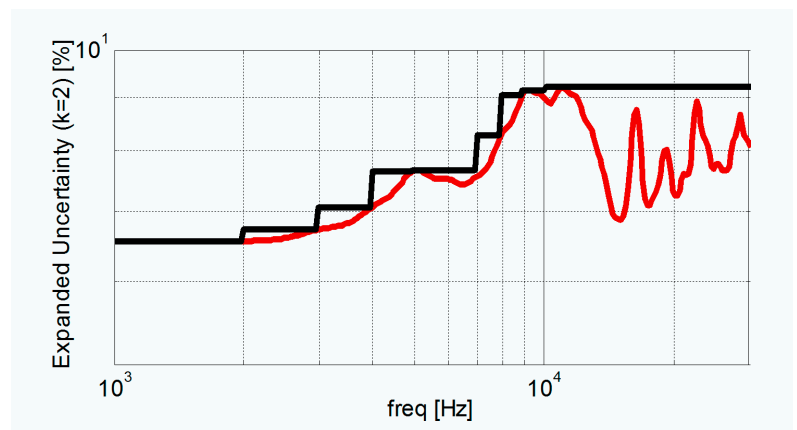


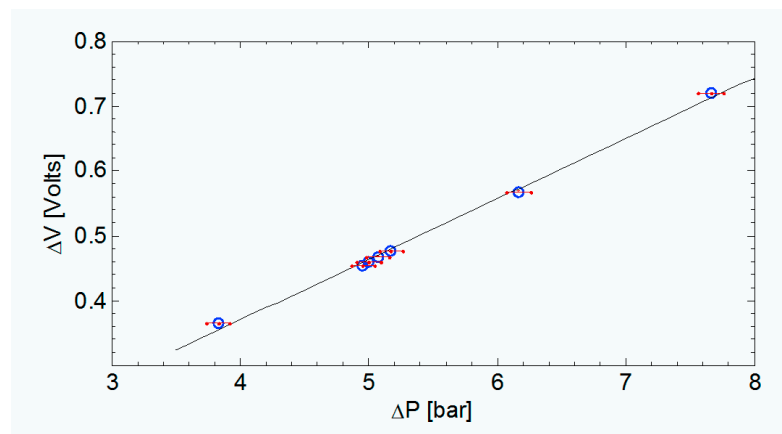
Table 6: Parameters for calculating the uncertainty components involved in the substitution method.

Source	Type	Comment	Distribution
Repeatability	A1	Standard deviation to evaluate the dispersion on the average of samples considered 4 by 4 in frequency domain of the transfer function based on an ideal step. Used in $u_{G_{dyn}}$.	$\sqrt{4}$
Experimental deviation of dynamic gain	B2	Average of differences between the gain measured and ideal gain ($G_{ideal} = 1$). Evaluated for each frequency.	$\sqrt{3}$
Amplitude of the step $u_{\Delta P_{ref}}$	B1	Chronometric calibration using Rankine-Hugoniot formulation. Detailed in [15].	2
Sensitivity of acquisition chain	B3	Calibration of the acquisition system at 1 kHz, involved in B1. Detailed in [15].	2
Dynamic gain of acquisition chain $u_{\Delta U_{dyn,c}}$	B4	Dynamic calibration of the acquisition system. Done following collective standard method in voltage.	2
Sensitivity S_c	B6	From the linear regression $\Delta U = S_c * \Delta P + P_0$ based on B1 and B3.	
Processing	B7	Evaluation of processing of FRF uncertainty. From differences between computational results of time models and their theoretical FRFs. [15] shows quasi normal distributions.	2

procedure. The tube will be re-built according to the “lessons learned” of this DynPT project. It will be possible in this pressure range to establish the same type of calibration at three initial pressure points rather than one in the middle. A 7 MPa, 50 Hz–6 kHz chronometric tube is about to be added to the calibration chain.

Amplitude steps of 10% of the calibration range were prioritized rather than Mach numbers of 1.1 for a mid-range pressure calibration on a point for dynamic characterization. The Mach number obtained in the tube is close to 1.05 and produces a satisfactory spectral content step. Operational choices remain to be refined to obtain the best metrological capabilities.

Figure 28: Determination of the sensitivity S_c by linear regression: $V = 0.0933 * \Delta P - 0.0032$. Experimental data is given in blue, error bars xy ($k = 1$) in red and linear regression in black.



4.2.3 Calibration using a collective standard at high pressure of 5 MPa

4.2.3.1 Method

The method is the collective standard already presented in Section 4.2.1. For the pressure range up to 5 MPa, a new step generator based on a rotating valve has been designed (FOD-DOR100). This type of generator has long shown its efficiency for calibrations by comparison. The rise time and the quality of the step today are satisfactory for use as a reference generator on the millisecond time scale. The rotating valve FOD was preliminary studied as a reference generator during Leodido’s thesis (2011) showing the need of improvement to approach the performance of FODs fitted with translational valves. The valve is actuated fast enough to produce rise times well suited for the 100 Hz range with time response 10 % to 90 % < 1.7 ms. The device is designed not to produce acceleration effects by solid contact. Figure 30 shows the FOD. The collective standard method is applied as presented in Section 4.2.1 for the evaluation of the uncertainty of pressure measurement involved in the dynamic sensitivity. The same reference sensor is tested, but at higher pressure than in Section 4.2.1.

Initially the full range of frequency at 5 MPa was

Device	Manufacturer	Type	Serial	Settings
Pressure transducer	KISTLER	601A	1381286	-15.22 pC/bar
Charge amplifier	KISTLER	5018A	4395531	10 bar/V, long
Voltage step generator	GE1	Quasi static	GE01	1 to 5V
Pressure manometer	Mensor	CPG2500	410012PA	100 bar
Temperature	WIKA/WIKA	CTR3000/ CPT5000	B14622	Ambient ~25 °C
Controller HP	GE 210 bar	Pace 5000	3156296	25 bar(g) – Δp : 0.25 bar
Controller BP	GE 210 bar	Pace 5000	3156295	20 bar(g)
Pressure step generator	TCMach	Higher frequency	LMD10	N2, P1- ΔP : 21 bar-5 bar
Analog filter	KEMO	VBF813	1048854	Butt., 99.9 kHz
Transient recorder	NICOLET	HBM GENESIS	05.01.8255	1 MHz
Transient recorder	HBM	Gen7TA/ GN8101B	IMB1900257	250 MHz
Processing	ENSAM	EDYCAP	V03.76	-

Table 7:
Experimental setup

Parameter	Symb.	Value	Stand. uncert.	Unit	Sens. coeff.	u^2
Adiabatic index	γ	1.4019	0.001	-	1.3E+02	1.6E-02
Gas constant	r	298.24	0.099	J·kg ⁻¹ ·K ⁻¹	5.9E-01	3.5E-07
Temperature	T	299.433	0.10	K	5.9E-01	3.5E-03
Speed of sound	C_I	353.90	1.4E-01	m·s ⁻¹		
Distance	Δl	3.60E-02	1.00E-05	m	1.0E+04	1.1E-02
Time interval	Δt	9.72E-05	6.00E-08	s	3.8E+06	5.2E-02
Shock speed	V_s	370.62	2.5E-01	m·s ⁻¹		
Speed of sound	C_I	353.90	1.4E-01	m·s ⁻¹	-3.0E-03	1.7E-07
Mach Number	M_s	1.0472	0.0008	-		
Driven pressure	P_I	2095100	196.00000	Pa	2.4E-01	2.1E+03
Mach Number	M_s	1.0472	0.0008	-	1.1E+07	8.4E+07
Pressure step	ΔP	495361	9188.43	Pa		
			1.85%			

Table 8:
Example of the contribution of uncertainty sources for ΔP_{ref} for one measurement.

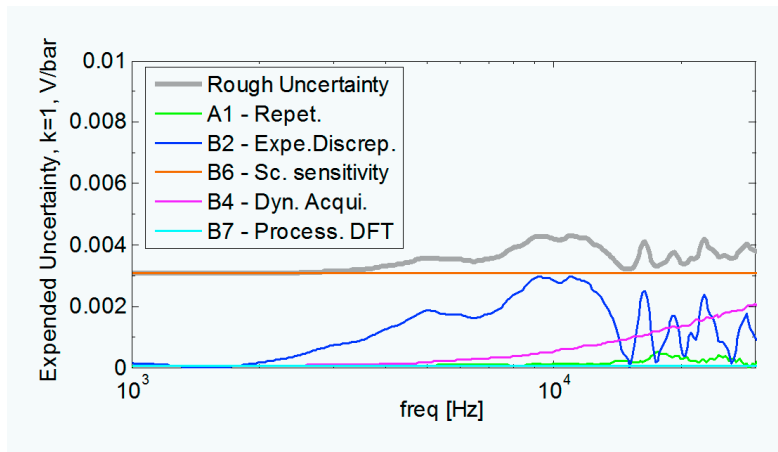


Figure 29: Components of the overall uncertainty of dynamic sensitivity in the high frequency range ($k = 1$)

thought to be covered by only this FOD and the 30 kHz shock tube, but as the step qualities of the devices between 400 Hz and 1.5 kHz have shown to be degraded at the 5 MPa range compared to 0.5 MPa used for preliminary tests, the choice was made to add an intermediate 10 m long tube, which should be operational by the end of 2021 to the cover full range of frequency following the collective standard method at 5 MPa.

4.2.3.2 Calibration of a reference transducer at 5 MPa at (1–100) Hz

Results of Calibration

Sensitivity of the sensor under test obtained for the conditioner settings: $T = -15.22$ pC/bar and $S = 10$ bar/V, $S_{ref} = 0.10080$ V/bar with $u = 4.3E-5$ V/bar ($k = 2$), i. e., $u = 0.042$ % of full range or $2.1E+3$ Pa. Figure 31 gives a graphical illustration of the results of the uncertainty calculation over the calibration range.

Discussion

The components of the overall uncertainty are compared to those of a similar treatment obtained at 0.5 MPa on the reference fast opening device using translational valve FOD-DOR20 (Table 10). The components have equivalent relative distributions, but the deviation from the measurement of a perfect step is shifted in frequency. The method of processing the tabulated uncertainties makes this difference almost imperceptible.

4.3 Shock tube and Fast Opening Devices for secondary reference transducer calibration – SSM method

4.3.1 Operating principle

Calibration is performed from a reference generator producing a pressure step in gas. This time the pressure is traced from a primary reference transducer calibrated by the Collective Standard Method (CSM) or Mach Number Method (MNM) method. The calibration is performed on one or several ranges of frequency. If several ranges are expected for a given certificate, they overlap. With this exception, the principle of the calibration is the same as for CSM calibration (Section 4.2.1).

4.3.2 Method

The Secondary Standard Method (SSM) allows the evaluation of the uncertainty of calibration of the dynamic sensitivity of a reference sensor. For this, the gain of the transfer function of the

Table 9: Experimental setup

Device	Manufacturer	Type	Serial	Settings
Pressure transducer	KISTLER	601A	-1381286	-15.22 pC/bar
Charge amplifier	KISTLER	5018A	4395531	10 bar/V, long
Voltage step generator	GE1	Quasi static	GE01	1 to 5 V
Pressure step generator	DOR100	Quasi static	LMD11	N2 up to 50 bar
Pressure step generator	DOR100	Dynamic	LMD11	N2, step 20–30 bar
Analog filter	KEMO	VBF813	1048854	Butt., 3 kHz
Transient recorder	NICOLET	HBM GENESIS	05.01.8255	5 kHz
Processing	ENSAM	EDYCAP	V03.76	-

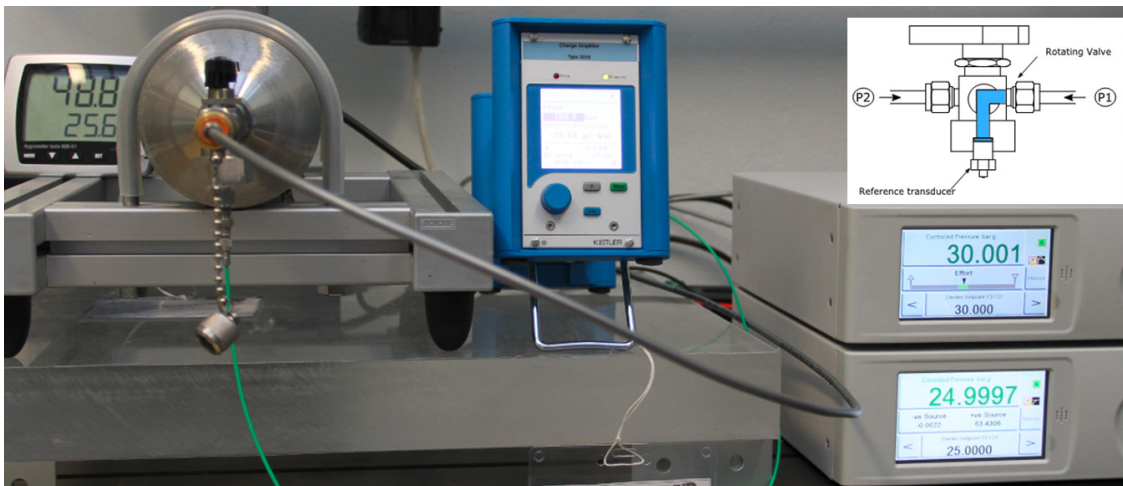


Figure 30: View of the 5 MPa fast opening device FOD - DOR100

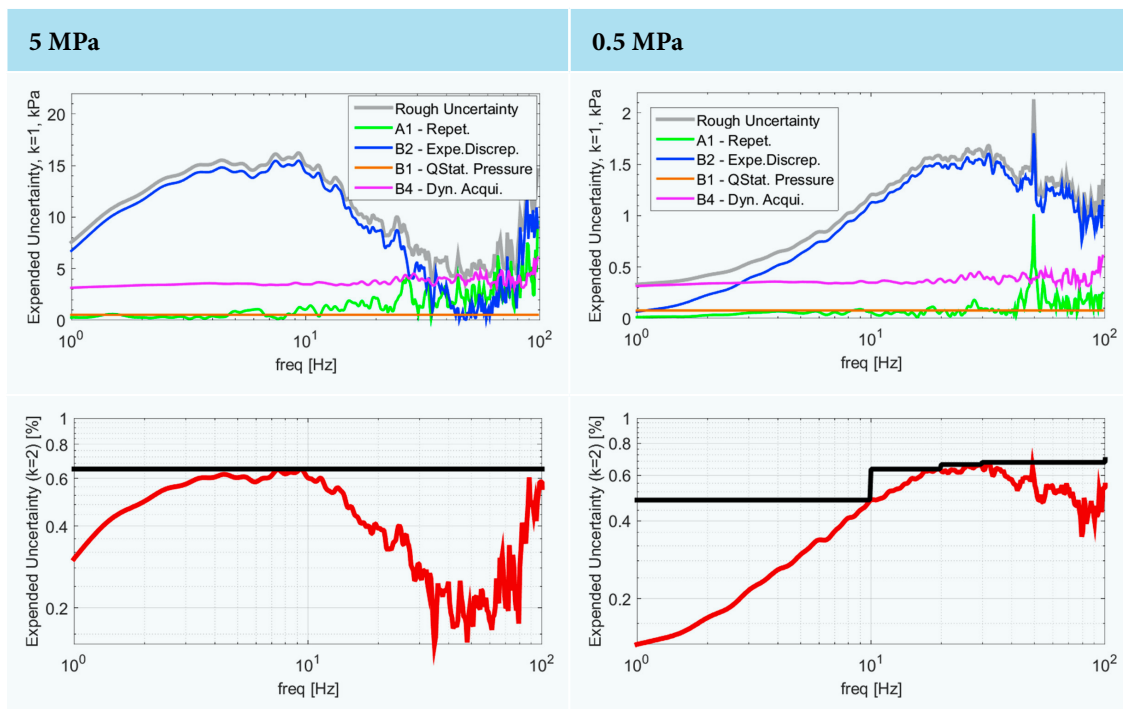


Table 10: Uncertainty components of the overall uncertainty and final results in the high- and low-pressure ranges. Left 5 MPa and right 0.5 MPa (note that the vertical scales on the first row are in the ratio of the pressure ranges, i.e., x10).

sensor is calculated based on a primary reference transducer output; other sources of uncertainty identified are also considered. The transfer function is determined by applying to the input of the measurement chain a pressure step $e(t)$ produced by a reference generator. The output signal of the sensor to be calibrated is $s(t)$. The signal from a reference sensor $u(t)$ is considered for the calculation. The transfer function $H(\nu)$ is defined as the ratio of the Fourier transform of the output $S(\nu)$ to the Fourier transform of the input $U(\nu)$. The schematic representation is given in Figure 32. The transfer function is a complex number represented as a gain (or amplitude ratio) curve versus frequency and a phase curve in degrees. In the SSM as for CSM, the gain curve is used to define uncertainty since a constant unity gain is expected over the entire frequency range for a primary reference sensor. The gain curve is

not a final result. Another method, the working sensor calibration by comparison, will provide the transfer function of a sensor with associated uncertainty of non-uniform dynamic sensitivity.

Figure 31: Graphical representation of the expanded uncertainty ($k = 2$). Raw data is shown in red.

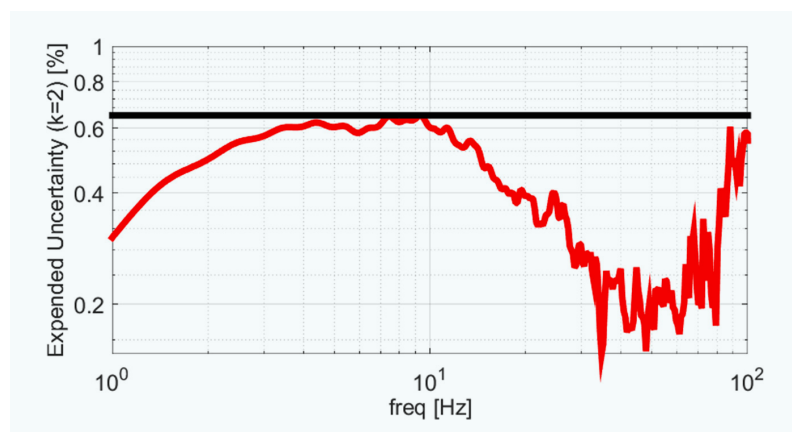
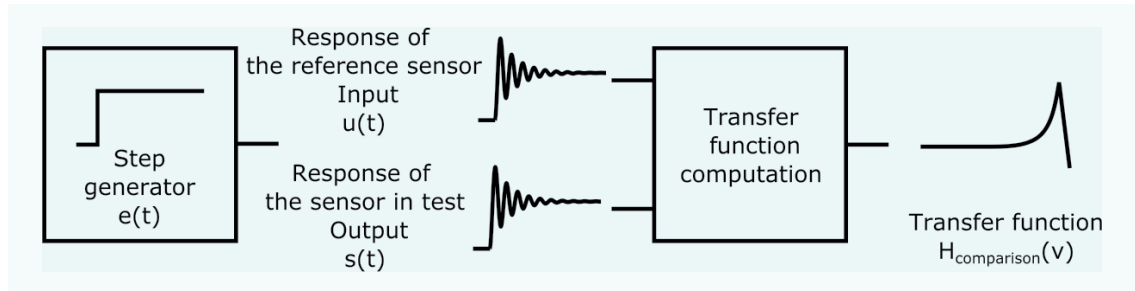


Figure 32: Schematic representation of the main steps of the dynamic calibration procedure of a primary reference sensor



4.3.3 Equipment

Generators are built and used according to the procedures to produce pressure steps as perfectly as possible. The generators are operated and maintained in metrology laboratories. Secondary dynamic calibration begins by quasi-static calibration of a transducer following a classical method. A manometer is used and amplitudes of steps generated by a FOD are traceable to the International System of Units (SI) for 5-point calibration using linear regression. FOD are afterwards used in the dynamic regime and followed by ST depending on the range of frequency targeted. The acquisition chain must also be dynamically calibrated beforehand.

4.3.4 Model

The step of amplitude ΔP_c in output is measured by the transducer to be calibrated according to the relationship given by the time dependent equation (29), where ΔU_c is the dynamic voltage measurement, S_c the quasi-static sensitivity of the transducer and G_c its dynamic gain. For a secondary calibration, G_c is also stated to be one and the model is similar to the equation used for a primary calibration with the CSM, but where subscript “ref” is replaced by *c*. The dynamic uncertainty u_{G_c} will result from the differences noted between this reference gain and the computed gain of the FRF. Note that the dynamic

sensitivity $S_c * G_c$ will only be expressed for the calibration of the working transducers. In that case G_c could be different from one. As the amplitude of the input step, ΔP , is defined according to the relationship (30), the final model for the uncertainty assessment is expressed by equation (31), where the input uncertainty $u_{\Delta P_{ref}}$ is taken into account. The cause-and-effect diagram is shown in Figure 34.

$$\Delta P_c = \frac{\Delta U_c}{S_c * G_c} \tag{29}$$

$$\Delta P = \Delta P_{ref} \tag{30}$$

$$u^2_{\Delta P_c} = \left(\frac{1}{S_c * G_c}\right)^2 u^2_{\Delta U_c} + \left(\frac{\Delta P_c}{S_c}\right)^2 u^2_{S_c} + \left(\frac{\Delta P_c}{G_c}\right)^2 u^2_{G_c} + u^2_{\Delta P_{ref}} \tag{31}$$

The sources of uncertainty retained for their potential significance are detailed in Table 11.

4.4 Shock tube and Fast Opening Devices for Working Standard calibration – WSM method

4.4.1 Principle

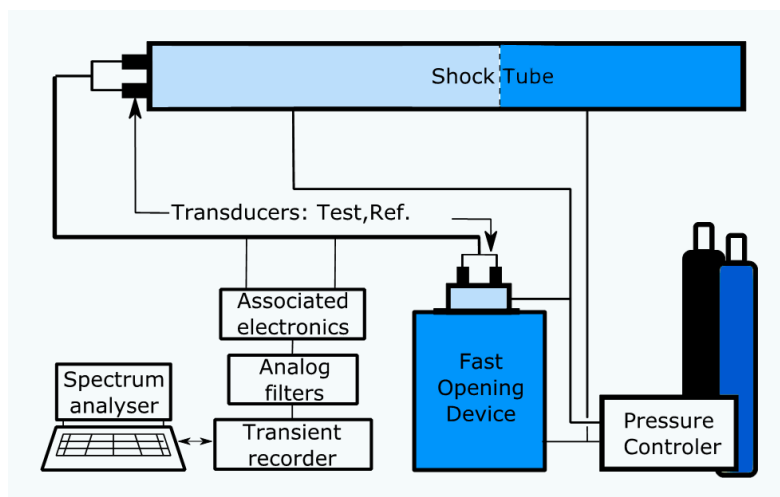
The dynamic calibration of a working pressure sensor consists of determining the dynamic sensitivity and the associated measurement uncertainty over a range of frequencies within a range of pressure.

Calibration is performed using a primary or secondary reference sensor. This reference is calibrated on the primary standard called “LNE-ENSAM collective standard”, on the primary standard called “chronometric standard” or on a transfer standard using a secondary method.

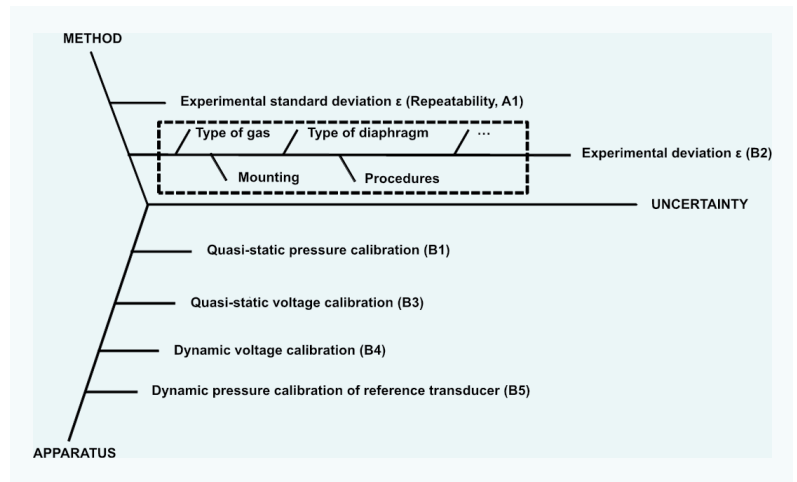
4.4.2 Method

The method of calibrating a Working Standard by comparison permits to determine the dynamic sensitivity of the sensor from its transfer function and to evaluate the uncertainty of this sensitivity. For this, the gain of the transfer function of the sensor is calculated based on the response of a primary reference or transfer sensor; other identified sources of uncertainty are also considered.

Figure 33: Equipment involved in the calibration process of the secondary dynamic pressure standard and the collective standard method (voltage step generators not shown)



The process for determining the transfer function is the same as before (in Figure 32). The transfer function is determined by applying to the input of the measurement chain a pressure step $e(t)$ produced by a generator, fast opening device or shock tube. The output signal of the sensor to be calibrated is $s(t)$. The signal from a reference primary or secondary transducer $u(t)$ is traceable and considered for the calculation. The transfer function $H(\nu)$ is defined as the ratio of the Fourier transform of the output $S(\nu)$ to the Fourier transform of the input $U(\nu)$. The transfer function is a complex number represented as a gain (or amplitude ratio) curve versus frequency and a phase curve in degrees. In the method of calibrating a working sensor, the gain curve is used to define the dynamic sensitivity of the sensor and the associated uncertainty. In contrast, for the primary calibration method, the transfer function



is used to define the deviation from the assumed perfect dynamic input; and is only used for the evaluation of measurement uncertainty.

Figure 34: Sources of uncertainties in the primary calibration of a reference sensor

Source	Type	Comment	Distribution	Settings
Repeatability	A1	Standard deviation to evaluate the dispersion on the average of samples considered 4 by 4 in the frequency domain of the transfer function. Re-dimensionalized in pressure by the sensitivity obtained during the quasi-static calibration phase of the reference sensor.	$\sqrt{4}$	-15.22 pC/bar
Dynamic Gain $u_{G_{ref}}$	B2	Average of differences between the gain measured and ideal gain ($G_{ideal} = 1$). Evaluated for each frequency.	$\sqrt{3}$	10 bar/V, long
Quasi-static sensitivity of the transducer $u_{S_{ref}}$	B1	Quasi-static calibration of the transducer.	2	1 to 5 V
Quasi-static sensitivity of acquisition chain	B3	Quasi-static calibration of the acquisition system (included in B4).	2	N ₂ up to 50 bar
Dynamic gain of acquisition chain $u_{\Delta U_{ref}}$	B4	Dynamic calibration of the acquisition system. Done with voltage reference steps generator by following an equivalent method as for dynamic pressure.	2	N ₂ , step 2030 bar
Dynamic gain of acquisition chain $u_{\Delta P_{ref}}$	B5	Dynamic calibration of the reference transducer.	2	Butt., 3 kHz
Processing	B6	Evaluation of processing of FRF uncertainty. From differences between computational results of time models and their theoretical FRFs (involved in B4).	2	5 kHz

Table 11: Parameters for calculating the uncertainty components involved in the substitution method

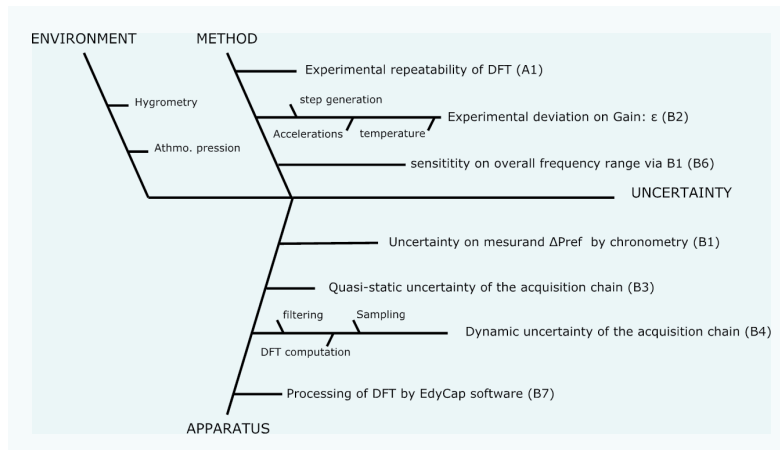


Figure 35: Sources of uncertainties in the calibration of a working sensor. The sources of uncertainty retained for their potential significance are detailed in Table 12

4.4.3 Equipment

A generator produces the input pressure step. Different generators may be needed to cover the frequency range frequency excitation considering limits of each. The low frequency excitation generator is a fast-opening device; it is followed by shock tubes for high frequencies.

If the calibration range exceeds that of a generator, the frequency ranges overlap on sub-ranges. These ranges were chosen according to the capabilities of the generators, to exclude ranges where in the shock tube the spectral content of the step is contaminated by pressure fluctuations due to the curvature of the membrane and in the FOD when it is limited by the rise time of the step. The measurand is generated by a reference generator developed and implemented to produce a pressure step as close to the ideal step as possible. The shock tubes are operated at Mach 1.1 to produce a step with full frequency content but with as low as possible viscous, thermal, and acceleration effects. The signal from the sensor to be calibrated and associated electronics is filtered, converted to digital and then stored in memory using a transient recorder. The transient response is transferred to a microcomputer and the transfer function is calculated using an appropriate method (DFT by segment approximation for example). Uncertainty assessment procedures are implemented.

Table 12: Parameters for calculating the uncertainty components involved in the substitution method.

Source	Type	Comment	Distribution
Repeatability	A1	Standard deviation to evaluate the dispersion on the average of samples considered 4 by 4 in the frequency domain of the transfer function. Re-dimensionalized in pressure by the sensitivity obtained during the quasi-static calibration phase of the reference sensor.	$\sqrt{4}$
Dynamic Gain of the reference transducer $u_{\Delta P_t}$	B1	Dynamic calibration of the reference transducer.	2
Uncertainty on the measurand	B2	Considered negligible through ABBA method for acoustical 1st mode, and procedure for acceleration and temperature.	-
Quasi-static sensitivity of acquisition chain	B3	Quasi-static calibration of the acquisition system (involved in B4), detailed in [15].	2
Dynamic gain of acquisition chain $u_{\Delta U_{ref}}$	B4	Dynamic calibration of the acquisition system. Done with voltage reference steps generator by following an equivalent method as for dynamic pressure, detailed in [15].	2
Quasi-static sensitivity of the transducer u_{S_c}	B5	Quasi-static calibration of the transducer, detailed in [15].	2
Gain curve fit	B6	Maximum value of the absolute values of the residuals per tabulated gain averaging interval.	$\sqrt{3}$
Processing	B7	Evaluation of processing of FRF uncertainty. From differences between computational results of time models and their theoretical FRFs (involved in B4); [15] shows quasi normal distributions.	2

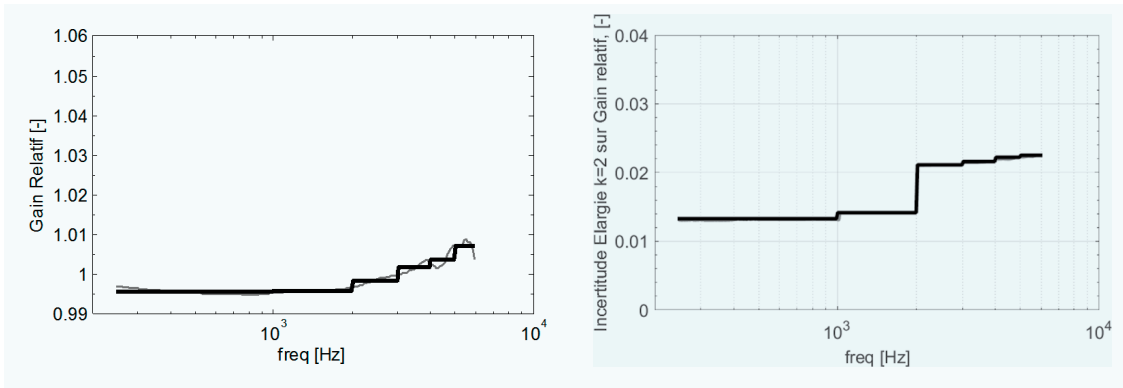


Figure 36: Graphical representation of the gain (left) and expanded uncertainty ($k = 2$) (right). Raw data in gray for information.

4.4.4 Model

Calibrating a working sensor involves determining the dynamic sensitivity and evaluating the related uncertainty. The law of variance propagation is used according to the recommendations of the GUM. The measurement of the dynamic reference load follows the relation (32), where ΔP_e is the measurand and ΔP_u is its measurement by reference sensor. The traceability of the measurement from the sensor to be calibrated to the measurand follows relation (33), where ΔP_c is the result. The measurement follows equation (34), where ΔU_c is the output voltage signal of the electronics associated with the sensor, S_c the quasi-static sensitivity and G_{dyn_c} the dynamic gain, which will be obtained by the calculation of the transfer function. The dynamic sensitivity of the sensor is S_{dyn_c} , which follows relation (35). Applying the law of propagation of

variances to dynamic sensitivity gives expression (36). The rearranged expression (34) gives the expression of the variance on the dynamic gain (37), where P_u is substituted for P_c because the uncertainty on the measurand is traceable via the reference sensor. The diagram of causes and effects on the uncertainty of S_{dyn_c} is given in Figure 35.

$$\Delta P_e = \Delta P_u \tag{32}$$

$$\Delta P_c = \Delta P_u \tag{33}$$

$$\Delta P_c = \frac{\Delta U_c}{S_c * G_{dyn_c}} \tag{34}$$

$$S_{dyn_c} = S_c * G_{dyn_c} \tag{35}$$

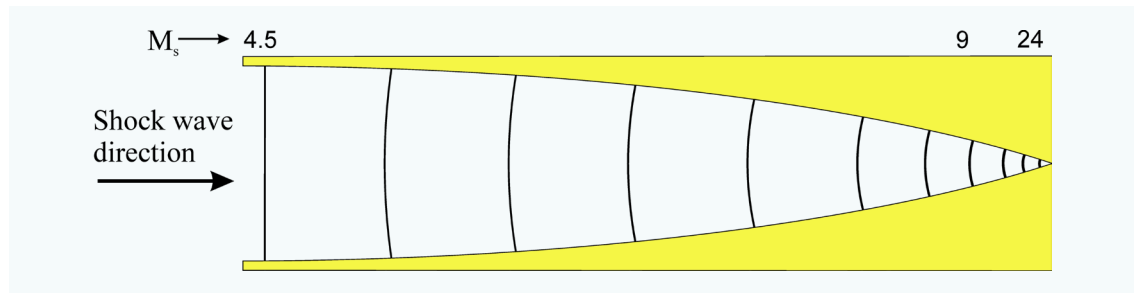
$$u^2_{S_{dyn_c}} = (G_{dyn_c})^2 u^2_{S_c} + (S_c)^2 u^2_{G_{dyn_c}} \tag{36}$$

$$u^2_{G_{dyn_c}} = \left(\frac{1}{\Delta P_u * S_c}\right)^2 u^2_{\Delta U_c} + \left(\frac{G_{dyn_c}}{\Delta P_u}\right)^2 u^2_{\Delta P_u} + \left(\frac{G_{dyn_c}}{S_c}\right)^2 u^2_{S_c} \tag{37}$$

Device	Manufacturer	Type	Serial	Settings
Transducer calibrated	AVL	GH12D	5225	-15.8 pC/bar
Charge amplifier	KISTLER	5011A	978421	1 bar/V, long
Reference transducer	KISTLER	601A	1381286	-15.22 pC/bar
Charge amplifier	KISTLER	5018A	4395531	1 bar/V, long
Pressure step generator	DOR16	Quasi static	LMD5	Air up to 5 bar
Pressure step generator	TC100	High frequency	LMD6	N ₂ , step 2 bar -3.75 bar
Analog filter	KEMO	VBF813	1048854	Butt., 40 kHz
Analog filter	KEMO	VBF813	1048855	Butt., 40 kHz
Transient recorder	NICOLET	HBM GENESIS	05.01.8255	5 kHz, 50 kHz, 1 MHz
Processing	ENSAM	EDYCAP	V03.76	-

Table 13: Experimental setup

Figure 37:
Schematic of shock
wave convergence
in a converging
channel



4.4.5 Calibration of a transducer – WSM Method:

4.4.5.1 Special conditions of calibration

The frequency range of the vertical shock tube TC100 is 250 Hz to 10 kHz under the selected experimental conditions. The substitution method (ABBA), which involves exchanging the positions of the sensors at the bottom of the tube, is used to make the first transverse acoustic mode of this generator unobservable. The mode frequency is 6 kHz when the medium is air or nitrogen at room temperature. However, in the current design of the tube, the mode orientation is not sufficiently fixed because the tube bottom is not indexed. The high frequency of the current calibration is therefore limited to 6 kHz.

4.4.5.2 Equipment identification

See Table 13.

4.4.5.3 Results of Calibration

Sensitivity of the sensor under test obtained for the conditioner settings: $T = -15.8$ pC/bar and $S = 1$ bar/V, $S_{ref} = 1.0161$ V/bar, with $u = 7.7E-4$ V/bar ($k = 2$), i. e., $u = 0.08$ % full range or 381 Pa.

Figure 36 is informative to graphically illustrate the final results of the uncertainty calculation over the frequency range.

4.5 Converging Shock tube (CST)

Due to the shock tube's inherent ability to generate pressure pulses of desired amplitude and fast rise time, they hold a distinct advantage in dynamic calibration methods. However, they are limited to the lower levels of peak pressure generation, in the range below 7 MPa for nominal operation. Theoretically, the peak pressure can be pushed up to a maximum of 10 MPa but at the expense of a large number of resources and material constraints leading to very high operating costs. To overlap the range between the 7MPa–40 MPa gap existing between shock tube and drop-weight method,

the upper limit of the “conventional” shock tube must be increased. This is done by implementing a novel method of converging the shock wave (generated from a conventional shock tube) using a converging test section attached at the end of the conventional shock tube. A schematic of the convergence process is shown in Figure 37. Since the peak pressure obtained is dependent on the Mach number (M_s), converging the shock wave through smooth area reduction techniques increases M_s resulting in relatively high peak pressures. Liverts and Apazidis [18] reported that upon converging a plane shock wave of $M_s = 4.5$ from an 80 mm diameter tube to 16 mm and thereafter to 0.6 mm resulted in a shock wave of $M_s = 9$ and 24, respectively.

A schematic of the converging shock tube facility is as shown in Figure 38. It is similar to a conventional shock tube, but with a converging section (test section) added to the assembly at the end. The driver and driven sections are generally constructed of cylindrical tubes separated by a diaphragm or fast-opening valve (FOV). While the driven section is a longer tube with uniform-cross section, the driver section is relatively shorter, but with constant or variable diameter. The FOV, as the name suggests, is a high-pressure valve with an opening time of few milliseconds. The advantage of the FOV is that it provides more control over the initial pressure set in driver and driven section as opposed to a diaphragm which always bursts at a set pressure difference. Moreover, it saves time and effort due to its relative ease of operation. Typically, helium and argon are used as the driver and driven gas, respectively, since Helium generates large M_s for similar initial condition due to its high speed of sound, and argon being a monoatomic gas can be considered a perfect gas up to $M_s < 10$ [18].

The converging test section, made up of the transformation section (TS) and conical section (CS), immediately follows the straight driven section. A close-up of the test section is shown in Figure 38(b). Since TS is where the plane shock wave transforms into a spherical shock wave, extreme care should be taken to design and construct it. The shape of the TS transformation was parametrized as:

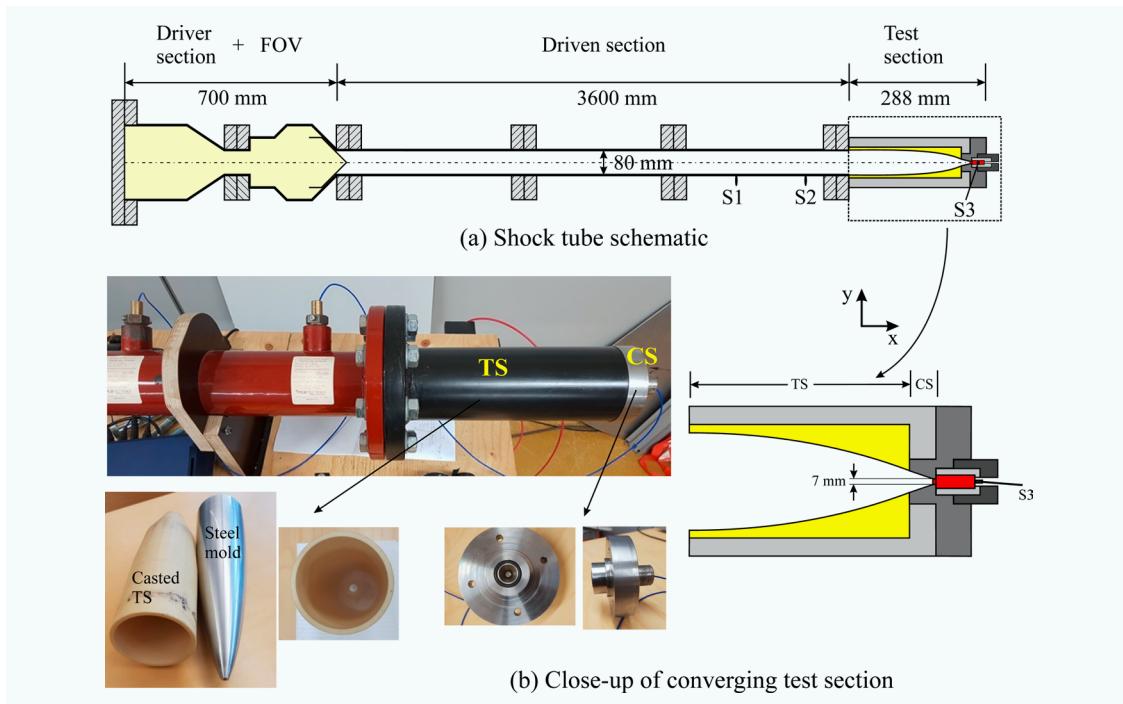


Figure 38: The converging shock tube facility along with the construction of the test section assembly mounted with TS and CS

$$x = A \sin\theta \tag{38}$$

$$y = B - R(1 - \cos\theta) \tag{39}$$

where $0 \leq \theta \leq 0.35\pi$, $A = 300.7$ mm, $B = 40$ mm and $R = 57.3$ mm. The shape was chosen to fulfil the condition that the shock foot remains normal to the wall without reflection/creation of a Mach stem during its convergence. Moreover, its surface should be smooth to not introduce additional wall reflections. Here, the TS was constructed by casting plastic around a CNC machined steel mould (Figure 38(b)). It can be scaled to any size provided its profile is preserved. The CS is an axisymmetric conical part which connects the TS to the desired end diameter (7 mm in this case) where the sensor under calibration is mounted. The whole assembly should be devoid of step/cavity at the connecting points and care should be taken during design and mounting. Using this method, a typical peak pressure of 3 MPa obtained from conventional shock tube can be pushed to around 40 MPa at the CS end wall.

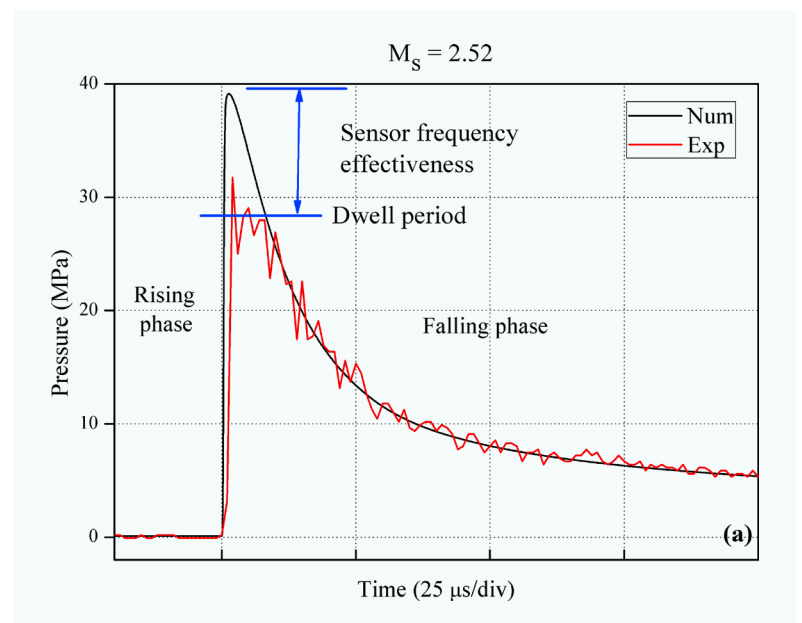
4.5.1 Uncertainty evaluation

For the conventional shock tube method, the peak pressure obtainable is dependent only on M_s and specific heat ratio (γ) of the driven gas. Since γ is constant with temperature for Argon, its uncertainty is zero, which leaves M_s as the sole contributor to the uncertainty estimation. However, in the converging shock tube method, calculating M_s at the instant of impact with the end wall is difficult due to the accelerating nature of the shock wave in the test section. To compare

and evaluate the pressure profile obtained from the sensor under study, numerical analysis is used in the current state. The numerical simulations were performed using an in-house code developed to solve the full set of compressible Euler equations using the Artificial Upstream Flux Vector Splitting Scheme. A detailed description of the code along with its validation is provided in [2]. An axisymmetric version of the code, specifically utilized for accelerating shock waves, is used in [18], where it is validated against experimental data.

A typical pressure profile, both numerical and experimental for initial $M_s = 2.52$, is as shown in Figure 39. Both the rising phase and falling phase of the profile match quite well between them.

Figure 39: Comparison plot between experimental and numerical pressure profile measured for an $M_s = 2.52$ shock wave



However, simulation predicts a relatively higher peak pressure compared to the experimental profile. This is because the reflection of the accelerating shock wave is a very quickly occurring event, where, by the time the sensor's element starts responding, the real pressure achieved is effectively lower. However, the sensor was still able to respond to such an ultra-fast dynamic process despite its unpreparedness. Since the simulation had no such limitations, it was able to estimate the profile at the peak more accurately. So, the numerical profile is used as a reference profile to establish the effectiveness of the sensor in pressure amplitude measurements.

By running the simulation with the estimated uncertainty in M_0 , an overall uncertainty of 3.4 % (based on the numerical pressure profile) up to 40 MPa was realized [2].

4.5.2 Future developments to establish SI traceability

The goal of pushing the upper ceiling of achievable pressure in shock tubes to the 40 MPa range through a state-of-the-art converging cone section was attained. However, it relies heavily on numerical simulation for the prediction of the achieved peak pressure as experimentally sensors could not measure the rapid events occurring near the peak. Since analytical solutions are unreliable in the vicinity of the cone, the uncertainty was estimated in conjunction with numerical simulations.

To eliminate the numerical simulation requirement, analytical solutions in the cone vicinity should become available to establish traceability. This can be achieved by further developing the conical test section to provide a step peak pressure profile (in the 50 μs – 100 μs range) at its end wall rather than the “blast” profile currently being generated. Generation of a step profile implies that the shock wave is of constant velocity from which its speed can be measured, thereby making analytical solutions readily available and providing a base for the expected peak pressure. Through this development, an uncertainty of 1 % or lower can be achieved.

5. Presentation of measurement results

5.1 Presenting data from drop-weight devices

Evaluation of calibration results can be done in two ways. The most obvious is to compare the peak pressures only. Another approach is to compare the time-dependent pressure pulse shape. Forming the ratio, point-by-point, of applied

dynamic pressure and sensor response, one obtains a time series of differences that can be Fourier transformed to obtain the frequency response of the sensor under test. In this case, any hysteresis between rising and falling edge of the pressure pulse needs to be properly addressed, in a way that necessarily must be specific to the device in question, so that no general rule can be given here. This is particularly so because the issue of different delays in different signal paths must be addressed in the steeper parts of the pulse. Information and results to be included on the calibration certificate:

- Identification of the DUT and related data acquisition unit (e. g., manufacturer, model, type, serial number)
- Relevant settings of the DUT (e. g., nominal sensor sensitivity pC/bar, applied filtering, sampling rate)
- Characteristics of the applied calibration pressure signal (e. g., pulse shape (half sine), pulse duration/frequency)
- Details on calculating the pressures (e. g., peak pressure, whole pressure curve as point-by-point pressure, number of averaged pressure measurements)
- Description of SI traceability (e. g., interferometric measurement, refractive index)
- Pressure calibration media (e. g., sebacate, glycerol)
- Calibration temperature (specified as probe/pressure media temperature)
- Environmental conditions (e. g., ambient temperature, pressure, and humidity)
- Calibration results including uncertainty (error/correction of the DUT reading as a function of pressure (for a nominal sensor sensitivity) or “calibrated” sensor sensitivity over a defined pressure range).

5.2 Presenting data from Shock tubes and FOD

5.2.1 Fast Opening Devices and/or Shock Tubes - CSM and SSM Methods

According to the model, the final uncertainty of the pressure measurement is rescaled to the range of pressure of the quasi-static calibration and not only to the amplitude of the step used to excite the

dynamics of the transducer. The information and results expected on the certificate are:

- Recall of the method and the model
- Equipment identification and settings of influence in brief (conditioner, filter, ...)
- Environmental conditions
- Calibration parameters: range of pressure and frequency
- Traceability to full settings, raw data, and processed data
- The quasi-static sensitivity of the transducer and associated uncertainty (can be from external calibration, but traceable by the certificate)
- Recall that dynamic gain is 1 by assumption
- Uncertainty $k = 2$ of the dynamic gain in % and in pressure units, evaluated from input rescaled to the full range of calibration and presented in a form exploitable by the final user (tabulated for example).

5.2.2 Chronometric Shock tube – MNM method

According to the model, the final uncertainty of the pressure measurement is rescaled to the range of pressure of quasi-static calibration and not only to the amplitude of the step used to excite the dynamics of the transducer. The information and results expected on the certificate are:

- Recall of the method and the model
- Equipment identification and settings of influence in brief (conditioner, filter, ...)
- Environmental conditions
- Calibration parameters: range of pressure and frequency, number of measurement points, initial conditions
- Traceability to full settings, raw data, and processed data
- The sensitivity of the transducer and associated uncertainty traceable by the certificate
- Recall that dynamic gain is 1 by assumption

- Uncertainty ($k = 2$) of dynamic gain in % and in pressure units, evaluated from input rescaled to the full range of calibration, presented in a form exploitable by the final user (tabulated for example).

These results can be used to trace the dynamic pressure measurement and used for calibration by comparison. Secondary and transfer calibrations are more efficient when they are performed from the uncertainty before tabulation.

5.2.3 Fast Opening Devices and/or Shock Tubes - WSM Methods

According to the model, the final uncertainty of the pressure measurement is rescaled to the range of pressure of the quasi-static calibration and not only to the amplitude of the step used to excite the dynamics of the transducer. The information and results expected on the certificate are:

- Recall of the method and the model
- Equipment identification and settings of influence in brief (conditioner, filter, ...)
- Environmental conditions
- Calibration parameters: range of pressure and frequency, number of measurement points, initial conditions
- Traceability to full settings, raw data, and processed data
- The sensitivity of the transducer and associated uncertainty traceable by the certificate
- Dynamic gain in % or dynamic sensitivity in V/pressure unit
- Uncertainty ($k = 2$) of dynamic gain in % and in pressure units, evaluated from the input rescaled to the full range of calibration, presented in a form exploitable by a final user (tabulated for example).

These results can be used to trace the dynamic pressure measurement and used for calibration by comparison. Secondary and transfer calibrations are more efficient when they are performed from the uncertainty before tabulation.

5.3 Presenting data independent of measurement technique

The multi-dimensional nature of a dynamic

calibration poses challenges not only for the measurement itself, but also for reporting, interpreting, and applying the calibration results in practice. One of the key characteristics of a SI traceable measurement is that it is independent of the measurement method. Dynamic pressure measurement standards (drop-weight devices, shock tubes, and fast-opening valves) presented in this report are based on different measurement principles, having different traceability routes and excitation signals with different pressure and frequency ranges. Although these measurement standards provide different information on the sensor performance, all results should be comparable (provided that SI traceability has been properly established), when results are expressed in a unified way.

A static calibration involves determining the calibration correction at certain pressure values. In a dynamic calibration also the pulse shape, i. e., signal frequency, needs to be considered, as it will have an influence on the calibration results. This was clearly shown for a commercial piezoelectric sensor (Figure 36), where the dynamic gain was found to deviate by up to 1 % from its nominal value at a frequency of 5 kHz, which is much lower than the natural frequency of the sensor of 215 kHz. Consequently, the characteristics of the calibration signal (signal shape/frequency and pressure) should match as closely as possible to the pressure signal in the application where the sensor is used.

Based on the experience of the DynPT project, we propose the following unified approach for reporting results of a dynamic pressure calibration,

in terms of pressure and sensor sensitivity.

Pressure correction

The results of a dynamic calibration can be reported by tabulating the sensor error or correction at different measurement points, as frequently done for a static pressure calibration. In this case, however, in addition to the pressure, also the frequency of the dynamic calibration signal needs to be reported for each measurement point. This is important information for the end-users, when applying the results for actual dynamic pressure measurements. An illustrative example of reporting results is given in Table 14.

Note 1. Depending on sensor linearity and applied calibration method (e. g., drop-weight or shock tube) calibration results can be reported for specific pressure and frequency points or a measurement range as above.

Note 2. For drop-weight devices, the calibration results are given for a specific frequency, rather than a frequency range.

Note 3. In the case of the drop-weight devices, the frequency can be derived from the duration of the half-sine pulse (t_{pulse}) as, $f = 1/(2 \cdot t_{\text{pulse}})$, i. e., a 4 ms pulse would correspond to 125 Hz frequency.

Sensor sensitivity

Another way of reporting the results would be to report the calibrated sensor sensitivity (pC/bar), i. e., the “correct” sensitivity value of the sensor that realizes the “true” pressure as given by the dynamic pressure reference. Sensor manufacturers

Table 14: Example of reporting calibration results in terms of pressure. Note that numbers given in the table are arbitrary and only for illustration purpose.

Pressure range (bar)	Frequency range (Hz)	Reference pressure (bar)	DUT pressure (bar)	Calibration correction (bar)	Uncertainty of pressure, ($k = 2$) (bar)	Uncertainty of pressure, ($k = 2$) (%)
0...1	10...100	1.000	1.001	-0.001	0.020	2.0
	100...1000	1.000	1.002	-0.002	0.020	2.0
	1000...10000	1.000	1.003	-0.003	0.020	2.0
0...10	10...100	10.00	10.04	-0.04	0.20	2.0
	100...1000	10.00	10.05	-0.05	0.20	2.0
	1000...10000	10.00	10.06	-0.06	0.20	2.0
0...100	10...100	50.0	50.1	-0.1	2.0	2.0
	100...1000	50.0	50.2	-0.2	2.0	2.0
	1000...10000	50.0	50.3	-0.3	2.0	2.0

Pressure range (bar)	Frequency range (Hz)	Sensor sensitivity (pC/bar)	Uncertainty of sensitivity, ($k = 2$) (pC/bar)	Uncertainty of sensitivity, ($k = 2$) (%)
0...1	10...100	1.000	0.011	1.1
	100...1000	1.000	0.012	1.2
	1000...10000	1.001	0.013	1.3
0...10	10...100	1.001	0.014	1.4
	100...1000	1.001	0.015	1.5
	1000...10000	1.002	0.016	1.6
0...100	10...100	1.002	0.017	1.7
	100...1000	1.002	0.018	1.8
	1000...10000	1.003	0.019	1.9

Table 15: Example of reporting calibration results in terms of sensor sensitivity. Note that numbers given in the table are arbitrary and only for illustration purpose.

typical give the sensitivity value of their sensors for some specific pressure range. This value is inserted to the signal readout unit (e.g., charge amplifier in case of piezoelectric sensors) to transform the sensor signal to pressure values. Therefore, in many cases, calibrated sensitivity values are the most convenient format of reporting results, because no additional corrections to the readout are needed. However, the condition for applying this approach is that the sensor is linear in the measurement range of interest. This is typically the case (at least for piezoelectric sensors) over wide pressure and frequency ranges. However, non-linearities are expected near the low pressure and high frequency end of the measurement range. Especially at higher frequencies the deviation can be significant already at values well below the sensor natural frequency, as shown in this report (Figure 36).

Note 1. Depending on sensor linearity and applied calibration method (e.g., drop-weight or shock tube) calibration results can be reported for specific pressure and frequency points or a measurement range as above.

6. Conclusions

Guidelines on designing, constructing, and validating dynamic pressure measurement standards have been given, including examples of developments made within the DynPT project. The guidelines include the principal methods of realizing a dynamic pressure standard, i.e., fast-opening valves, shock tubes and drop-weight

devices. With these methods it is possible to provide SI traceable calibrations in a wide pressure and frequency range from 0.1 MPa–400 MPa and 1 kHz–30 kHz, respectively, and pressure steps with rise times as short as microseconds. The target measurement uncertainty of 1 % was achieved in the measurement pressure and frequency range up to 5 MPa and 100 Hz, respectively. At higher pressures — measured with drop-weight devices — the current uncertainty level is around 1.5 %–2.0 %. At higher frequencies, the uncertainties of shock tube calibrations become higher, reaching a level of around 6 % at 30 kHz. However, sub-millisecond pressure step amplitudes can be generated at uncertainties around 2 %. Several ideas for improvements of shock-tubes and drop-weight devices have been identified in this project, which will enable reaching the 1 % uncertainty target over a wider measurement range. As an important outcome of this project, a unified (method independent) way of presenting results of dynamic pressure calibrations has been proposed. The aim with the recommendation is to support harmonization of reporting results within the measurement community, and most importantly to ensure that calibration results are given in a metrologically sound way to ensure reliability of measurements, i.e., SI traceability.

References

- [1] S. Downes, A. Knott and I. Robinson, "Towards a shock tube method for the dynamic calibration of pressure sensors," *Philosophical Transactions of the Royal Society A: Mathematical, Physical and Engineering Sciences*, pp. 372(2023), 20130299, 2014.
- [2] S. Sembian and M. Liverts, "On using converging shock waves for pressure amplification in shock tubes," *Metrologia*, vol. 57, no. 3, 2020.
- [3] J. Salminen, R. Högström, S. Saxholm, A. Lakka, K. Riski and M. Heinonen, "Development of a primary standard for dynamic pressure based on drop weight method covering a range of 10 MPa–400 MPa," *Metrologia*, vol. 55, no. 2, 2018.
- [4] J. Salminen, S. Saxholm, J. Hämäläinen and R. Högström, "Advances in traceable calibration of cylinder pressure transducers," *Metrologia*, vol. 57, no. 4, 2020.
- [5] Y. Durgut, O. Ganioglu, B. Aydemir, A. Turk, R. Yilmaz, A. Hamarat and E. Bagci, "Improvement of dynamic pressure standard for calibration of dynamic pressure transducers," in *19th International Congress of Metrology (CIM2019)*, *EDP Sciences*, Paris, 2019.
- [6] T. Bruns, E. Franke and M. Kobusch, "Linking dynamic to static pressure by laser interferometry," *Metrologia*, vol. 50, no. 6, pp. 580–585, 2013.
- [7] O. Slanina, S. Quabis, S. Derksen, J. Herbst and R. Wynands, "Comparing the adiabatic and isothermal pressure dependence of the index of refraction in a drop-weight apparatus," *Applied Physics B*, vol. 126, p. 175, 2020.
- [8] J. Yang, S. Fan, B. Li, R. Huang, Y. Shi and B. Shi, "Dynamic modeling of liquid impulse pressure generator for calibration of pressure sensors," *Sensors and Actuators A: Physical*, vol. 279, pp. 120–131, 2018.
- [9] S. Fei and D. Kong, "Bulk modulus measurement of hydraulic oil based on drop-hammer calibration device," in *International Conference on Electric Information and Control Engineering*, 2011.
- [10] A. G. Lyapin, E. L. Gromnitskaya, I. V. Danilov and V. V. Brazhkin, "Elastic properties of the hydrogen-bonded liquid and glassy glycerol under high pressure: comparison with propylene carbonate," *RSC advances*, vol. 7, pp. 33278–33284, 2017.
- [11] ISO 16063-13:2001, Methods for the calibration of vibration and shock transducers — Part 13: Primary shock calibration using laser interferometry, Geneva: ISO, 2001.
- [12] T. Gu, D. Kong, F. Shang and J. Chen, "A calculation and uncertainty evaluation method for the effective area of a piston rod used in quasi-static pressure calibration," *Measurement Science and Technology*, pp. 29(4), 045015, 2018.
- [13] W. E. Danforth, Jr., "The dielectric constant of liquids under high pressure," *Physical Review*, 38(6), p. 1224, 1931.
- [14] S. S. Bair, High pressure rheology for quantitative elasto-hydrodynamics, Elsevier, 2019.
- [15] A. B. Olivera, "Contribution à l'étalonnage dynamique des capteurs de pression," *Modélisation de l'incertitude associée. Thèse de l'école doctorale ENSAM Paris*, (2004).
- [16] J. L. Schweppe, L. C. Eichberger, D. F. Muster, E. L. Michaels and G. F. Paskusz, Methods for the dynamic calibration of pressure transducers: National Bureau of Standards Monograph, 67, Washington-DC: US Government Printing Office, (1963).
- [17] C. Sarraf and J. P. Damion, "Dynamic pressure sensitivity determination with Mach number method," vol. 29(5), no. 054006, (2018).
- [18] M. Liverts and N. Apazidis, "Limiting Temperatures of Spherical Shock Wave Implosion," *Physical Review Letters*, vol. 116, no. 1, p. 014501, 2016.

Validation of dynamic temperature calibration methods for the range up to 3000 °C, with a response time below 1 ms

S. Sundarapandian¹, M. Liverts², G. Jönsson³, P. Broberg⁴, A. Fateev⁵, G. Sutton⁶, D. Lowe⁷, R. Högstrom⁸, S. Saxholm⁹

1. Introduction

This article is a slightly adapted version of the deliverable D2 in the EMPIR project 17IND07 – DynPT: “Validation report on the developed dynamic temperature calibration methods for measuring temperature range up to 3000 °C, with a target uncertainty up to 3 % and response time below 1 ms”. This project has received funding from the EMPIR programme co-financed by the Participating States and from the European Union’s Horizon 2020 research and innovation programme.

The developed methods along with the primary contribution of the participants are as follows:

RISE – Develop a calibration system and method for calibration of radiance thermometers based on rapid shutter systems and high temperature black bodies in the range up to 2200 °C.

KTH – Design, construct, and optimize an automated diaphragm-less shock tube facility (temperature bench) for dynamic measurement of temperature in the range of 50 °C–3500 °C.

NPL – Develop a calibration procedure, to test the temperature benches at KTH and RISE, based on radiance calibration of dynamic thermometers traceable to ITS-90 via high temperature black body facilities in the range up to 3000 °C with uncertainty less than 1 %.

2. Radiance Thermometer

2.1 Modelling, construction and operation

At RISE, a new calibration resource was

developed to verify the dynamic behavior of radiation thermometers. The approach was to use a conventional black-body cavity as a static temperature reference and an external rotating optical chopper to vary the radiation periodically. A chopper can operate at fast enough rotational speed that it can generate 1 ms periodic pulses. It also lets all radiation through when it is open and blocks all radiation when it is closed (with a metal chopper disk). One downside is that for shorter times the openings in the disk must be smaller. As the openings become small compared to the diameter of the measuring spot, the effect of the transition between open and closed becomes larger. The shape of the rise and fall slopes can affect the measurement and here has been studied theoretically as well as with a numerical model. An optional iris aperture can be used in front of the chopper to reduce the spot size and reduce the effect of the transition. The response from this setup was first modelled and then experimentally evaluated using two different pyrometers.

Mathematical model

For simple cases it is possible to model the transition between fully open and fully closed mathematically. One such case is when the blades are straight, and the measurement spot has a top-hat distribution and is smaller than the blades. It can be shown [1] that the area of the spot covered by a blade in this case is given by

$$A = r^2 \left(\pi - \beta + \frac{\sin 2\beta}{2} \right)$$

where r is the radius of the measurement spot

¹ Dr. Sembian Sundarapandian (KTH), E-mail: sembian@kth.se

² Dr. Michael Liverts (KTH), E-mail: liverts@mech.kth.se

³ Dr. Gustav Jönsson (RISE), E-mail: gustav.jonsson@ri.se

⁴ Dr. Patrik Broberg (RISE)

⁵ Dr. Alexander Fateev (DTU), E-mail: alfa@kt.dtu.dk

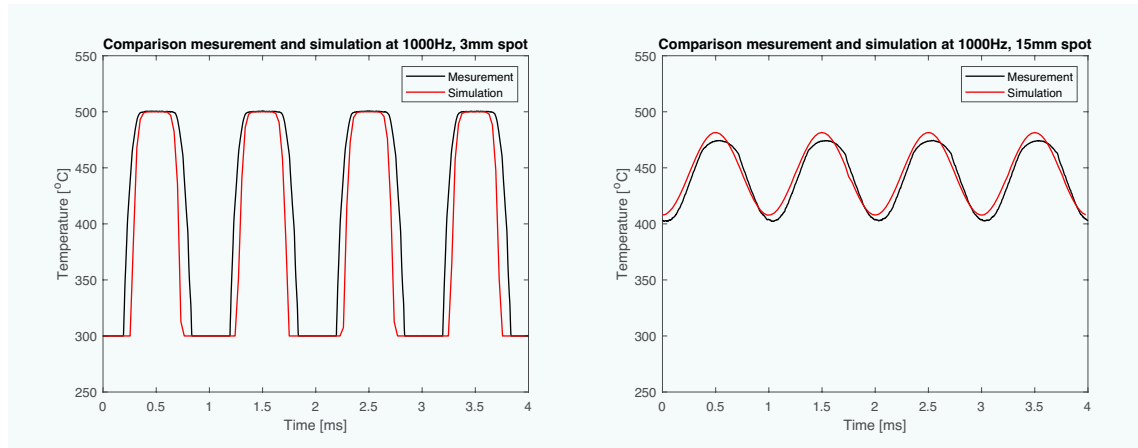
⁶ Dr. Gavin Sutton (NPL), Department of Thermal and Radiometric Metrology, E-mail: gavin.sutton@npl.co.uk

⁷ Dr. Dave Lowe (NPL), Department of Thermal and Radiometric Metrology, E-mail: dave.lowe@npl.co.uk

⁸ Dr. Richard Högstrom (VTT), National Metrology Institute VTT MIKES, E-mail: richard.hogstrom@vtt.fi

⁹ Sari Saxholm (VTT), National Metrology Institute VTT MIKES, E-mail: sari.saxholm@vtt.fi

Figure 1: Comparison between the model and measurement data for 3 mm and 15 mm spot size



and $\beta = \arccos \frac{\sin(\delta - \theta)}{\sin(\delta)}$ with $\sin(\delta) = \frac{r}{R}$. R is the distance from the center of rotation of the chopper disk and the center of the spot and θ is the rotation angle of the chopper disk. With this it is possible to calculate the area of the spot that is covered by a blade during the transition from fully open to fully closed. This model has limitations in the blade shapes and measurement spot distribution that it can be used for. For more general spots and blades, a numerical approach can be used.

Numerical model

A numeric model of the chopper setup was also made. This model included an aperture to determine if it could be used to reduce the effect of the transition. The measurement spot was

defined with values between 0 and 1. A Gaussian distribution was used here but any distribution is possible. An aperture was placed in front of the chopper, defined with either 0 or 1. The geometry of the chopper was defined in a similar way. The three parts were then summed up by multiplying the images, pixel by pixel, and then adding the values in every pixel together. Next the chopper is rotated one step and the sum in the last step is calculated again. This is repeated for a full period of the chopper. Since there is no radiation source in this model the results are normalized and then multiplied by a temperature for a result that can be compared to measurement data.

Figure 1 shows the results of the model compared to data acquired from a fast pyrometer. The model data has been scaled to 500 °C, as that

Table 1: Uncertainty budget for 2200 °C ($\lambda = 0.65 \mu\text{m}$, values in K)

Uncertainty contribution	Estimate $\pm \delta_{xi}$	Distribution Φ_i	Standard level $u(x_i) = \delta_{xi} * \Phi_i$	Sensitivity coeff. c_i	Uncertainty component $ui = u(x_i) * c_i$
Resolution 0.1 °C	0.05	R	0.03	1	0.03
Repeatability/stability	1	R	0.58	1	0.58
Distance dependence	1	R	0.58	1	0.58
Calibration	2	N	1	1	1
Drift	1	R	0.58	1	0.58
Resolution	0.05	R	0.03	1	0.03
Stability	1	R	0.58	1	0.58
Gradients	2	R	1.15	1	1.15
Effect of surrounding temperature, emissivity	2	R	1.15	1	1.15
Combined standard uncertainty (k = 1)					2.24 K
Expanded uncertainty (k = 2)					4.5 K

was the reference used, and cut off at 300 °C as this was the lower temperature limit for the pyrometer.

Experimental setup

Figure 2 shows the equipment when it is set up. The pyrometer measures the radiation from a blackbody cavity through an aperture and a chopper. The aperture is optional and is used for reducing the effect of the transition if the measurement spot is large compared to the chopper blades. The chopper is connected to a controller that sets the rotation speed and reads the real speed of the disk using an optical sensor which in turn is connected to a computer. The pyrometer is connected to an analog to digital converter (NI-9222) and then to the computer, as well.

A program was written that sets a chopper speed, waits for it to stabilize, reads the speed and records the response from the thermometer. This is repeated for a given set of rotation speeds. Individual responses can then be analyzed, or the result can be plotted as a function of frequency. When investigating the response time of the radiation thermometer it is of interest to determine the shortest exposure time required to get the full temperature response. This can be done by plotting the amplitude difference as a function of half the period of the signal. An example of the amplitude difference as a function of both frequency and half-period can be seen in Figure 3.

The specified response time for the pyrometer in question was 30 ms. As can be seen in the half period plot, this time correspond well to when the amplitude starts to stabilize, which means that the exposure time is just long enough for the thermometer to reach the correct temperature value.

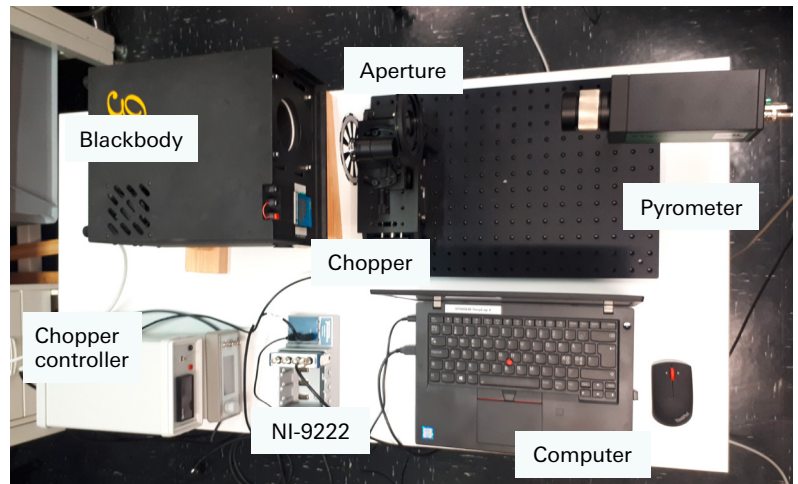


Figure 2:
Experimental setup

2.2 Uncertainty estimation for measurement methods

Temperature uncertainty

The temperature measured by the radiation thermometer will periodically alter between two temperatures using this setup. When the chopper is closed it will measure the temperature of the blade at room temperature. The emissivity of the blade is unknown but high to avoid reflections. The exact temperature measured on the blade is most often not of interest.

When the chopper is open there is a free line of sight between the blackbody cavity and the radiation thermometer. This case can be considered as if there is no chopper when it comes to the uncertainty of the measurement. It should be noted that this is only true if the measurement spot is small compared to the chopper blades so that the chopper does not affect the measurement. The case where a blade is partially covering the measurement spot is also not considered. An uncertainty budget for the case where a 2200 °C blackbody cavity is used is shown in Table 1.

The uncertainty for the case of the 500 °C

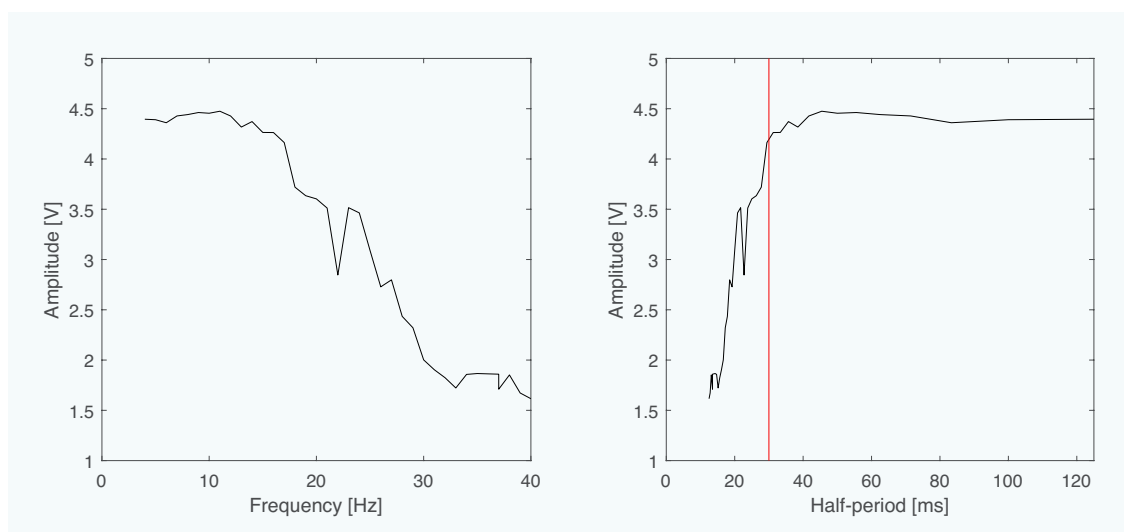


Figure 3:
Amplitude difference as a function of frequency and half-time

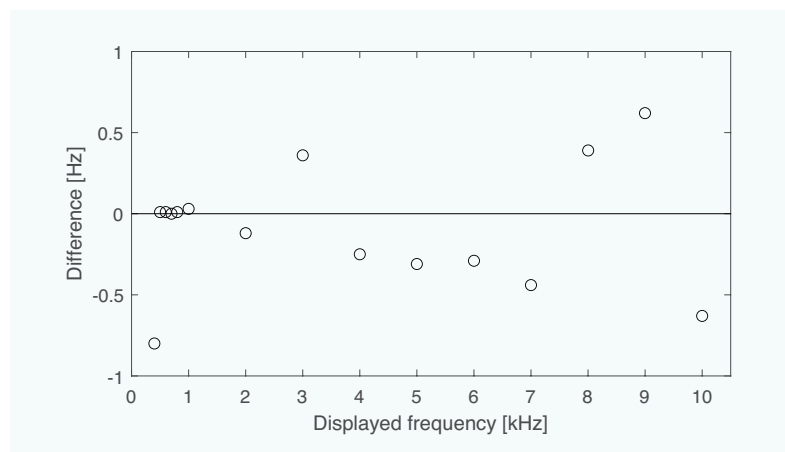


Figure 4: Difference between measured and displayed frequency

blackbody can be calculated in a similar way to a combined standard uncertainty ($k = 1$) of 1.1 K or an expanded uncertainty ($k = 2$) of 2.2 K.

Frequency uncertainty

The controller for the chopper monitors the rotational frequency of the disk via an outer ring on the disk with 100 slots, and a photodetector. The measured frequency can be read on the display on the controller, can be acquired by the computer by sending a command to the controller, or be measured by an external frequency counter via a frequency output from the controller. The value acquired by the computer is the same as on the display and is the value used for further calculations.

A Fluke PM 6680B frequency counter was used to find the difference between the measured value and that acquired from the controller and thereby an estimate of the error in the exposure time. The expanded uncertainty for this counter is less than ± 3 mHz for frequencies from 1 Hz to 10 kHz. Figure 4 shows the difference between the frequency of the outer ring on the disk displayed on the controller, and that measured with the frequency counter. All displayed values were within 1 Hz of those measured, which correspond to 0.1 Hz of the blades on this particular disk.

When the time difference is calculated the difference for one period using the displayed frequency compared to the measured frequency is less than ± 1 μ s for all values except for 40 Hz where the difference is about 50 μ s. This is because the displayed value was off by almost 1 Hz resulting in the relatively large error. These time differences are for a full period, therefore the difference for when the thermometer is exposed to radiation will be half of these values. All differences are small compared to the shortest time (1 ms) that is measured with this setup.

Another source of uncertainty is the transition between a fully open and a fully closed chopper. Unfortunately, this is harder to quantify. The

time it takes for the transition depends on the rotational speed of the chopper and the size of the measurement spot in the plane of the chopper. To minimize the transition time the spot should be as small as possible and the rotational speed as large as possible.

Two more things that make the transition less predictable is the distribution of the spot and the response of the detector. The distribution of the measurement spot, which is often unknown, in the plane of the chopper will affect the shape of the transition curve. It is also unknown what the response of the detector is during the transition, especially at chopper frequencies close to the response time of the radiation thermometer. A slower transition might then either aid or hurt the detector, resulting in response times slightly faster or slower than the actual time.

3. NPL DynPT high-speed fibreoptic pyrometer

3.1 Instrument design and model

A schematic of the thermometer system design is shown in Figure 5. It consists of:

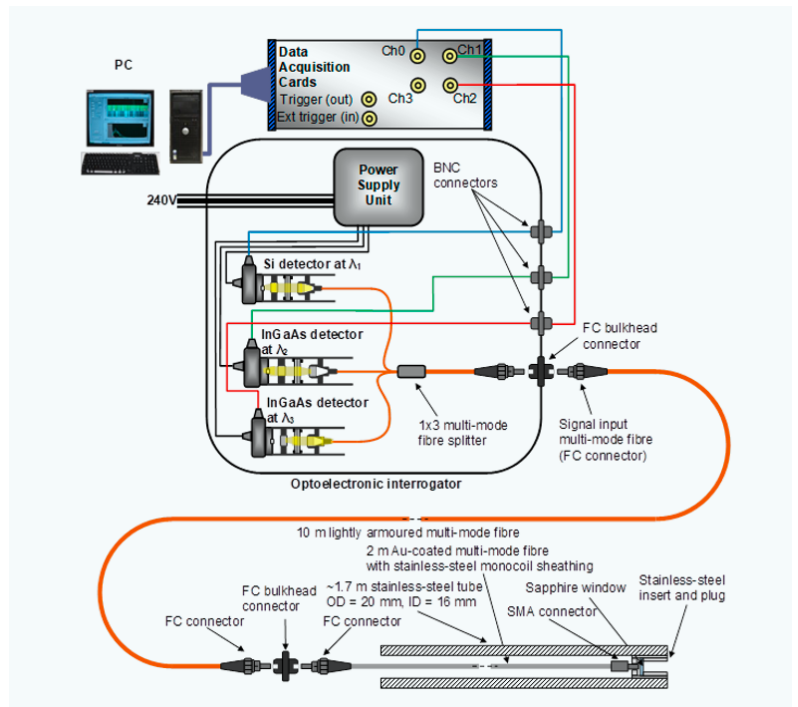
- A sensor: a 2 m long gold-coated multi-mode (MM) step-index fibre, with 400 μ m core diameter, numerical aperture $NA = 0.22$, stainless-steel monocoil sheathing, an SMA connector on one end (hot front end) and an FC connector on the other end (cold back end)—for testing purposes, this was placed inside a ~ 1.7 m long stainless-steel tube (outer diameter: 20 mm, inner diameter: 16 mm), with the SMA connector protected by a recessed sapphire window; sensor and packaging can be tailored to the final application and installation requirements (e.g., addition of a collimating lens).
- An extension lead fibre: a lightly-armoured 10 m long MM step-index fibre patch-cord, with 600 μ m core diameter, $NA = 0.22$, dual acrylate coating, 3 mm diameter PVC sleeve and FC connectors on both ends—this connects the sensor (on the FC connector) to the interrogator.
- A passive optoelectronic interrogator, assembled in-house and consisting mainly of:
 - ▷ A custom-made 1×3 MM step-index fibre coupler/splitter with 600 μ m core diameter, $NA = 0.22$ and FC connectors on all ports.

- ▷ Three photodetector assemblies, using off-the-shelf components, for measuring optical thermal radiation at 3 different wavelengths: $\lambda_1 = 850 \text{ nm}$, $\lambda_2 = 1050 \text{ nm}$ and $\lambda_3 = 1300 \text{ nm}$.
- ▷ a power supply unit to power the photodetectors.

Fibres with large core diameter and large NA were chosen to maximise collection of optical thermal radiation; the gold (Au) coating allows the fibre to withstand high temperatures, up to $\sim 1000 \text{ K}$, although the core diameter of Au-coated fibres is limited to $400 \mu\text{m}$.

The wavelengths of the photodetector assemblies were chosen based on previous experience to avoid spectral features (emission and absorption lines) from the combustion by-products and the components of the pyrotechnic charges (see figures below, taken from earlier spectroscopic experiments), as well as to test the assumption that the measured combustion process behaves like a blackbody (emissivity $\epsilon = 1.0$)—good agreement amongst the temperatures estimated at different wavelengths can be used to confirm that the blackbody condition is met. Figure 6a shows the emission spectrum captured with a Si spectrometer, along with the blackbody spectrum from a tungsten calibration lamp (with a temperature of 3165 K) overlapped to the measured spectrum. The agreement between the shape of the two spectra suggests that the blackbody assumption for a fireball is a valid hypothesis. Figure 6b shows the emission spectrum captured with an InGaAs spectrometer.

The minimum and maximum temperatures measurable by the instrument are dictated, respectively, by the noise level (experimentally measured as $\sim 1 \text{ mV}$ for most values of gain G) and the saturation level ($\sim 10 \text{ V}$) of the photodetectors. Voltage signals generated by the three photodetectors were plotted versus temperature for all values of gain G and bandwidth B . Figure 7



shows two of these plots for representative values of G and B .

Figure 5: Schematic of the system

- With a gain of $G = 20 \text{ dB}$ ($B = 1 \text{ MHz}$ —Figure 7a), the instrument can measure a minimum temperature of $\sim 1150 \text{ K}$ at a single wavelength ($\lambda_3 = 1300 \text{ nm}$) or $\sim 1400 \text{ K}$ at all three wavelengths.
- With a gain of $G = 30 \text{ dB}$ ($B = 260 \text{ kHz}$), the minimum measurable temperature can be brought down to $\sim 1025 \text{ K}$ for single-wavelength measurement ($\lambda_3 = 1300 \text{ nm}$) and $\sim 1275 \text{ K}$ at all three wavelengths, but at cost of reduced sampling speed ($f \leq B = 260 \text{ kHz}$), while still avoiding saturation at 3300 K , our maximum temperature of interest.
- With a gain of $G \geq 40 \text{ dB}$ ($B = 90 \text{ kHz}$ —Figure 7b), the photodetectors would start saturating at $T_{\text{MAX}} < 3300 \text{ K}$ and their bandwidth would

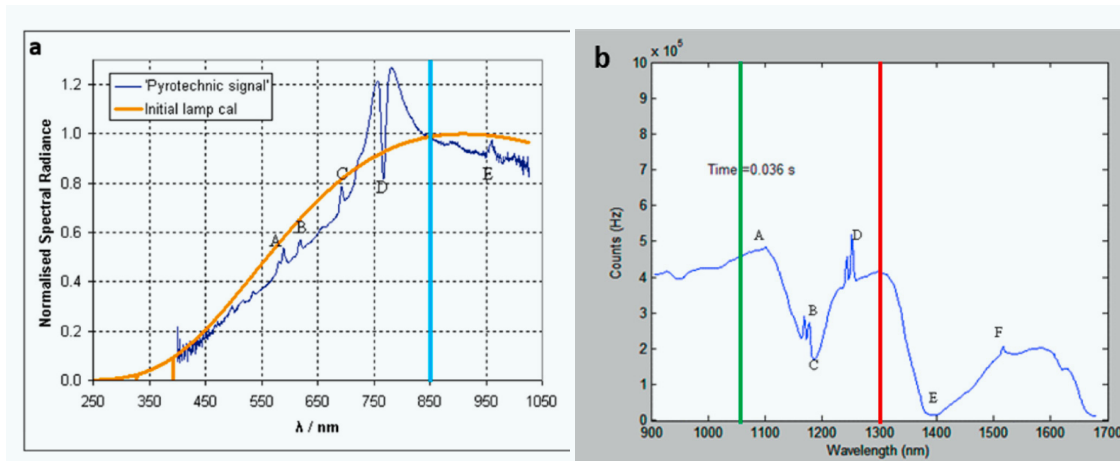


Figure 6: Pyrotechnic emission spectrum from (a) Si spectrometer, (b) InGaAs spectrometer, $\sim 36 \text{ ms}$ after ignition. The coloured vertical lines identify the chosen wavelength: 850 nm (blue line in (a)), 1050 nm (green line in (b)) and 1300 nm (red line in (b))

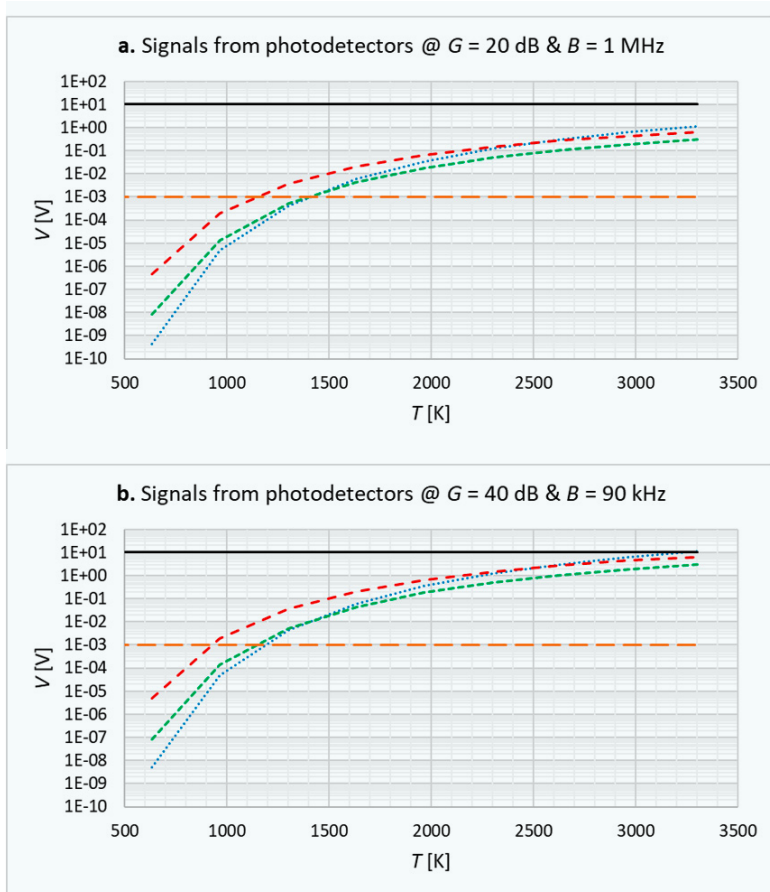


Figure 7: Modelled signals from photodetectors versus blackbody temperature at different G and B settings: (a) $G = 20$ dB and $B = 1$ MHz, (b) $G = 40$ dB and $B = 90$ kHz

decrease significantly, down to $B = 3$ kHz at $G = 70$ dB.

Hence, the optimum photodetector gain is $G = 30$ dB, which allows temperatures above 1025 K to be measured for $\lambda_3 = 1300$ nm, or temperatures above 1275 K to be measured for all wavelengths, with a maximum sampling rate $f \leq B = 260$ kHz.

3.2 Instrument calibration

The instrument was calibrated using a Thermo Gauge blackbody radiation furnace and a KE-Technologie GmbH LP3 linear pyrometer calibrated traceably to the ITS-90 [2], with the stainless-steel tube of the packaged sensor filled with sand to avoid overheating the Au-coated fibre that could be irreversibly damaged. A photograph of part of the test rig is shown in Figure 8: the hot Thermo Gauge blackbody furnace and temperature sensor are visible in the background and foreground, respectively. The latter is placed on a stainless-steel V-groove mounted on an optical breadboard and safely held in place by removable brackets bolted to the breadboard. This breadboard is installed on a motorised stage, controlled by a computer, for horizontal and vertical alignment. The LP3 (not visible in Figure 8) is mounted on the same framework,

so that it can be easily moved in front of the blackbody, in place of the sensor, to measure the temperature at each setpoint of the calibration. Data from the instrument were acquired using a NI LabVIEW program, written in-house and executed on the PC that is part of the system, whereas the blackbody furnace was controlled with a separate desktop computer that also controls the motorised framework.

The instrument was configured with the photodetectors set with optimum gain $G = 30$ dB ($B = 260$ kHz) and the sampling rate set at $f = 250$ kHz for the temperature range $T = (1073-2873)$ K, in steps of $\Delta T = 200$ K. The raw voltage signals were analysed to find the optimum calibration point in each signal. The average signal at each setpoint was measured for each wavelength/photodetector and plotted versus the set-point temperature measured from the LP3 linear pyrometer. Figure 9 shows good agreement between experimental data and the theoretical model at $G = 30$ dB, with the signal from the 1300 nm photodetector higher than predicted, most likely due to overestimated losses, as a single figure was used for all three wavelengths. Figure 9 also shows that the instrument can measure a temperature as low as 1073 K at $\lambda_3 = 1300$ nm or 1273 K at all three wavelengths—these minimum temperatures match with those expected from the theoretical model, with relative temperature differences within $\pm 1\%$ (absolute differences are within ± 15 K).

Dynamic tests

To demonstrate the speed of the instrument, dynamic tests were performed using theatrical flash charges [3] in the pyrotechnic facility at NPL. This consists of a vented enclosure where pyrotechnic charges, placed on a stage, are remotely triggered with a controller that is connected and synchronised with the instrument. The sensor is mounted such that its front end protrudes into the enclosure with its tip ~ 15 cm above and ~ 5 cm away from the centre of the charge. The optimum position of the sensor is based on experience from previous tests, when we also conducted absorption/transmission experiments, from which no optical transmission was observed during the explosion, thus suggesting that the fireball is opaque and supporting our blackbody assumption, and an initial absorption coefficient $\alpha_0 = 0.25 \text{ cm}^{-1}$ was estimated at $\lambda \approx 850$ nm. The photodetector gain was set at $G = 30$ dB, as the instrument was calibrated only with this setting.

The set of tests with pyrotechnic charges, shown in Figure 10, produced consistent results and good agreement among temperatures measured at different wavelengths, meaning that the blackbody

condition ($\epsilon = 1$) is more closely met. In these tests, the maximum temperatures estimated at different wavelengths agree with each other within up to ~ 137 K or $\sim 4.5\%$. It is also worth observing that the temperature measured at $\lambda_1 = 850$ nm was always the highest, whereas the temperature measured at $\lambda_3 = 1300$ nm was always the lowest.

In summary, a novel ultra-high-speed combustion pyrometer, based on collection of thermal radiation via an optical fibre, was successfully designed, developed and tested. The instrument was traceably calibrated to the ITS-90 over the temperature range $T = (1073\text{--}2873)$ K with residuals $< 1\%$. Dynamic tests with pyrotechnic charges demonstrated that the instrument could measure rapid (sub-ms) events, due to its high sampling rate (up to 250 kHz): a temperature rise of up to ~ 3.25 K/ μs was estimated for explosions of large pyrotechnic charges. The accuracy of the temperature measurements can be assessed by considering the extent of agreement between readings at the three wavelengths—a self-diagnostic feature that is a critical strength of the technique. However, even when agreement between temperatures is poor, we can say, with a high level of confidence, that the fireball temperature is at least that reported by the reading at 850 nm.

Figure 9: Experimental data compared with theoretical model

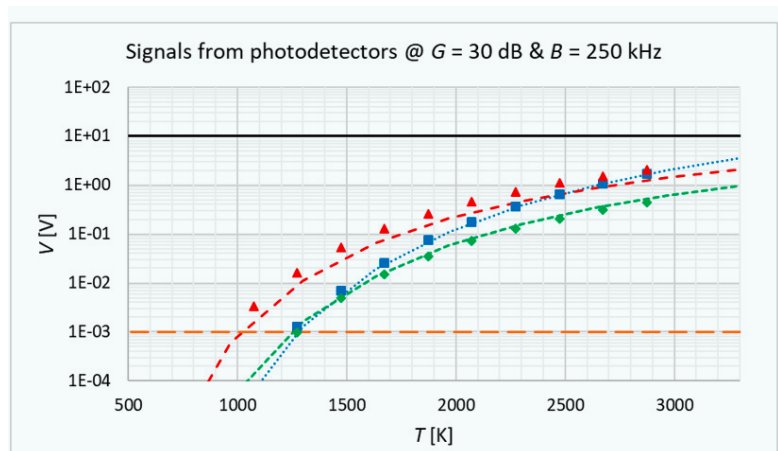
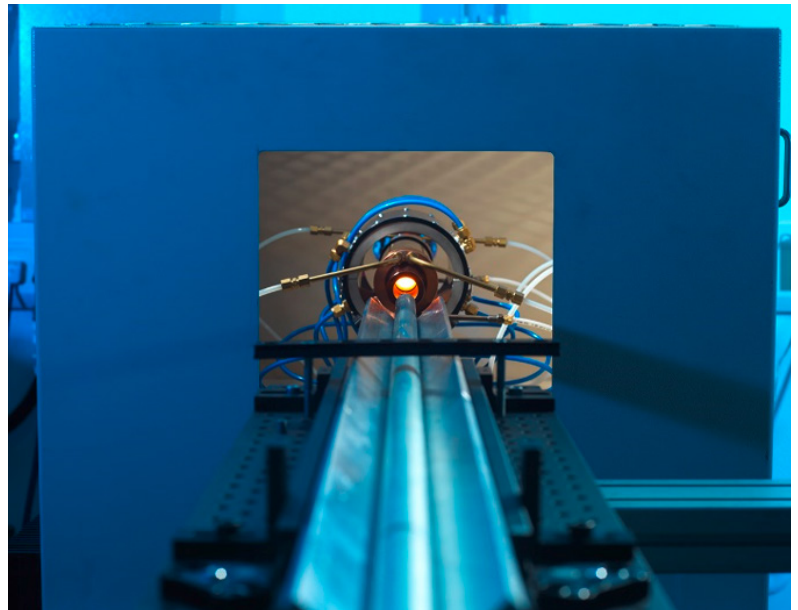
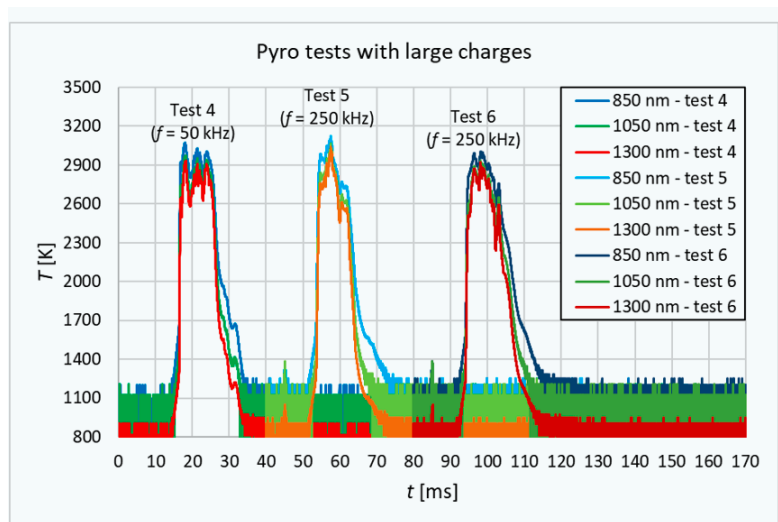


Figure 10: Time trend of temperatures for pyrotechnic tests—temporal offset introduced for clarity

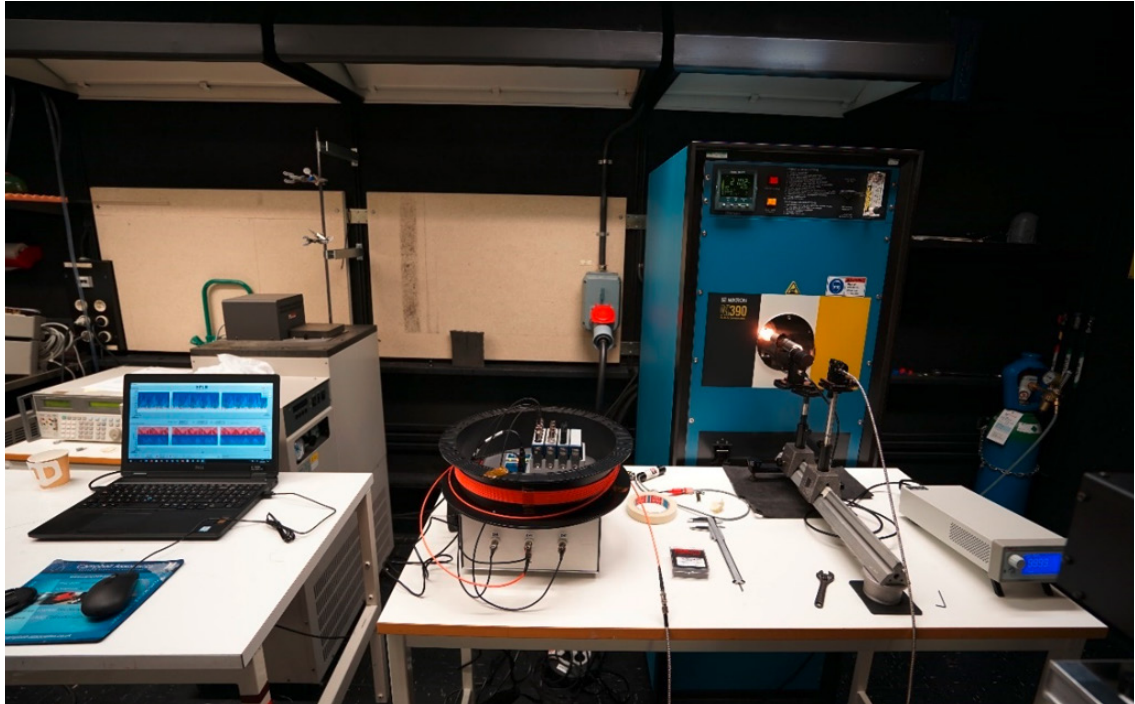


4. Cross-validation tests

The description of the cross-validation tests performed on a modified version of the NPL's DynPT system at RISE in Borås (Sweden) along with its results are presented and discussed in this section.

Figure 8: Photograph of the calibration furnace: the instrument sensor, housed in a steel tube, is sitting on the V-groove placed in front of blackbody furnace, ready to be manually moved in and out of it for dynamic calibration at a set temperature

Figure 11: Photo of the test rig, showing: the Dryad PC on the left; the optical interrogator, with the DAQ system and the reel of extension lead fibre on top of it, in the middle; the Mikron M390 blackbody cavity in the background on the right, in front of which is visible the rail, the chopper and the front (hot) end of the DynPT sensor; the chopper controller is visible on the bottom right corner



4.1 Test rig

The DynPT system was tested using the facilities at RISE (see Figure 11), consisting of:

- a Mikron M390 blackbody radiation furnace by LumaSense Inc.,
- a movable LP5 linear pyrometer by KE Technologie GmbH (not visible in Figure 11),
- a rail on a bench, aligned with the blackbody cavity,
- a removable post with a Thorlabs kinematic mount and an adaptor to hold the front (hot) end of the DynPT sensor with the collimating lens, at ~ 52 cm from the back wall of the blackbody cavity,
- a movable optical chopper (Thorlabs MC1F10HP), placed between the blackbody and the sensor, and its controller (Thorlabs MC2000B), for dynamic tests, to simulate fast temperature transients.

Data from the DynPT system was acquired using the New Explosion Thermometer with continuous measurement and logging with a LabVIEW program on the Dryad laptop, whereas the blackbody furnace was controlled manually and the LP5 with a separate desktop computer.

4.2 Calibration tests

Calibration tests were performed without the chopper in between the blackbody cavity and the front (hot) end of the DynPT sensor, as shown in Figure 12. Unless otherwise stated, the DynPT system was configured with the photodetectors set with gain $G = 30$ dB ($B = 260$ kHz) and the sampling rate set at $f_s = 250$ kHz; then, the voltage offset from the three photodetectors was measured once, in order to zero the photodetectors. Calibration coefficients from the Calibration check test of the DynPT system with collimating lens at NPL were loaded onto the system.

The DynPT system was calibrated in the temperature range $T = (1200 - 2200) \text{ }^\circ\text{C} \approx (1473 - 2473) \text{ K}$, in steps of $\Delta T = 200$ K, according to the following procedure:

1. the blackbody furnace was set at the required temperature set-point;
2. the temperature of the blackbody cavity was monitored using the LP5 pyrometer, with the DynPT sensor off the rail;
3. once the blackbody temperature reached stability, a measurement was taken from the LP5 and the DynPT sensor moved back into

Table 2: Test parameters

Photodetector gain	G [dB]	30
Sampling rate	f_s [kHz]	250
Temperature range	T [K]	1473 – 2473
Temperature step	ΔT [K]	200
Number of measurements at each step	N	1

place (so that it was in line with and parallel to the long axis of the blackbody furnace, as in Figure 12);

4. data was acquired and logged on the DynPT system for $t < 1$ s;
5. only one measurement was made at each set-point temperature.

Raw data, i. e., temperature signals measured by the DynPT optoelectronic interrogator at the three different wavelengths ($\lambda_1 = 850$ nm, $\lambda_2 = 1050$ nm, $\lambda_3 = 1300$ nm), was analysed using National Instruments DIAdem software to calculate the average temperature at each set-point. The average measurements (at different wavelength) were then compared with the reference temperature measurements from the LP5 pyrometer for cross-validation. Table 3 below shows data collected from the calibration check test.

Figure 13 and Figure 14 show plots of absolute and relative temperature difference between the DynPT system and the LP5 from the calibration check test. Good agreement can be noticed between temperature measurements at different wavelengths (< 10 K from each other). However, these plots clearly show a positive difference against the LP5, increasing with temperature, suggesting a systematic error.

5. Shock tube facility

5.1 Construction and operation

The KTH shock tube facility constructed in this project is as shown in Figure 15. It consists of two sections, namely the driver/high pressure section and the driven/low pressure section separated by a Fast-opening valve (FOV). The driver section is of circular construction with a uniform diameter of 80 mm (small driver) or variable diameter of (80–160) mm (large driver). The choice of the driver used for a particular run depends on the gas combination and Mach number of the generated shock wave. The overall length of the driver-FOV combination is 0.7 m. The driven section is of rectangular cross-section measuring 120×50 mm² and constructed with 15 mm thick steel material. The test section, part of the driven section, is specially constructed with transparent plexi-glas windows as its sides to provide access for visual/optical measurement. Also, the driven section is equipped with 8 sensor measurement stations. The overall length of the driven and test section combination is 3.5 m. The operation and data acquisition of the shock tube is fully automated and controlled via a LabVIEW computer program. The shock tube can run with different gas

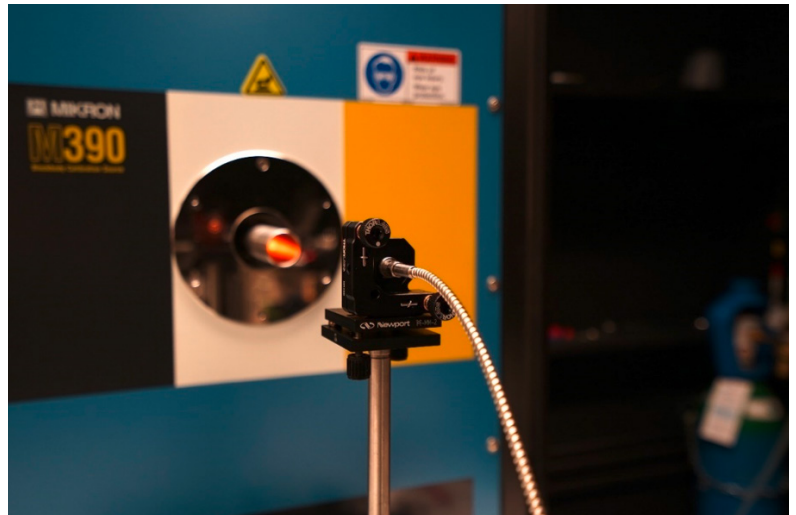


Figure 12: Photo of the test rig set-up for static calibration check tests

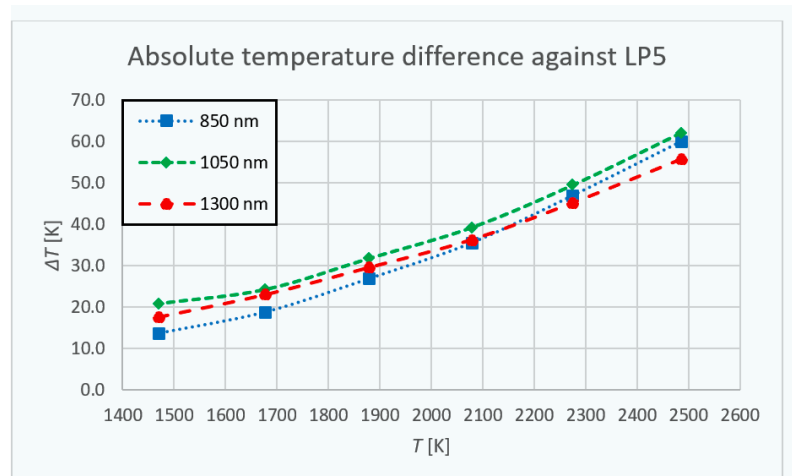


Figure 13: Absolute difference of temperature measurements between the DynPT system and LP5

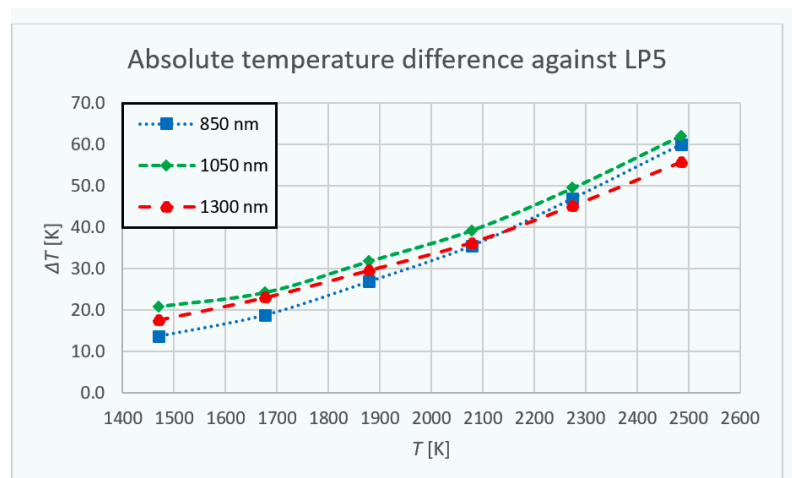


Figure 14: Relative difference of temperature measurements between the DynPT system and LP5

Nominal T [°C]	Nominal T [K]	LPS T [K]	DynPTT [K]			ΔT [K]			ΔT/T [%]		
			850 nm	1050 nm	1300 nm	850 nm	1050 nm	1300 nm	850 nm	1050 nm	1300 nm
2200	2473.16	2485.3	2545.3	2547.37	2540.93	60.0	62.1	55.6	2.413133	2.497679	2.238497
2000	2273.16	2274.6	2321.5	2324.07	2319.71	46.9	49.5	45.1	2.063458	2.175006	1.983354
1800	2073.16	2078	2113.5	2117.23	2114.2	35.5	39.2	36.2	1.707964	1.88769	1.742148
1600	1873.16	1878	1904.9	1909.77	1907.5	26.9	31.8	29.5	1.430114	1.691846	1.570685
1400	1673.16	1677.2	1696	1701.51	1700.17	18.8	24.3	23.0	1.122416	1.44948	1.369412
1200	1473.16	1469.7	1483.4	1490.6	1487.26	13.7	20.9	17.6	0.931919	1.422278	1.194599

Table 3: Data from calibration check test

combinations in the driver and driven sections, with the predominant combinations being air + air, air + argon (Ar), helium (He) + air, and He + Ar.

Data acquired from a typical run in the shock tube is as shown in Figure 16. Here Air + Ar gas combination is used with a driven pressure (P_1) of 30000 Pa. The shock Mach number (M_s) is calculated by measuring its time of arrival at sensor stations S2 and S3, which are separated by 600 mm. All stations are equipped with PCB piezotronics pressure sensors (113B24 and 113B23), connected to an oscilloscope (Tektronix TDS 2014C) via a signal conditioner (PCB Model 482C).

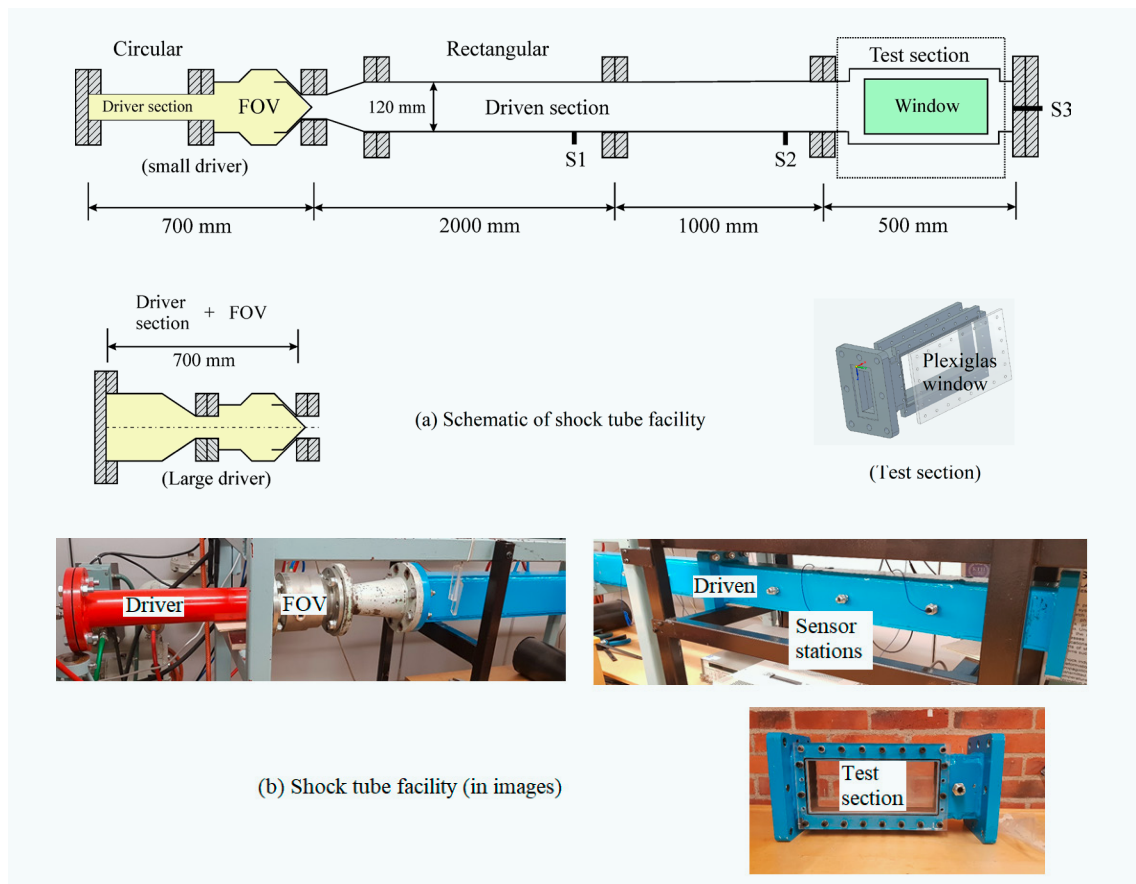
5.2 Uncertainty estimation for measurement methods

Shock Jump relations/shock velocity measurement: In this method, the temperature is calculated using the following shock jump relation,

$$\frac{T_5}{T_1} = \frac{[2(\gamma - 1)M_s^2 + (3 - \gamma)] [(3\gamma - 1)M_s^2 - 2(\gamma - 1)]}{(\gamma - 1)M_s^2}$$

where γ is the specific heat ratio (of the driven gas) and state 5 represents expected conditions. It is evident from the relation that the temperature obtained is only dependent on M_s and γ of the driven gas used. Since γ is constant with temperature for Ar (for the temperature range considered in this project), its uncertainty is zero which leaves the M_s determination as the sole contributor to uncertainty estimation. Here M_s

Figure 15: The design and construction of the shock tube facility



Source	Mean	Standard uncertainty	Expanded uncertainty ($k = 2$)	Relative uncertainty
Time _{S2-S3} (μs)	1026	3.8	-	-
Velocity (V , m/s)	638	3.9	-	-
Sound speed (a , m/s)	321	1.2	-	-
M_s (Time of arrival)	2	0.015	0.03	1.5 %
T_5	1020	15.6	31.2	3 %

a)
Uncertainty budget for the time-of-arrival shock velocity method

Source	Mean	Standard uncertainty	Expanded uncertainty ($k = 2$)	Relative uncertainty
Time between frames (μs)	50	0.1	-	-
Velocity (V , m/s)	640	10	-	-
Sound speed (a , m/s)	321	1.2	-	-
M_s (Optical)	2	0.03	0.06	3 %
T_5	1020	31	62	6 %

b)
Uncertainty budget for the optical method

Table 4:
Temperature uncertainty estimates for both shock velocity methods

is the ratio of velocity of the shock wave (V) and speed of sound (a). To measure the velocity of the shock wave, two methods are employed:

- Pressure sensor time-of-arrival method, where the time taken by the shock wave to pass over two sensors at a set distance is measured.
- Optical method, where the shock propagation through the test section is captured with a high-speed camera using the shadowgraph technique and velocity is measured between each pair of consecutive frames.

The high-speed camera (Shimadzu HPV-X2) was set to capture 128 frames at the rate of 0.1 million fps. Typical shadowgraph images of the shock wave at two locations are shown in Figure 17.

The uncertainty for both methods is estimated based on the law of propagation of uncertainties with the following parameters:

- The uncertainty in time of shock arrival between sensors S2 and S3 (Time_{S2-S3}) comprises sampling rate and resolution of the oscilloscope, rise time of the sensors and its resolution limit.
- Owing to optimal filling conditions with sufficient time allowed for equilibrium in a temperature-controlled laboratory, the uncertainty in initial temperature at the shot instant was estimated to be 3 K.
- For the optical method, the distance travelled by the shock is based on a pixel reference measurement made with a metric scale with an uncertainty of 0.5 mm.

The assumed probability density distribution was rectangular for sources without manufacturer specification. The uncertainty budget for nominal $M_s = 2$ is given in Table 4.

Source	Mean	Standard uncertainty	Expanded uncertainty ($k = 2$)	Relative uncertainty
Sensor resolution (MPa)	35×10^{-6}	-	-	-
Sensor sensitivity (MPa)	0.03	-	-	-
P_1 (MPa)	0.03	0.002	-	-
P_5 (MPa)	0.46	0.03	0.06	11.8 %

Table 5:
Uncertainty budget for pressure sensor measurement

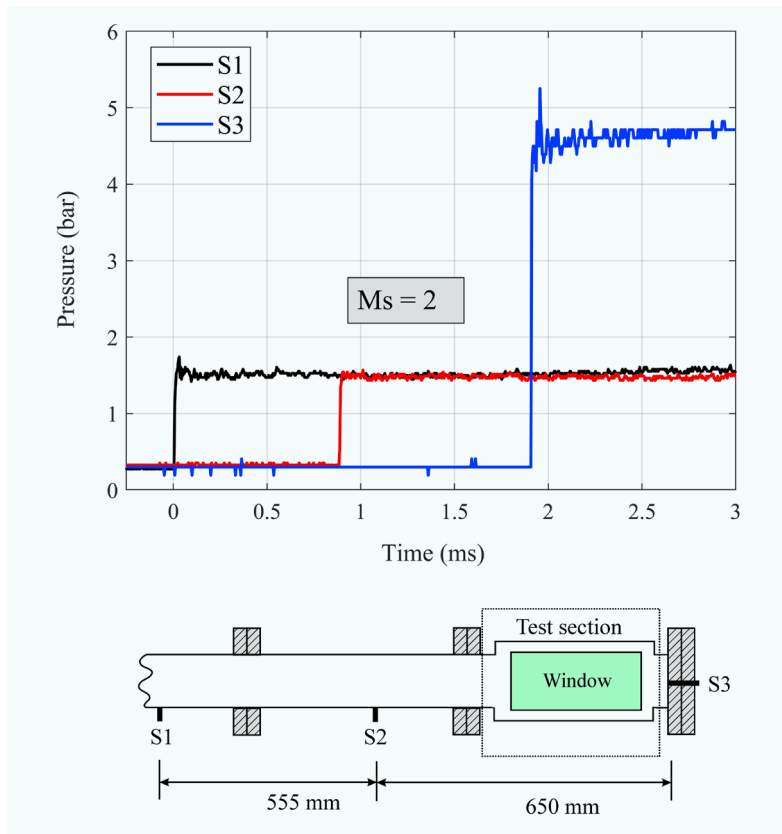


Figure 16: Pressure profile recorded for air – Ar gas combination with $M_s = 2$

Pressure sensor/optical density measurement: In this method, temperature is calculated from the ideal gas law,

$$P = \rho RT$$

where ρ is the density of gas and R is the gas constant. Pressure (P) and ρ are obtained from pressure sensor readings and interferometric (optical) measurement, respectively. The pressure sensor employed in the measurements are piezoelectric based from PCB (model 113B24) with a rise time of $1 \mu s$ and frequency response of 500 kHz. Table 5 summarizes the parameters considered, namely sensor sensitivity, sensor resolution, LSD of the sensor and oscilloscope, and driven pressure (P_1), and their uncertainty budget in pressure sensor measurement.

The uncertainty in estimating the pressure value alone greatly surpasses the shock velocity method. Since the goal is to determine the feasible method

for temperature, this method was discarded at this stage since the uncertainty will only increase upon adding parameters from density measurement.

Numerical simulation: Results from numerical simulation are only used for reference purposes and not for actual sensor calibration. As the obtainable numerical temperature is sensitive to variations in M_s , the uncertainty is heavily dependent on the reliability of the experimental M_s . The temperature is determined by subjecting the numerical simulation to the mean M_s with an uncertainty of 1.5 % (Table 6).

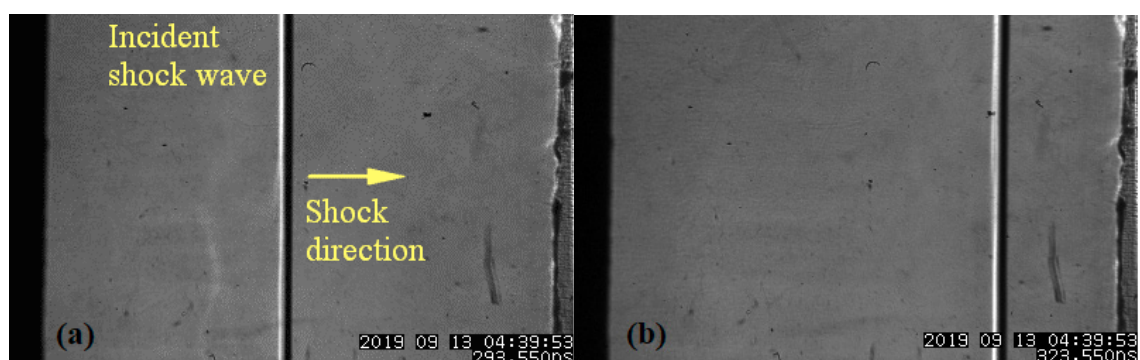
Direct measurement: The direct measurement of temperature generated in the shock tube was planned based on the DynPT system developed by NPL. The tests at the KTH shock tube facility were conducted between March 3rd – March 5th, 2020. In the tests, the DynPT system was set with a gain of three photodetectors at $G = 30$ dB (as per calibration) and with a sampling rate $f = 250$ kHz. The voltage and temperature signals measured by the DynPT optoelectronic interrogator at three different wavelengths ($\lambda_1 = 850$ nm, $\lambda_2 = 1050$ nm, $\lambda_3 = 1300$ nm) were analyzed using the New Explosion Thermometer v1.0 LabVIEW program for He + air and He + Ar gas combinations.

In the tests performed at different conditions and with different sensor configurations, no signal was measured – no temperature pulse was observed above the noise floor. For the conditions, temperature pulses of up to 3000 K were generated in the facility, however, this temperature is too low to induce radiation emission at the photodetector wavelengths of the DynPT instrument which has been designed to measure blackbody radiation emission from sooty flames.

5.3 Temperature validation curve

Based on the methods tested, the shock jump relations/shock velocity measurement technique provided the least uncertainty (3 % at $k = 2$) and was determined the feasible method for temperature measurement. The validation curve of the KTH shock tube facility as a function of temperature and shock Mach number is given in Figure 18.

Figure 17: Typical shadowgraph image of the shock wave (dark line) at two instances



6. Conclusion

Three calibration methods and standards for dynamic measurement of temperature were successfully designed, developed, and validated. The calibration system, based on rapid shutter systems, for calibrating radiance thermometer and high temperature black bodies was able to measure up to 2200 °C with temperature uncertainties below 5 °C and response time of 1 ms. A novel ultra-high-speed combustion pyrometer (DynPT system), based on collection of thermal radiation via an optical fibre, was traceably calibrated to the ITS-90 over the temperature range $T = (1073\text{--}2873)$ K with residuals < 1 %. A temperature bench, based on a shock tube method, was constructed with necessary measurement stations and diagnostic setups that achieved temperatures in the range up to 3000 °C with an uncertainty of 3 % ($k = 2$).

References

- [1] V. F. Duma, "Theoretical approach on optical choppers for top-hat light beam distributions," *Journal of Optics A: Pure and Applied Optics*, p. 064008, 2008.
- [2] H. Preston-Thomas, "The international temperature scale of 1990 (ITS-90)," *Metrologia*, vol. 27, pp. 3–10, 1990.
- [3] [Online]. Available: <https://www.lemaitreltd.com/products/pyrotechnics/pyroflash/theatrical-flashes-stars/theatrical-flashes/sds-flashes-robotics-spds/>. [Accessed 22 November 2020].

M_s	Temperature (T_s)	Relative difference (K)	Uncertainty
1.97	965	31	3.1 %
2 (mean)	996	0	0
2.03	1025	29	2.9 %

Table 6

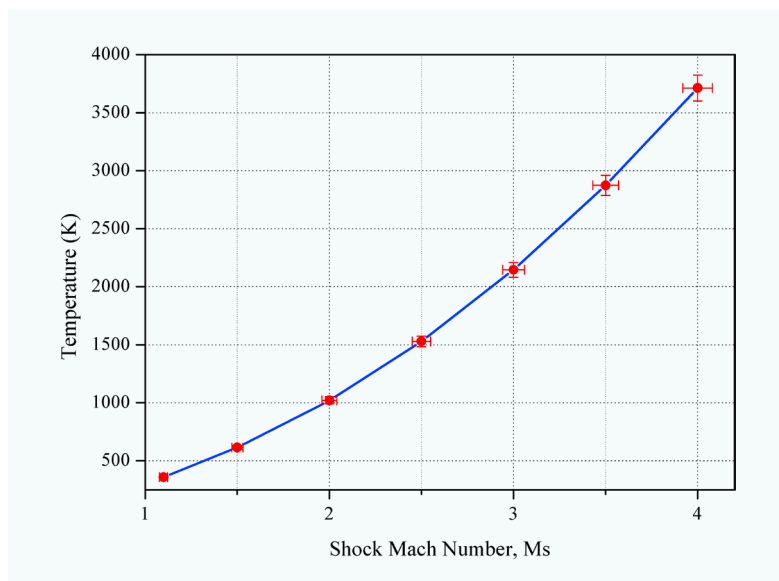


Figure 18: Temperature validation curve of the shock tube calibration bench

Validation of IR-based and UV-based sensors for dynamic temperature measurements

Alexander Fateev¹, Anders Öster²

¹ Dr. Alexander Fateev (DTU),
E-mail: alfa@kt.dtu.dk

² Anders Öster (Wärtsilä Finland Oy),
E-mail: anders.oster@wartsila.com

1. Introduction

This article is an abridged version of chapter 2 of deliverable D5 in the EMPIR project 17IND07 – DynPT: “Validation report on the performance of the newly developed dynamic pressure and temperature sensors covering the range up to 30 MPa with a target uncertainty of 2 % and up to 3000 °C, with a target uncertainty of 5 %, respectively”. This project has received funding from the EMPIR programme co-financed by the Participating States and from the European Union’s Horizon 2020 research and innovation programme. The full report has been prepared by VSL B.V. (VSL) together with project partners from Danmarks Tekniske Universitet (DTU), Minerva meettechniek B.V. (Minerva), National Physical Laboratory (NPL), RISE Research

Institutes of Sweden AB (RISE) and Teknologian tutkimuskeskus VTT Oy (VTT).

2. IR-based and UV-based sensors

2.1 Development of an IR-based sensor

The newly developed IR-based sensor utilizes a passive concept, i. e., uses a hot medium as a thermal source, and consists of a compact (0.15 m focal length) grating spectrometer with two changeable gratings and a fast IR camera with 640 × 512 pixels InSb array. The camera has its own optics and can be used as a stand-alone system for, e. g., thermal imaging. For matching of the camera with the spectrometer a special home-made optics has been designed.

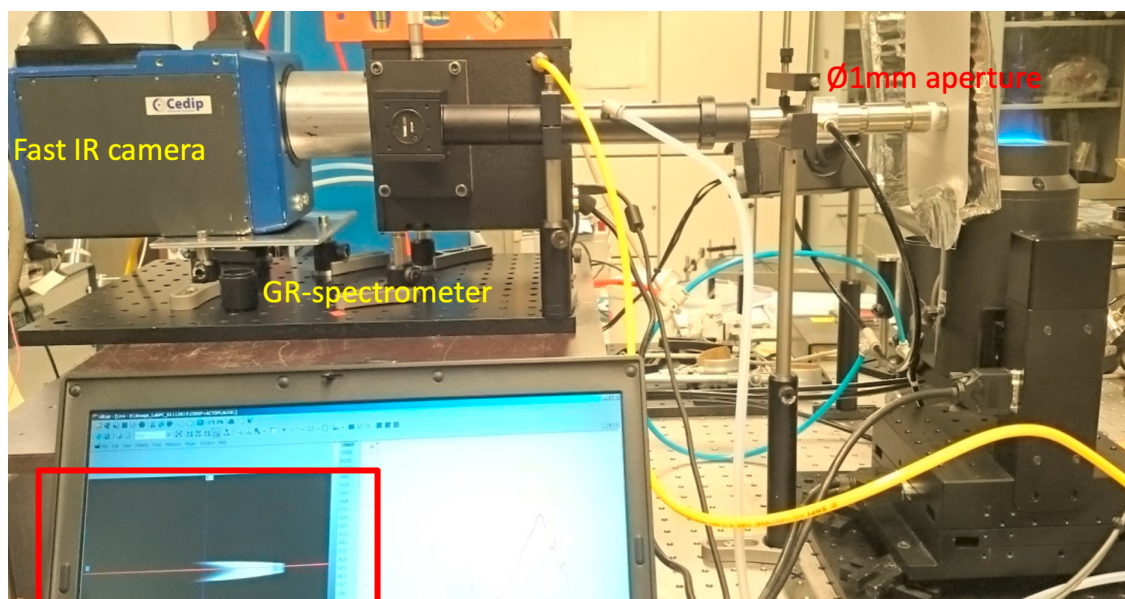


Figure 1: IR-based sensor at NPL’s STD flame. The flame thermal image is shown in the red box as a narrow, white-colored strip

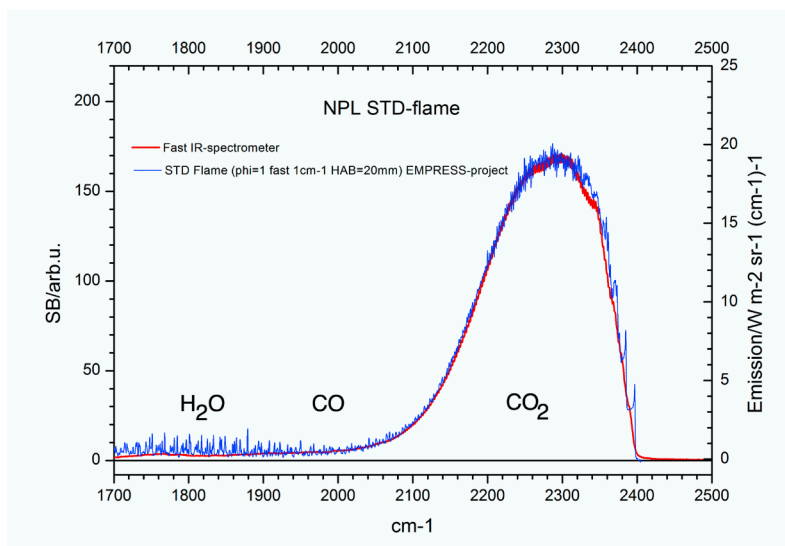


Figure 2: Low-resolution CO₂ emission spectrum measured in NPL's STD post flame using the IR-based sensor (red) and a high-resolution (1 cm⁻¹) FTIR spectrometer (blue). Positions for H₂O and CO bands are shown

The gratings have blazing angles at 2.5 mm and 3.6 mm and are optimized for CO₂ emission band measurements at 4.3 mm and CO₂/H₂O emission bands measurements at 2.5 mm.

The sensor can be used for emission/transmission measurements on hot gases and flames. The camera can be triggered externally. Minimum acquisition time for one spectrum is defined by the size of the selected area on the InSb array and the intensity of the incoming light. For combustion applications a 50 ms acquisition time is generally achievable. Sensor installation at the STD flame setup is shown in Figure 1. Because the flame image on the array is a strip-like band there are possibilities for coupling 2–3 optical fibers to the spectrometer. Hence, simultaneous measurements from different locations are possible, i. e., a tomography-like approach.

The measured CO₂ IR-emission spectrum of a propane-air post flame at stoichiometric combustion conditions is shown in Figure 2 (red) together with a similar spectrum measured with a

fast-scanning FTIR spectrometer at 1 cm⁻¹ spectral resolution (blue) (in the EURAMET funded EMPRESS project). The STD flame gives a very uniform temperature profile in the middle of the flame with a gas temperature of 2253 K [1].

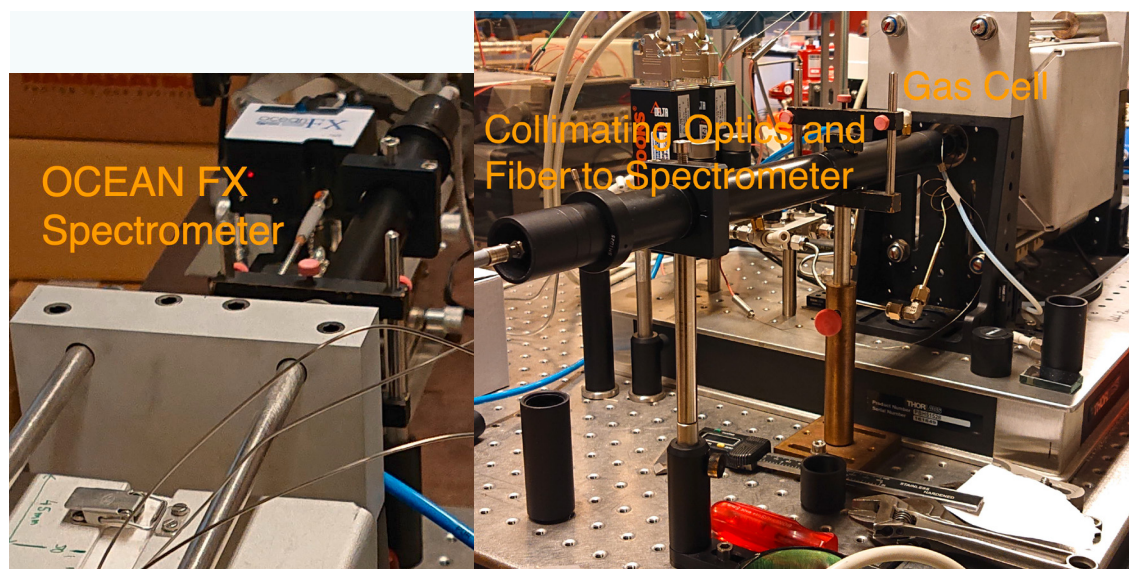
The IR-based sensor was calibrated with a traceable compact blackbody light source at 900 °C. The shape of the CO₂ band in Figure 2 is defined by the gas temperature. The tail of the band at (2100–2250) cm⁻¹ defines the hottest temperature in the gas while the band start at (2300–2400) cm⁻¹ defines flame/hot gas temperature gradients (boundaries) normally obscured by CO₂ self-absorption in the ambient air. The shapes of the two CO₂ bands around (2100–2250) cm⁻¹ are in excellent agreement. As it was shown in [1], combined temperature uncertainties are within 1 % of temperature (compared to Rayleigh scattering technique, traceable to ITS-90).

The IR-based system shown in Figure 1 is a bit voluminous and also expensive, because of the camera. However, in the last two years new 1D IR arrays by HAMAMATSU appeared on the market. Arrays, however, require further development, such as integration with pre-amplifiers and analog-digital conversion. DTU has experience with the development of a compact IR spectrometer and data analysis, which was successfully used for on-site long-term demonstration of gas composition measurements and Wobbe index calculations for natural gas and biomethane. DTU believes that the new 1D array can be integrated with a new version of the IR spectrometer, and therefore the IR-based sensor can be made more compact and less expensive.

2.2 Development of a UV-based sensor

The newly developed UV-based sensor is based

Figure 3: UV-based sensor installation at the high-pressure/temperature gas cell at DTU



on a compact commercial fast UV spectrometer (OCEAN FX, 10 ms acquisition time per spectrum with 50,000 spectra/s rate), optical fiber, and light-focusing optics. The spectrometer can be “tuned” to various spectral ranges by grating re-alignment. The sensor can be used either in passive (collect light emission from a medium) or in active arrangements (with an external UV-VIS light source). The major benefits of this approach are:

- No need for physical contact with the medium: optical access through a window
- Low sensor body temperature (follows ambient temperature)
- No high spectral resolution (HR) required: low resolution (LR) small spectrometers are sufficient, with a short (full spectrum) measurement time (from 10 ms)
- Can be used for particle temperature measurements in the visible spectral range.

An example of the UV-based sensor at high-pressure/temperature gas cell at DTU is shown in Figure 3 (active arrangement).

An external UV-VIS light source is coupled to the gas cell through a fiber and focusing optics. Light transmitted through the cell is focused into the fiber connected to the spectrometer. An example of the installation at NPL's sooty flame facility is shown in Figure 4.

The UV-based sensor is targeting fast in situ measurements of NO and OH in flames or hot exhaust gases. The sensor was used to study



Figure 4: A UV-VIS light beam is transmitted through the soot cloud after a pyrotechnic explosion at NPL. The light is focused into the fiber connected to a spectrometer.

combined effects of pressure and temperature on NO band shape variations at high-pressure/temperature conditions achievable at DTU (Figure 3).

As one can see from Figure 5, NO band shape is changed with pressure increase. In the measurements shown in Figure 5, a high-resolution spectrometer was used (instead of the OCEAN FX). The fine structure disappears when the pressure exceeds 10 bar.

At pressures higher than 10 bar the band shapes are smooth, and therefore there is no need for using a high-resolution spectrometer. The NO spectra at various temperatures and low pressures (below 10 bar) can be modelled very well (Figure 6). The band top shift is a linear function of pressure (Figure 7).

This top shift can be used for pressure calculations in a system at low temperatures. At higher pressures and temperatures, band tops decrease while the band tails increase for the

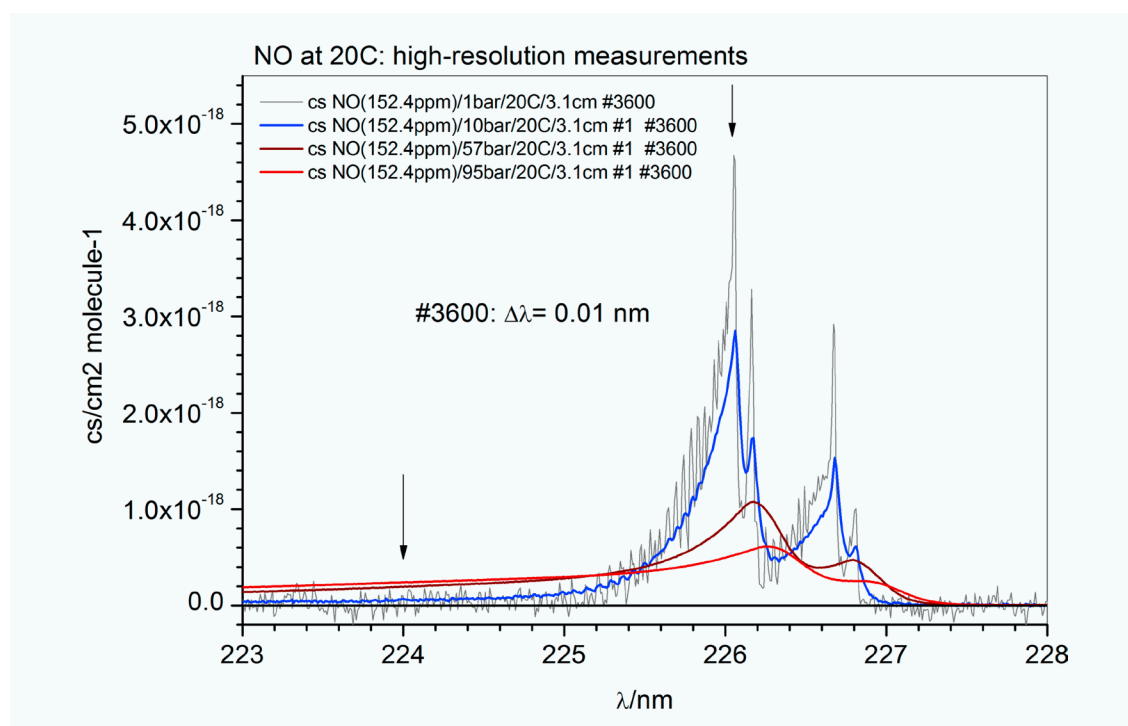


Figure 5: NO absorption cross sections at 20 °C and various pressures measured at high spectral resolution (0.01 nm). The band top (marked by a vertical arrow at 226 nm) is reduced and shifted with temperature rise. The band tail (marked by a vertical line at 224 nm) is increased.

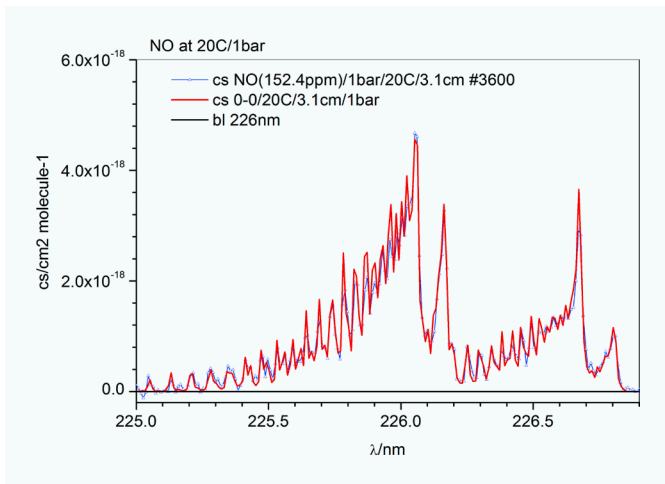


Figure 6: Measured (blue) and calculated (red) NO absorption cross-sections at 20 °C and 1 bar

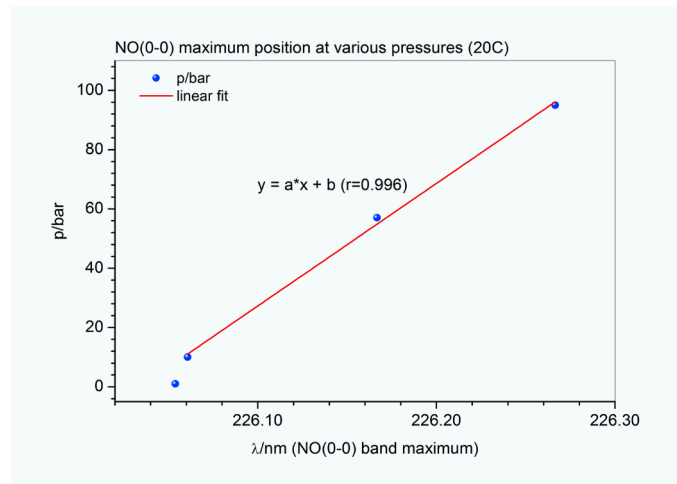


Figure 7: Band top position (in nm) from Figure 5 as a function of pressure. Note that the correlation coefficient of the linear fit is close to 1.

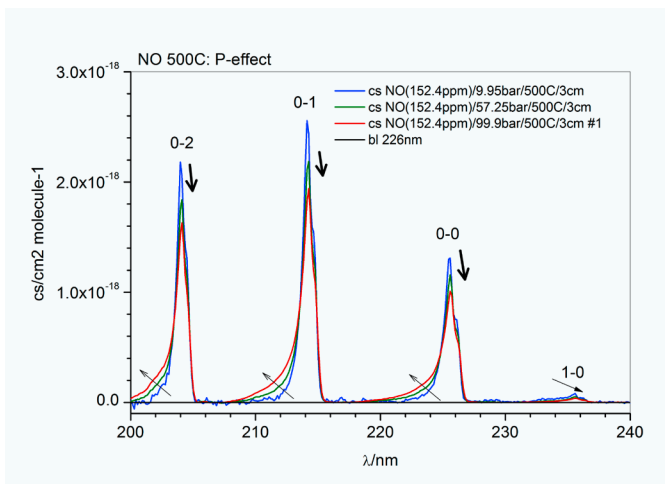


Figure 8: NO absorption cross-sections at various pressures (10 bar - 100 bar) and 500 °C. Arrows show trends in band tops and tail variations.

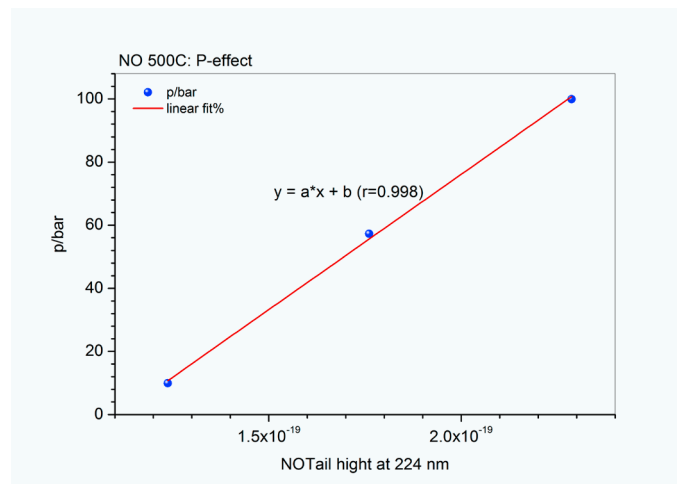


Figure 9: NO tail at 224 nm behavior for pressure variation from 10 bar to 100 bar and 500 °C

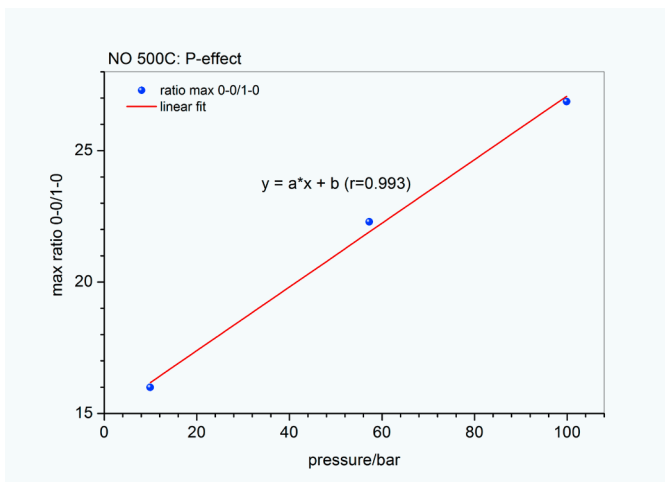


Figure 10: NO 0-0/1-0 band top ratio at 226 nm and 236 nm for pressure variation from 10 bar to 100 bar and 500 °C

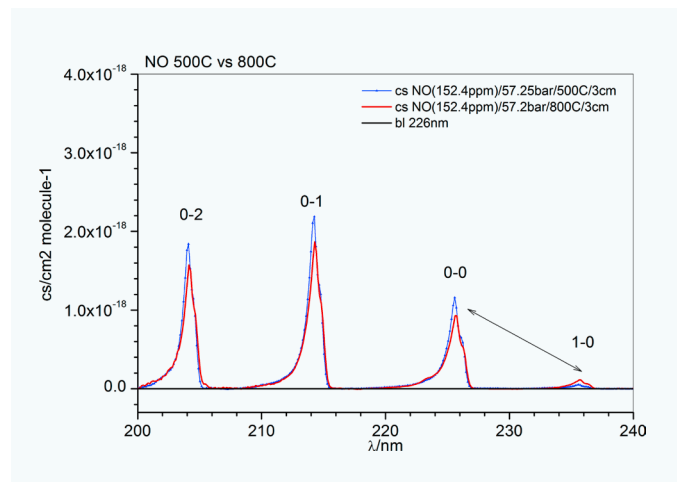


Figure 11: Variations in NO band tops with temperature at about 57 bar

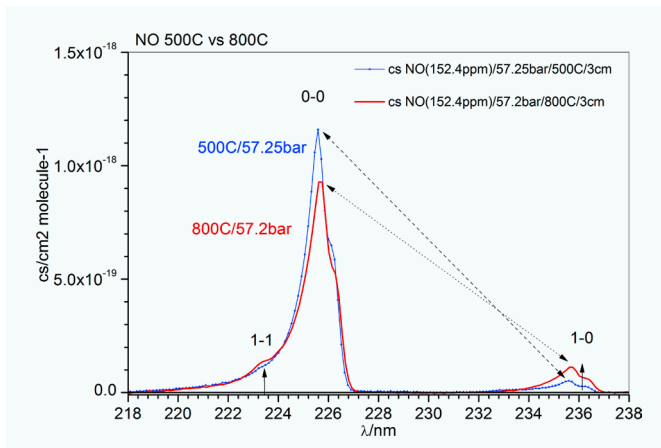


Figure 12:
NO bands at 226 nm and 237 nm at
different pressures and temperatures

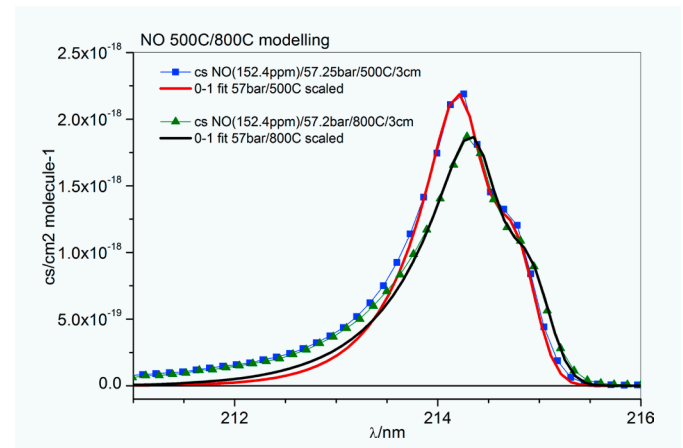


Figure 13:
Measured NO absorption cross sections at 500 °C
(blue) and 800 °C (olive) at about 57 bar and their
modelling (red and black, respectively)

majority of the NO bands except for the 1-0 band at 237 nm, where there is a systematic intensity decrease in both band top and tail (Figure 8).

Variations in the NO band tail have a linear behavior and therefore can be used for pressure deductions (at known temperature). As seen from Figure 9, the 0-0 and 1-0 band top ratio is a linear function of pressure and can be used for pressure deduction from the measurements at known temperature (Figure 10).

Temperature increase (at constant pressure) has a similar effect on NO bands in the range 200 nm–230 nm: the band tops decrease with rising temperature. The NO 1-0 band at 236 nm has an opposite behavior: its intensity increases with temperature (Figure 11).

The band 1-0 (236 nm) corresponds to absorption from the next to ground vibrational state which is thermally populated according to the Boltzmann distribution. The 226 nm and 236 nm NO bands are shown in Figure 12 at various pressures and temperatures. At temperatures above 800°C, the additional 1-1 band at 223 nm starts to be seen. A ratio of 0-0 and 1-0 bands and appearance of the 1-1 band gives an indication of high gas temperatures and can be used for gas temperature deduction.

However, the most accurate temperature calculations can be done by a modelling of the NO band top in the range 213.5 nm–216 nm (Figure 13).

As mentioned above, the band top can be modelled very well, while modelling of the NO tail below 213 nm will require further theoretical developments in spectrum modelling, which are outside the scope of this project. It should be noted that in the NO top modelling there is no need to know the absolute NO concentration *a priori*. The modelling can be performed on a relative Y-scale, because temperature affects the relative variations

in the NO overall band shape. NO concentration should, however, not be “too high” or, in other words, the measured NO absorbance should not be in saturation (or NO transmittance should be above zero).

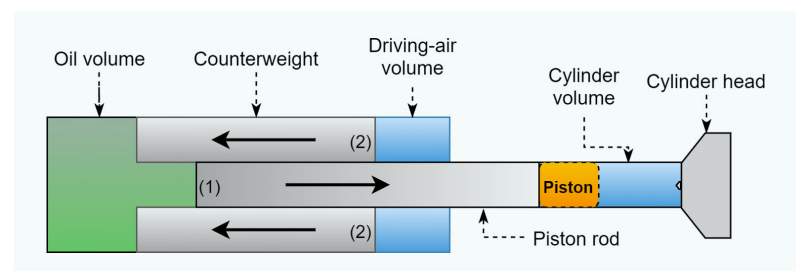
Therefore a “recipe” for pressure and temperature deductions from NO absorption spectra is: 1) To model the NO band top at any available NO bands in the range 200 nm–240 nm and then 2) using a decrease/increase in band tops/tails and NO top position (in nm) to calculate pressure, e.g., as shown in the Figure 7, Figure 9 and Figure 10. This method will work at pressures from 10 bar and up.

Unfortunately, we were not able to demonstrate simultaneous pressure/temperature calculations from measurements at shock wave facilities (KTH) and RCEM (Wartsila), because for the former we used low NO concentration (very weak NO absorbance) and for the latter NO measurements were not possible, because of the UV light transmission cut off in the test rig windows, see next chapter.

2.3 Demonstration of a UV-based sensor in combustion environment

The UV-based sensor from 2.2 has been used for in-situ time-resolved gas temperature measurements on the Rapid Compression Expansion Machine (RCEM) at Wärtsilä’s fuel

Figure 14:
Schematic of RCEM
and its operation



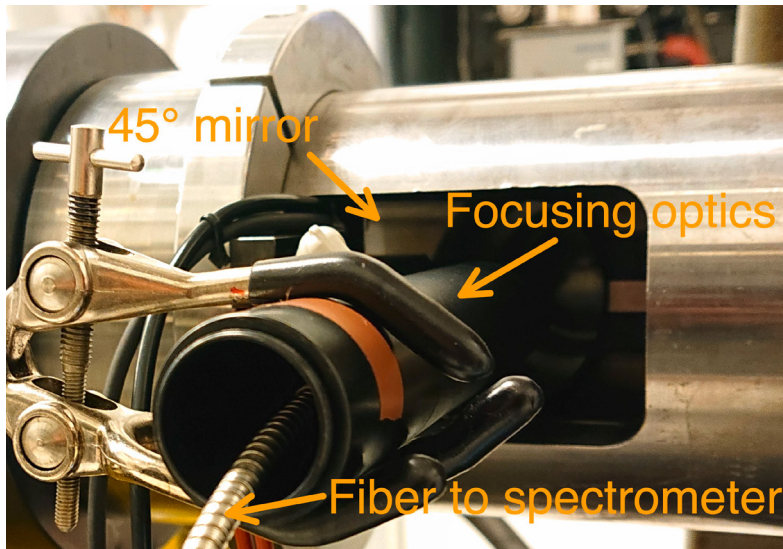


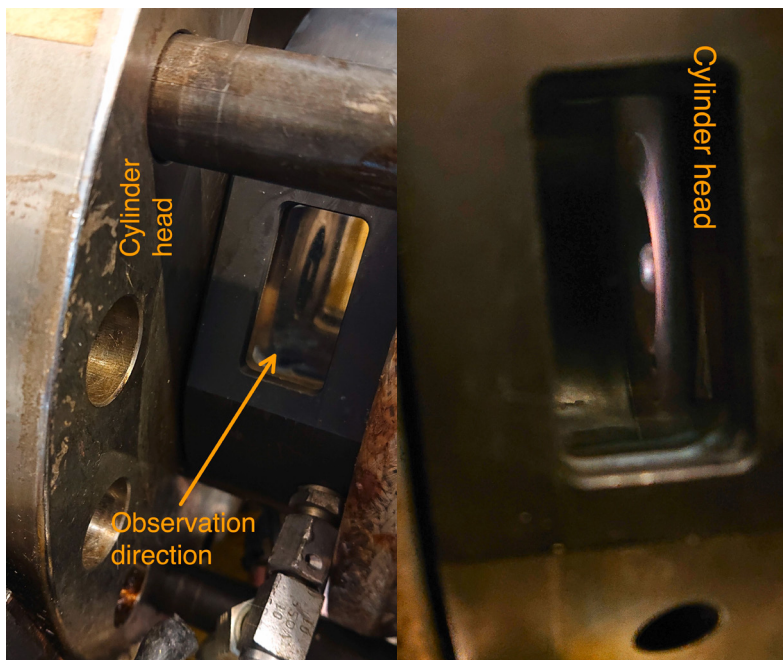
Figure 15:
Optical setup at location 1. Flame emission is diverted by a 45° mirror and is focused into an extremely solarization-resistant fiber connected to the fast compact spectrometer

laboratory facilities. The RCEM is a flexible tool used for investigating combustion events in various types of pure fuels and fuel blends. The schematic of the RCEM is shown in Figure 14.

The operation principle of the RCEM is as follows:

1. The driving-air and cylinder volumes are filled up to desired pressure levels and air-fuel mixture.
2. Pressure is released causing the piston rod with piston to rapidly compress the cylinder volume.
3. The ignition spark in the cylinder volume is timed to a set cylinder distance from the bottom (mm).
4. Piston bounces back. Cycles can be repeated in ~2 minutes.

Figure 16:
Optical setup at location 2. Light is collected just above the surface of the cylinder head surface (see visualization to the right)



Overall technical specifications of the RCEM:

- 180 mm “stroke” from bottom to top
- 1 liter closed cylinder volume
- No fixed connecting rod → Variable “compression ratio”
- Pre-chamber to increase turbulence and improve flammability (same equivalence ratio)
- Cylinder walls pre-heated to 85 °C
- An optical window can be placed in the piston body (window thickness about 32 mm)
- A visibility ring with 3 windows can be used for optical measurements and video filming in the vicinity of the cylinder head. The head has two windows facing each other and one placed at 90 degrees compared to the first two (each window is 24 mm thick)
- External trigger output with programming off-set (for synchronization of external equipment with spark timing event).

In the demonstration of the UV-based sensor a CH₄-Air mixture was used at $\lambda = 1$ (stoichiometric) condition for all measurements.

The UV measurements were performed using two approaches: passive and active. In the passive approach an optical emission in the 180 nm–400 nm spectral range produced by a fuel combustion was collected with a fast compact spectrometer (minimum acquisition time is 10 ms). In the active approach an external UV-VIS light source was used for flame transmittance measurements. Transmitted UV light was collected by the fast compact spectrometer (OCEAN FX).

2.3.1 Passive measurements

The passive measurements have been performed at two locations: 1) see-through the piston, Figure 15, and 2) at the visibility ring (Figure 16).

2.3.2 Active measurements

For the active measurements a Xe light source (1000 W) was used. The Xe light was first focused into the extremely solarization-resistant UV fiber and then transformed to a parallel light beam using collimating optics (Figure 17). After passing through the gas the light was focused into another extremely solarization-resistant UV fiber connected to the fast compact spectrometer (OCEAN FX). The optical alignment of the

system was made to ensure that the light beam was passing the gas just above the surface of the cylinder head (as in passive measurements).

The fast compact OCEAN FX spectrometer with its own trigger generator is shown in Figure 18. The trigger generator first receives an RCEM trigger signal and then triggers the spectrometer. It was made to eliminate OCEAN FX software issues caused by the external trigger set-up option in the OCEAN FX software. A rectangular box in the middle is a simple connection adapter (from BNC type to DB15/DD4) between trigger generator and OCEAN FX.

2.3.3 Results of passive measurements

Flame emission from both measurement locations 1) and 2) was found to be quite weak. Therefore, it was decided to increase the acquisition time from the minimum of 10 ms (defined by the spectrometer) to 250 ms. Furthermore, the S/N ratio of the measured spectra was optimized by on-site optimization of the UV sensor, such as re-alignment of the collimating optics and changing the spectrometer slit. Measurements could also be performed at 125 ms acquisition time, but with lower S/N ratio. Out of the 250 ms acquisition time 211 ms is for readout (transfer of the measured spectrum to internal spectrometer buffer memory), i. e., during 211 ms there is no data acquisition.

Emission spectra were measured in the 180 nm–408 nm range (defined by the grating position in the spectrometer). The spectra mainly consist of OH* radical emission bands in the 280 nm–330 nm range and a CO₂ emission (chemiluminescence) continuum in the 250 nm–408 nm range. Spectra measured at two locations are the same, i. e., the same spectral features were observed. However, the best spectra in terms of S/N ratio were measured at the visibility ring from one (of three) flame pre-ignition inlet sides (with the sensor facing the flame inlet), see Figure 19.

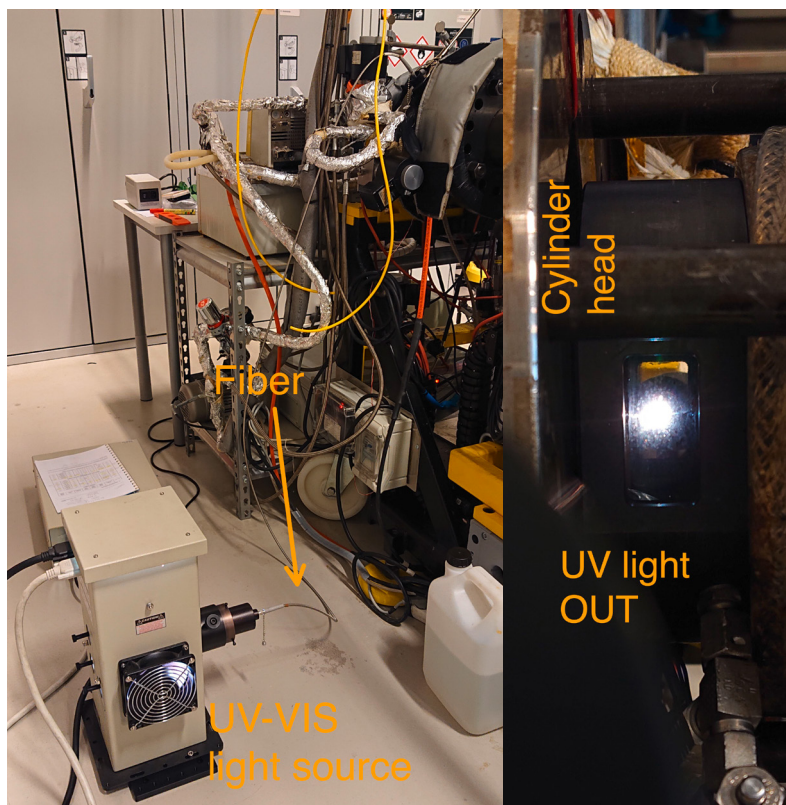


Figure 17: Left: UV-VIS light source. Right: UV-VIS light transmitted through two quartz windows on the visibility ring

As one can see from Figure 19, OH* emission spectra are very broad, which reflects the high OH* rotational temperature, which is equal to the gas temperature. The emission OH* peak at about 310 nm is significantly reduced in the late combustion phase (4.150 ms).

Variations in OH* (310 nm) and soot (200 nm) (light scattered) signals are shown in Figure 20. One can see that the OH* emission has two maxima at about 1.384 ms and 2.767 ms that correspond to two combustion phases (pre-combustion, flame ignition) and main combustion. OH* emission is significantly reduced by about 5 ms and slowly decays from then on.

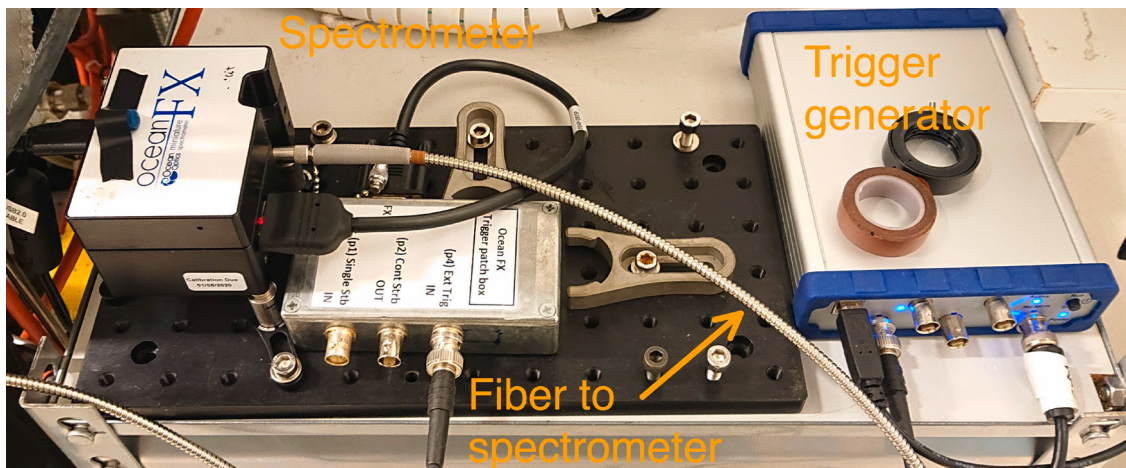


Figure 18: Fast compact UV spectrometer with own trigger generator

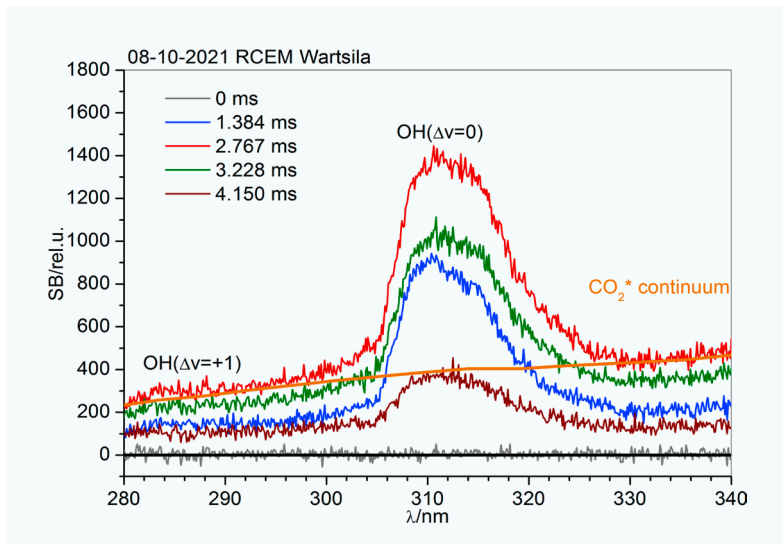


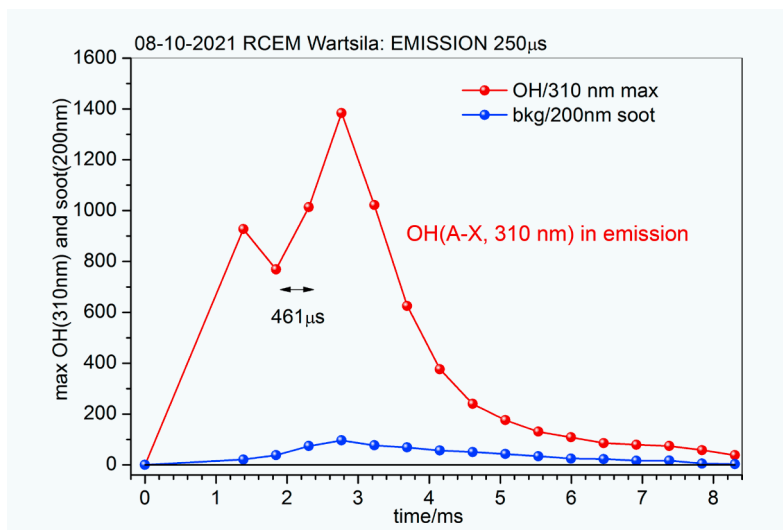
Figure 19: Time sequence of UV emission spectra in the 280 nm–340 nm range. The measurements were started 2.1 ms before the combustion event (labelled as “0 ms”, grey line).

2.3.4 Results of active measurements

The active measurements are essentially absorbance measurements. The measurements were also performed in the 280 nm–408 nm spectral range. Due to the thickness of the visibility ring windows (48 mm in total), no UV light was transmitted below 250 nm. Therefore, no NO absorption measurements were possible. A few measured absorption spectra in the 280 nm–340 nm range are shown in Figure 21.

The absorption spectra are dominated by OH ground state absorption and soot absorption and scattering. The latter increases towards shorter wavelengths. The OH band shape in the 300 nm–330 nm range depends on pressure and temperature variations. Higher temperatures cause an extension and rise of the OH tail in the 315 nm–330 nm range. At high pressures and temperatures (early combustion stage: red and blue, Figure 21) the characteristic P and R OH branches are undistinguishable, while at higher temperatures and low pressures (later combustion

Figure 20: Variation of OH* (310 nm) emission signal with time (red line). Soot (scattered signal at 200 nm) is shown by the blue line.



stage: orange, olive and black) both branches are clearly seen in the spectra.

Temporal variations in OH band maxima at 310 nm ($0 \leftarrow 0$ transition) and 290 nm ($2 \leftarrow 1$ transition) are shown in Figure 22. One can see that there are two maxima as it was observed in OH* emission measurements, Figure 20. The second OH maximum in absorption appears at the same time as that for OH* in emission (at 2.767 ms). OH stays in the gas much longer compared to OH* in emission measurements: OH (310 nm) extends to about 15 ms while OH* (310 nm) is mainly limited to about 8 ms. OH plays an important role in NO flame formation. OH*/OH has also been observed in all self-ignition cases at RCEM (so-called misfiring conditions).

Because the origin of the 290 nm band is caused by absorption from the $\nu = 1$ state of OH, which is thermally populated according to the Boltzmann law, the ratio of OH (290 nm) / OH (310 nm) is temperature dependent and therefore can also be used for vibrational temperature calculations in the system.

References

[1] G. Sutton, A. Fateev, M. A. Rodríguez-Conejo, M. A. Meléndez and G. Guarnizo, “Validation of Emission Spectroscopy Gas Temperature Measurements Using a Standard Flame Traceable to the International Temperature Scale of 1990 (ITS-90),” *International Journal of Thermophysics*, 40(11), p. 1–36, 2019.

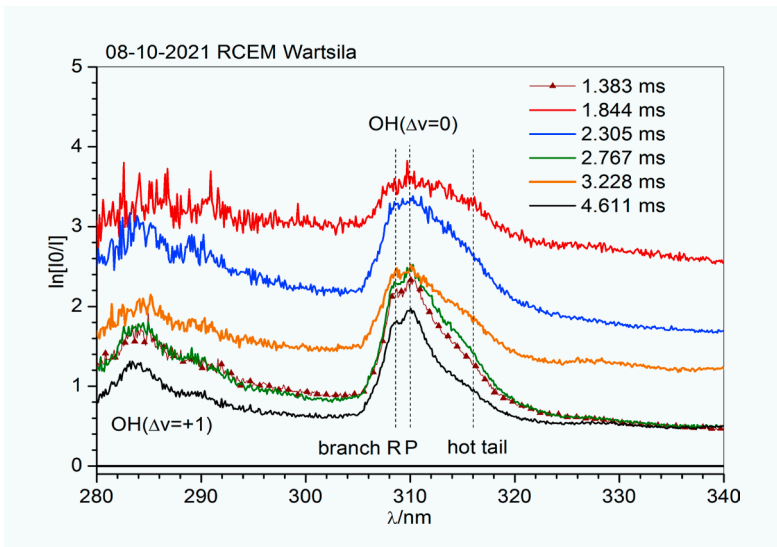


Figure 21: Absorption spectra. The offset in the Y-direction is caused by soot (light absorption and scattering).

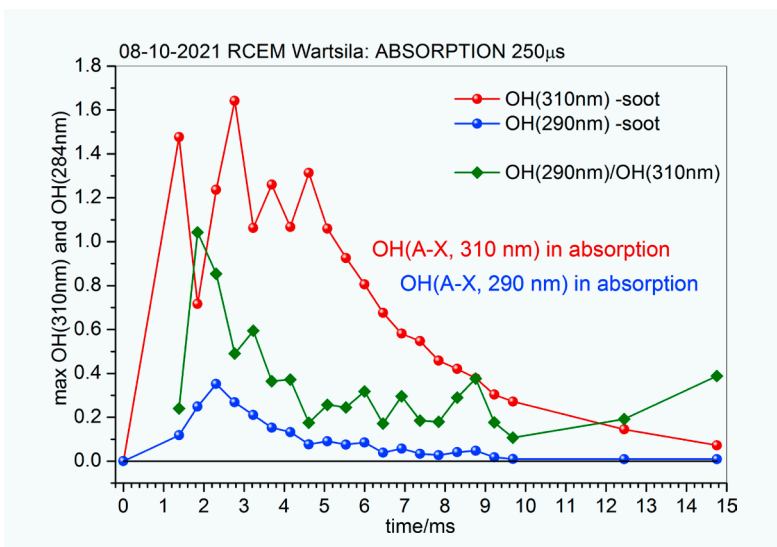


Figure 22: Temporal variations of OH band maxima at 310 nm (red) and 290 nm (blue) and their ratio (olive)

Validation of a fiber optic based dynamic thermometer

G. Sutton¹, D. Lowe², A. Sposito³, A. Öster⁴, V. Grahn⁵, P. Nyberg⁶, J. Hyvönen⁷, J. Leino⁸

1. Introduction

This article is an abridged version of chapter 3 of deliverable D5 in the EMPIR project 17IND07 – DynPT: “Validation report on the performance of the newly developed dynamic pressure and temperature sensors covering the range up to 30 MPa with a target uncertainty of 2 % and up to 3000 °C, with a target uncertainty of 5 %, respectively”. This project has received funding from the EMPIR programme co-financed by the Participating States and from the European Union’s Horizon 2020 research and innovation programme. The full report has been prepared by VSL B.V. (VSL) together with project partners from Danmarks Tekniske Universitet (DTU), Minerva meettechniek B.V. (Minerva), National Physical Laboratory (NPL), RISE Research Institutes of Sweden AB (RISE) and Teknologian tutkimuskeskus VTT Oy (VTT).

2. The fiber optic based dynamic thermometer

2.1 Introduction

Traceable, reliable measurement of combustion temperature is important because it can improve the understanding of the combustion process and provide a mechanism for the optimisation of engine power, fuel consumption, and emissions [1]. These measurements are performed under highly dynamic conditions, with temperature changes of up to ~3300 K occurring on a millisecond timescale. Conventional temperature sensors based on contact thermometry (e. g., thermocouples) are inadequate in this context, due to their slow response time (~10 ms), temperature limitation (≤ 2100 K), drift, and perturbation of the combustion process. To address this challenge,

with particular reference to internal combustion and diesel engines, NPL have developed a novel ultra-high-speed combustion pyrometer within the framework of the European joint research project DynPT - Development of measurement and calibration techniques for dynamic pressures and temperatures, part of the European Metrology Programme for Innovation and Research (EMPIR) [2].

2.2 System design

A schematic of the thermometer system design is shown in Figure 1. It consists of:

- A sensor: a 2 m long gold-coated multi-mode (MM) step-index fiber, with 400 μm core diameter, numerical aperture $NA = 0.22$, stainless-steel monocoil sheathing, an SMA connector on one end (hot front end) and an FC connector on the other end (cold back end). For testing purpose this is placed inside a ~1.7 m long stainless-steel tube (outer diameter: 20 mm, inner diameter: 16 mm), with the SMA connector protected by a recessed sapphire window; however, sensor and packaging can be tailored to the final application and installation requirements (e. g., addition of a collimating lens).
- An extension lead fiber: a lightly-armoured 10 m long MM step-index fiber patch-cord, with 600 μm core diameter, $NA = 0.22$, dual acrylate coating, 3 mm diameter PVC sleeve and FC connectors on both ends – this connects the sensor (on the FC connector) to the interrogator.
- A passive optoelectronic interrogator, assembled in-house and consisting mainly of:

¹ Dr. Gavin Sutton (NPL), Department of Thermal and Radiometric Metrology
E-mail: gavin.sutton@npl.co.uk

² Dr. Dave Lowe (NPL), Department of Thermal and Radiometric Metrology
E-mail: dave.lowe@npl.co.uk

³ Dr. Alberto Sposito (NPL), Department of Thermal and Radiometric Metrology
E-mail: alberto.sposito@npl.co.uk

⁴ Anders Öster (Wärtsilä Finland Oy),
E-mail: anders.oster@wartsila.com

⁵ Viljam Grahn (Wärtsilä Finland Oy)

⁶ Dr. Patrik Nyberg (Wärtsilä Finland Oy)

⁷ Dr. Jari Hyvönen (Wärtsilä Finland Oy)

⁸ Juha Leino (Wärtsilä Finland Oy)

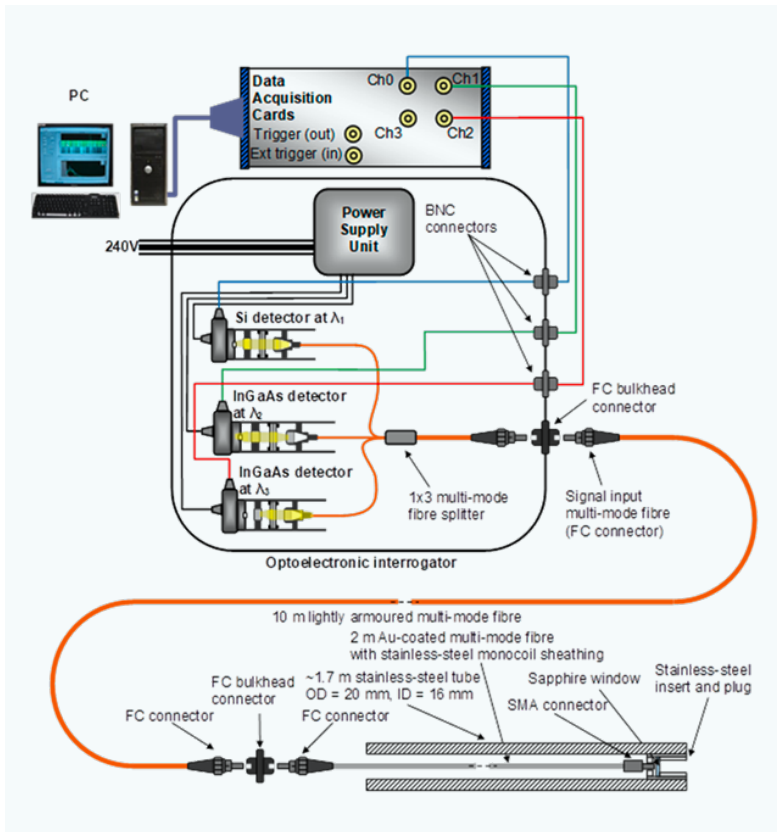


Figure 1: Schematic of the system

Figure 2: Pyrotechnic emission spectrum from (a) Si spectrometer, (b) InGaAs spectrometer, ~36 ms after ignition. The colored vertical lines identify the chosen wavelength: 850 nm (blue line), 1050 nm (green line) and 1300 nm (red line)

- ▷ A custom-made 1 × 3 MM step-index fiber coupler/splitter with 600 μm core diameter, NA = 0.22 and FC connectors on all ports
- ▷ Three photodetector assemblies, using off-the-shelf components, for measuring optical thermal radiation at three different wavelengths: $\lambda_1 = 850$ nm, $\lambda_2 = 1050$ nm and $\lambda_3 = 1300$ nm
- ▷ a power supply unit to power the photodetectors.
- A National Instrument (NI) data acquisition (DAQ) system, with maximum sampling rate $f_{MAX} = 1$ MHz, connected to the optoelectronic interrogator via BNC cables and to a Personal Computer (PC) via a USB cable.

Fibers with large core diameter were chosen to maximize collection of optical thermal radiation; the gold (Au) coating allows the fiber to withstand high temperatures, up to ~1000 K, although the core diameter of Au-coated fibers is limited to a maximum of 400 μm.

The wavelengths of the photodetector assemblies were chosen based on previous experience to avoid spectral features (emission and absorption lines) from the combustion by-products and the components of the pyrotechnic charges (see Figure 2, taken from earlier spectroscopic experiments), as well as to test the assumption that the measured combustion process behaves like a blackbody (emissivity $\epsilon = 1.0$): a good agreement among the temperatures estimated at different wavelengths means the blackbody condition is met.

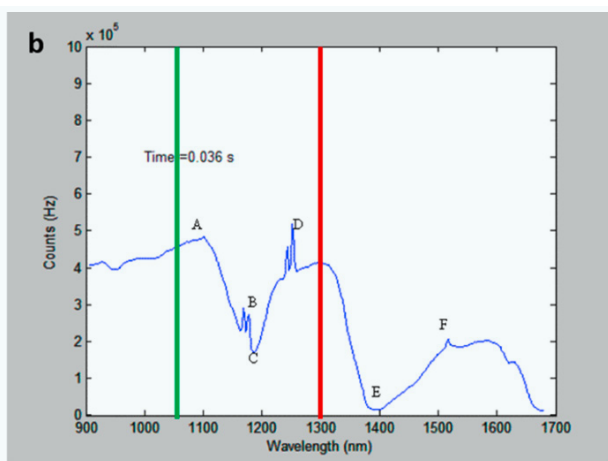
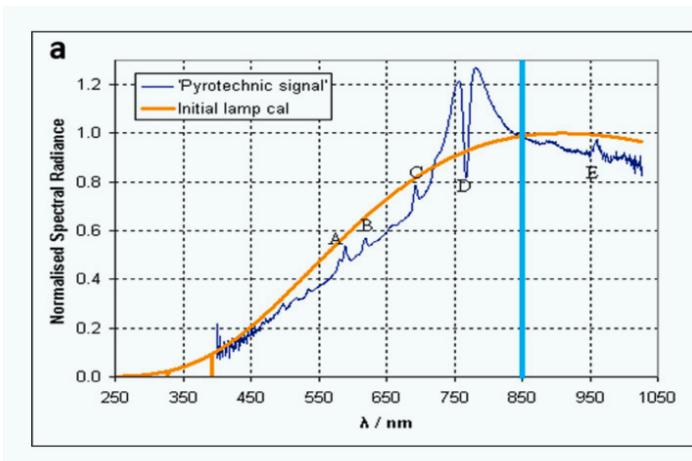
Figure 2(a) shows the emission spectrum captured with a Si spectrometer, where the following features were identified:

- A) 589 nm – Sodium (Na) emission lines
- B) 619 nm – CaOH emission lines
- C) 693 nm – Potassium (K) emission lines
- D) 767 nm – K emission and absorption lines
- E) 960 nm – Uncertain of assignment.

Figure 2(a) also shows the blackbody spectrum from a tungsten calibration lamp (with a temperature of 3165 K) overlapped to the measured spectrum. The agreement between the shape of the two spectra suggests that the blackbody assumption for a fireball is a valid hypothesis. Figure 2(b) shows the emission spectrum captured with an InGaAs spectrometer, where the following features were identified:

- A) 1104 nm – K emission lines
- B) 1169 nm – K emission lines
- C) Broad OH absorption in the fiber
- D) 1243 and 1252 nm – K emission lines
- E) Broad OH absorption in the fiber
- F) 1517 nm – K emission lines.

As photodetectors with variable gain G are used, a simple theoretical model was developed to



estimate the optical power measured by each photodetector and how their voltage signals change with G . Their bandwidth B also decreases with increasing G , adjustable in 10 dB steps from 0 dB to 70 dB. First of all, the blackbody radiation power coupled into the core of the optical fiber (see geometry sketched in Figure 3) was calculated, assuming an emissivity $\varepsilon = 1$ and optical transmission of the fiber over the range $\lambda = (0.3 - 2.4) \mu\text{m}$ as specified in the Au-coated fiber datasheet.

Neglecting the Fresnel reflection losses from the end-facet of the fiber and from the sapphire window, the total blackbody radiation power coupled into the fiber core over the full blackbody radiation spectrum (i. e., all wavelengths) is $P_{\text{in,TOT}}(T) = \sigma \Omega A \varepsilon T^4 / \pi$, where:

- T is the blackbody temperature in K
- $\sigma = 5.67 \times 10^{-8} \text{ W} \cdot \text{m}^{-2} \cdot \text{K}^{-4}$ is the Stefan-Boltzmann constant
- $A = \pi d^2 / 4 = 1.25664 \times 10^{-7} \text{ m}^2$ is the fiber core area
- $\Omega = \pi \tan^2(\theta)$ is the maximum solid acceptance angle of the Au-coated fiber, with θ the maximum acceptance half-angle of the Au-coated fiber, which is related to the NA of the fiber as: $NA = n \sin(\theta) = 0.22$.

As the refractive index of air is $n \approx 1$, the maximum solid acceptance angle can be re-written as $\Omega = \pi \tan^2(\arcsin(NA)) \approx 0.16 \text{ sr}$. Hence, the total blackbody radiation power coupled into the optical fiber is $P_{\text{in,TOT}}(T) = 3.624 \times 10^{-16} (T/K)^4 \text{ W}$.

The fractional power coupled into the optical fiber over the wavelength range $\lambda = (0.3 - 2.4) \mu\text{m}$, $P_{\text{in}}(T)$, can be calculated numerically or through tabulated values, considering the wavelength-temperature products. With such a model, approximately 10 mW of optical thermal radiation is coupled into the optical fiber for $T \approx 2500 \text{ K}$; however, for $T = 300 \text{ K}$: $P_{\text{in}}(T) < 10 \text{ pW}$.

To calculate the optical power measured by each photodetector and the associated voltage signals, the losses in the optical transmission line from the sensor head to the detectors need to be considered. To estimate the signals accurately, the following contributions need to be considered:

1. The transmission factor of the sapphire window placed in front of the fiber end-facet, due to Fresnel reflection losses (7 % at each interface/surface): $t_0 = 0.93 \times 0.93 = 0.8649$.
2. The transmission factor at the end-facet of the Au-coated fiber, due to Fresnel reflection losses: $t_1 = 0.96$.



Figure 3: Geometry of the end of the sensor (Au-coated fiber): d = fiber core diameter; θ = maximum acceptance half-angle

3. Transmission losses of 12 m of fiber (2 m sensor + 10 m of extension lead fiber) – considering that typical losses for large-core multi-mode fiber are of the order of 10 dB/km or less at $\lambda = (0.6 - 1.6) \mu\text{m}$: $t_{\text{fiber}} = -0.12 \text{ dB} \approx 0.973$.
4. Losses due to optical connectors (3), typically of the order of 0.3 dB each, i. e., a transmission factor $t_{\text{connector}} = 0.933$.
5. The splitting ratio of the 1×3 optical coupler/splitter: $t_{\text{splitter}} \approx 0.333$.
6. The optical transmission (t_{filter}) of the bandpass filters in the photodetector assemblies – it is worth noting that the filters used have different values of optical transmission peak and Full-Width-at-Half-Maximum (FWHM):
 - ▷ $t_{850 \text{ nm}} = 70 \%$
 - ▷ $t_{1050 \text{ nm}} = 45 \%$
 - ▷ $t_{1300 \text{ nm}} = 40 \%$
 - ▷ $\text{FWHM}_{850 \text{ nm}} = 40 \text{ nm} \pm 8 \text{ nm}$
 - ▷ $\text{FWHM}_{1050 \text{ nm}} = 10 \text{ nm} \pm 2 \text{ nm}$
 - ▷ $\text{FWHM}_{1300 \text{ nm}} = 30 \text{ nm} \pm 6 \text{ nm}$.

Hence, the optical power incident on the photodetectors can be calculated as:

Finally, to calculate the voltage signal, we need to also consider the photodetector transimpedance gain G_i [V/A] and responsivity $R(\lambda_i)$ [A/W], which is a function of wavelength; hence:

$$P_i(\lambda, T) = t_0 t_1 t_{\text{fiber}} t_{\text{splitter}} (t_{\text{connector}})^3 t_{\text{filter}}(\lambda) P_{\text{in}}(\lambda, T) \approx 0.22 t_{\text{filter}}(\lambda) P_{\text{in}}(\lambda, T) \quad (1)$$

where $P_{\text{in}}(\lambda, T) = A \Omega L_b(\lambda, T)$, with $L_b(\lambda, T) = \frac{2c_1}{\lambda^5} \frac{1}{e^{c_2/\lambda T} - 1} \approx \frac{2c_1}{\lambda^5} e^{-c_2/\lambda T}$ and where c_1 and c_2 are the first and second radiation constants equal to $0.59552197 \times 10^{-16} \text{ W} \cdot \text{m}^{-2} \cdot \text{sr}^{-1}$ and

$$V_i = \int G_i R_i(\lambda) P_i(\lambda, T) d\lambda = 0.22 G_i \int t_{\text{filter}}(\lambda) R_i(\lambda) P_{\text{in}}(\lambda, T) d\lambda \quad (2)$$

$1.438769 \times 10^{-2} \text{ m} \cdot \text{K}$, respectively, and the expression after the \approx symbol is the Wien approximation valid for $c_2 \gg \lambda T$.

Equations (1) and (2) have been evaluated at different temperatures, and the results compared with preliminary experimental data. These showed a lower signal than expected (by a factor of ~ 2),

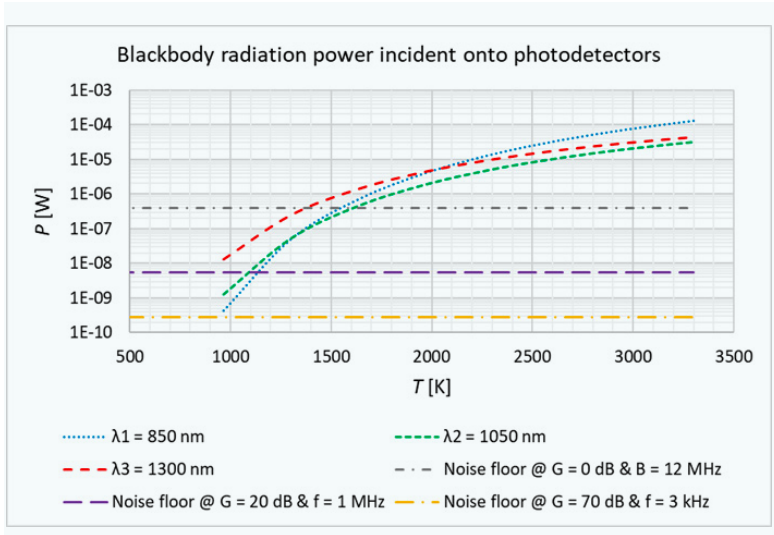


Figure 4: Blackbody radiation power incident onto photodetectors as a function of blackbody temperature

likely due to extra connection losses. This has been fed back into the model, which gives the results shown in Figure 4 in terms of optical power incident onto the photodetectors – noise floors are shown only for: $G = 0$ dB & $B = 12$ MHz (highest noise floor), $G = 20$ dB & $B = 1$ MHz and $G = 70$ dB & $B = 3$ kHz (lowest noise floor).

Noise floor has been estimated for each photodetector as $P_{n,i} = NEP \times B^{1/2} \times R_{MAX} R(\lambda_i)$, where NEP is the Noise Equivalent Power and R_{MAX} is the peak responsivity, both provided in the photodetector datasheets.

Figure 4 shows that, in any case, the instrument should be capable of measuring temperatures $T > 1600$ K at all wavelengths, with photodetectors set at $G = 0$ dB and $B = 12$ MHz. However, considering that the maximum sampling rate of the DAQ system is $f_{MAX} = 1$ MHz, a gain setting of $G = 20$ dB ($B = 1$ MHz) would allow measurement of temperatures as low as ~ 1100 K with the 1300 nm photodetector (but not at $\lambda_1 = 850$ nm and $\lambda_2 = 1050$ nm) with no penalty in terms of speed.

The minimum and maximum temperatures measurable by the instrument are dictated, respectively, by the noise level (experimentally measured as ~ 1 mV for most values of G) and the

saturation level (~ 10 V) of the photodetectors. To find the photodetector settings that optimize the measurable temperature range, Equation (2) has been evaluated at different temperatures for different G and B settings of the photodetectors. Voltage signals generated by the three photodetectors have been plotted versus temperature for all values of G and B . Figure 5 shows two of these plots for representative values of G and B .

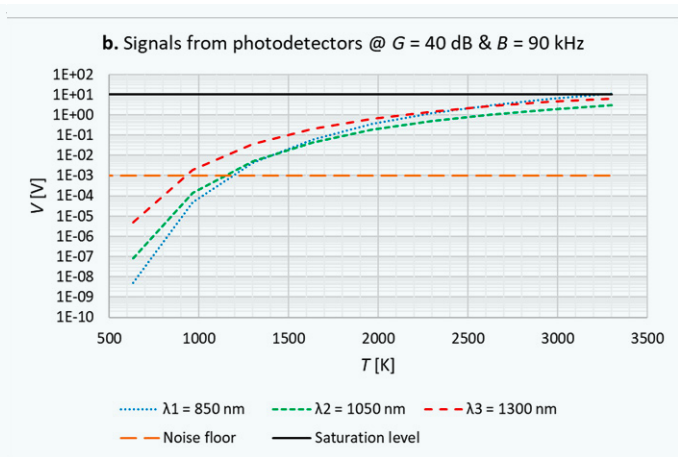
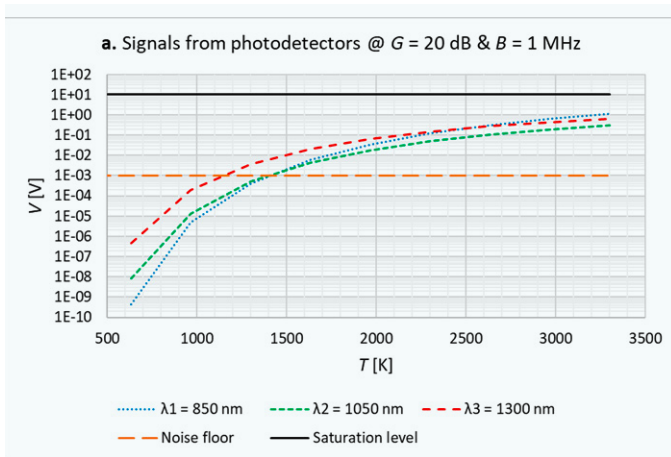
- With a gain of $G = 20$ dB ($B = 1$ MHz – Figure 5(a), the instrument can measure a minimum temperature of ~ 1150 K at a single wavelength ($\lambda_3 = 1300$ nm) or ~ 1400 K at all three wavelengths.
- With a gain of $G = 30$ dB ($B = 260$ kHz), the minimum measurable temperature can be brought down to ~ 1025 K for single-wavelength measurement ($\lambda_3 = 1300$ nm) and ~ 1275 K at all three wavelengths, but at cost of reduced sampling speed ($f \leq B = 260$ kHz), while still avoiding saturation at 3300 K, our maximum temperature of interest.
- With a gain of $G \geq 40$ dB ($B = 90$ kHz – Figure 5(b), the photodetectors would start saturating at $T_{MAX} < 3300$ K and their bandwidth would decrease significantly, down to $B = 3$ kHz at $G = 70$ dB.

Hence, the optimum photodetector gain is $G = 30$ dB, which allows temperatures above 1025 K to be measured for $\lambda_3 = 1300$ nm, or temperatures above 1275 K to be measured for all wavelengths, with a maximum sampling rate $f \leq B = 260$ kHz.

2.3 Fiber connection reproducibility

Here we describe the repeatability tests performed on the DynPT system, including the extension lead fiber (10 m-long FiberCore step index multi-mode

Figure 5: Modelled signals from photodetectors versus blackbody temperature at different G & B settings: (a) $G = 20$ dB & $B = 1$ MHz, (b) $G = 40$ dB & $B = 90$ kHz



fiber, with 600 μm core diameter, $NA = 0.22$, dual-layer acrylate coating and FC/UPC connectors on both ends), in order to determine the effect of disconnecting and reconnecting the extension lead fiber on the measurements. Test rig and test methods are first described, together with the data analysis method; then test results are presented and discussed.

Test rig

The DynPT system was tested using: a Thorlabs SLS201L/M stabilized fiber-coupled tungsten-halogen light-source and a sensor/probe (i. e., a 2 m-long FiberGuide AnhydroGuide AFS400/440/510G gold-coated MM step-index fiber with 400 μm core diameter, $NA = 0.22$, stainless steel monocoil sheathing, an SMA connector on one end and an FC/PC connector on the other end), connected to the former through the SMA connector and to the extension lead fiber through the FC/PC connector; the other end of the extension lead fiber is connected to the optoelectronic interrogator. A photo of the test rig and a schematic of the measurement set-up are shown in Figure 6 and Figure 7, respectively. When disconnecting and reconnecting a fiber connector cassette-cleaner (Thorlabs FCC-7020) and a one-step bulk-head connector cleaner (Thorlabs FBC1) were used. A simple LabVIEW program was used to collect and process data from the system, either continuously (for the baseline test) or on demand (for the reconnection test).

Test method

The system was tested using a gain $G = 20$ dB (bandwidth $B = 1$ MHz) and sampling frequency $f = 1$ MHz. Data was sampled over a time window of $\Delta t = 1$ s; hence the number of sampled points was $N = f / \Delta t = 10^6$. The LabVIEW program was set up and operated to record the mean value (mean) and standard deviation (std. dev.) of the voltage signals coming from the photodetectors over the $\Delta t = 1$ s time window. The tungsten-halogen light-source was left on for more than 45 minutes to warm up, as recommended in the manual, before starting the test.

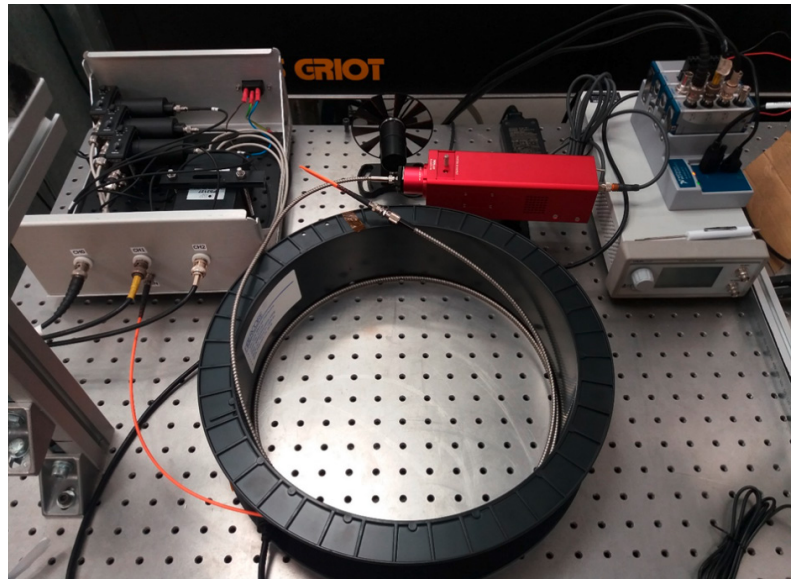


Figure 6:
Photo of test rig

After warming up, a preliminary test was performed to calculate losses introduced by the extension lead fiber, then continuous baseline data was collected over 10 minutes in order to assess measurement repeatability without disconnecting and reconnecting the optical fiber. After collecting baseline data, two tests were performed, according to the following procedure, repeated 10 times:

1. Disconnect one of the FC/UPC connectors of the extension lead fiber from the bulk-head connector
2. Clean the bulk-head connector with the Thorlabs FBC1 cleaner
3. Clean the disconnected FC/UPC connector of the extension lead fiber with the Thorlabs FCC-7020 cassette-cleaner
4. Reconnect the FC/UPC connector of the extension fiber with the bulk-head connector
5. Take a measurement.

This test was repeated twice: first for the connection between the sensor/probe and the extension lead fiber (point A in Figure 7) and then for the connection between the extension lead

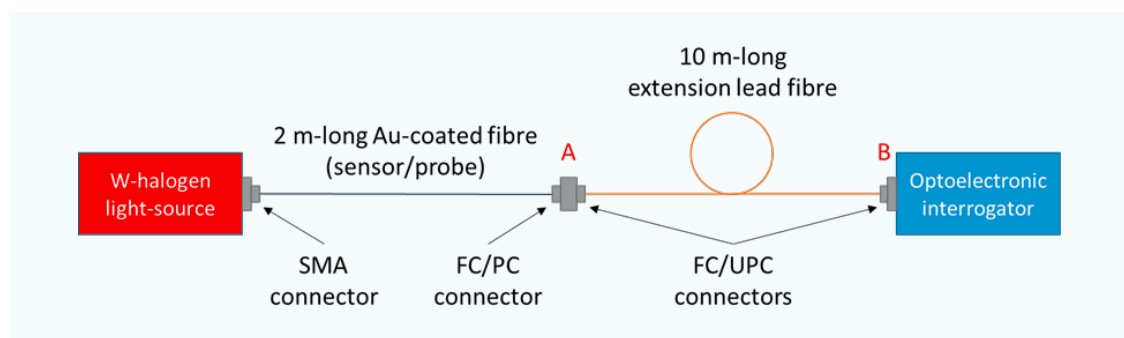


Figure 7:
Schematic of test rig (optical chain). A and B identify the two connection points that were tested for mating repeatability

Table 1:
Summary of
baseline test
results – statistics
of signal mean
values

	$\lambda_1 = 850 \text{ / nm}$	$\lambda_1 = 1050 \text{ / nm}$	$\lambda_1 = 1300 \text{ / nm}$
Min. [mV]	137.86	43.01	155.19
Max. [mV]	138.12	43.18	155.35
Average [mV]	137.99	43.10	155.27
Max. - min. [mV]	0.26	0.17	0.16
Std. dev. [mV]	0.05	0.03	0.03
Rel. std. dev.	0.04 %	0.08 %	0.02 %

fiber and the optoelectronic interrogator (point B in Figure 7).

Test results - Baseline

Figure 8 shows the results from the baseline test, with a summary of results given in Table 1, showing the statistics of signal mean values measured from the three photodetectors.

The data above clearly show very good measurement stability (without disconnecting/reconnecting the fiber): in fact, the standard deviation of signal mean relative to the average over the whole duration of the baseline test (10 minutes) is ~0.04 % for $\lambda_1 = 850 \text{ nm}$, ~0.08 % for $\lambda_2 = 1050 \text{ nm}$ and ~0.02 % for $\lambda_3 = 1300 \text{ nm}$. Knowing that the voltage signal from the photodetector is proportional to the measured blackbody radiation, according to

$$V_i(T) = A_i / (e^{\frac{c_2}{\lambda_i T}} - 1) \tag{3}$$

with A_i a proportionality constant for different λ_i , and defining the relative standard deviation of the signal as: $\Delta V_i / V_i$, by differentiating $V_i(T)$ by T , assuming that $e^{\frac{c_2}{\lambda_i T}} \gg 1$, we can then calculate the

relative temperature error as

$$\frac{\Delta T}{T} = \frac{\lambda_i \cdot T \Delta V_i}{c_2 \cdot V_i} \tag{4}$$

Notice that the proportionality constant A_i does not play a role here.

Table 2 shows the expected repeatability of temperature measurements in terms of relative and absolute temperature errors, derived from the signal standard deviation of the baseline test, in the expected operational temperature range $T = (900 - 3600) \text{ K}$, assuming that $\Delta V_i / V_i$ is constant with temperature T .

Test results – Reconnection test 1 (point A)

Table 3 and Figure 9 show the data collected in the reconnection test 1 at point A, performed by disconnecting, cleaning and reconnecting the extension lead fiber to the sensor/probe and then taking one measurement at each iteration. Statistics are also included at the bottom of the table.

The data above clearly show good measurement repeatability (when disconnecting / reconnecting the extension-lead fiber to the sensor/probe), although it is not as good as in the baseline test:

Table 2:
Measurement
repeatability in
terms of relative
and absolute
temperature errors
derived from signal
relative standard
deviation of
baseline test

$T \text{ [K]}$	Relative temperature error ($\Delta T / T$) [%]			Absolute temperature error (ΔT) [K]		
	$\lambda_1 = 850 \text{ nm}$	$\lambda_1 = 1050 \text{ nm}$	$\lambda_1 = 1300 \text{ nm}$	$\lambda_1 = 850 \text{ nm}$	$\lambda_1 = 1050 \text{ nm}$	$\lambda_1 = 1300 \text{ nm}$
900	0.002	0.005	0.002	0.02	0.05	0.01
1200	0.003	0.007	0.002	0.03	0.08	0.03
1500	0.003	0.009	0.003	0.05	0.13	0.04
1800	0.004	0.010	0.003	0.07	0.19	0.06
2100	0.005	0.012	0.004	0.10	0.26	0.08
2400	0.005	0.014	0.004	0.13	0.33	0.10
2700	0.006	0.016	0.005	0.16	0.42	0.13
3000	0.007	0.017	0.005	0.20	0.52	0.16
3300	0.007	0.019	0.006	0.24	0.63	0.20
3600	0.008	0.021	0.006	0.29	0.75	0.23

Iteration #	$\lambda_1 = 850 \text{ nm}$		$\lambda_1 = 1050 \text{ nm}$		$\lambda_1 = 1300 \text{ nm}$	
	Mean [mV]	Std. dev.[mV]	Mean [mV]	Std. dev. [mV]	Mean [mV]	Std. dev. [mV]
1	137.9	0.28	43.02	0.28	155.21	0.29
2	139.89	0.28	43.63	0.28	157.57	0.29
3	137.32	0.28	42.99	0.29	154.79	0.29
4	139.86	0.28	43.61	0.28	157.66	0.29
5	139.68	0.28	43.55	0.28	157.35	0.29
6	139.86	0.28	43.71	0.29	157.53	0.29
7	139.63	0.28	43.62	0.28	157.41	0.29
8	139.34	0.28	43.56	0.28	157.1	0.29
9	139.72	0.28	43.67	0.28	157.49	0.29
10	139.45	0.28	43.61	0.28	157.3	0.29
	Mean	Std. dev.	Mean	Std. dev.	Mean	Std. dev.
Min. [mV]	137.32	0.28	42.99	0.28	154.79	0.29
Max. [mV]	139.89	0.28	43.71	0.29	157.66	0.29
Mean [mV]	139.27	0.28	43.50	0.28	156.94	0.29
Max. - min. [mV]	2.57	0.00	0.72	0.01	2.87	0.00
Std. dev. [mV]	0.85	0.00	0.25	0.00	0.99	0.00
Rel. std. dev.	0.61 %	0.00 %	0.57 %	1.42 %	0.63 %	0.00 %

the standard deviation of signal mean relative to the average is between $\sim 0.57\%$ and $\sim 0.63\%$, versus $\sim (0.02 - 0.08)\%$ of the baseline test. Figure 9 shows better repeatability in the last 7 iterations than in the first 3.

We calculate the relative and absolute temperature errors at different blackbody temperatures from the relative standard deviation of the signal ($\Delta V_i / V_i$), assuming that this is constant with temperature. The results are shown in Table 4. Comparing this table with Table 3, we can see that in this case the relative temperature error is about one order of magnitude larger than in the previous case (baseline test), but repeatability is still at acceptable levels, reaching $\sim 0.2\%$ at $T = 3600 \text{ K}$; in terms of absolute temperature measurement repeatability, this goes

up to $\sim 7.4 \text{ K}$ at $T = 3600 \text{ K}$ (for $\lambda_3 = 1300 \text{ nm}$).

Figure 10 shows how temperature measurement errors increase with temperature; again, the expected temperature measurement repeatability is very good, with a relative temperature error $\Delta T / T < 0.25\%$ and an absolute temperature error $\Delta T < 8 \text{ K}$.

Test results – Reconnection test 2 (point B)

Table 5 and Figure 11 show the results of the reconnection test 2 (at point B), performed by disconnecting, cleaning and reconnecting the extension-lead fiber to the optoelectronic interrogator and then taking one measurement at each iteration. Statistics are included at the bottom of the table.

Table 3: Summary of results of reconnection test 1 at point A – data and statistics

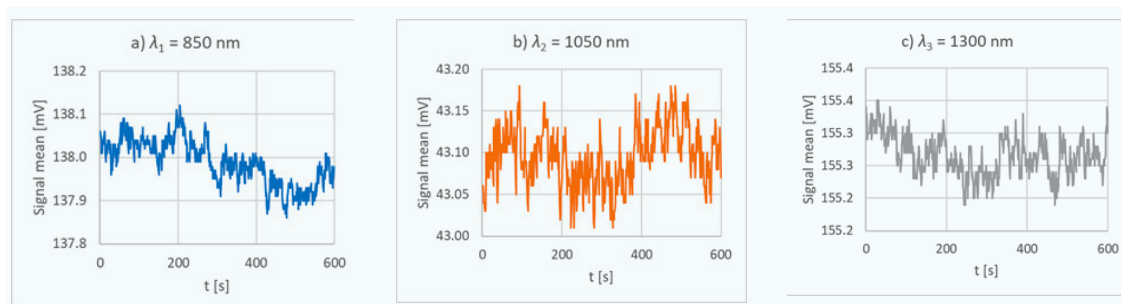


Figure 8: Time trend of mean value of all three detector signals – baseline test

Table 4: Measurement repeatability in terms of relative and absolute temperature errors derived from signal relative standard deviation of reconnection test 1 (at point A)

T [K]	Relative temperature error ($\Delta T / T$) [%]			Absolute temperature error (ΔT) [K]		
	$\lambda_1 = 850 \text{ nm}$	$\lambda_1 = 1050 \text{ nm}$	$\lambda_1 = 1300 \text{ nm}$	$\lambda_1 = 850 \text{ nm}$	$\lambda_1 = 1050 \text{ nm}$	$\lambda_1 = 1300 \text{ nm}$
900	0.03	0.04	0.05	0.29	0.34	0.46
1200	0.04	0.05	0.07	0.52	0.60	0.82
1500	0.05	0.06	0.09	0.82	0.94	1.28
1800	0.07	0.08	0.10	1.17	1.36	1.84
2100	0.08	0.09	0.12	1.60	1.85	2.50
2400	0.09	0.10	0.14	2.09	2.42	3.27
2700	0.10	0.11	0.15	2.64	3.06	4.14
3000	0.11	0.13	0.17	3.26	3.78	5.11
3300	0.12	0.14	0.19	3.95	4.57	6.18
3600	0.13	0.15	0.20	4.70	5.44	7.36

The data above clearly show good measurement repeatability (when disconnecting/reconnecting the extension-lead fiber to the optoelectronics interrogator), although it is not as good as in the baseline test, but better than the results of reconnection test 1 at point A: the standard deviation of signal mean relative to the average is between $\sim 0.34\%$ and $\sim 0.36\%$, versus $\sim (0.02 - 0.08)\%$ of the baseline test and $\sim (0.57 - 0.63)\%$ of test 1.

We calculate the expected relative and absolute temperature errors at different blackbody temperatures from the relative standard deviation of the signal ($\Delta V_i / V_i$), assuming that this is constant with temperature. The results are shown in Table 6. Comparing this table with Table 3 and Table 4, we can see that these test results are better than those of reconnection test 1 (at point A) by a factor of ~ 2 ; relative temperature error is about one order of magnitude larger than in baseline test, but

Figure 9: Time trend of mean value of all signals – reconnection test 1 (at point A)

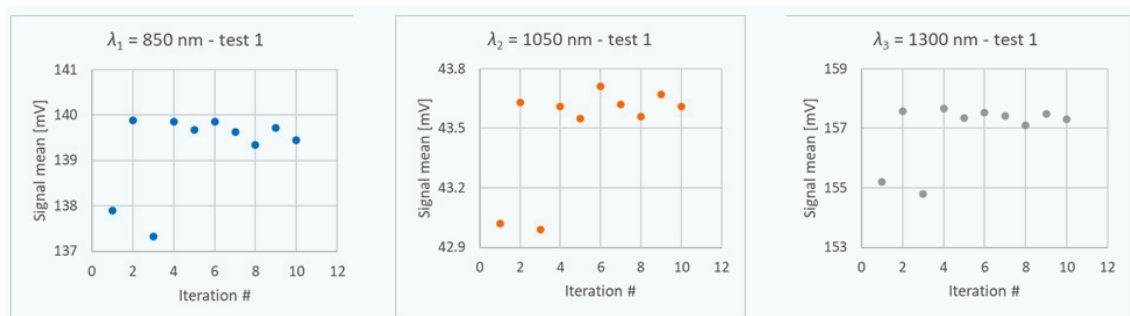
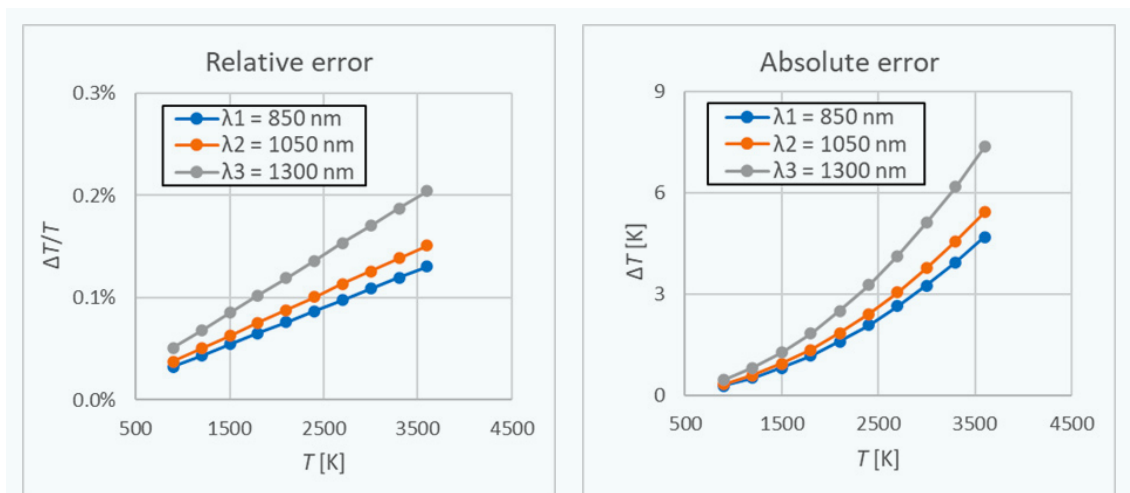


Figure 10: Expected temperature repeatability derived from reconnection test 1 (at point A)



Iteration #	$\lambda_1 = 850 \text{ nm}$		$\lambda_1 = 1050 \text{ nm}$		$\lambda_1 = 1300 \text{ nm}$	
	Mean [mV]	Std. dev.[mV]	Mean [mV]	Std. dev. [mV]	Mean [mV]	Std. dev. [mV]
1	139.43	0.28	43.53	0.28	157.25	0.29
2	139.48	0.28	43.58	0.28	157.47	0.29
3	140.7	0.28	43.94	0.29	158.83	0.29
4	140.76	0.28	43.95	0.29	158.85	0.29
5	140.84	0.28	43.92	0.29	158.83	0.29
6	140.74	0.28	43.91	0.29	158.79	0.29
7	140.72	0.28	43.96	0.29	158.79	0.29
8	140.7	0.28	43.93	0.28	158.69	0.29
9	140.73	0.28	43.92	0.28	158.7	0.29
10	140.48	0.28	43.79	0.28	158.4	0.29
	Mean	Std. dev.	Mean	Std. dev.	Mean	Std. dev.
Min. [mV]	139.43	0.28	43.53	0.28	157.25	0.29
Max. [mV]	140.84	0.28	43.96	0.29	158.85	0.29
Mean [mV]	140.46	0.28	43.84	0.29	158.46	0.29
Max. - min. [mV]	1.41	0.00	0.43	0.01	1.60	0.00
Std. dev. [mV]	0.51	0.00	0.15	0.00	0.57	0.00
Rel. std. dev.	0.36 %	0.00 %	0.34 %	1.75 %	0.36 %	0.00 %

Table 5: Summary of results of reconnection test 2 (at point B) – data and statistics

repeatability is still at acceptable levels, reaching ~0.12 % at $T = 3600 \text{ K}$; in terms of absolute temperature measurement repeatability, this goes up to ~4.2 K at $T = 3600 \text{ K}$ (for $\lambda_3 = 1300 \text{ nm}$).

Figure 12 shows how temperature measurement errors increase with temperature; again, the expected temperature measurement repeatability is very good, with a relative temperature error $\Delta T / T < 0.12 \%$ and an absolute temperature error $\Delta T < 4.5 \text{ K}$. It is worth noting that, as in the test 1 at point A, in this case the temperature error (either relative or absolute) is largest at the longest wavelength, i. e., $\lambda_3 = 1300 \text{ nm}$.

Conclusions

The tests performed and described here have shown very good measurement repeatability with the DynPT system. The baseline test has shown that, without disconnecting the fiber, we can expect a temperature measurement repeatability better than 0.025 % or 1 K up to $T = 3600 \text{ K}$. The reconnection tests have shown that, when disconnecting, cleaning, and reconnecting the extension lead fiber, the temperature measurement repeatability gets worse, but is still at acceptable levels:

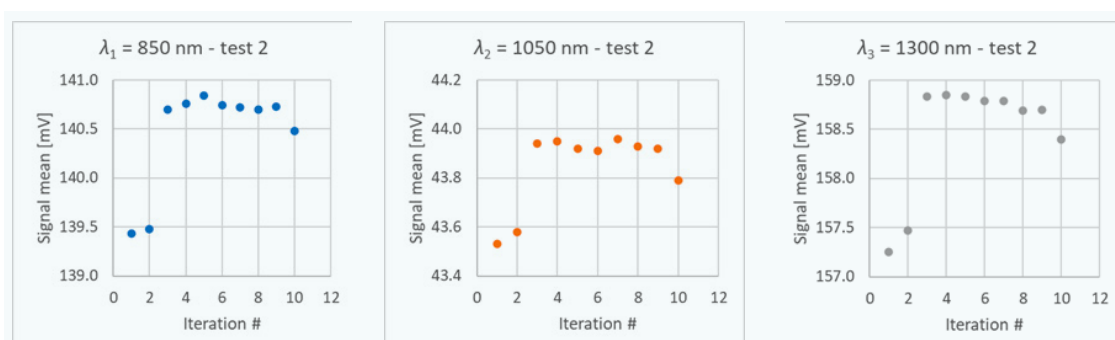


Figure 11: Time trend of mean value of all signals – reconnection test 2 (at point B)

Table 6: Measurement repeatability in terms of relative and absolute temperature errors derived from signal relative standard deviation of reconnection test

T [K]	Relative temperature error ($\Delta T / T$) [%]			Absolute temperature error (ΔT) [K]		
	$\lambda_1 = 850 \text{ nm}$	$\lambda_1 = 1050 \text{ nm}$	$\lambda_1 = 1300 \text{ nm}$	$\lambda_1 = 850 \text{ nm}$	$\lambda_1 = 1050 \text{ nm}$	$\lambda_1 = 1300 \text{ nm}$
900	0.02	0.02	0.03	0.17	0.20	0.26
1200	0.03	0.03	0.04	0.31	0.36	0.46
1500	0.03	0.04	0.05	0.48	0.57	0.73
1800	0.04	0.05	0.06	0.69	0.82	1.05
2100	0.04	0.05	0.07	0.94	1.11	1.42
2400	0.05	0.06	0.08	1.23	1.45	1.86
2700	0.06	0.07	0.09	1.56	1.83	2.35
3000	0.06	0.08	0.10	1.93	2.26	2.90
3300	0.07	0.08	0.11	2.33	2.74	3.51
3600	0.08	0.09	0.12	2.77	3.26	4.18

- $\Delta T / T < 0.25 \%$ or $\Delta T < 8 \text{ K}$ up to $T = 3600 \text{ K}$ for test 1 at point A,
- $\Delta T / T < 0.12 \%$ or $\Delta T < 4.5 \text{ K}$ up to $T = 3600 \text{ K}$ for test 2 at point B.

This means that fiber disconnection and reconnection can be tolerated, making installation and transportation easier, as we can disassemble the system after calibration, without incurring significant errors when the system is moved and re-installed.

System calibration

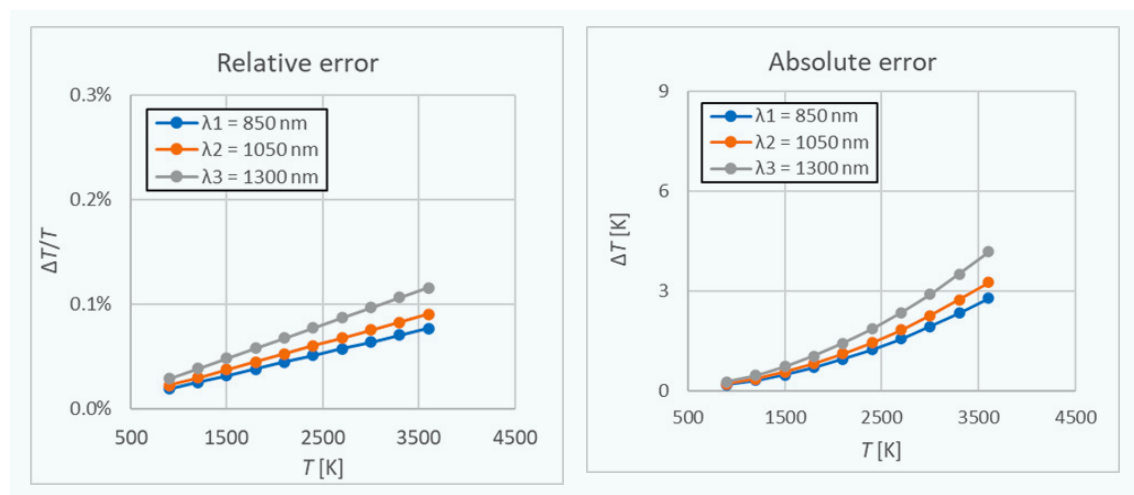
Test rig

The instrument was calibrated using a Thermo Gauge blackbody radiation furnace and a *KE-Technologie GmbH* LP3 linear pyrometer calibrated traceably to the ITS90 [3], with the

stainless-steel tube of the packaged sensor filled with sand to avoid overheating the Au-coated fiber that otherwise could have been irreversibly damaged. A photograph of part of the test rig is shown in Figure 13(a): the hot Thermo Gauge blackbody furnace and temperature sensor are visible in the background and foreground respectively. Figure 13(b) shows the probe fiber mounted inside the steel tube. The tube is placed on a stainless-steel V-groove mounted on an optical breadboard and safely held in place by removable brackets bolted to the breadboard. This breadboard is installed on a motorized stage, controlled by a computer, for horizontal and vertical alignment. The LP3 (not visible in the figure) is mounted on the same framework, so that it can be easily moved in front of the blackbody, in place of the sensor, to measure the temperature at each setpoint of the calibration.

Data from the instrument was acquired using a NI LabVIEW program, written in-house and

Figure 12: Expected temperature repeatability derived from reconnection test 2 (at point B)



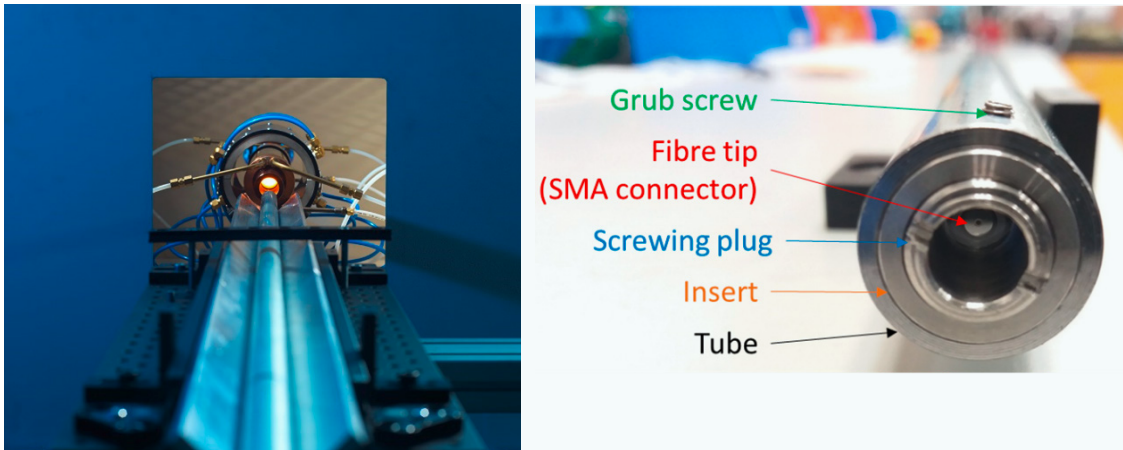


Figure 13: a) Photograph of the calibration furnace and b) the instrument sensor, housed in a steel tube, sits on the V-groove placed in front of blackbody furnace, ready to be manually moved in and out of it for dynamic calibration at a set temperature

executed on the PC that is part of the system, whereas the blackbody furnace was controlled with a separate desktop computer that also controls the motorized framework.

Test method

The instrument was configured with the photodetectors set with optimum gain $G = 30$ dB ($B = 260$ kHz) and the sampling rate set at $f = 250$ kHz. At the beginning of the calibration, the voltage offset from the three photodetectors was measured once, to zero the photodetectors. The instrument was calibrated in the temperature range $T = (1073 - 2873)$ K, in steps of $\Delta T = 200$ K, according to the following procedure:

1. The blackbody furnace was set at the required temperature set-point
2. The temperature of the blackbody cavity was monitored using the LP3
3. Once the blackbody temperature reached stability, a measurement was taken from the LP3, by measuring the average and standard deviation over ~ 30 s (the LP3 is sampled at 1 Hz)
4. The LP3 was moved out of the way and the sensor moved into place, so that it was in line with and parallel to the long axis of the blackbody, as shown in Figure 13
5. Data acquisition and logging were started on the instrument
6. Manually, the sensor was quickly moved into and out of the blackbody (within a few seconds)
7. Two measurements were made at each set-point temperature.

Test data analysis method

The raw voltage signals from the three photodetectors of the optoelectronic interrogator were analyzed to find the optimum calibration point in each signal. This is explained in Figure 14, showing typical measurement traces – the signal from the 1050 nm photodetector is the lowest, because of the combined effect of the responsivity of the photodetector and the transmission and the bandwidth of the optical bandpass filter.

Considering Figure 14(b):

- $t < 1.3$ s: the blackbody cavity has a temperature gradient along the cavity wall and across its rear surface, it is hotter to the outside, and this is seen as the sensor approaches: the radiance signal rises as the field of view of the sensor is initially filled.
- $t \approx (1.3 - 1.6)$ s: the signal falls as the sensor progressively sees more of the cooler central section of the back wall.
- $t \approx (1.6 - 1.77)$ s: there is a period when the blackbody temperature falls, due to heat lost to the cold sensor.
- $t \approx (1.77 - 1.92)$ s: as the sensor is withdrawn, the hotter regions of the blackbody cavity are seen again, so that the signal increases.
- $t > 1.92$ s: the signal decreases, as the sensor is withdrawn from the blackbody cavity.
- The maximum in the signal during sensor removal is lower than during insertion. This is consistent with the cooling of the blackbody cavity.
- The voltages recorded for calibration were chosen at the inflection point of each

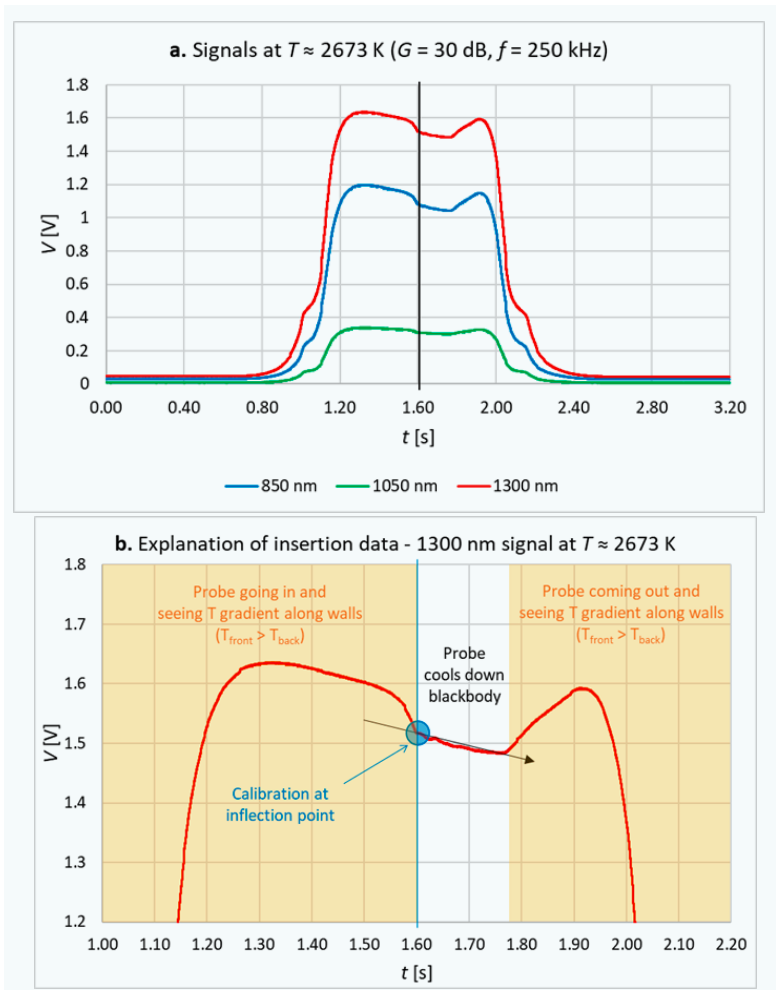


Figure 14: Typical calibration measurement traces: the black line in the middle of chart (a) identifies the points used for calibration; (b) is a close-up on the 1300 nm signal and its calibration point

signal, highlighted by the blue circle, as it corresponds to the point when the field of view of the fiber is filled with thermal radiation from the back wall, before any further cooling.

Calibration was performed by fitting experimental data to the Sakuma-Hattori version of the Planck equation with three adjustable parameters A_i , B_i and c_i for each wavelength λ_i [4]:

$$V_i = A_i / (e^{c_i / (\lambda_i T + B_i)} - 1). \quad (5)$$

At each calibration point, the two voltage measurements for each wavelength/photodetector were averaged; each average is then converted into temperature using the inverse function of equation (5):

$$T_i = \frac{1}{\lambda_i} \left(\frac{c_i}{\ln\left(\frac{A_i}{V_i} + 1\right)} - B_i \right). \quad (6)$$

Optimum values of the adjustable parameters were found using the Generalized Reduced Gradient (GRG) solving method for smooth non-linear problems, to minimize the sum of the squares of temperature differences with the LP3.

Test results

The average signal at each setpoint was measured for each wavelength/photodetector and plotted versus the set-point temperature measured from the LP3 linear pyrometer. Figure 15 shows good agreement between experimental data and the theoretical model at $G = 30$ dB, as used for the calibration, although the signal from the 1300 nm photodetector is higher than predicted, most likely due to overestimated losses, as a single figure was used for all three wavelengths. The dashed noise-floor line in the figure also shows that the instrument can measure a temperature as low as 1073 K at $\lambda_3 = 1300$ nm or 1273 K at all three wavelengths – these minimum temperatures match with those expected from the theoretical model.

Using the inverse Planck function, i. e., Equation (6), average voltage measurements for each wavelength at each set-point were converted into temperatures and the adjustable parameters were optimized to minimize the sum of the squares of calibration residuals. The optimum calibration coefficients are shown in Table 7 (B_i coefficients are not included, because they were found to be close to zero) and the residuals are shown in Figure 16, showing relative temperature differences within ± 1 % (absolute differences are within ± 15 K).

λ_i [nm]	A_i [V]	C_i [$\mu\text{m K}$]
850	527.6	14082.2
1050	53.0	14431.8
1300	91.7	14307.3

Table 7: Optimum values of the adjustable calibration coefficients, minimizing the sum of squares of relative errors

Having calibrated the sensor, the maximum measurable temperatures can be estimated by extrapolation of the Planck function in Equation (5) until the photodetector saturation level ($V_{\text{MAX}} = 10$ V) is reached or, more accurately, by using this value in the inverse Planck function, i. e., Equation (6). In a similar way, minimum measurable temperatures can be estimated by using the noise level ($V_{\text{noise}} \approx 1$ mV) in the inverse Planck function. Table 8 shows minimum and maximum measurable temperatures.

λ_i [nm]	T_{MIN} [K]	T_{MAX} [K]
850	1260	4160
1050	1260	7470

1300	960	4740
------	-----	------

Table 8: Minimum and maximum measurable temperatures

Similar calibrations were also made with a collimating lens on the end of the measurement probe. In this configuration, there is no requirement to insert the probe into the blackbody cavity itself - a stand-off of up to approximately 500 mm is possible. The results are similar for this simpler method and this method will be used for future pre/post field trial calibrations of the DynPT system.

The calibration uncertainty budget comprises the following components:

1. LP3 pyrometer calibration
2. Emissivity correction to measurement wavelengths
3. Field of view of the sensor (assumed to be 12 mm)
4. Size of source effect (SSE)
5. Measurement repeatability
6. Probe heating effect
7. Connection/reconnection errors
8. Fitting residuals.

All components are first converted to the equivalent values associated with a normal distribution ($k = 1$), summed in quadrature, and then expressed with a coverage factor of $k = 2$ (~95 % confidence interval).

Figure 17 shows how the uncertainty varies with temperature for the three measurement wavelengths 850 nm, 1050 nm and 1300 nm. The relative uncertainty is given in a) and the absolute uncertainty is given in b). We see that the calibration uncertainty is less than 3 % for all wavelengths and all temperatures. It should be noted that during measurements on a source other than a calibration blackbody (e.g., during field trials), the uncertainty is likely to be larger. However, the level of agreement between the temperatures measured at each wavelength can be used to assess the validity of the calibration, i.e., if all three measurements report a similar temperature, it is likely that the measurement uncertainty will be similar to the calibration uncertainty.

Tabulated values for the calibration uncertainty are given in Table 9.

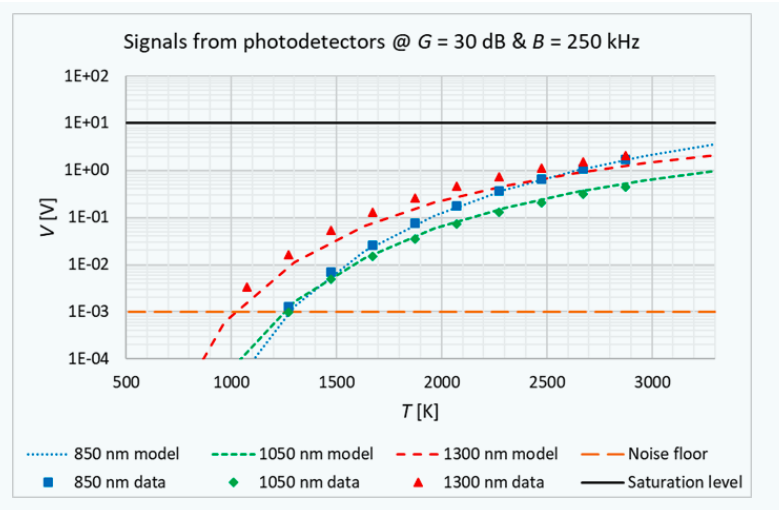


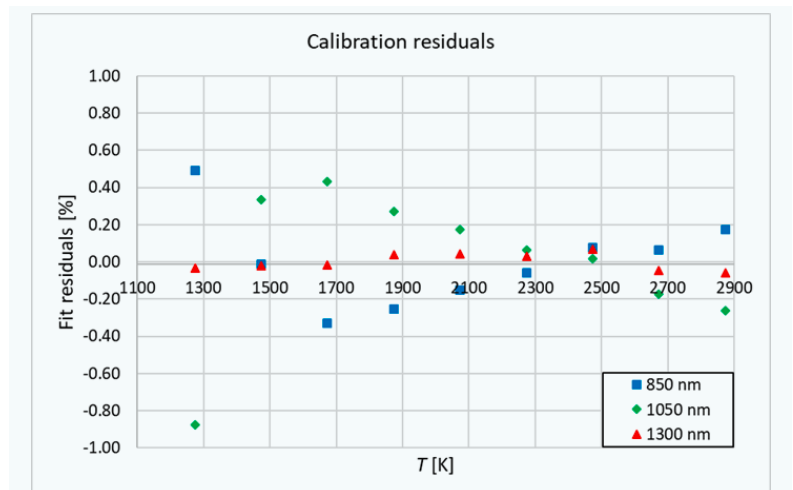
Figure 15: Experimental data compared with theoretical model

2.4 Dynamic tests in laboratory

Test rig

To demonstrate the speed of the instrument, dynamic tests were performed using theatrical flash charges [5] in the pyrotechnic facility at NPL. This consists of a vented enclosure where pyrotechnic charges, placed on a stage, are remotely triggered with a controller that is connected and synchronized with the instrument. The sensor is mounted such that its front end protrudes into the enclosure with its tip ~15 cm above and ~5 cm away from the center of the charge. The optimum position of the sensor is based on experience from previous tests, when we also conducted absorption/transmission experiments from which no optical transmission was observed during the explosion, thus suggesting that the fireball is opaque and supporting our blackbody assumption, and an initial absorption coefficient $\alpha_0 = 0.25 \text{ cm}^{-1}$ was estimated at $\lambda \approx 850 \text{ nm}$.

Figure 16: Calibration residuals



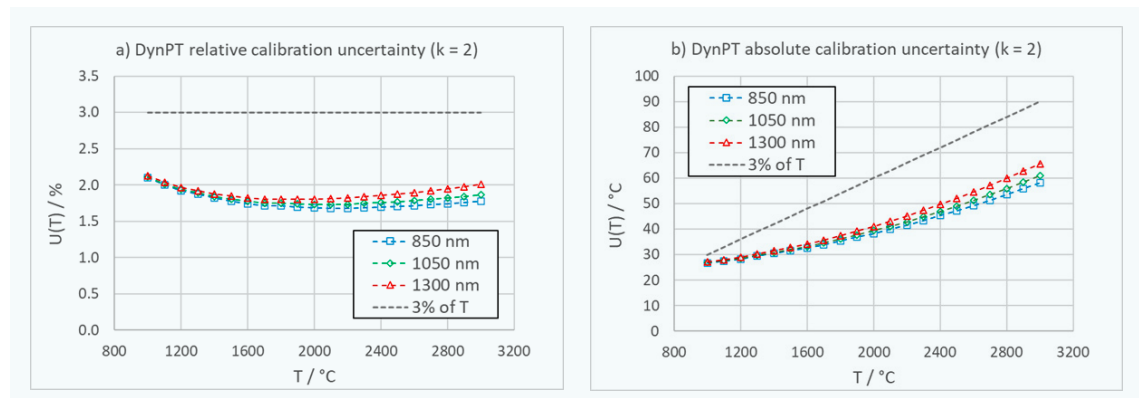
Component:		1) LP3	2) emissivity			3) Field of view	4) SSE		
$T / ^\circ\text{C}$	T / K	Ref pyro	850 nm	1050 nm	1300 nm	FOV (12 mm)	850 nm	1050 nm	1300 nm
1000	1273	0.15	-0.02	0.05	0.13	0.90	3.06	3.37	3.82
1100	1373	0.18	-0.02	0.06	0.15	0.90	3.56	3.92	4.45
1200	1473	0.20	-0.02	0.07	0.17	0.90	4.10	4.51	5.12
1300	1573	0.23	-0.02	0.07	0.20	2.10	4.67	5.14	5.84
1400	1673	0.26	-0.03	0.08	0.22	2.10	5.28	5.81	6.61
1500	1773	0.30	-0.03	0.09	0.25	2.10	5.94	6.53	7.42
1600	1873	0.34	-0.04	0.11	0.28	2.10	6.62	7.29	8.28
1700	1973	0.38	-0.04	0.12	0.31	2.10	7.35	8.08	9.19
1800	2073	0.42	-0.04	0.13	0.34	2.90	8.11	8.93	10.14
1900	2173	0.46	-0.05	0.14	0.38	2.90	8.92	9.81	11.14
2000	2273	0.51	-0.05	0.16	0.41	2.90	9.75	10.73	12.19
2100	2373	0.56	-0.06	0.17	0.45	2.90	10.63	11.70	13.29
2200	2473	0.61	-0.06	0.18	0.49	2.90	11.55	12.70	14.43
2300	2573	0.66	-0.07	0.20	0.53	3.30	12.50	13.75	15.62
2400	2673	0.72	-0.07	0.22	0.57	3.30	13.49	14.84	16.86
2500	2773	0.78	-0.08	0.23	0.62	3.30	14.52	15.97	18.15
2600	2873	0.84	-0.08	0.25	0.66	3.30	15.58	17.14	19.48
2700	2973	0.90	-0.09	0.27	0.71	3.30	16.69	18.36	20.86
2800	3073	0.97	-0.09	0.28	0.76	3.30	17.83	19.61	22.29
2900	3173	1.03	-0.10	0.30	0.81	3.30	19.01	20.91	23.76
3000	3273	1.11	-0.11	0.32	0.86	3.30	20.23	22.25	25.28

Figure 17: DynPT calibration uncertainty budget ($k = 2$): a) relative, b) absolute

Test method

Two sets of explosion tests were performed: a preliminary set of 3 tests with medium pyrotechnic charges and another set of 3 tests with large

pyrotechnic charges. In all cases the photodetector gain was set at $G = 30$ dB, as the instrument was calibrated only with this setting. Sampling rate and number of samples were set, respectively, at $f = 50$ kHz and $N = 50000$ (giving an acquisition



	5) Repeatability	6) Probe heating	7) Reconnection	8) Fit residuals	Combined ($k = 2$)		
	Repeatability	$T \leq (350 \text{ }^\circ\text{C})$	Reconnection	Fit residuals	850 nm	1050 nm	1300 nm
	8.66	7.22	0.84	6.37	26.72	26.87	27.11
	8.66	7.22	0.98	6.87	27.47	27.67	27.99
	8.66	7.22	1.13	7.37	28.30	28.55	28.96
	8.66	7.22	1.29	7.87	29.45	29.76	30.28
	8.66	7.22	1.46	8.37	30.44	30.82	31.45
	8.66	7.22	1.64	8.87	31.50	31.97	32.74
	8.66	7.22	1.83	9.37	32.65	33.21	34.13
	8.66	7.22	2.03	9.87	33.89	34.55	35.64
	8.66	7.22	2.24	10.37	35.44	36.21	37.48
	8.66	7.22	2.46	10.87	36.84	37.74	39.20
	8.66	7.22	2.69	11.37	38.33	39.36	41.04
	8.66	7.22	2.94	11.87	39.91	41.09	42.99
	8.66	7.22	3.19	12.37	41.58	42.91	45.06
	8.66	7.22	3.45	12.87	43.46	44.94	47.34
	8.66	7.22	3.73	13.37	45.30	46.96	49.63
	8.66	7.22	4.01	13.87	47.23	49.07	52.02
	8.66	7.22	4.30	14.37	49.25	51.28	54.53
	8.66	7.22	4.61	14.87	51.36	53.59	57.15
	8.66	7.22	4.92	15.37	53.56	56.00	59.88
	8.66	7.22	5.25	15.87	55.84	58.50	62.72
	8.66	7.22	5.59	16.37	58.22	61.10	65.67

Table 9: DynPT calibration uncertainty budget – all components have been converted to an equivalent normal distribution ($k = 1$), combined in quadrature, and reported with a coverage factor of $k = 2$ (i. e., ~95 % confidence)

time $t = N / f = 1$ s) for the first 4 tests and then at $f = 250$ kHz and $N = 25000$ (giving an acquisition time $t = N / f = 0.1$ s) for the last 2 tests. Sampling rate f and number of samples N were initially chosen based on experience from previous explosion tests, to collect enough data at a high speed but without having to record excessive data. N and f were changed in the last two tests, based on observations from the previous test, again to avoid recording data where no signal was present, but also to capture finer details and test the maximum sampling speed.

Test results

The preliminary set of tests with medium pyrotechnic charges, shown in Figure 18, demonstrated that $f = 50$ kHz was sufficient to

measure the rapid temperature rise and decay and identify signal structure in between. Variability in temperature evolution was observed from test to test – this was to be expected as no two charges are the same. Nevertheless, there was a good correlation among all traces for a given test, although the temperature agreement was poor – in particular, the temperature estimated from the signal at $\lambda_3 = 1300$ nm was significantly lower than the other two, by up to ~600 K. This suggested that the effective emissivity at the longest wavelength is significantly less than unity, i. e., the blackbody condition necessary for successful thermometry is not met. On the contrary, the set of tests with large pyrotechnic charges shown in Figure 19 produced more consistent results and better agreement among temperatures measured at different wavelengths, meaning that the blackbody

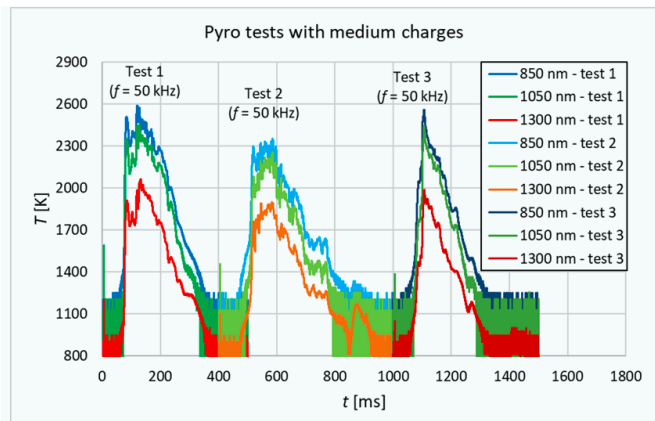


Figure 18: Time trend of temperatures for pyrotechnic tests with medium charges – temporal offset introduced for clarity

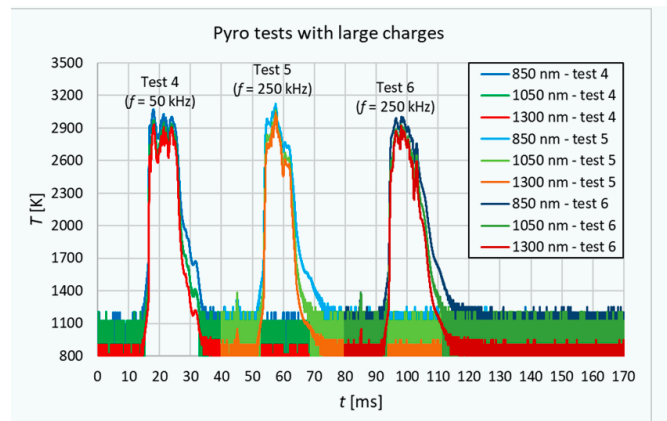


Figure 19: Time trend of temperatures for pyrotechnic tests with large charges – temporal offset introduced for clarity

condition ($\varepsilon = 1$) is more closely met than with medium charges. In explosion tests with large charges, the maximum temperatures estimated at different wavelengths agree with each other within up to ~ 137 K or ~ 4.5 %.

Figure 19 shows again that a sampling rate of $f = 50$ kHz was still fast enough to capture events from large charges, despite shorter pulse duration (< 20 ms versus ~ 200 ms), sharper rise time (< 1 ms versus ~ 10 ms) and faster decay times (~ 10 ms versus ~ 100 ms) than medium charges. The sampling rate was increased to $f = 250$ kHz in the last two trials to test the maximum sampling frequency allowed by the gain set in the photodetectors ($G = 30$ dB). A temperature rise rate of up to ~ 3.25 K/ μ s was estimated for explosions of large charges.

Figure 20 shows that large pyrotechnic charges produced not only more consistent results, but also higher peak temperatures than medium charges, by ~ 700 K. It is also worth observing that the temperature measured at $\lambda_1 = 850$ nm is always the highest, whereas the temperature measured at $\lambda_3 = 1300$ nm is always the lowest.

In any case, having calibrated our instrument with a blackbody cavity, it is possible to state that the fireball will have reached at least the highest measured temperature, regardless of the emissivity and of the blackbody assumption. In fact, if the blackbody assumption is made ($\varepsilon = 1$), but the true emissivity is $\varepsilon < 1$ and constant with wavelength (i. e., the fireball is not a blackbody, but a greybody), then the difference between the true temperature T and the measured temperature, also called color temperature, T_c , can be written as $\frac{1}{T} = \frac{1}{T_c} + \frac{A}{c_2} \ln(\varepsilon)$. From this expression, an error in emissivity of $\Delta\varepsilon$ will lead to an error in the inferred temperature $\Delta T = -\frac{\lambda T^2}{c_2} \Delta\varepsilon$, where $\Delta T = T_c - T$ and $\Delta\varepsilon = 1 - \varepsilon$.

From the expression above, it is clear that the temperature error is temperature- and wavelength-dependent and that a greybody would not provide identical temperature readings at different wavelengths (as in the blackbody case), as shown also in Figure 21, where temperature error is plotted versus wavelength at three given emissivity values (at $T = 3000$ K), and in Figure 22, where temperature error is plotted versus true temperature at the three wavelengths used for $\varepsilon = 0.8$.

It is worth observing that, for a given emissivity, the error is smaller for shorter wavelength, which agrees with the experimental findings (see Figure 20).

Conclusions

In summary, a novel ultra-high-speed combustion pyrometer, based on collection of thermal radiation via an optical fiber, has been successfully designed, developed and tested. The instrument has been traceably calibrated to the ITS-90 over the temperature range $T = (1073 - 2873)$ K with residuals < 1 %. Dynamic tests with pyrotechnic charges have demonstrated that the instrument can measure rapid (sub-ms) events, due to its high sampling rate (up to 250 kHz): a temperature rise rate of up to ~ 3.25 K/ μ s has been estimated for explosions of large pyrotechnic charges. The accuracy of the temperature measurements can be assessed by considering the extent of agreement between readings at the three wavelengths, a self-diagnostic feature that is a critical strength of the technique. However, even when agreement between temperatures is poor, we can say, with a high level of confidence, that the fireball temperature is at least that reported by the reading at 850 nm. In future the instrument will be tested in a maritime test engine.

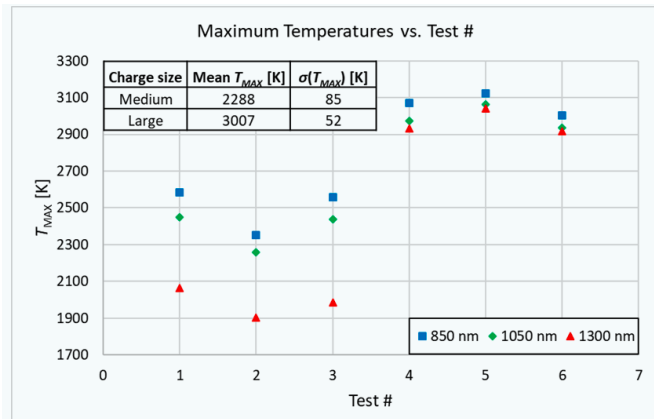


Figure 20: Plot of maximum temperatures versus test number. The inset on the upper left shows some statistics: Mean T_{MAX} and $\sigma(T_{MAX})$ are respectively the mean and the standard deviation of peak temperatures measured at different λ

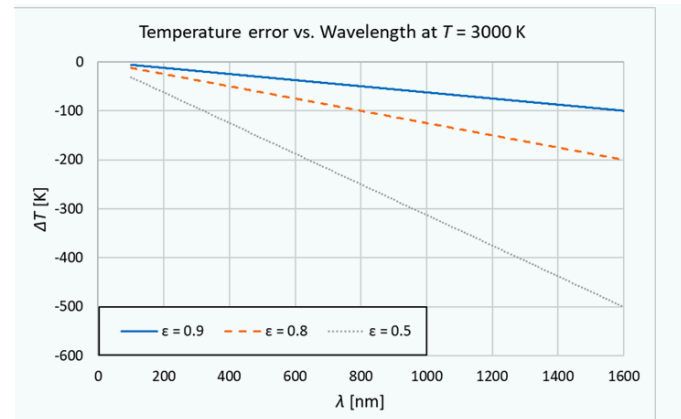


Figure 21: Plot of temperature error versus wavelength at $T = 3000$ K for different values of emissivity

2.5 Engine tests

Introduction

Following development and testing of the NPL dynamic combustion pyrometer system, field trials were carried out at Wärtsilä on the newly commissioned combustion spray chamber facility. The instrument (schematic shown in Figure 23) measures thermal radiance at three separate wavelengths - 850 nm, 1050 nm and 1300 nm. By prior calibration against a traceable (to ITS-90) blackbody cavity, the measured detector signals can be converted into temperatures. Since luminous combustion events are both turbulent and semi-transparent (at times), the assumption that they are similar to that of a blackbody may not be a valid one. By measuring at three independent wavelengths, the assumptions can be tested, i. e., the level of agreement between the three temperature measurements gives a good indication of the validity of the assumption and the level of uncertainty.

Prior to trials, the system was calibrated at NPL in terms of ITS-90 from 1000 °C to 3000 °C, measuring through a spare window taken from the test chamber. This allowed transmission losses through the test chamber window to be accounted for during the calibration process.

Test Chamber

Wärtsilä provided information on the x-profile mounting options, and NPL shipped the thermometer, alignment hardware, PC with control software and mounting hardware. The chamber is shown in Figure 24. The measurement head was clamped to the framework so that it could be directed at the region of interest inside

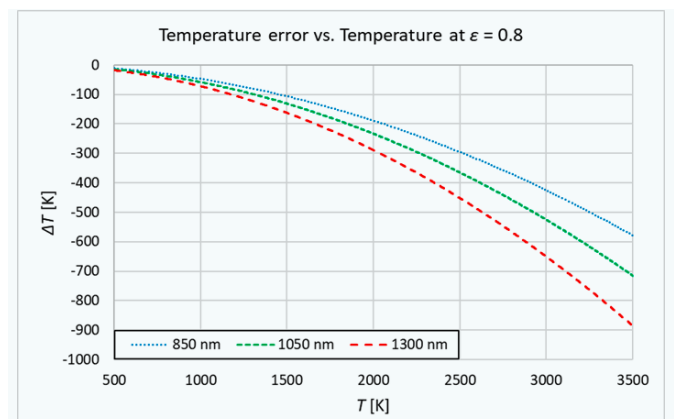


Figure 22: Plot of temperature error versus temperature for $\epsilon = 0.8$ and for the three chosen wavelengths

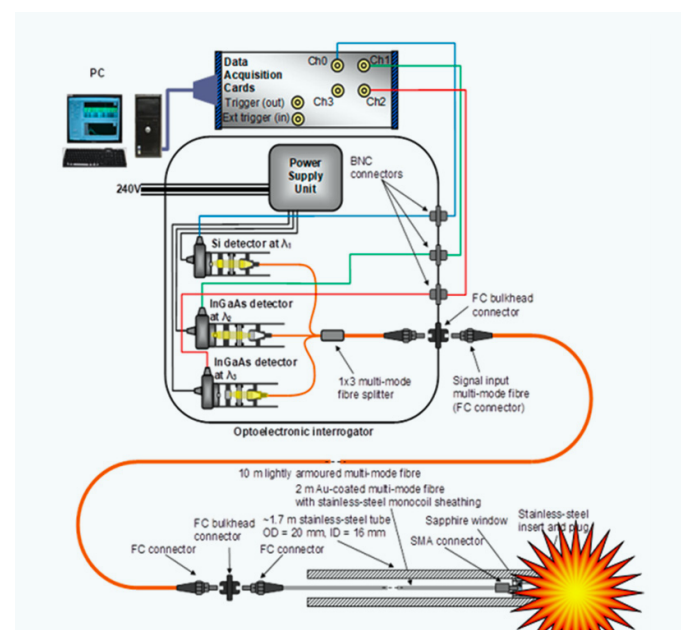
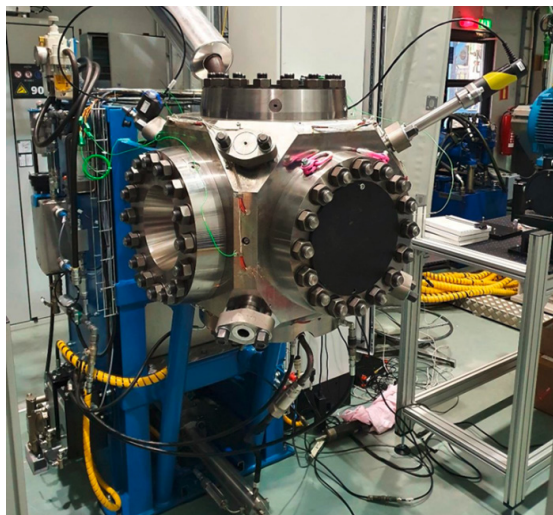


Figure 23: The NPL Dynamic combustion pyrometer

Figure 24:
Wärtsilä
combustion spray
chamber



the chamber, viewing through the window. Initially a pilot light was connected to the measurement fiber system to allow for accurate alignment with the region of interest. This was removed and the fiber reconnected to the instrument before measurements were started.

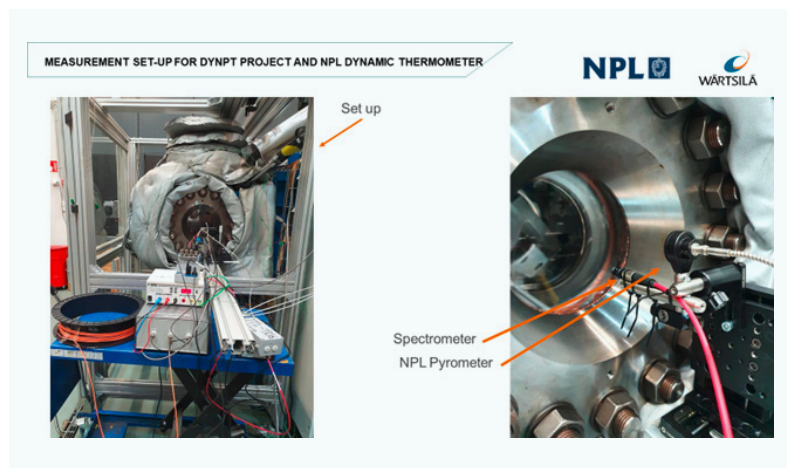
The measurement arrangement is shown in Figure 25 with the optical interrogator and fiber spool on the left and the mounted measurement head next to a spectrometer input on the right. A second instrument, a spectrometer, can also be seen in the figure but was not part of the NPL measurement campaign.

The actual measured region is shown in Figure 26. Notice that the field of view (FOV) is through the chamber so the only signal detected will be light emitted from the burning fuel, an example of which is shown in Figure 27.

Data analysis

Initially data was logged at 250 kHz. This was later reduced to 100 kHz to reduce the data set size. Data recording is started manually before an event is triggered and stopped afterward. The trigger signal is used to identify the time base. It lasts 0.1 ms and this is taken to be the uncertainty in

Figure 25:
DynPT thermometry
hardware mounted
to the test chamber



the timing. Data is stored as a LabVIEW tdms file. Only files with a significant (~ 2000 K) temperature were assessed. Each such file had the temperature recorded by the three independent channels plotted from the trigger set at $t = 0$ and the peak temperature noted.

Results

Measurements were made on four different days 7th, 19th, 20th, 21st October 2021. All figures that follow have titles that identify the date and time of each test in the format *Data_2021_MM_DD_HH_MM_SS*.

Each plot shows the temperature measured at the three wavelengths. From the geometry (straight through viewing) it is unlikely there is any significant reflected component. In other words, the only thing the system “sees” is the combustion event. For an ideal blackbody (which in this case would correspond to the combustion being optically thick) the three measurements would be the same and at the true temperature (although this would only be true if the temperature was uniform throughout the penetration depth of all three wavelengths). In the plots below we see agreement as good as 50 K at over 2000 K, which we consider to be a successful result for this type of test.

Note that as we seem to have a largely opaque fireball the temperatures found are lower limits. We would expect the shortest wavelength result (850 nm) to be nearest the true temperature, and this is consistently found to be the highest temperature.

Tests of 7th Oct 2021

The tests performed on the 7th of October were all done with a single test point. The test point was chosen according to an operating point relevant for a diesel engine in practice, here a W31 engine running on a 59 % load case with light fuel oil. The operating conditions in the optical spray combustion are generated by a pre-combustion event of a lean gas mixture with hydrogen as fuel gas. As the gas residues after the pre-burn event are cooling down, diesel fuel is injected at a pre-defined pressure level, and diesel combustion similar to that in an engine cylinder takes place. In present tests, the pressure level at start of injection was chosen to be 88 bar. Recording is started after filling the gas inside the chamber for pre-combustion. The operator of the chamber then starts the combustion sequence with a signal that begins the Start of Injection (SOI). At this moment a signal is also sent to the NPL DAQ equipment that represents the triggering of the combustion. This trigger signal is shown on the figures. As

the recording and combustion sequence are done manually, unnecessary data is recorded as a precaution.

The results shown in Figure 28 indicate that the peak temperature is around 2100 K and is consistently found at 9 ms after start of injection, at the indicated measurement point seen in Figure 27. In general, the shape of the temperature curve is slightly varying from test to test as there are flame to flame variations. From Figure 28 it can also be noticed that there is a consistent 5 ms delay between start of injection and detection of a luminous sooty flame. Additionally, the total duration of the combustion is roughly 10 ms and is characterized by a rapid temperature increase in the beginning of the measurements and a slower decline from the peak values as the injected fuel is consumed. The slow decline is due to the mushroom cloud shape that is caused by the impingement of the flame onto the plate. The head of the mushroom cloud stays close to the plate and slowly diminishes, starting from the inner circle, until it reaches the full radius of the flame. An example of the mushroom cloud is seen in Figure 27.

Tests of 19th Oct 2021

From the 19th October onwards the measurement point was changed to be closer to the nozzle. The new measurement point is shown in Figure 29. This was done by realigning the pyrometer with the pilot light. The measurement point was changed to see how the temperature line would change if the point is not in the mushroom cloud. The distance from the plate was approximately 4 cm. The previously used plate was changed to an instrumented plate with the same alignment as in the first measurement campaign. Recording was done similarly as in previous tests. When starting the measurement campaign, offset from noise was removed with the cover on the pyrometer. The gas mixture and fuel used in the test on 19th and 20th October were the same as on the 7th. The windows of the chamber were cleaned before the tests but over time due to soot the visibility became worse. However, as seen in measurements done during the measurement campaign it had no visible issue for the signal received by the pyrometer when comparing result done on the same day.

Figure 30 and Figure 31 show that changing the measurement point closer to the nozzle has made the recorded event shorter. As the injected fuel ends, so does the measured luminosity from the soot. Thus, the recorded flame from most of the spray length ends soon after the injected fuel ends. However, some flames that have spread around the plate can form high dimension clouds that can be measured by the pyrometer if measuring

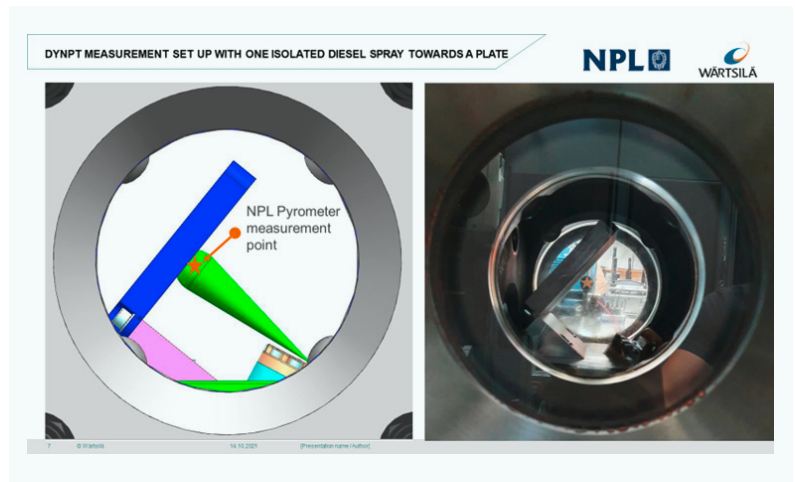


Figure 26:
Fuel spray
measurement
geometry

too close to the plate. The graphs in Figure 30 and Figure 31 show that the flame temperature had a more rapid increase of the peak temperature when compared to tests done on 7th October. In addition, the flame temperature starts to decline slowly after reaching the peak temperature. In Figure 31 the graph *Data_2021_10_20_13_46_18* shows a second combustion that is caused by the residue fuel that is stuck in the thimble, causing an afterburn inside the chamber. This has happened during other measurements before. Data *2021_19_15_03_06* on Figure 30 shows two peaks during the temperature line. This second peak at 9 ms shows when a large mushroom cloud flame has formed that causes the flame to reappear in the pyrometer field of view. A similar event is shown in *Data_2021_10_20_14_16_51* of Figure 31.

Tests of 20th Oct 2021

See Figure 31.

Tests of 21st Oct 2021

The last set of measurements were performed at the same position as shown by Figure 29.



Figure 27:
Mid combustion
test with the
measurement FOV
indicated by a star

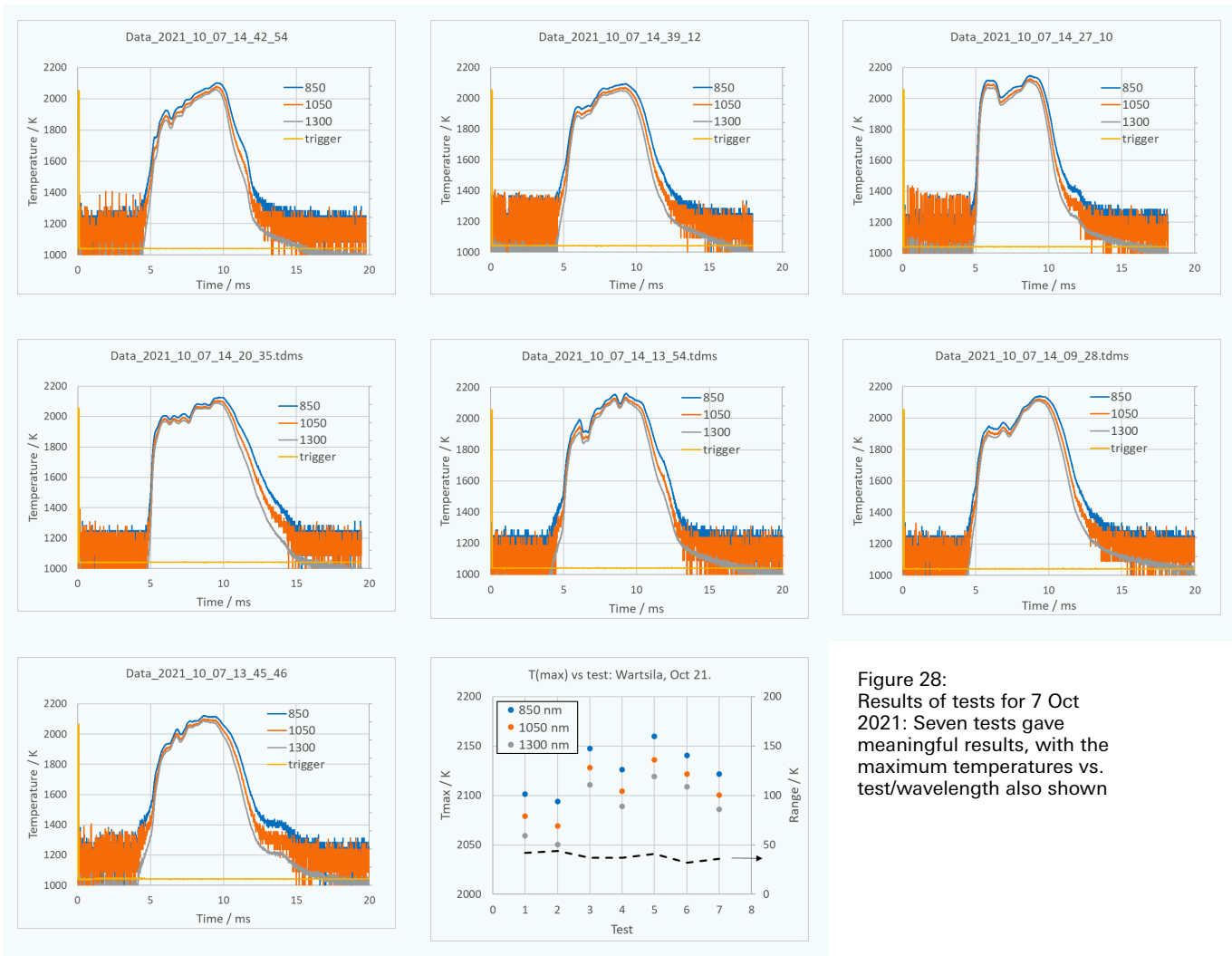
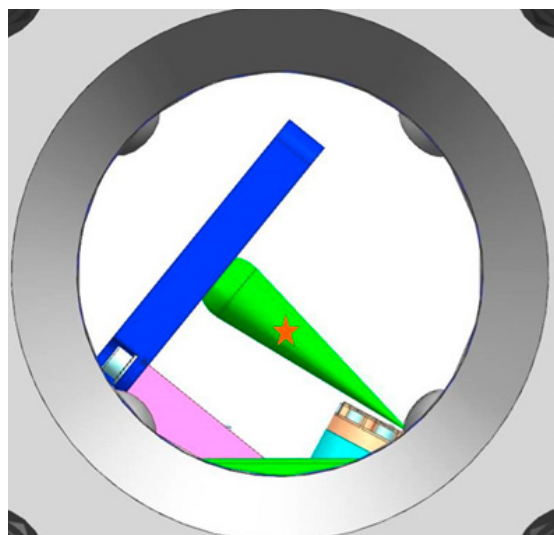


Figure 28: Results of tests for 7 Oct 2021: Seven tests gave meaningful results, with the maximum temperatures vs. test/wavelength also shown

Furthermore, the corresponding engine condition was also kept the same as earlier tests. Instead of using light fuel oil, these tests were performed with n-heptane. By evaluating Figure 33 and Figure 34, they appear to be quite similar to the ones where light fuel oil was used. Also, in these results several secondary temperature peaks were measured. The flame bounces back, creating the

secondary peak at 9 ms after start of injection. This has been highlighted in Figure 32 where the 11th and 14th combustion measurements from 21st of October are compared at 9 ms after start of injection. The flame sequence is almost over in the 14th measurement when the 11th test reaches its secondary peak.

Figure 29: Updated measurement point 19th October



Conclusions

In general, the conclusions from the pyrometer tests yield an understanding of the maximum temperature of a reacting diesel flame and the duration of the combustion. Additionally, the results indicated that n-heptane can be used as a surrogate of light fuel oil, as the temperature and profile remained unchanged while the windows on the chamber were not fouling as quickly as in those cases where light fuel oil was used. During the measurement campaign no issues occurred with the pyrometer from the sooty windows. Although windows were cleaned only between some of the measurement days, the pyrometer was able to record over 15 combustions in a row without any issue.

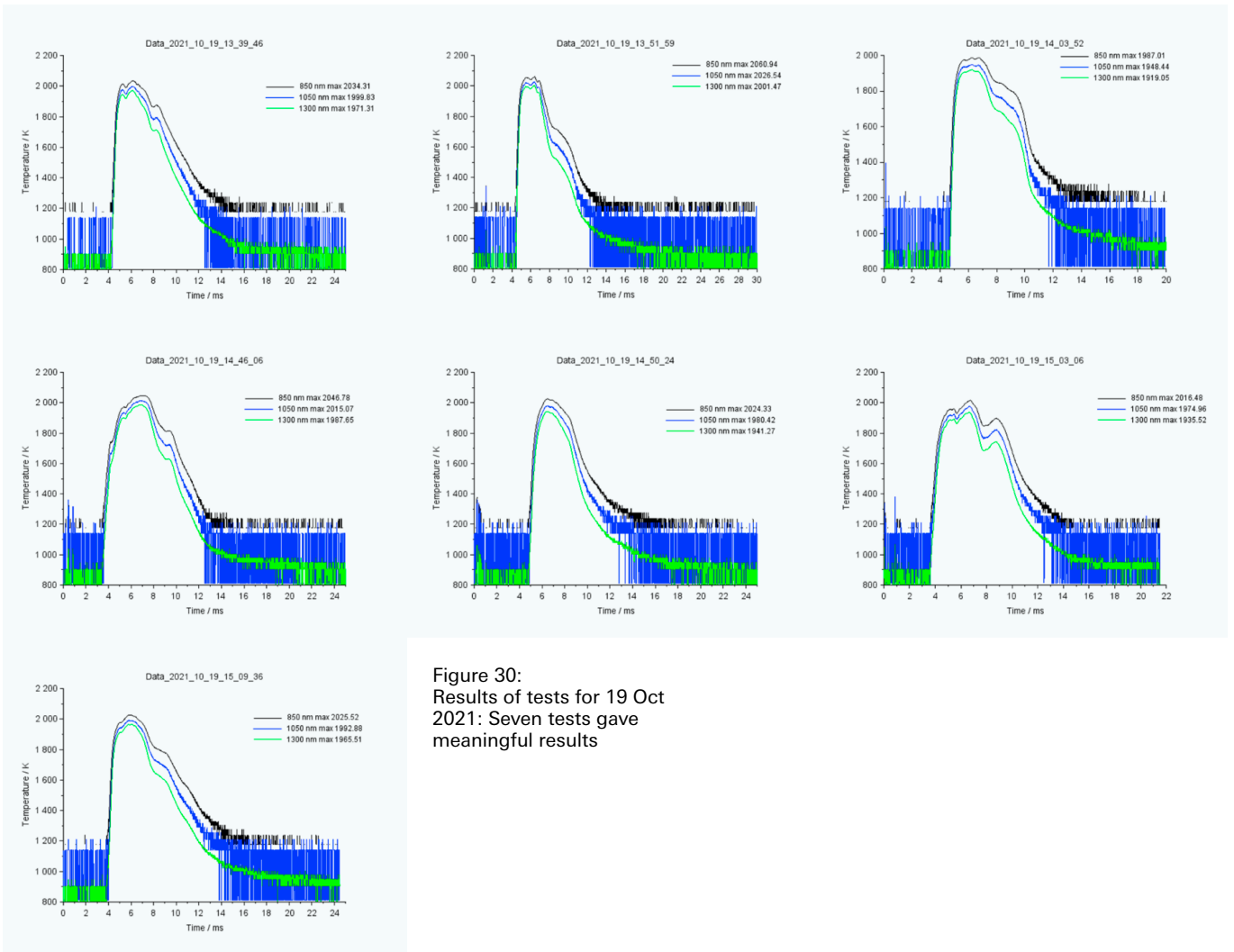


Figure 30:
Results of tests for 19 Oct
2021: Seven tests gave
meaningful results

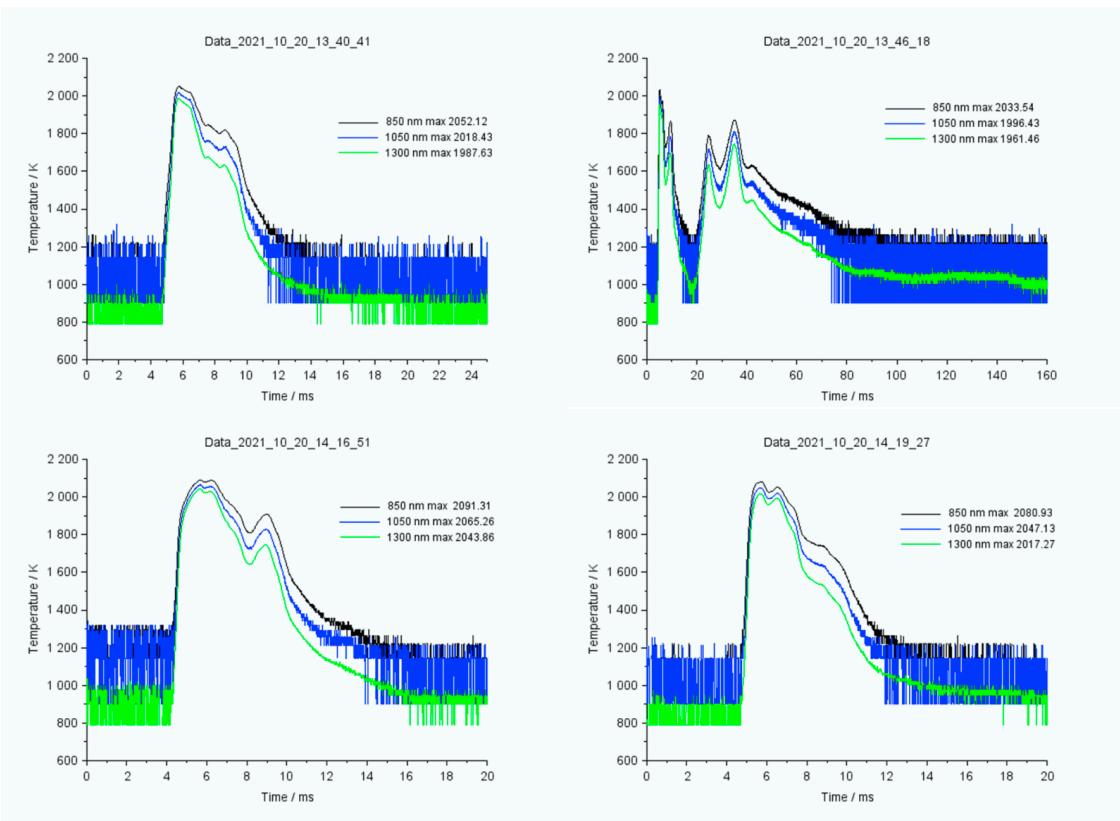
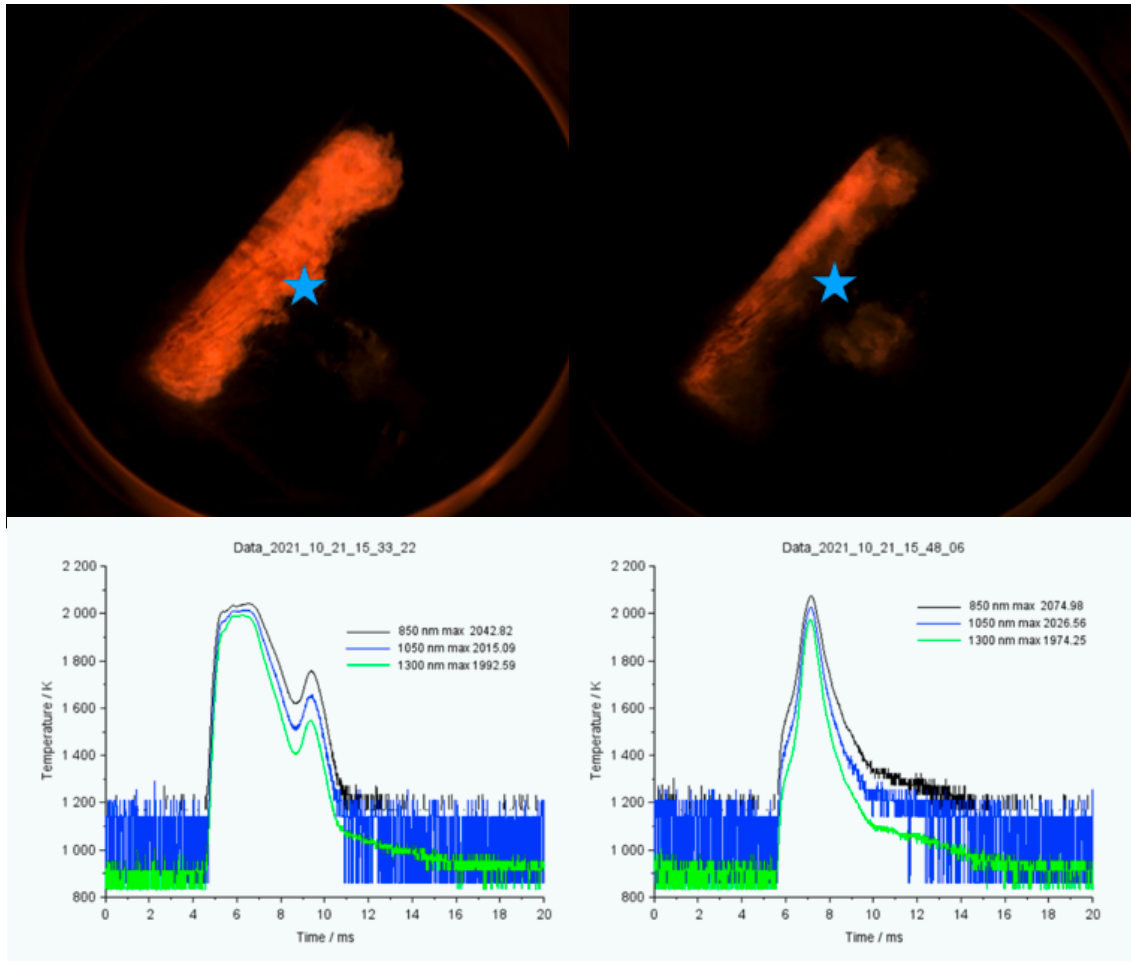


Figure 31:
Results of tests for 20 Oct 2021:
Four tests gave
meaningful results

Figure 32:
Comparison of
measurements 11
and 14 at 9 ms after
start of injection



These tests were done on a measurement where a reacting fuel spray is directed perpendicularly towards a plate, resulting in a flame bouncing backwards into the field of view, when the measurement point was moved closer to the fuel injector. These flames that reappear are mainly shown to be appearing in the outer rings of the mushroom cloud flame that forms around the plate. That is why the time duration of the flame peak is related to the closeness of the plate when measuring with pyrometer on this angle compared to the plate and flame.

References

- [1] G. P. Merker, C. Schwarz and R. Teichmann, *Combustion engines development: mixture formation, combustion, emissions and simulation*, Springer Science & Business Media, 2011.
- [2] S. Saxholm, R. Högström, C. Sarraf, G. Sutton, R. Wynands, F. Arrhén, G. Jönsson, Y. Durgut, A. Peruzzi, A. Fateev, M. Liverts, C. Adolfse and A. Öster, “Development of measurement and calibration techniques for dynamic pressures and temperatures (DynPT): background and objectives of the 17IND07 DynPT project in the European Metrology Programme for Innovation and Research (EMPIR),” *Journal of Physics: Conference Series. IOP Publishing.*, pp. Vol. 1065, No. 16, p. 162015, 2018.
- [3] H. Preston-Thomas, “The International Temperature Scale of 1990 (ITS-90),” *Metrologia*, pp. 27(1), 3–10, 1990.
- [4] P. Saunders and D. R. White, “Physical basis of interpolation equations for radiation thermometry,” *Metrologia*, pp. 40(4), 195, 2003.
- [5] “Safety Datasheet of LeMaitre Ltd. Theatrical flashes,” 22.11.2020. [Online]. Available: <https://www.lemaitreltd.com/products/pyrotechnics/pyroflash/theatrical-flashes-stars/theatrical-flashes/sds-flashes-robotics-spds/>.

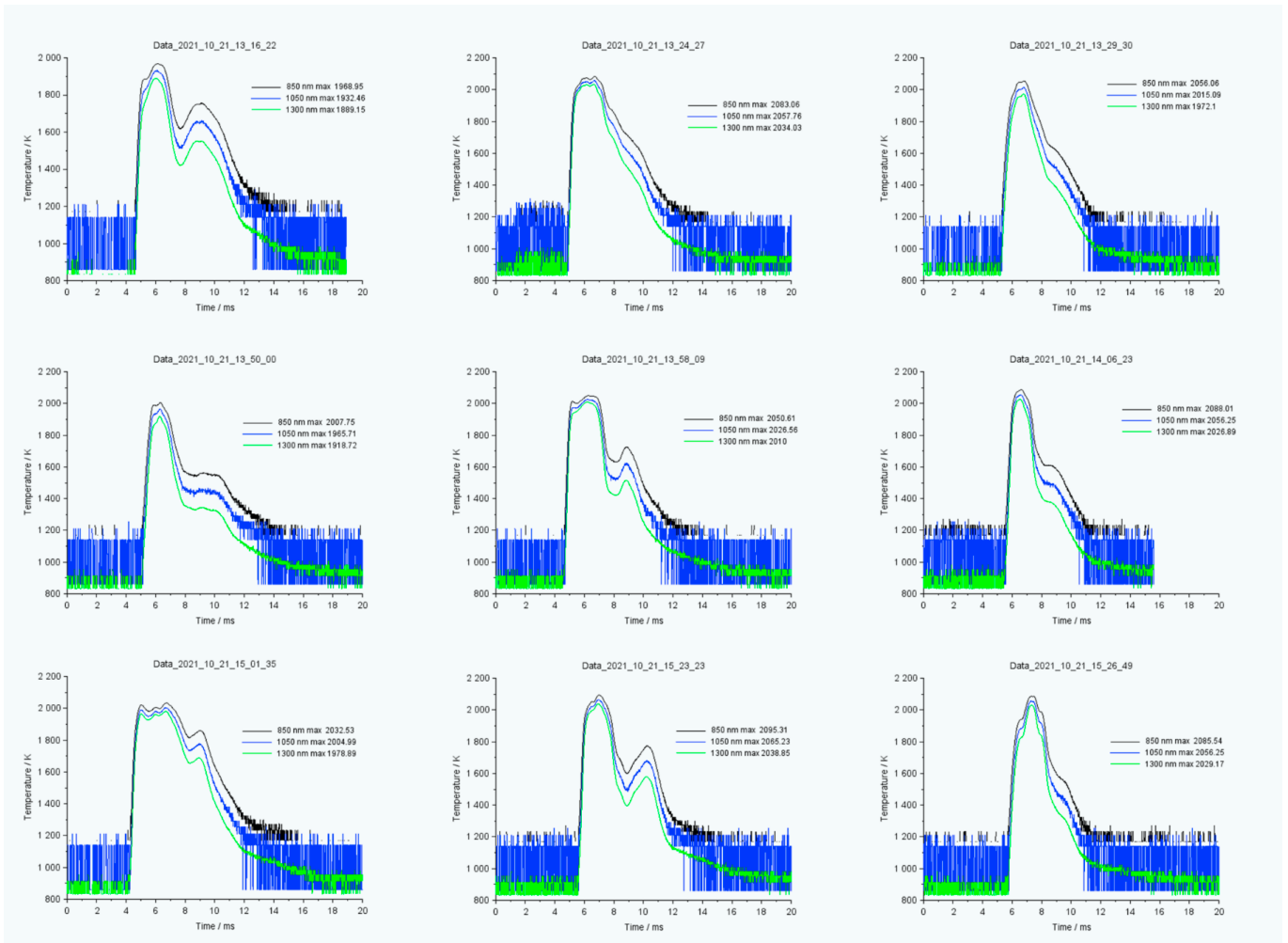


Figure 33: Results of tests for 21 Oct 2021: First 9 tests of 15 shown

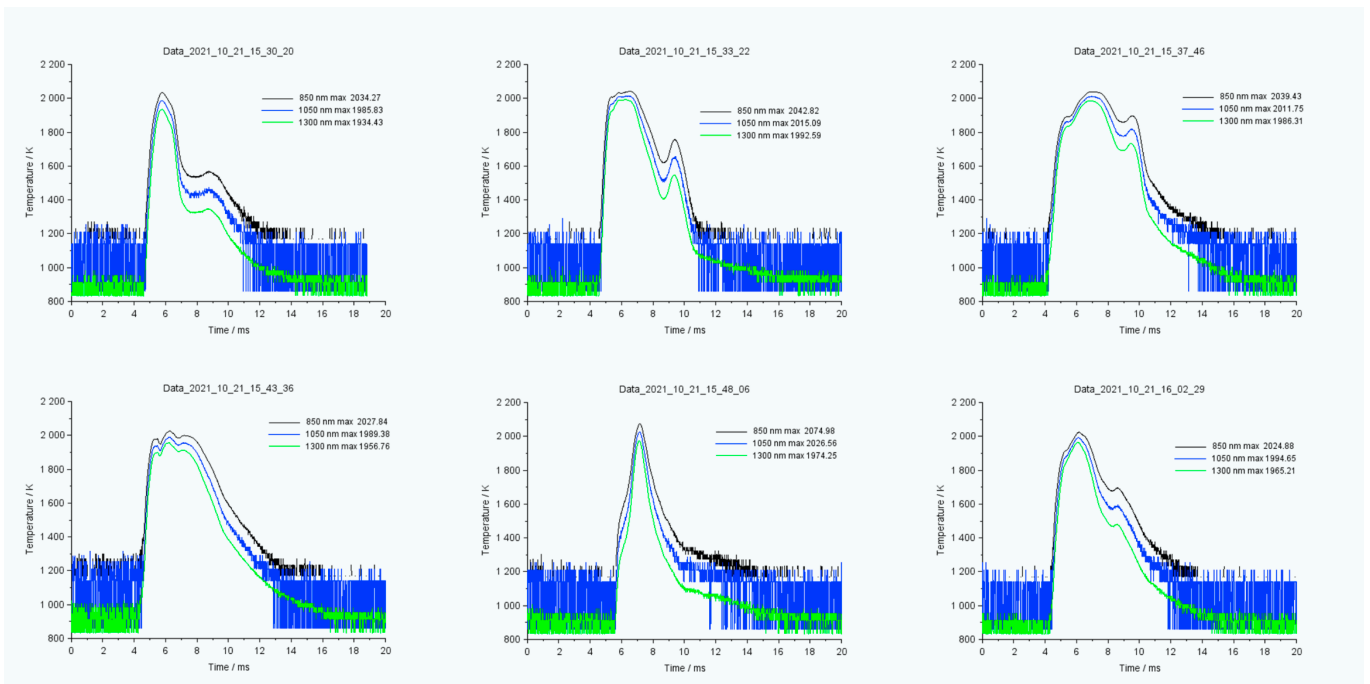


Figure 34: Results of tests for 21 Oct 2021: Last 6 tests of 15 shown

Validation of a prototype commercial dynamic pressure sensor

E. Amer¹, G. Jönsson²

¹ Eynas Amer (RISE),
E-mail: Eynas.amer@ri.se

² Dr. Gustav Jönsson (RISE),
E-mail: gustav.jonsson@ri.se

1. Introduction

This article is an abridged version of chapter 4 of deliverable D5 in the EMPIR project 17IND07 – DynPT: “Validation report on the performance of the newly developed dynamic pressure and temperature sensors covering the range up to 30 MPa with a target uncertainty of 2 % and up to 3000 °C, with a target uncertainty of 5 %, respectively”. This project has received funding from the EMPIR programme co-financed by the Participating States and from the European Union’s Horizon 2020 research and innovation programme. The full report has been prepared by VSL B.V. (VSL) together with project partners from Danmarks Tekniske Universitet (DTU), Minerva meettechniek B.V. (Minerva), National Physical Laboratory (NPL), RISE Research Institutes of Sweden AB (RISE) and Teknologian tutkimuskeskus VTT Oy (VTT).

2. The prototype commercial dynamic pressure sensor

2.1 Introduction

Two prototype pressure sensors ID:10 and ID:13 were calibrated statically and characterized dynamically. The static calibration of the two sensors was done using a pressure balance in the pressure range from 0 bar to 350 bar. The dynamic response of the two sensors was measured using the shock tube existing at the Swedish National Laboratory for pressure. The amplitude part of the transfer function of the two sensors was calculated at four different nominal pressure steps 15 bar, 52 bar, 123 bar, and 257 bar. The dynamic characterization was done using two setups. For the pressure of 15 bar a straight shock tube was used. For pressure levels above 15 bar the

shock tube was equipped with an amplification device. The vibration signal was recorded using an accelerometer at the back plate of the shock tube/amplification device. One observes that the vibration is less pronounced when using the amplification device. The uncertainty budget was calculated for the case of using the shock tube, while the evaluation of measurement uncertainty when using the amplification device is under development.

2.2 Static calibration

The static calibration of the two sensors was done using a pressure balance Desgranges & Huot 5203 s/n 4081 with piston/cylinder 4633 in the pressure range from 0 bar to 350 bar gauge pressure.

Static calibration of sensor 10

The corrected sensor reading relates to the indicated signal via the following equation:

$$p_{\text{meas}} = (I_{\text{ind}} - 4) \cdot 21.875 + p_{\text{corr}} \quad (1)$$

Here p_{meas} is the corrected measured pressure, I_{ind} is the indicated current, and p_{corr} is the correction term.

Table 1:
Calibration in the range from 0 bar to 350 bar, sensor 10

Pressure level	Indicated value	Correction term	Expanded uncertainty
(bar)	(mA)	(bar)	(± bar)
0	4.06744	-1.475	0.134
75	7.50473	-1.666	0.481
150	10.94058	-1.825	0.526
225	14.37116	-1.869	0.445
350	20.08507	-1.861	0.081

Pressure level	Indicated value	Correction term	Expanded uncertainty
(bar)	(mA)	(bar)	(± bar)
0	4.05819	-1.273	0.035
75	7.48967	-1.336	0.086
150	10.91471	-1.259	0.063
225	14.33442	-1.065	0.050
350	20.02664	-0.583	0.068

Table 2: Calibration in the range from 0 bar to 350 bar, sensor 13

Static calibration of sensor 13

The corrected sensor reading relates to the indicated signal via the following equation:

$$p_{\text{meas}} = (I_{\text{ind}} - 4) * 21.875 + p_{\text{corr}} \tag{2}$$

2.3 Dynamic characterization

The dynamic characterization of the two sensors was measured using the shock tube existing at the Swedish National Laboratory for pressure.

Dynamic pressure realization procedure

Figure 1 shows a schematic illustration of the shock tube used to realize dynamic pressure steps. The shock tube is cylindrical, has an inner diameter of 100 mm and driver and driven sections with nominal lengths of 3 m and 7 m, respectively. The two sections are separated by a fast-opening valve to generate the shocks. The

driven section is equipped with six piezoelectric (PE) pressure sensors (113A21, PCB) mounted at well-defined positions on the circumference along a straight line parallel to the central axis of the shock tube. These sensors allow both monitoring of shock formation and measurement of shock propagation velocity.

Static absolute pressure transmitters were mounted on the driver section (EJX 310A, Yokogawa) and the driven section (EJX 510A, Yokogawa) to monitor the initial pressures of these volumes. The transmitter on the driven section is regularly calibrated. The driver and driven sections can be filled, vented, and evacuated independently. Ar (99.999%, Air Liquide) was used in both volumes for the pressure step of 52 bar. For pressure steps of 15 bar, 123 bar and 257 bar, Ar was used in the driven section and He (99.999%, Air Liquide) in the driver. To ensure pure and well-known gas composition in driver and driven sections, the system is equipped with a dry roots vacuum pump (NeoDry 15E, Kashiwama) to evacuate the volumes before filling with appropriate gases.

For realizing pressure steps with amplitude larger than 15 bar, an amplification device that smoothly transforms the incident plane shock wave into a spherical shock wave was used. That in turn converges, accelerates, and amplifies the shock wave. A schematic illustration of the shock tube equipped with the amplification device is shown in Figure 2.

The output signals were digitized using an 8 channel 12 bit 60 MS/s per channel oscilloscope (PXI-5105, NI). In this work, the data acquisition was done using LabVIEW with a sampling rate

Figure 1: Schematic illustration of the shock tube; FOV: fast-opening valve, DUT: device under test

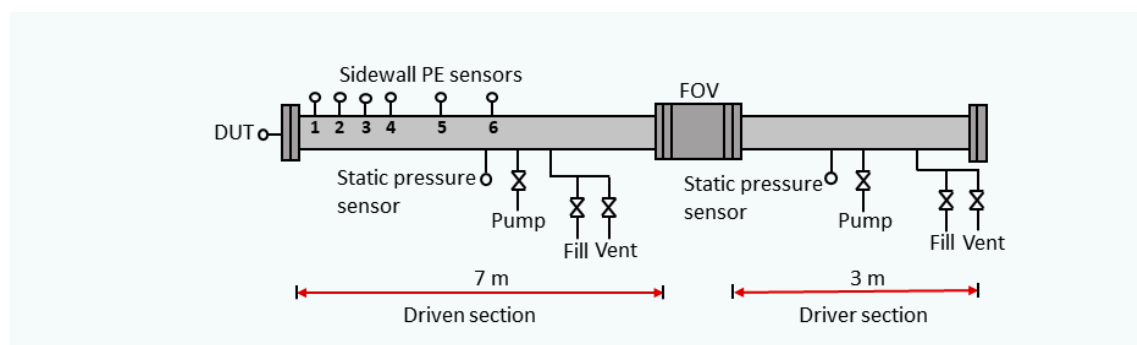
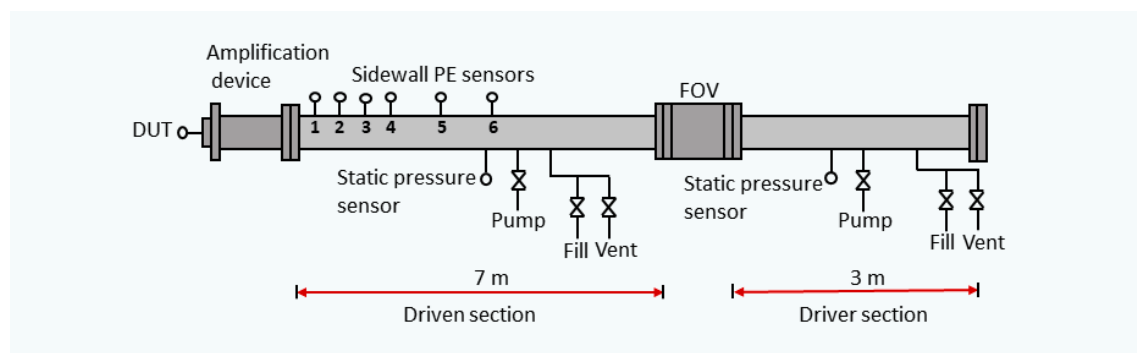


Figure 2: Schematic illustration of the shock tube equipped with the amplification device



of 3 MS/s and a sample size of 10^5 samples. The device under test (DUT) was flush mounted at the center of the backplate of the shock tube/the amplification device. The shock tube is positioned in a temperature-controlled laboratory with an initial gas temperature of $(20.5 \pm 0.7) ^\circ\text{C}$.

The amplitude of the shock wave generated using the shock tube without the amplification device was calculated using a 1-D model. The amplitude when using the amplification device was calculated using a numerical method taking the shock amplitude from the 1-D model and the geometry of the amplification device as inputs.

Typical pressure steps realized by the shock tube and by the shock tube equipped with the amplification device recorded by the prototype sensor are shown in Figure 3 and Figure 4, respectively. A calibrated load shunt of 40Ω was used to convert the output signal from current to voltage.

To calculate the transfer function of the DUT, the Fast Fourier Transform (FFT) was used. For applying FFT, a Gaussian window centered at the indicated pressure rise with a FWHM of 0.5 ms was used to apodize both ends of the signal to zero.

The acoustic vibration that arises from the shock generation was measured at the position of the DUT (the back plate of the shock tube/the amplification device). An accelerometer Brüel & Kjær 4397 was used to measure the signal in the time domain. A Gaussian window centered at the indicated signal rise with a FWHM of 7.5 ms and a Fast Fourier Transform (FFT) were used to obtain the frequency components.

Results

The results from the dynamic characterization of both sensors as well as vibration measurements will be presented in the following.

Dynamic characterization of sensor 10

Figure 5 to Figure 8 show the average sensitivity calculated from three records at nominal pressure steps of 15 bar, 52 bar, 123 bar, and 257 bar, respectively. For a pressure step of 15 bar a straight shock tube was used, while for pressure levels above 15 bar the shock tube was equipped with an amplification device. In addition, Figure 5 shows the expanded uncertainty of the sensitivity, while Figure 6 to Figure 8 show the repeatability. A comparison of the sensitivity calculated from dynamic characterization at 0 Hz and that calculated from static calibration is presented in Figure 9.

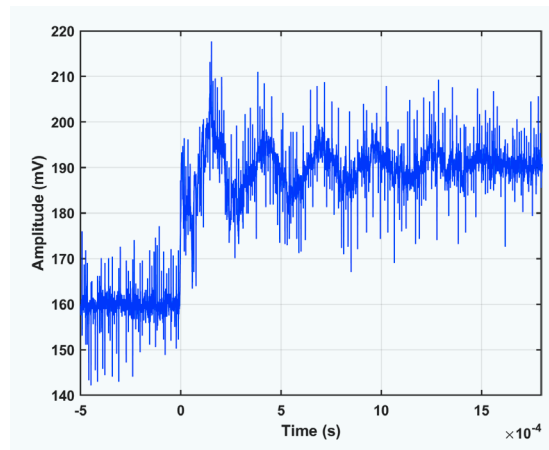


Figure 3: A typical pressure step realized by the shock tube recorded by the prototype sensor; nominal pressure step is 15 bar

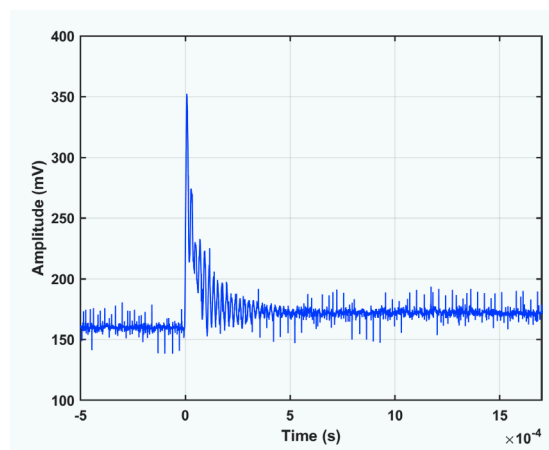


Figure 4: A typical pressure step realized by the shock tube equipped with the amplification device recorded by the prototype sensor; nominal shock amplitude is 123 bar

Dynamic characterization of sensor 13

Figure 10 to Figure 13 show the average sensitivity calculated from three records at nominal pressure steps of 15 bar, 52 bar, 123 bar, and 257 bar, respectively. The setup is the same as before. In addition, Figure 10 shows the expanded uncertainty of the sensitivity while Figure 11 to Figure 13 show the repeatability. A comparison of the sensitivity calculated from dynamic characterization at 0 Hz and that calculated from static calibration is presented in Figure 14.

Vibration measurements

The vibration signal at the back plate of the shock tube and the amplification device are shown in Figure 15 and Figure 16, respectively.

Discussion

In case of using the shock tube to realize the dynamic pressure (15 bar), the expanded uncertainty was calculated and shown in Figure 5 and Figure 10 for both sensors, respectively. A detailed description of the uncertainty calculation is presented in the next section. We believe the

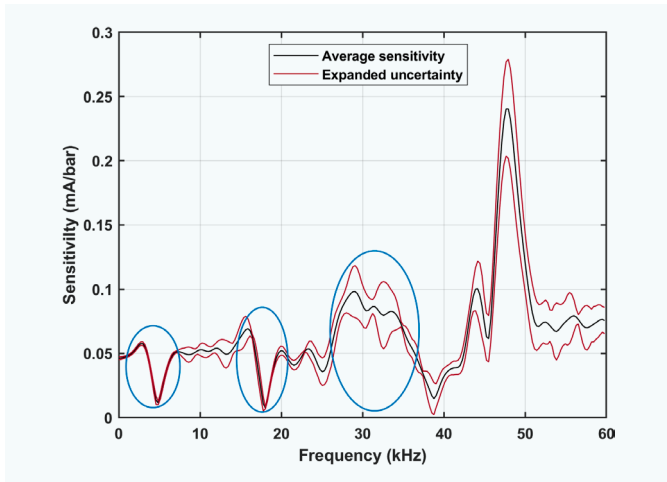


Figure 5:
The transfer function for a pressure step of 15 bar.
Artefacts from sensor vibration are indicated by blue ellipses

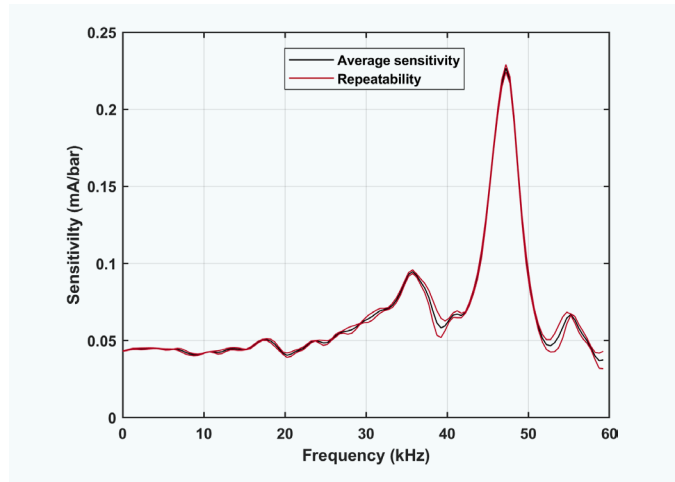


Figure 6:
The transfer function at a shock amplitude of 52 bar

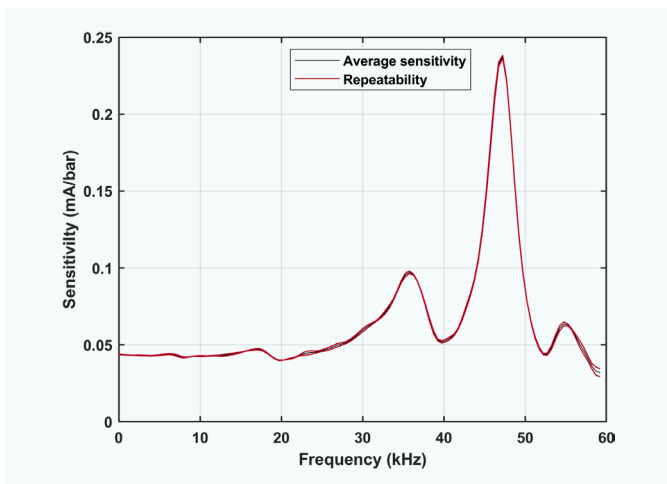


Figure 7:
The transfer function at a shock amplitude of 123 bar

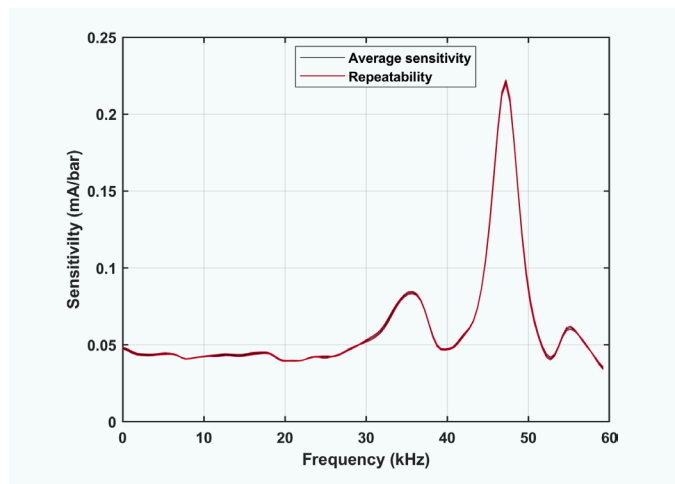


Figure 8:
The transfer function at a shock amplitude of 257 bar

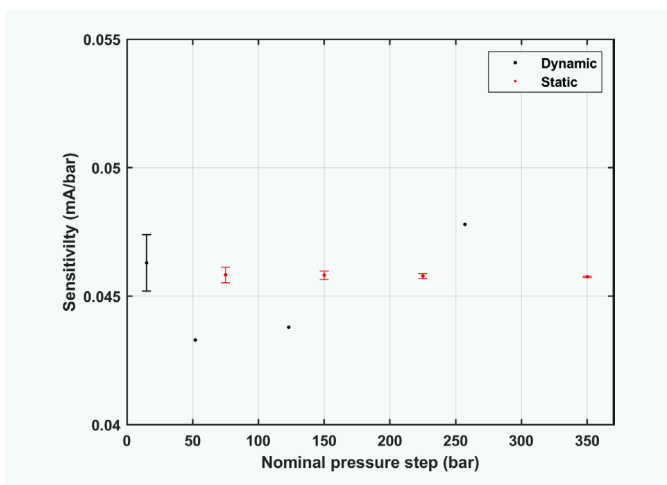


Figure 9:
A comparison of the sensitivity calculated from dynamic characterization at 0 Hz and that calculated from static calibration. The error bars represent the expanded uncertainty. No uncertainty is presented for dynamic sensitivities except for the lowest nominal pressure (15 bar)

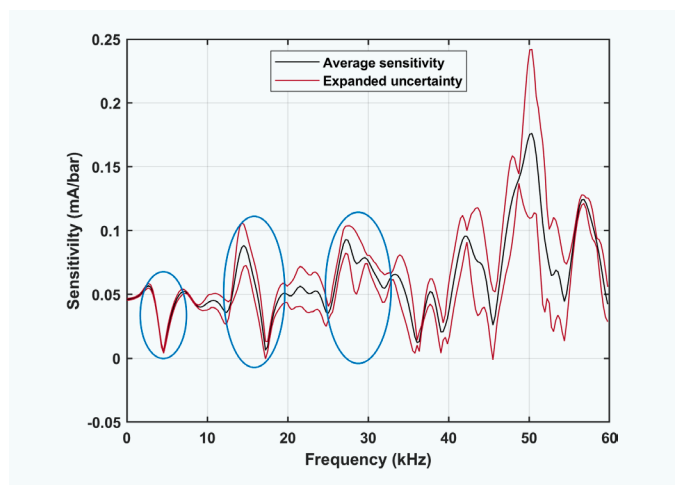


Figure 10:
The transfer function for a pressure step of 15 bar.
Artefacts from sensor vibration are indicated by blue ellipses

marked features in Figure 5 and Figure 10 are due to interference of the pressure signal with the vibration signal. Figure 15 shows that there are vibration peaks at the frequencies where these features appear.

In case of using the shock tube equipped with the amplification device to realize the dynamic pressure (above 15 bar), only the repeatability is shown in Figure 6 to Figure 8 and Figure 11 to Figure 13 for both sensors, respectively. The uncertainty budget for the amplification device is under development. The vibration signal is less pronounced. It can be also seen in Figure 16 that the vibration signal is not pronounced at the back plate of the amplification device.

The sensor 10 exhibits a relatively flat response up to 25 kHz and the resonance is clearly seen at 47 kHz, while the resonance of sensor 13 does not show the same behavior. The repeatability is higher for sensor 10 compared to 13 specifically at higher pressure levels at 0 Hz.

Figure 9 and Figure 14 show that the sensitivity of both sensors is about 0.0457 mA/bar. A good correspondence between the sensitivity at 0 Hz from dynamic characterization and that calculated from static calibration for both sensors can be seen in the figures.

The uncertainty budget

The uncertainty budget when realizing the dynamic pressure using the shock tube without amplification device (15 bar) calculated from three repetitions is presented in Table 3. The uncertainty in the reflected shock wave amplitude (p_s) was calculated from the uncertainties in the following parameters; temperature, time, sensors' positions, specific heat ratio and initial driven pressure (p_1). Monte Carlo integration with 10^6 iterations was used to calculate the uncertainty. The uncertainties in the respective input parameter were estimated as following:

- The uncertainty in temperature was estimated to be ± 0.7 K including uncertainty from calibration and temperature gradients.

Parameter	Absolute uncertainty, $k = 1$	Distribution
Temperature (K)	0.7	Rectangular
Time (s)	$5 \cdot 10^{-7}$	Normal
Sensors positions (m)	$1 \cdot 10^{-4}$	Normal
Specific heat ratio γ	0	Normal
Initial driven pressure p_1 (Pa)	361	Normal

- The uncertainty in time comprises the time resolution of the measurements (sampling rate of 3 MHz) and the deviation between the recorded and the fitted arrival time of the shock front to the sensors used to calculate the shock wave speed. The shock wave speed was calculated using sensor 1, 2 and 3 shown in Figure 1 using the time-of-flight method. Uncertainty in the time base is neglected.
- The sensor positions were calibrated and the uncertainty in those measurements was used.
- The uncertainty in specific heat ratio γ was taken to be zero, since for Ar gas γ changes by $25 \cdot 10^{-9}$ as the temperature changes from 21 °C to 600 °C, which can be neglected.
- The uncertainty in p_1 was calculated considering the following parameters: temperature effect, drift effect, the uncertainty in the calibration of the pressure transmitter at different pressure levels, and the uncertainty in calibrating the signal converter.

The uncertainty in the pressure step ($\Delta p = p_s - p_1$) was calculated as $u_{\Delta p} = \sqrt{u_{p_1}^2 + u_{p_s}^2}$.

The standard uncertainty, $k = 1$, in the sensor sensitivity was calculated as:

$$u_S = \sqrt{u_{S_{ap}}^2 + u_{S_{repeatability}}^2} \tag{3}$$

The expanded uncertainty is twice the standard uncertainty.

Table 3: Uncertainty budget for a nominal pressure step of 15 bar

Engine setting	Proportionality factor	Zero offset [bar]	Min pressure (prototype) [bar]	Max pressure (prototype) [bar]
Diesel 40 % load	0.1878	-0.1211	0.69	80.39
Diesel 80 % load	0.1919	-0.2859	2.15	144.56
Gas 40 % load	0.1464	-0.1001	0.44	73.10
Gas 80 % load	0.1476	-0.2196	1.54	146.21

Table 4: Scaling factors for all experiments (engine settings) analogous to the results presented in Figure 18. Also included here are the pressure ranges reported by the prototype sensor for the respective engine setting

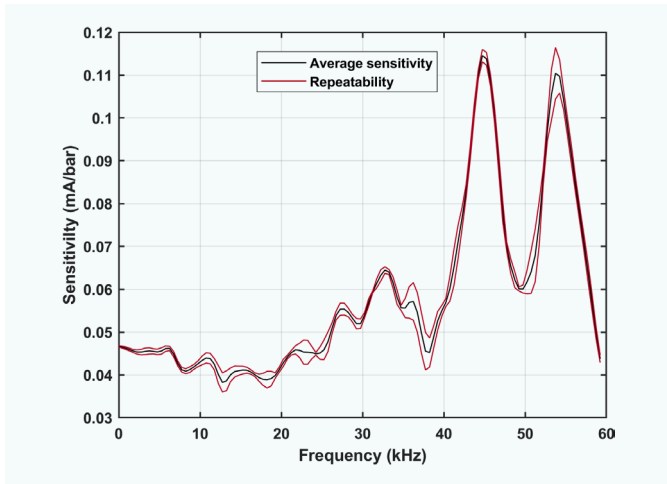


Figure 11: The transfer function at a shock amplitude of 52 bar

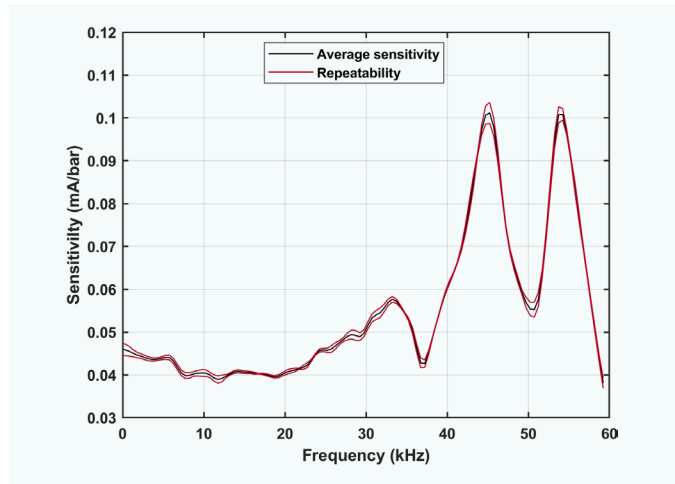


Figure 12: The transfer function at a shock amplitude of 123 bar

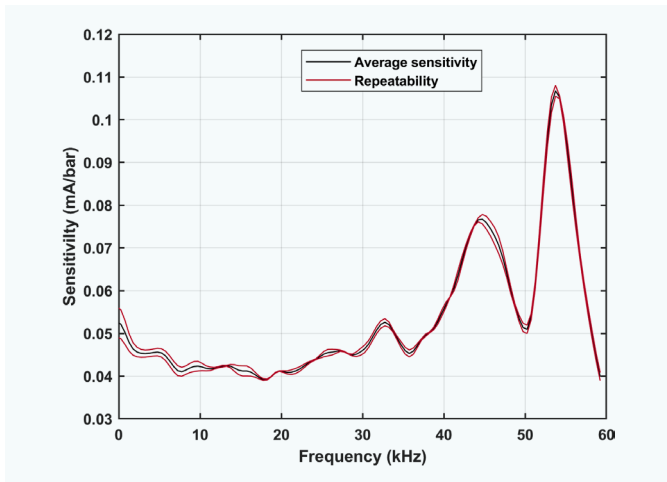


Figure 13: The transfer function at a shock amplitude of 257 bar

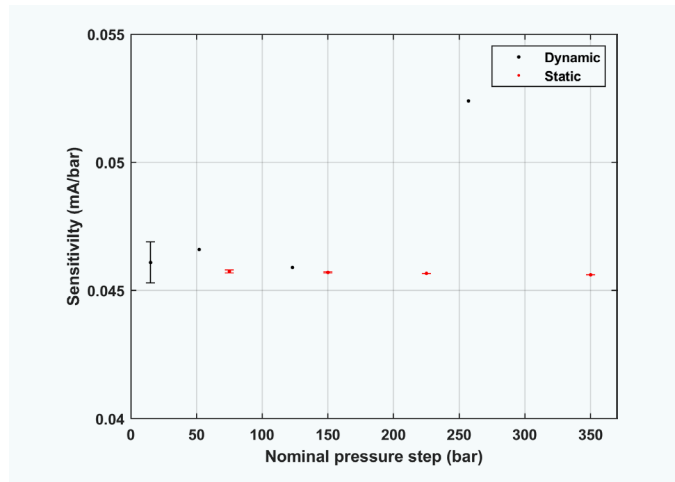


Figure 14: A comparison of the sensitivity calculated from dynamic characterization at 0 Hz and that calculated from static calibration. The error bars represent the expanded uncertainty. No uncertainty is presented for dynamic sensitivities except for the lowest nominal pressure (15 bar)

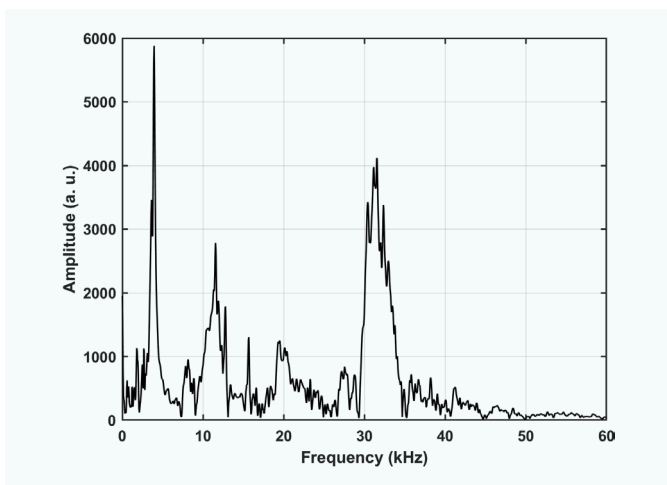


Figure 15: The vibration signal at the back plate of the shock tube

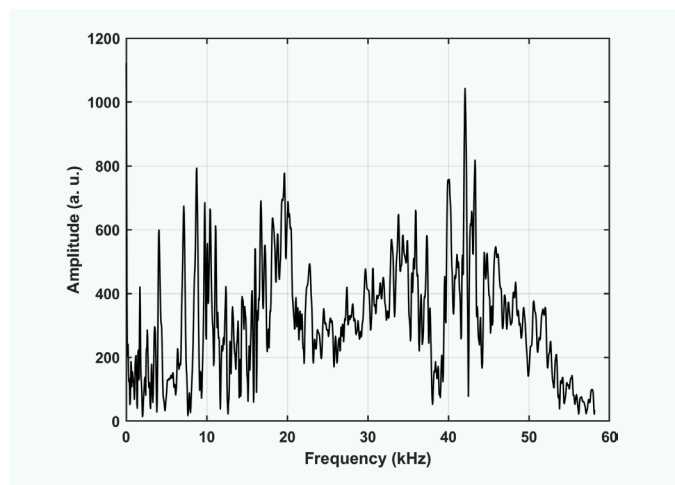


Figure 16: The vibration signal at the back plate of the amplification device

2.4 Engine tests

Procedure

The prototype sensors were mounted on separate cylinders on a Wärtsilä four-stroke piston/cylinder internal combustion engine. Reference pressure was recorded using Wärtsilä in-house sensors mounted on the same cylinders as the prototype sensors. The engine was running at 600 rpm at 40 % and 80 % loads. Separate tests were done for fuelling the engine with diesel and with gas.

The prototype sensors were connected to a Wärtsilä in-house measurement acquisition system linearly scaling the (4–20) mA sensor signal to (0–350) bar. Measurements were sampled at every 0.1° crankshaft angle. At 600 rpm this corresponds to 36000 samples per second.

Results

Of the two sensors characterized by RISE the one with serial number 10 provided a pressure signal. The one with serial number 13 failed to provide a pressure signal. Results are therefore only presented for sensor 10.

Figure 17 shows the average pressure profile over 25 recorded four-stroke cycles by the Wärtsilä reference sensor and by the prototype sensor. From the figure it is apparent that the prototype sensor reports the same profile albeit with a scaling factor.

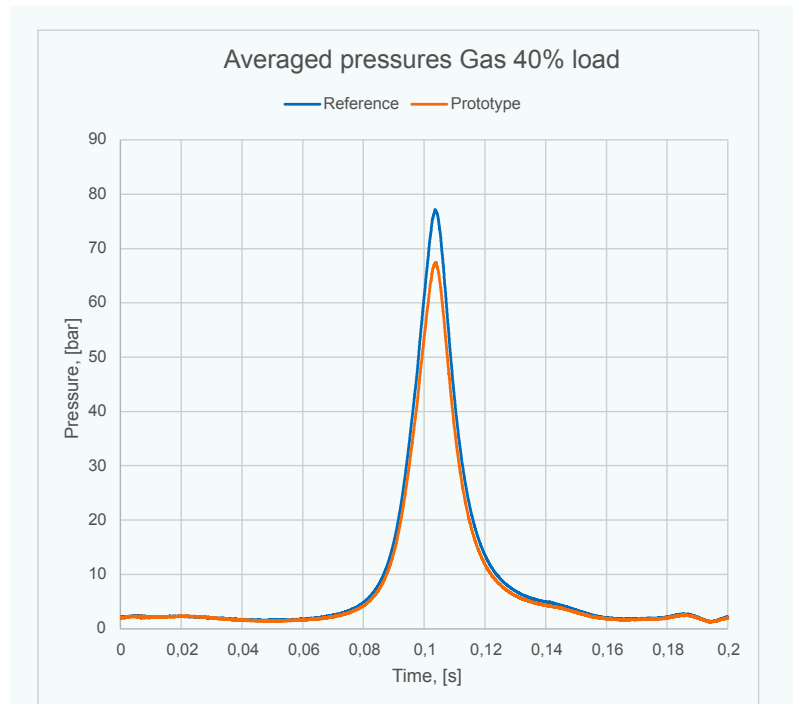
To investigate the scaling, Figure 18 plots the difference in pressure reported by the reference and the prototype sensor, as presented in Figure 17, against the pressure reported by the prototype sensor. The figure suggests that the two pressures have a zero-offset of 0.1 bar and on top of that a proportional scaling factor of 15 %. A hysteresis at higher pressures is also evident.

The same qualitative behavior is prevalent for all engine settings. The respective results are listed in Table 4.

From the results listed in Table 4 it is seen that the proportional scaling factor is invariant for different loads using the same fuel but differs considerably between different fuels. This may be due to cross-sensitivity to other process conditions, e. g., temperature, of either sensor.

From the table it can also be seen that the zero-offset seems to be dependent on the maximum pressure. This is probably an effect from pivoting of the linear regression due to larger hysteresis at higher pressures.

A less pronounced effect in the form of ripples in the prototype sensor signal is shown in Figure 19. These ripples are probably originating from excitation of the resonance frequencies found around 47 kHz during dynamic characterization of the sensor. Due to the Nyquist frequency being



18 kHz these resonances are folded. The main peak should be folded to around 11 kHz, but the side peaks originally around 35 kHz and 55 kHz, respectively, are also folded to around 0 Hz and 18 kHz. What the total aliasing would look like is impossible to tell without knowing the frequency content of the exciting pressure. However, the existence of ripples implies that the resonance oscillation of the prototype sensor has been excited and that the real cylinder pressure therefore contains events with frequencies above the current Nyquist frequency.

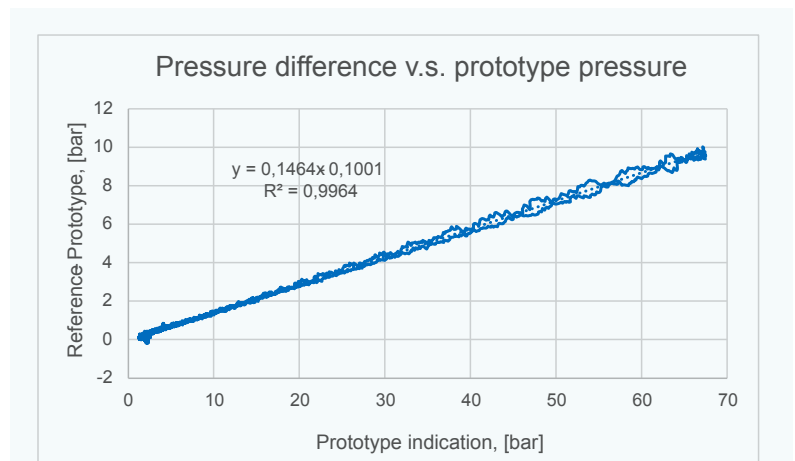
2.5 Re-characterization after engine tests

The prototype sensor 10 was returned to RISE for re-characterization after engine testing at Wärtsilä. The total testing amounted to more than is presented here and the sensor was deemed broken by Wärtsilä upon return to RISE.

However, as Table 5 shows, the sensor still

Figure 17: Pressure averaged over 25 four-stroke cycles combusting gas at 40 % load. Pressures from Wärtsilä reference sensor and prototype sensor 10 are presented

Figure 18: Difference in pressure reported by the two sensors in Figure 17 plotted against prototype pressure. Also included is a linear regression



Reference pressure (bar)	Indicated value after tests (mA)	Uncertainty, $k = 2$ (bar)
0	7,7953	0.14
75	10,6761	0.49
150	13,5565	0.53
225	16,4349	0.45
350	21,2217	0.13

Table 5: Indicated current during static calibration after engine tests

produced a signal during static calibration. Static calibration was done using the same reference and method as before. The signal was still linear over the whole pressure range but had drifted to an output between 7.80 mA and 21.22 mA.

Dynamic characterization after the engine tests, presented in Figure 20, revealed that the dynamic behavior of the sensor was basically unchanged,

except that the sensitivity had decreased. Note that in the dynamic characterization the offset is cancelled and that the sensitivity at low frequencies should be approximately 13.5 mA over 350 bar, as found from static calibration, and which equals 0.039 mA/bar. This is close to what is seen in Figure 20.

2.6 Concluding remarks

Dynamic calibration of sensors may give deeper insights into the measurement results from real processes. However, it is important that the sensors are calibrated at relevant conditions, including operating temperature, to minimize influences from secondary parameters.

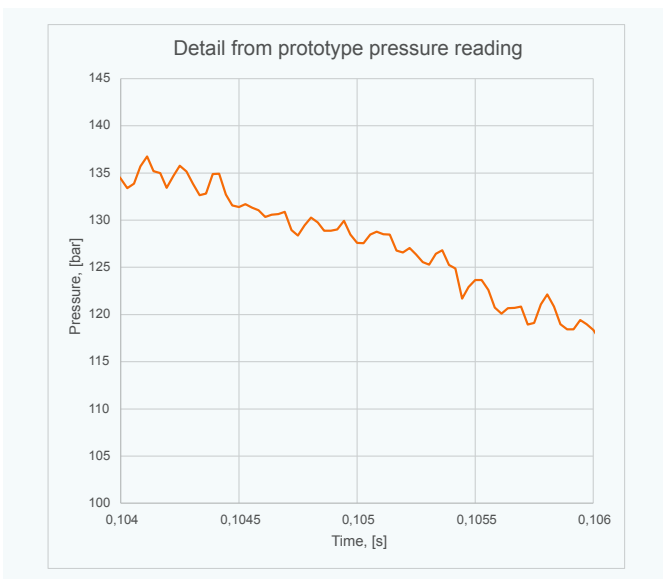


Figure 19: Detail of prototype pressure reading from a single four-stroke cycle fuelled with gas at 80 % load

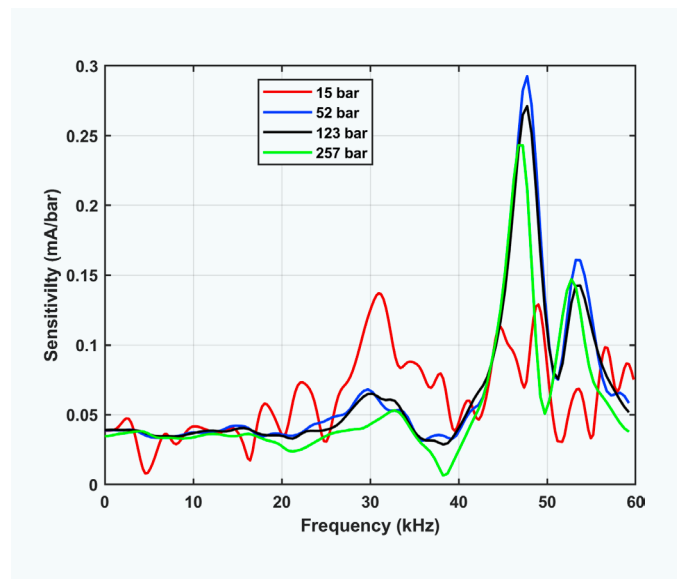


Figure 20: Transfer function for all pressure levels after the engine tests

Validation of a novel dynamic pressure sensor

M. Aspiala¹, J. Hämäläinen², T. Sillanpää³, S. Nyysönen⁴, S. Saxholm⁵, R. Högström⁶, J. Salminen⁷

1. Introduction

This article is an abridged version of chapter 5 of deliverable D5 in the EMPIR project 17IND07 – DynPT: “Validation report on the performance of the newly developed dynamic pressure and temperature sensors covering the range up to 30 MPa with a target uncertainty of 2 % and up to 3000 °C, with a target uncertainty of 5 %, respectively”. This project has received funding from the EMPIR programme co-financed by the Participating States and from the European Union’s Horizon 2020 research and innovation programme. The full report has been prepared by VSL B.V. (VSL) together with project partners from Danmarks Tekniske Universitet (DTU), Minerva meettechniek B.V. (Minerva), National Physical Laboratory (NPL), RISE Research Institutes of Sweden AB (RISE) and Teknologian tutkimuskeskus VTT Oy (VTT).



Figure 1:
VTT Dynamic Pressure Sensor

2. A novel dynamic pressure sensor

2.1 Introduction

VTT has developed a new sensing technology for dynamic pressure measurements in harsh conditions, such as inside a maritime combustion engine, where cylinder pressures can reach up to 300 bar. Moreover, sensors mounted into the cylinder head need to withstand temperatures up to 200 °C. To demonstrate the performance of the developed technology, validation measurements were performed using the primary dynamic pressure standard of VTT MIKES. Moreover, a heating option was implemented to enable SI traceable calibrations at temperatures corresponding to the actual operating environment. This is important as sensors are known to have temperature dependent sensitivities. Finally, the sensor was validated in field measurements in a real maritime combustion engine. The VTT sensor was compared to state-of-the-art piezoelectric sensors to benchmark the performance.

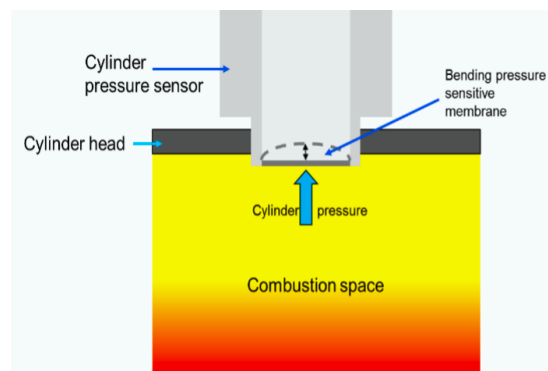


Figure 2:
VTT capacitive pressure sensor is based on sensing the change in capacitance between the bending membrane and the static electrode

¹ Dr. Markus Aspiala (VTT), National Metrology Institute VTT MIKES, E-mail: markus.aspiala@vtt.fi

² Jussi Hämäläinen (VTT), National Metrology Institute VTT MIKES, E-mail: jussi.hamalainen@vtt.fi

³ Teuvo Sillanpää (VTT), MEMS team, E-mail: teuvo.sillanpp@vtt.fi

⁴ Sami Nyysönen (VTT), Efficient engines and vehicles team, E-mail: sami.nyysonen@vtt.fi

⁵ Sari Saxholm (VTT), National Metrology Institute VTT MIKES, E-mail: sari.saxholm@vtt.fi

⁶ Dr. Richard Högström (VTT), National Metrology Institute VTT MIKES, E-mail: richard.hogstrom@vtt.fi

⁷ Juho Salminen (Vaisala Oyj), E-mail: juho.salminen@vaisala.com

Parameter	Value
Measurement range	(0...35) MPa (350 bar)
Over pressure	80 MPa (800 bar)
Temperature range*	up to 200 °C
Sensitivity	34.8 μ A/bar
Signal bandwidth	2000 Hz
Output noise, rms (0-1) kHz BW	2 bar

* Average sensor head temperature

Table 1: VTT dynamic pressure sensor performance specifications

2.2 VTT dynamic pressure sensor

The VTT dynamic pressure sensor (Figure 1) is based on a remote reading of the bending membrane (Figure 2). The sensing element is not in direct contact with the bending membrane, which makes the sensor very durable. Besides durability, a major advantage of the sensor is its unique patented capacitive sensing technology. This innovation enables reliable static calibrations of the sensor even though it is used under dynamic pressures. This in turn makes the calibration of the sensor cost-effective, because unlike dynamic calibrations, static calibrations can be carried out using existing pressure calibration instrumentation. Key performance specifications are given in Table 1.

2.3 Laboratory validation of sensor performance

2.3.1 Measurement setup

The VTT MIKES dynamic pressure standard was used as a reference for investigating the performance of the VTT sensor. The measurement standard is based on the drop-weight method, in which an impact mass is dropped onto a piston, which compress the liquid inside a measurement chamber, giving rise to a pressure pulse with

millisecond duration. The primary measurement is realized by interferometric measurement of the acceleration a of the impact mass m when it hits the piston. With the effective area A of the piston cylinder assembly, dynamic pressure $p(t)$ can be derived as:

$$p(t) = m \cdot a(t) / A. \quad (1)$$

Details on the operation of the primary standard can be found in [1].

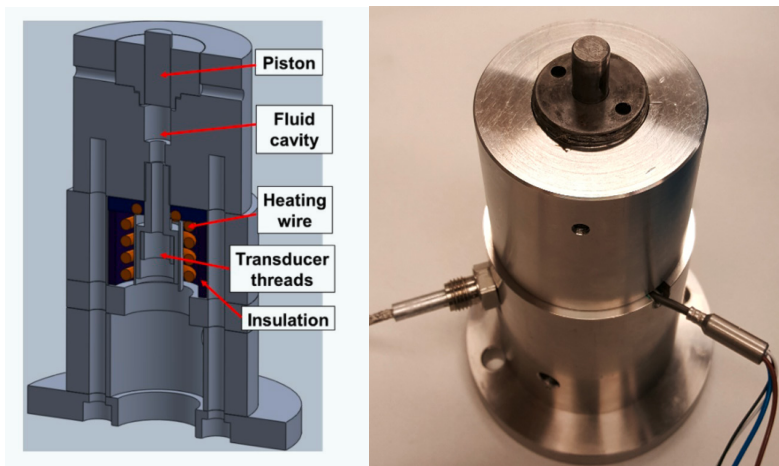
An important aspect of the laboratory validations was to perform calibrations at elevated temperatures corresponding to the actual conditions inside an engine. It is commonly known that the response of dynamic pressure sensors is influenced by temperature, known as temperature sensitivity. Despite of this, standard practice in industry is to perform calibrations only at room temperature, which might cause systematic errors when sensors are used at elevated temperatures, e. g., inside a combustion engine. In other words, to reach optimum measurement accuracy, sensors need to be calibrated at operating temperatures. To realize this, the measurement head of the VTT MIKES primary standard was modified to enable heating the sensor and measurement media up to a temperature of about 200 °C (typical for an internal combustion engine environment). In the modified measurement head, a heating wire is wrapped around the sensor thread to enable controlled heating of the sensor under calibration, as well as the fluid in contact with the sensor (Figure 3). Silicon oil, similar to what is used in thermal baths, was used as pressure medium in the fluid cavity. The oil has good thermal properties and withstands heating to high temperatures (up to 300 °C).

2.3.2 Validation results

Calibration measurements were performed at peak pressures of 7 MPa, 12 MPa, 20 MPa, and 30 MPa at temperatures of 20 °C, 120 °C, and 180 °C. Generated pressure pulses have a half sine shape and a duration of around 4 ms (Figure 4), i. e., the peak pressure and pulse shape correspond to pressure pulses inside an internal combustion engine. To benchmark the performance of the VTT sensor, calibrations were also performed for a commercial piezoelectric sensor.

Calibration results (Figure 5 and Figure 6) show that both sensors have similar characteristics with respect to linearity, repeatability, accuracy, and temperature sensitivity. Both sensors exhibit a slight drop in sensitivity at lower pressure values of around 10 MPa. This is typical for dynamic pressure sensors, and consequently sensitivity values are often stated for different ranges separately. Also, the repeatability is similar

Figure 3: Modified measurement head with heating option. The sensor is connected from below using sensor threads of the measurement head. The fluid inside the cavity is in contact with the sensor membrane, thus transferring pressure generated by piston compression to the sensor



and within $\pm 0.5\%$ of reading. The temperature sensitivity was about $1\%/100\text{ }^\circ\text{C}$ for both sensors. This value corresponds well with the manufacturer specifications stating a temperature sensitivity of less than $\pm 0.02\%/^\circ\text{C}$. Moreover, the temperature sensitivity was found to be constant for different pressures.

One of the key features of the VTT sensor is that it can be calibrated at static pressures, unlike commercial piezoelectric sensors that only sense pressure changes. To investigate the validity of such a calibration, a static calibration with a pressure balance was performed and the results were compared to a dynamic calibration performed with the VTT MIKES dynamic pressure primary standard. The results of the static and dynamic calibration were found to agree within 0.4% (Figure 7), which is well within the 1.5% measurement uncertainty of the dynamic calibration. The results indicate that for the VTT sensor a factory calibration using static calibration methods can be made instead of a dynamic calibration. This implies significant cost savings, as existing pressure calibration equipment can be used. However, it is important to note that a static calibration will not provide SI traceability for a sensor used for dynamic measurements. To fully characterize sensor performance and ensure reliability of measurements, dynamic pressure sensors need to be calibrated against dynamic measurement standards.

2.4 Engine tests for validating sensor performance

2.4.1 Engine test measurement setup

Cylinder pressure sensors are exposed to extremely harsh conditions, where cyclic pressure and temperature changes take place, as well as strong vibrations from the engine. To validate sensor performance and reliability in real operating environments, engine tests are necessary.

Engine tests were performed in a four-stroke Wärtsilä marine diesel engine (type Wärtsilä Vasa 4R32) with rated brake power 1640 kW and engine speed 750 rpm (Figure 8). The performance of the VTT sensor was compared against Kistler piezoelectric sensors (type 7013C/CA, Quartz Pressure Sensor for Engine Diagnostics). The Kistler sensors have been factory calibrated by the manufacturer. Before testing, the sensors had been in engine use only for 364 drive hours, i. e., the sensors can be considered as “new” and in good operational condition.

Sensors were mounted into the cylinder head using shoulder sealing so that the sensors were located as close to the combustion chamber as

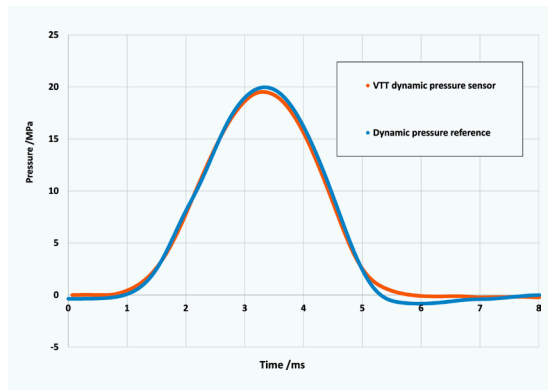


Figure 4: Pressure pulse generated with the VTT MIKES dynamic pressure standard and corresponding reading of the VTT dynamic pressure sensor

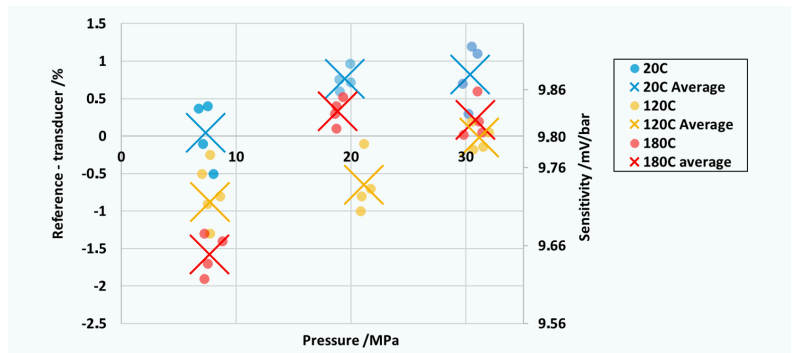


Figure 5: Calibration results of the VTT dynamic pressure sensor

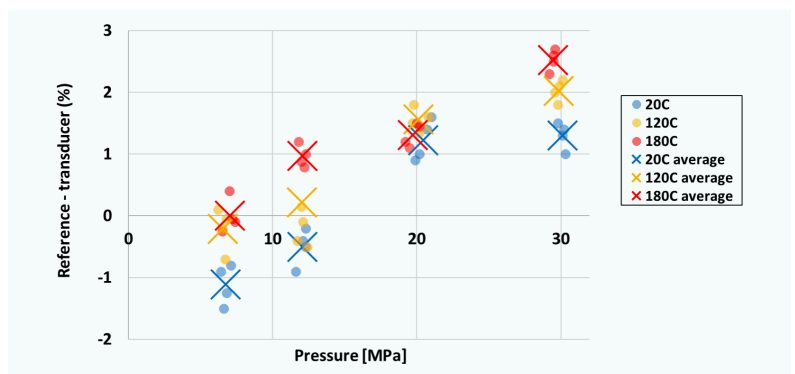


Figure 6: Calibration results for a commercial piezoelectric sensor

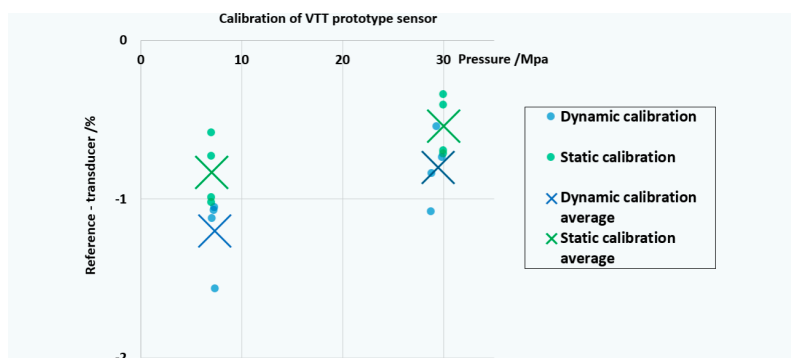
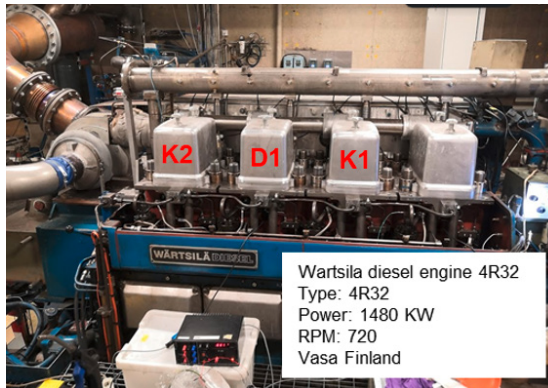


Figure 7: Comparison of static and dynamic calibration results of the VTT dynamic pressure sensor

Figure 8: Marine test engine. VTT sensor (D1) and Kistler sensors (K1 and K2) mounted in the heads of separate cylinders



possible, and thus potential disturbance caused by the connecting volume was minimized. The sensors were installed into different cylinders due to limited space for mounting. Before engine tests, a static calibration was performed for the VTT sensor to adjust the sensor output (results shown in Figure 9).

2.4.2 Engine test results

Engine tests were performed at engine loads of 90 %, 75 %, 50 %, 25 %, and 17 %. Each test run lasted for 3.5 hours. Results at 90 % engine load show that the pressure pulses measured by different sensors have a similar shape (Figure 10). Small differences of about ± 2 % can be seen when comparing peak pressure values (Figure 11). The observed deviations in peak pressure readings are similar to the cylinder-to-cylinder pressure variations of this type of engine.

Results at low engine loads of 25 % are similar to the results at a high load of 90 % (Figure 12). All sensors are able to track the pressure variations, which can be seen as a similar pulse shape. Also, at low engine loads, small differences of about ± 2 % were observed in the peak pressures measured by different sensors (Figure 13). The bump on the rising edge of the pressure curve is caused by unstable operation of the engine at low loading conditions.

From the summary of the engine test results in Table 2, it can be seen that the VTT sensor is showing slightly higher values than the Kistler

sensors at high engine loads (high pressures), and slightly lower values at low engine loads (low pressures). This indicates that there might be a small difference in the linearity of the sensors. Further investigations of the Kistler sensor, e.g., by calibrating the sensor against the VTT MIKES primary standard, is needed to verify this. During this rather short (2 day) engine testing, no drift in the sensors' response was observed.

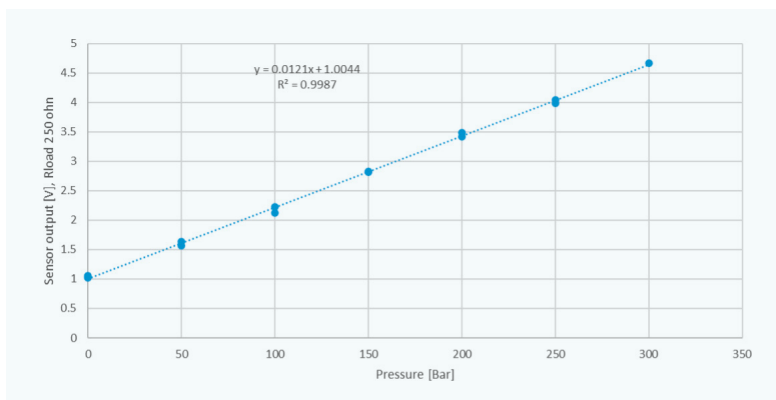
2.5 Conclusions

Validation results show that the VTT sensor performance is comparable to a state-of-the-art piezoelectric sensor, with respect to accuracy, repeatability, linearity, and temperature sensitivity. The operation of the VTT sensor was successfully demonstrated in a real engine environment. An agreement of ± 2 % was achieved when compared to the VTT MIKES primary standard and when compared against a piezoelectric sensor, which is considered an industry standard. Moreover, it was shown that a static calibration provides similar results as a dynamic calibration for the VTT sensor. Consequently, a factory calibration can be performed using existing (static) pressure standards, which gives VTT technology a significant cost advantage compared to commercial piezoelectric sensors, which need to be calibrated by means of dynamic methods.

References

- [1] J. Salminen, S. Saxholm, J. Hämäläinen and R. Höglström, "Advances in traceable calibration of cylinder pressure transducers," *Metrologia*, pp. 57(4), 045006, 2020.

Figure 9: Linearization of the VTT sensor output based on static calibration



Sensor	Peak pressure [bar]				
	90 % load	75 % load	50 % load	25 % load	17 % load
Kistler (K1)	149.3	134.3	105.2	65.7	51.4
VTT (D1)	153.2	137.0	103.9	61.7	47.8
Kistler (K2)	146.5	131.1	103.1	64.5	50.8
Injection pressure	750.6	680.3	570.3	460.9	430.1

Table 2: Summary of engine test results

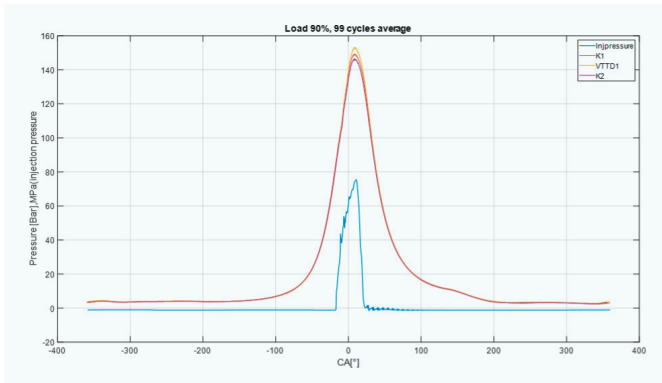


Figure 10: Cylinder pressure at 90 % load averaged over 99 cycles for the VTT sensor (VTTD1) and the Kistler sensors (K1 and K2) as a function of crankshaft rotation angle (CA). Injection pressure (in MPa) is shown in blue

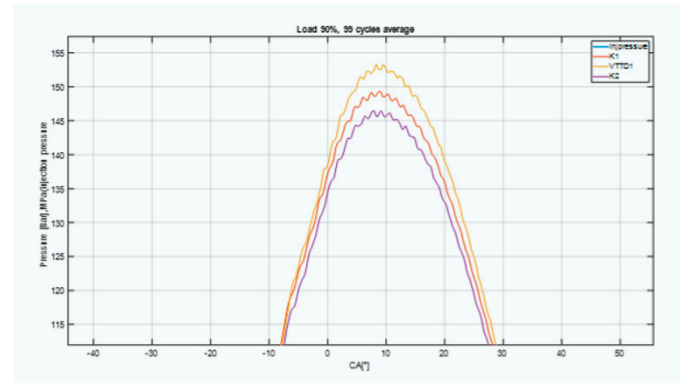


Figure 11: Peak pressure at 90 % load averaged over 99 cycles for the VTT sensor (VTTD1) and the Kistler sensors (K1 and K2)

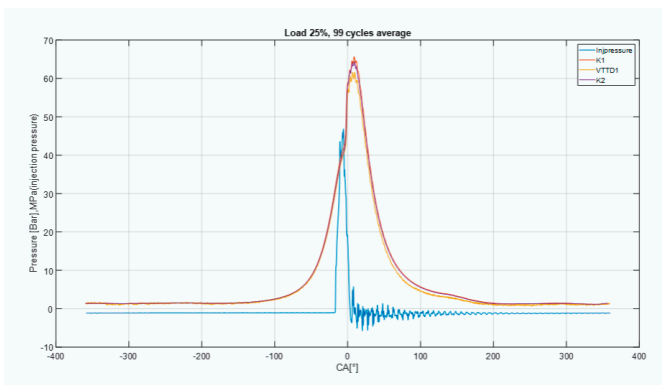


Figure 12: Cylinder pressure at 25 % load averaged over 99 cycles for the VTT sensor (VTTD1) and the Kistler sensors (K1 and K2) as a function of crankshaft rotation angle (CA). Injection pressure (in MPa) is shown in blue

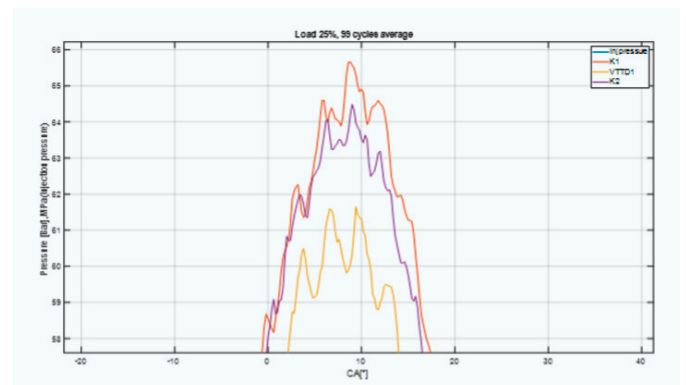


Figure 13: Peak pressure at 25 % load averaged over 99 cycles for the VTT sensor (VTTD1) and the Kistler sensors (K1 and K2)

Ultraschall-exposimeter für den praktischen Arbeitsschutz

An vielen modernen Arbeitsplätzen liegen dominante Schallbelastungen im hochfrequenten Hörschallbereich oder sogar durch Ultraschall vor. Diese Lärmexposition muss auch in diesem Frequenzbereich mit geringer Messunsicherheit erfasst werden können. Die PTB hat hierzu gemeinsam mit dem Institut für Arbeitsschutz das neuartige Konzept eines Hochfrequenzpersonenschallexposimeters entworfen. Das kompakte Messgerät ermöglicht die Erfassung einer Vielzahl von Messgrößen typischer Handschallpegelmesser – erweitert bis in den Ultraschallbereich – und liefert so einen wichtigen Beitrag zu einem verbesserten Arbeitsschutz.

Herkömmliche Handschallpegelmesser und Personenschallexposimeter beschränken sich auf die Messung von Hörschall oder Hörschall in Anwesenheit von Ultraschall. Die Schallbelastung von Beschäftigten an vielen Arbeitsplätzen durch hochfrequenten Hörschall oder Ultraschall macht jedoch die valide Bestimmung der Lärmexposition bis in den Ultraschallbereich hinein erforderlich. Nur so kann der gesetzlichen Verpflichtung eine Gefährdungsbeurteilung auch in diesem Frequenzbereich durchzuführen vollumfänglich nachgekommen werden.

Gemeinsam mit dem Institut für Arbeitsschutz (IFA) der Deutschen Gesetzlichen Unfallversicherung (DGUV) wurde an der PTB ein Hochfrequenzpersonenschallexposimeter konzipiert, welches typische Exposimetermessgrößen gemäß IEC 61252 und relevante Messgrößen von Schallpegelmessern gemäß IEC 61672-1 bis mindestens 40 kHz unter Berücksichtigung diverser Zeit- und Frequenzbewertungen bestimmen kann. Mit seiner eigens hierfür programmierten Messgerätesoftware ermöglicht das Exposimeter die Erfassung eines zeitaufgelösten Oktav- oder Terzbandspektrums und die Aufzeichnung der lokalen Klimadaten. Durch die bereitgestellte Konnektivität zu einem PC oder einem mobilen Endgerät ist die Konfiguration sowie die Steuerung des Exposimeters und das Auslesen von Messdaten möglich.

Wirtschaftliche Bedeutung

Durch die gesetzliche Verpflichtung der Lärmmessung besteht Bedarf an einem solchen Gerät bei Arbeitgebenden und Beschäftigten des Arbeitsschutzes. Als erstes Messgerät zur personengebundenen Messung der Schallexposition bis in den Ultraschallbereich kommt dem Hochfrequenzpersonenschallexposimeter eine beträchtliche wirtschaftliche Bedeutung zu.

Entwicklungsstand

Das Konzept wurde im Rahmen eines TransMeT-Projektes bereits als Funktionsmuster realisiert. Bei Interesse bieten wir Ihnen an, in gemeinsamen Projekten diese Erfindung weiterzuentwickeln oder direkt zu lizenzieren.



Funktionsmuster des Hochfrequenzpersonenschallexposimeters an einem Kunstkopf

Vorteile:

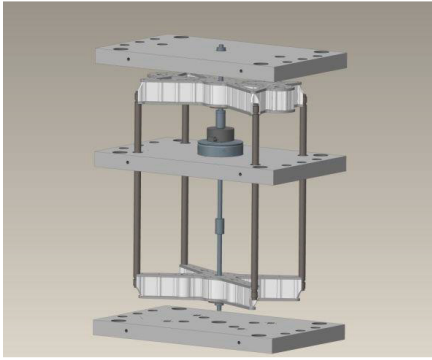
- Messung von hochfrequentem Hörschall und Ultraschall
- Bestimmung der personenbezogenen Schallexposition
- Verbessertes Arbeitsschutz

Ansprechpartner:

Andreas Barthel
 Technologietransfer
 Telefon: +49 531 592-8307
 Telefax: +49 531 592-69-8307
 E-Mail: technologietransfer@ptb.de

Christoph Kling
 1.63 Geräuschesmesstechnik

PTB-Nummer 7095



Schematische Darstellung des Rahmens zur Umlenkung der Krafteinleitung von Zug- auf Druckkraft und umgekehrt

Vorteile:

- Messung von Zug- und Druckkräften in einem Aufbau
- Keine Umrüstung erforderlich
- Messszenarien mit Nulldurchgang
- Nur eine Klimakammer notwendig

Kraftmesseinrichtung für Zug- und Druckkräfte

Kraftmesseinrichtungen messen entweder Zug- oder Druckkräfte und müssen für den jeweils anderen Betriebszustand umgerüstet werden. Bei der neuen PTB-Umlenkeinrichtung entfallen diese Umrüstzeiten. Dadurch sind neuartige und somit schnellere Kalibrierungen auch für den gesamten Zug- Druckkraft Messbereich mit Nulldurchgang möglich. Ein weiterer Vorteil z. B. bei hochgenauem Messen ist, dass nur eine gemeinsame Klimakammer für Zug- und Druckmessungen benötigt wird. Das Umlenkprinzip kann für Kraft-Messeinrichtungen mit direkter Massewirkung, Hebel- oder hydraulischer Übersetzung, Referenzaufnehmer und anderen Prinzipien aber auch Werkstoffprüfmaschinen eingesetzt werden.

Die Umlenkeinrichtung ist mit drei verfahrbaren Traversen so konstruiert, dass in der Kraftmesseinrichtung innerhalb eines Aufbaus die Belastung durch Zug- und Druckkräfte erfolgen kann. In einer weiteren Ausführungsform ist es ebenfalls möglich, eine Kraftumleitung über ein Lager zu realisieren. Hierbei wird im Druckeinbauraum zunächst die Druckkraft über die Belastungskörper erzeugt. Eine Zugkraftenerzeugung wird dann durch eine Kraftumlenkung über ein entsprechendes Lager erreicht.

Wirtschaftliche Bedeutung

Auf Basis der neuen Umlenkeinrichtung können innovative Kraftmesseinrichtungen auch für Anwendungen mit Nulldurchgang konzipiert werden und bieten Kalibrierlaboratorien in Forschung und Industrie sowie anderen NMIs neue anwendungsnahe Kalibriermöglichkeiten.

Entwicklungsstand

Die Erfindung wird derzeit in der PTB als Funktionsmuster entwickelt. Ein Patent wurde erteilt. Lizenzen für die Nutzung dieser neuen Methode sind verfügbar.

Ansprechpartner:

Andreas Barthel
 Technologietransfer
 Telefon: +49 531 592-8307
 Telefax: +49 531 592-69-8307
 E-Mail: technologietransfer@ptb.de

Dr. Rolf Kumme
 Fachbereich Festkörpermechanik

PTB-Nummer 0349

Optisches Positions- und Winkelmessgerät basierend auf Mehrstrahlinterferenzen

Zur hochgenauen und gleichzeitigen Messung von Winkeländerungen (Nick-, Gier- und Rollwinkel) ist ein neues Verfahren entwickelt worden, welches einfach in Messprozesse zu integrieren ist. Eine Lichtquelle, die ein Interferenzmuster erzeugt, wird auf einem Objekt, dessen Bewegung gemessen werden soll, angebracht. Über zwei Bildsensoren wird das Interferenzbild ausgewertet. Durch die Auswertungen kann die Position und insbesondere die Winkelposition des Objekts mit hoher Genauigkeit bestimmt werden.

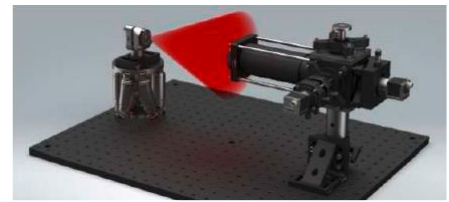
Die derzeit etablierten Verfahren zur hochgenauen und gleichzeitigen Messung von Positions- und Winkeländerungen eines Objektes sind nicht über genügend großen Winkelbereich mit hoher Genauigkeit einsetzbar. Diese Einschränkung ist offensichtlich, wenn große Freiformflächen vermessen werden sollen, beispielsweise Spiegelsegmente für astronomische Teleskope oder Spiegel für die EUV-Lithografie. In dem neuen PTB-Verfahren wird ein zur bisherigen Technik alternatives Verfahren zur hochpräzisen Winkelmesstechnik dargestellt. Der Aufbau besteht aus einer Lichtquelle, die auf dem bewegten Objekt angebracht ist, und einem Detektor, der das emittierte Licht mit zwei Bildsensoren detektiert. Als Lichtquelle dient ein frequenzstabilisierter HeNe-Laser. Mit dem Licht wird ein Interferenzmuster erzeugt, dies kann auf verschiedene Weisen geschehen. Die Detektionseinheit nimmt das Interferenzmuster auf, und berechnet die Position und die Winkel der Strahlen des Interferenzmusters. Anhand dieser Information werden die Position und Winkelstellung der Lichtquelle bestimmt. Der Winkelmessbereich ist dabei nur durch den Öffnungswinkel der Lichtquelle beschränkt. Der Detektorarm für die Winkelmessung entspricht einem Autokollimator und kann den Winkel vieler Strahlen der Lichtquelle gleichzeitig bestimmen. Wenn ein Strahl den Messbereich verlässt, kommt ein neuer Strahl in den Messbereich, wodurch er beliebig erweitert wird.

Wirtschaftliche Bedeutung

Durch die Kombination aus abbildenden Systems und Autokollimator, zur Messung von Winkel und Position, eröffnen sich neue Möglichkeiten im Bereich der Formmessung, Deflektometrie, Positionierungssysteme und Projektion des Musters als Winkelreferenz.

Entwicklungsstand

Die Erfindung wurde zum deutschen Patent angemeldet. Lizenzen für die Nutzung sind verfügbar.



CAD-Modell des Aufbaus

Vorteile:

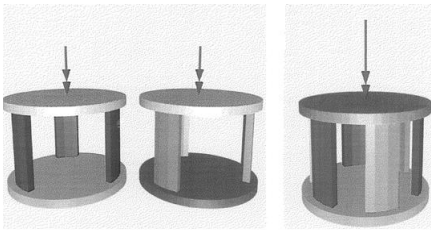
- Großer Messbereich
- Hohe Auswertegenauigkeit
- Preiswerte Komponenten

Ansprechpartner:

Nataša Lalović
 Technologietransfer
 Telefon: +49 531 592-8306
 Telefax: +49 531 592-69-8306
 E-Mail: Technologietransfer@ptb.de

Jan Spichtinger
 4.21 Form- und Wellenfrontmetrologie
 4.22 Ebenheitsmetrologie

PTB-Nummer 0529



Schematischer Aufbau eines Built-Up-Systems

Vorteile:

- Kalibrierung von Messwertaufnehmern für Drehmomente bis zu mehreren MN·m
- Vervielfachung des Messbereiches von Drehmomentaufnehmern
- Verschachtelung einzelner Drehmomentaufnehmer möglich

Built-Up-System für Drehmomente

Die rückführbare Kalibrierung von Drehmomentmessgeräten im Messbereich oberhalb von 1 MN·m ist bisher weltweit nicht möglich, aber eine Anlage für 5 MN·m befindet sich im Aufbau. Die neue Technologie der PTB gestattet jedoch, durch die Verschachtelung mehrerer Messwertaufnehmer eine gezielte Vervielfachung des zu kalibrierenden Bereichs. Durch dieses Messprinzip können Messwertaufnehmer kombiniert und für größere Belastungen in der Drehmomentmessung ausgelegt werden.

Built-Up-Systeme sind bei Kraftaufnehmern in longitudinaler Kombination derzeit bekannt, jedoch prinzipbedingt nicht für torsive Verformungskörper wie z.B. bei Drehmomentaufnehmern geeignet. Unter einem Built-Up-System versteht man die Kombination mehrerer Messsysteme, die obwohl einzeln kalibriert auch in Kombination einen kalibrierten Messwert ergeben – jedoch mit der entsprechenden mehrfachen Verstärkung. Das neuartige Built-Up-System der PTB ermöglicht es, bekannte Verformungskörper für die Drehmomentmessung durch spezifische Flansche bzw. Sensorgeometrien z. B. in einem „Käfigprinzip“ ineinander zu verschachteln. Somit werden einzelne kalibrierte Aufnehmer zu einem Gesamtsystem kombiniert. Das Verfahren bietet insbesondere bei hohen Drehmomenten einen wesentlich geringeren apparativen Aufwand bei der Kalibrierung.

Wirtschaftliche Bedeutung

Die Kalibrierung von Drehmomentaufnehmern im MN·m-Bereich ist insbesondere beim Einsatz großer Antriebswellen von Schiffen, der Windenergie und bei konstruktiven Belastungstests in der Bauphysik zu sehen. Durch sie wird eine sicherheitsrelevante Überprüfung derzeit verwendeter Messwertaufnehmer über den gesamten Messwertbereich ermöglicht. Darüber hinaus lassen sich, mit begrenztem Aufwand, auf Basis bestehender Messeinrichtungen Build-Up-Systeme für die Produktions- und Qualitätsüberwachung erstellen, die so den Messbereich verdoppeln oder verdreifachen können.

Entwicklungsstand

Das Patent zum Konzept ist unter DE 10 2010 024812 A1 erteilt. Ein Funktionsmuster wird im Rahmen von weiteren Forschungstätigkeiten erstellt. Lizenzen für die Nutzung dieses Verfahrens sind verfügbar.

Ansprechpartner:

Andreas Barthel
 Technologietransfer
 Telefon: +49 531 592-8307
 Telefax: +49 531 592-69-8307
 E-Mail: technologietransfer@ptb.de

Dr. Rolf Kumme
 Fachbereich 1.2 Festkörpermechanik

PTB-Nummer 0270

Faserbasierte Rollwinkelmessung

Um den Rollwinkel bei hochpräzisen Linearverstellern in der optischen Messtechnik oder in der industriellen Fertigung absolut zu messen, besitzt die PTB ein erteiltes Patent, das einen Autokollimator mit einem Rollwinkelmessgerät betrifft. Dabei kann der Rollwinkel mit einer geringen Messunsicherheit gemessen werden, wodurch in Kombination mit dem Autokollimator die Bestimmung aller drei Winkelpositionen eines Objekts möglich ist.

Außerdem kann dieses Winkel-Messsystem zur Topografie-Messung einer Oberfläche in Verbindung mit einem scannenden Topografie-Sensor verwendet werden.

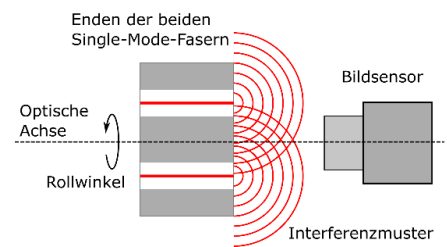
Zwei eng zueinander positionierte optische Single-Mode-Fasern befinden sich auf einem bewegten Objekt, beispielsweise auf einem Verschiebetisch. Das aus den Fasern emittierte Laserlicht erzeugt ein Interferenzmuster, das auf einen Bildsensor fällt, der an einem unbewegten Bezugsteil montiert ist. Beim Rollen des bewegten Objektes um die Achse der linearen Bewegung dreht sich das Interferenzmuster mit. Das Interferenzmuster wird mittels zeilenweiser Fast-Fourier-Transformation (FFT) der Sensordaten ausgewertet, und daraus wird seine Rotation berechnet. Der Messbereich von 360° Grad ist mit einer Auflösung von besser als 0,001° erfassbar. Zudem ist das Verfahren weitestgehend unempfindlich gegenüber kleinen Nick- und Gier-Bewegungen. Für die Erzeugung des Interferenzmusters kann prinzipiell jede Wellenlänge verwendet werden.

Wirtschaftliche Bedeutung

Die Erfindung dieses Autokollimators mit Rollwinkelmessung ersetzt komplexere Verfahren der Rollwinkelmessung, die auf einer Polarisationsmessung beruhen. Sie ist für scannende Systeme in der Oberflächenmesstechnik geeignet. Hersteller optischer Komponenten können es zur Qualitätssicherung bei der Herstellung von Linearverstellern einsetzen. Ebenso kann die hochpräzise Zuführung von Bauteilen im Produktionsprozess überwacht und gesteuert werden.

Entwicklungsstand

Ein deutsches Patent ist unter der Nr. DE 10 2020 113 675 B4 vorhanden. Lizenzen für die Nutzung sind verfügbar.



Die beiden faserbasierten Punktlichtquellen befinden sich auf dem bewegten Objekt. Mit dem Bildsensor wird das Interferenzmuster detektiert, dessen Orientierung den Rollwinkel angibt.

Vorteile:

- Auflösung besser als 0,001°
- Einfache Bauelemente
- Unempfindlich gegenüber Nick- und Gier-Bewegungen

Ansprechpartner:

Nataša Lalović
 Technologietransfer
 Telefon: +49 531 592-8306
 Telefax: +49 531 592-69-8306
 E-Mail: technologietransfer@ptb.de

Jan Spichtinger
 4.21 Form- und
 Wellenfrontmetrologie
 4.22 Ebenheitsmetrologie

PTB-Nummer 0513

 **PTB** mitteilungen

Impressum

Die PTB-Mitteilungen sind metrologisches Fachjournal der Physikalisch-Technischen Bundesanstalt, Braunschweig und Berlin. Als Fachjournal veröffentlichen die PTB-Mitteilungen wissenschaftliche Fachaufsätze zu metrologischen Themen aus den Arbeitsgebieten der PTB. Die PTB-Mitteilungen stehen in einer langen Tradition, die bis zu den Anfängen der Physikalisch-Technischen Reichsanstalt (gegründet 1887) zurückreicht.

Herausgeber

Physikalisch-Technische Bundesanstalt (PTB)

ISNI: 0000 0001 2186 1887

Postanschrift:

Postfach 33 45,
38023 Braunschweig

Lieferanschrift:

Bundesallee 100,
38116 Braunschweig

Redaktion/Layout

Presse- und Öffentlichkeitsarbeit, PTB

Priv.-Doz. Dr. Robert Wynands (wissenschaftlicher Redakteur)

Dr. Dr. Jens Simon (verantwortlich)

Sabine Siems (Redaktion / Lektorat)

Sebastian Baumeister / stilsicher.design (Layout / Satz)

Telefon: (05 31) 592-82 02

Telefax: (05 31) 592-30 08

E-mail: sabine.siems@ptb.de

Erscheinungsweise und Copyright

Die PTB-Mitteilungen erscheinen viermal jährlich. Alle Rechte vorbehalten. Kein Teil dieser Zeitschrift darf ohne schriftliche Genehmigung des Verlages vervielfältigt oder verbreitet werden. Unter dieses Verbot fällt insbesondere die gewerbliche Vervielfältigung per Kopie, die Aufnahme in elektronische Datenbanken und die Vervielfältigung auf CD-ROM und in allen anderen elektronischen Datenträgern.

Printed in Germany ISSN 0030-834X

Die fachlichen Aufsätze aus dieser Ausgabe der PTB-Mitteilungen sind auch online verfügbar unter:
doi: 10.7795/310.20220499



Bundesministerium
für Wirtschaft
und Klimaschutz

Die Physikalisch-Technische Bundesanstalt, das nationale Metrologieinstitut, ist eine wissenschaftlich-technische Bundesoberbehörde im Geschäftsbereich des Bundesministerium für Wirtschaft und Klimaschutz.



Bundesministerium
für Wirtschaft
und Klimaschutz

Die Physikalisch-Technische Bundesanstalt, das nationale Metrologieinstitut, ist eine wissenschaftlich-technische Bundesoberbehörde im Geschäftsbereich des Bundesministeriums für Wirtschaft und Klimaschutz.



Physikalisch-Technische Bundesanstalt
Nationales Metrologieinstitut

Bundesallee 100
38116 Braunschweig

Presse- und Öffentlichkeitsarbeit

Telefon: (05 31) 592-82 02
Fax: (05 31) 592-30 08
E-mail: presse@ptb.de
www.ptb.de